博士論文

Electromagnetic and Mechanical Properties Reconstruction of Biological Tissues Using MRI

（MRI を用いた生体組織の電磁気および機械特性再構成）

伏見幹史

指導教員　奈良高明 教授

2021 年 3 月

東京大学大学院情報理工学系研究科システム情報学専攻

Abstract

This thesis explores EPT, QCM, MRE, and QSM, which are noninvasive modalities to reconstruct electrical, mechanical, and magnetic properties of biological tissues using MRI. The material properties of biological tissues reflect physiological and pathological conditions. Therefore, an early diagnosis of a lesion is expected by detecting changes in these material properties. First, this thesis shows that EPT, QCM, and MRE can be formulated in a common impedivity inverse problem framework. Then, a global and direct method is proposed that can reconstruct three-dimensional (3D) material properties, which has not been achieved using conventional methods. Second, we improve the conductivity reconstruction in the framework of the simultaneous reconstruction of electromagnetic properties, i.e., QCM and QSM by applying our proposed QCM reconstruction method, and reveal its effectiveness in vivo.

In Chapter 2, a new formulation of the EPT problem is described, which considers the impedance estimation problem. Further, a method is proposed to reconstruct electrical properties by solving the integral equations (IEs) derived from Helmholtz's decomposition of the vector field. The proposed method achieves accurate reconstruction at different tissue boundaries and exhibits robustness against noise. Its effectiveness was confirmed by numerical simulations and verified by phantom experiments.

In Chapter 3, we discuss how the MRE problem can be described in a common framework with the EPT problem and the IE for the mechanical properties is derived based on Helmholtz's decomposition for tensor fields. Numerical simulations show that the proposed method can reconstruct the general 3D distribution without making the assumptions about compressibility that are common in many extant methods.

In Chapter 4, we propose a boundary-value-free reconstruction method for EPT that does not require EPs on the boundary of the region of interest (ROI). This is accomplished by modifying our previous method that reconstructs EPs in a slicewise manner. In addition, a hybrid reconstruction formula is derived that only uses the values of EPs only on the fraction of the boundary of the ROI to reduce the artifact when EP values are available on a fraction of the boundary. In future work, this method will be extended to the Helmholtz's decomposition-based reconstruction method proposed in Chapter 2.

In Chapter 5, conductivity and susceptibility reconstruction are performed simultaneously from a single image acquisition. A method for maximum likelihood estimation of the B1 phase and the B0 field is proposed by considering the nonlinearity of the MRI signal equation. In addition, we apply the proposed QCM method presented in Chapter 2 with regularization based on morphological information used in the susceptibility reconstruction to stabilize the B1 field to conductivity inversion. While conductivity and susceptibility images have a consistent structure, they may give different contrasts as shown in the analysis of in vivo data. Therefore, extra information can be provided by performing conductivity reconstruction in addition to susceptibility reconstruction.

Finally, Chapter 6 concludes the thesis.

Acknowledgements

First and foremost, I would like to thank my supervisor Prof. Takaaki Nara, who has greatly influenced and supported me in pursuing my doctoral studies. His guidance was essential for me to conduct this research. Through daily discussions, I learned how to understand physical phenomena and how to construct mathematical logic.

I am also very grateful to Dr. Keisuke Hasegawa and Dr. Hiroki Miyazako for their constant guidance throughout my research. Their extensive knowledge spanning a wide range of fields has been of significant benefit to my research.

Ms. Keiko Kaneko made all the necessary arrangements in terms of research and conference support services, which helped my research activities run smoothly.

I had many discussions with students in my lab, including weekly meetings, and we were able to learn from each other. Particular thanks in this respect go to fellow members of the MRI project: Mr. Naohiro Eda and Mr. Osamu Kojima.

The MRI experiments in this study were conducted under the supervision of the MRI Steering Committee of the Center for Evolutionary and Cognitive Sciences, University of Tokyo. In particular, Dr. Hironori Nakatani was very attentive and helpful in all aspects concerning use of the MRI scanner. I am also grateful to Mr. Katsutoshi Murata, Siemens Healthcare K.K., for his invaluable support in manipulating the MR scanner.

Part of this study was conducted in Prof. Yi Wang's lab at Cornell University; his guidance and steadfast support were invaluable in terms of helping me to complete this thesis.

I am deeply indebted to Dr. Pascal Spincemaille and Dr. Thanh Nguyen for their useful advice. Their expertise and guidance helped me to hone my knowledge and skills at the intersection between engineering and biomedicine.

Dr. Kelly Gillen offered constant help in terms of administration and logistics. Her generous assistance made it possible for me to carry out my research activities in the tough and challenging environment of living overseas.

At Cornell University, I was fortunate to have many outstanding colleagues, notably, Dr. Junghun Cho, Dr. Ramin Jafari, Dr. Yan Wen, Dr. Jinwei Zhang, Dr. Qihao Zhang, and Dr. Liangdong Zhou, who supported me in all aspects of my research.

This study was supported in part by Japan's society for the promotion of science (JSPS) and Canon Medical Systems Corporation.

Finally, I would like to acknowledge the committee members who agreed to examine this thesis: Prof. Takaaki Nara, Prof. Kenji Kawashima, Prof. Hiroshi Saruwatari, Assoc. Prof. Koji Tsumura, and Prof. Masaki Sekino.

Notation and Convention

Quantities

A Scalar (italic, serif)
$\boldsymbol{A}$ Vector (bold, italic, serif)
$\mathbf{\mathit{A}}$ Tensor (bold, italic, sans-serif)

Physical Constants

ϵ_0 Dielectric permittivity of free space
μ_0 Magnetic permeability of free space
γ_0 Gyromagnetic ratio of proton nuclei

Integral Symbols

$\oint$ Contour integral along a closed curve.
$⨍$ Cauchy's principal value integral.
$⨎$ Hadamard's finite part integral.

Function Spaces

Let Ω be a connected open subset of $\mathbb{C} \cong \mathbb{R}^2$ or $\mathbb{R}^3$, k be a nonnegative integer, and α be a real number satisfying $0 < \alpha \leq 1$.

$C^k(\Omega)$ The set of functions whose derivatives up to the k-th order are continuous in Ω.
$C_0^k(\Omega)$ The set of functions that belong to C^k and whose support is a compact subset of Ω.
$C^{k,\alpha}(\Omega)$ The set of functions whose derivatives up to the k-th order are α-Hölder continuous in Ω.
$L^p(\Omega)$ The set of functions the p-th power of whose absolute value is Lebesgue-integrable in Ω.
$L^p_{\mathrm{loc}}(\Omega)$ The set of functions that belong to $L^p(K)$, where K is an arbitrary compact subset of Ω.
$W^{k,p}(\Omega)$ The set of functions whose weak derivatives up to the k-th order belong to $L^p(\Omega)$. $L^p(\Omega) = W^{0,p}(\Omega)$.
$W_0^{k,p}(\Omega)$ The set of functions that belong to $W^{k,p}(\Omega)$ and whose support is a compact subset of Ω.

Vector and Tensor Algebra

Dyadic, dot, and cross products of three dimensional vectors and tensors are defined as follows:

$$\begin{aligned}
\boldsymbol{ab} &= a_i b_j \boldsymbol{e}_i \boldsymbol{e}_j, & \boldsymbol{a} \cdot \boldsymbol{b} &= a_i b_i, & \boldsymbol{a} \times \boldsymbol{b} &= \epsilon_{ijk} a_i b_j \boldsymbol{e}_k, \\
\boldsymbol{ab} &= a_{ij} b_k \boldsymbol{e}_i \boldsymbol{e}_j \boldsymbol{e}_k, & \boldsymbol{a} \cdot \boldsymbol{b} &= a_{ij} b_j \boldsymbol{e}_i, & \boldsymbol{a} \times \boldsymbol{b} &= \epsilon_{jkl} a_{ik} b_l \boldsymbol{e}_i \boldsymbol{e}_j, \\
\boldsymbol{ab} &= a_i b_{jk} \boldsymbol{e}_i \boldsymbol{e}_j \boldsymbol{e}_k, & \boldsymbol{a} \cdot \boldsymbol{b} &= a_i b_{ij} \boldsymbol{e}_j, & \boldsymbol{a} \times \boldsymbol{b} &= \epsilon_{ijk} a_i b_{jl} \boldsymbol{e}_k \boldsymbol{e}_l.
\end{aligned}$$

The inner product and the norm of vectors and tensors are denoted by single brackets.

$$\begin{aligned}
\langle \boldsymbol{a}, \boldsymbol{b} \rangle &= \bar{\boldsymbol{a}} \cdot \boldsymbol{b}, & |\boldsymbol{a}| &= \sqrt{\langle \boldsymbol{a}, \boldsymbol{a} \rangle}, \\
\langle \boldsymbol{a}, \boldsymbol{b} \rangle &= \bar{\boldsymbol{a}} : \boldsymbol{b}, & |\boldsymbol{a}| &= \sqrt{\langle \boldsymbol{a}, \boldsymbol{a} \rangle}.
\end{aligned}$$

Vector and Tensor Calculus

Gradient, divergence, and curl of three dimensional vector and tensor fields are defined as follows:

$$\begin{aligned}
\nabla \boldsymbol{f} &= \partial_i f_j \boldsymbol{e}_i \boldsymbol{e}_j, & \nabla \cdot \boldsymbol{f} &= \partial_i f_i, & \nabla \times \boldsymbol{f} &= \epsilon_{ijk} \partial_i f_j \boldsymbol{e}_k, \\
\nabla \boldsymbol{f} &= \partial_i f_{jk} \boldsymbol{e}_i \boldsymbol{e}_j \boldsymbol{e}_k, & \nabla \cdot \boldsymbol{f} &= \partial_i f_{ij} \boldsymbol{e}_j, & \nabla \times \boldsymbol{f} &= \epsilon_{ijk} \partial_i f_{jl} \boldsymbol{e}_k \boldsymbol{e}_l.
\end{aligned}$$

The inner product and the norm of two vector and tensor fields over the function space are denoted by double brackets.

$$\begin{aligned}
\langle\!\langle \boldsymbol{f}, \boldsymbol{g} \rangle\!\rangle_\Omega &= \int_\Omega \bar{\boldsymbol{f}}(\boldsymbol{r}) \cdot \boldsymbol{g}(\boldsymbol{r}) \mathrm{d}V(\boldsymbol{r}), & \|\boldsymbol{f}\|_\Omega &= \sqrt{\langle\!\langle \boldsymbol{f}, \boldsymbol{f} \rangle\!\rangle_\Omega}, \\
\langle\!\langle \boldsymbol{f}, \boldsymbol{g} \rangle\!\rangle_\Omega &= \int_\Omega \bar{\boldsymbol{f}}(\boldsymbol{r}) : \boldsymbol{g}(\boldsymbol{r}) \mathrm{d}V(\boldsymbol{r}), & \|\boldsymbol{f}\|_\Omega &= \sqrt{\langle\!\langle \boldsymbol{f}, \boldsymbol{f} \rangle\!\rangle_\Omega}.
\end{aligned}$$

Contents

Chapter 1

Introduction

1.1 Material Properties of Biological Tissues

Electrical, mechanical, and magnetic properties of biological tissues reflect physiological and pathological states of the tissues, and thus serve as useful biomarkers to diagnose various diseases.

Electrical properties (EPs), namely electric conductivity and dielectric permittivity, of biological tissues are related to intracellular sodium concentration and osmotic pressure, which are regulated by cell homeostasis. If cell homeostasis breaks down, the ion concentration and water content of the cells are affected and these abnormalities are manifested as changes in EPs. EP maps are useful in the diagnosis of acute stroke and other ischemic diseases [1, 2].

Mechanical properties (MPs), namely shear modulus and viscosity, have also been of great concern since they reflect fibrogenesis and calcification in the extracellular matrix. Many malignant breast cancers are stiffer than benign tumors or normal surrounding fibroglandular tissues. During tumor growth, increased cellular stiffness and compaction of surrounding tissues can combine to alter mechanical properties of the tissues [3]. MP maps contribute to the early diagnosis of liver cirrhosis and aortic aneurysms [4].

The magnetic susceptibility of tissues is mainly determined by the amount of iron and calcium ions, which are highly regulated to maintain homeostasis, and their overload causes cellular damage. Susceptibility maps enable us to diagnose many neurological diseases such as Alzheimer's disease, Huntington's disease and osteoporosis [5–7].

Therefore, imaging modalities that quantitatively map electrical, mechanical, and magnetic properties of biological tissues have been extensively studied in recent years to realize early diagnoses of various diseases. Furthermore, the quantitative nature of these material properties enables precision diagnosis such as tumor grading [8], which is beyond the ability of ordinary anatomical images obtained by conventional imaging modalities. This study focuses on emerging MRI-based modalities of material properties mapping.

1.2 Techniques for Material Properties Mapping

In this section, we explain classic techniques for material properties mapping of biological tissues and their limitations as well as MRI-based modalities, which are the focus of this thesis.

Biopsy is the most basic method for investigating the material properties of biological tissues. However, it is invasive and can fail to detect important changes in tissues unless sampling occurs at an appropriate location.

Imaging modalities based on external measurements allow us to map material properties with simple hardware configurations. Electrical impedance tomography (EIT) is a technique to reconstruct the conductivity of a human body from the electric potential data at the surface electrodes during current injection through the electrodes [9]. Magnetic induction tomog-

raphy (MIT) is a similar technique but measures the induced electromotive force driven by external coils applying electric currents inside the body. Although these methods can be realized with relatively simple hardware configurations, reconstructing internal material properties from the measurement data obtained only on the surface results in low-resolution images due to the ill-posed nature of the involved inverse problem. Techniques to quantify the distribution of stiffness such as Young's and shear moduli are called elastography [10], and ultrasound (US) has often been used in this context, especially in the early days [11]. Magnetic susceptibility measurements have been conducted using superconducting quantum interference devices [12]. However, as is the case of EIT and MIT, it is mathematically difficult to reconstruct the distribution of elastic and magnetic properties inside the body from surface measurements, and thus it is not possible to obtain information on the depth of the body.

To obtain reconstruction results with higher resolution, MRI is an effective method since it can access internal data. Magnetic resonance electrical impedance tomography (MREIT) is one of the methods for imaging EPs using MRI [13, 14]. In MREIT, similar to EIT, a weak electric current is applied to the body from external electrodes, and a conductivity map is reconstructed from the internal magnetic field data. One of the challenges of MREIT is that it is still invasive because it applies currents directly from external electrodes. Electrical properties tomography (EPT) [15–17] is an emerging modality that also uses MRI, but instead of directly applying a low-frequency current, it reconstructs EPs from the response to the magnetic field at the radiofrequency (RF) applied during the MRI measurements. Currently, EPT is being actively studied; it is superior to MREIT in that it is noninvasive and does not require additional hardware. We note that EPT reconstructs conductivity and permittivity in the RF range, whereas MREIT maps conductivity at low frequencies typically around 1 kHz.

High-resolution imaging of MPs has been achieved by magnetic resonance elastography (MRE) [18–20], which uses MRI to measure the internal displacement field and reconstruct shear elasticity. Magnetic susceptibility has long been recognized as a cause of artifacts in MR images. Quantitative susceptibility mapping (QSM) is a growing modality that reconstructs a magnetic susceptibility map from information concerning static magnetic field variation encoded in MRI phase images [21–24].

In the following, we further describe the concepts and problem formulations of each of these promising MRI-based modalities.

1.2.1 Electrical and Mechanical Properties Mapping

We first explain the imaging modalities of electrical and mechanical properties, which can be described in a unified manner as we will see in the next section.

In MRI, the time-harmonic electromagnetic fields oscillating at the Larmor frequency ω_0, called the B1 field, are transmitted by the RF coil enclosing the body. The distribution of the amplitude and phase of the electromagnetic fields are determined depending on the EPs inside the body. Thus, the governing equations are time-harmonic Maxwell's equations:

$$\nabla \times \boldsymbol{E} = -\mathrm{i}\omega_0 \mu_0 \boldsymbol{H}, \tag{1.1}$$

$$\nabla \times \boldsymbol{H} = (\sigma + \mathrm{i}\omega_0 \epsilon_0 \epsilon_\mathrm{r})\boldsymbol{E} = \gamma \boldsymbol{E}, \tag{1.2}$$

where $\boldsymbol{E}$ and $\boldsymbol{H}$ are the complex amplitudes of the electromagnetic fields and ϵ_0 and μ_0 are the dielectric permittivity and magnetic permeability of free space. We define the admittivity γ as $\sigma + \mathrm{i}\omega_0\epsilon$, where σ and ϵ are the conductivity and permittivity. While the admittivity is the inhomogeneous quantity to be reconstructed, the magnetic permeability is assumed to be constant and identical to μ_0 throughout the entire body since the magnetic susceptibility of the human body is sufficiently small [25].

An overview of EPT is shown in Fig. 1.1. Using the receiver coils, both the amplitude and

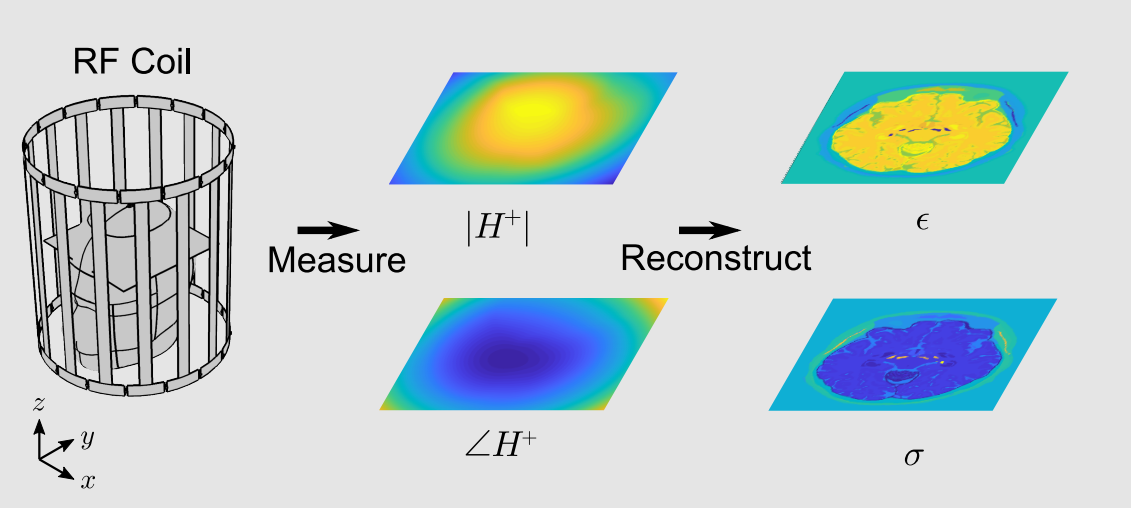

Fig. 1.1: Overview of EPT. Electric conductivity σ and dielectric permittivity ϵ are reconstructed from the positively rotating component of the RF magnetic field $H^+ := (H_x + \mathrm{i}H_y)/2$ measured using MRI.

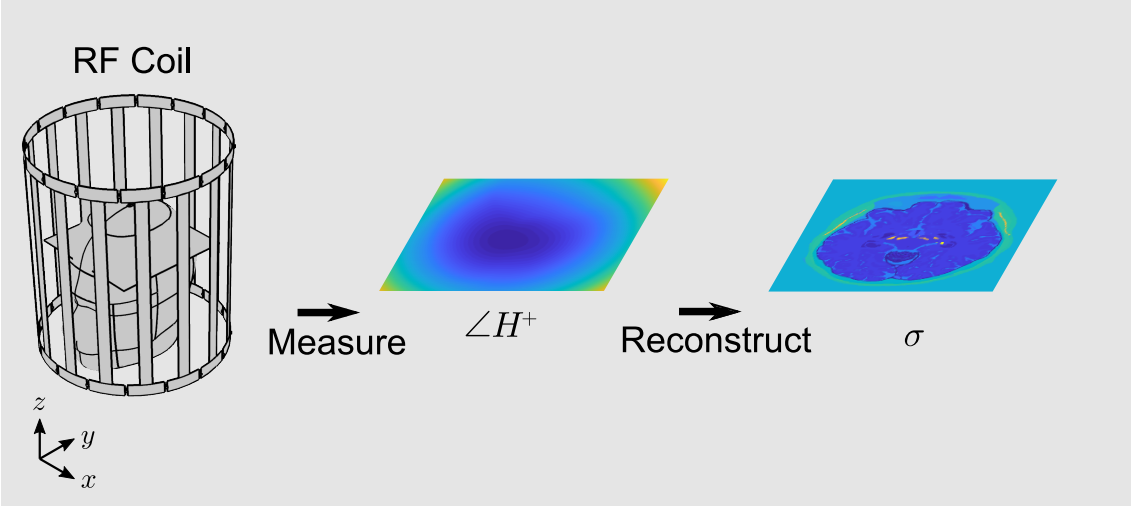

Fig. 1.2: Overview of QCM. Unlike EPT, only the phase of H^+ is measured to reconstruct the electric conductivity map.

phase of the positively rotating component of the magnetic field $H^+ := (H_x + \mathrm{i}H_y)/2$, where the z-axis is set parallel to the body axis, can be measured inside the body. Therefore, the EPT problem is to reconstruct γ from the measured H^+ according to Eqs. (1.1) and (1.2).

In ordinary EPT, both the amplitude and phase of H^+ are required to reconstruct EPs. While the B1 phase measurement can be realized by fast sequences used in clinical routines, measurement of the B1 magnitude takes longer, facilitating the phase-based conductivity mapping technique [26] shown in Fig. 1.2, in which conductivity is reconstructed from only the phase of the B1 field. Following Kim *et al.* [27], we refer to this technique as quantitative conductivity mapping (QCM) hereafter.

In MRE, as shown in Fig. 1.3, a transducer is placed against the body and a time-harmonic mechanical oscillation at the frequency ω_1 is applied during the MRI acquisition [28, 29]. The distribution of the displacement field is determined depending on the MPs inside the body.

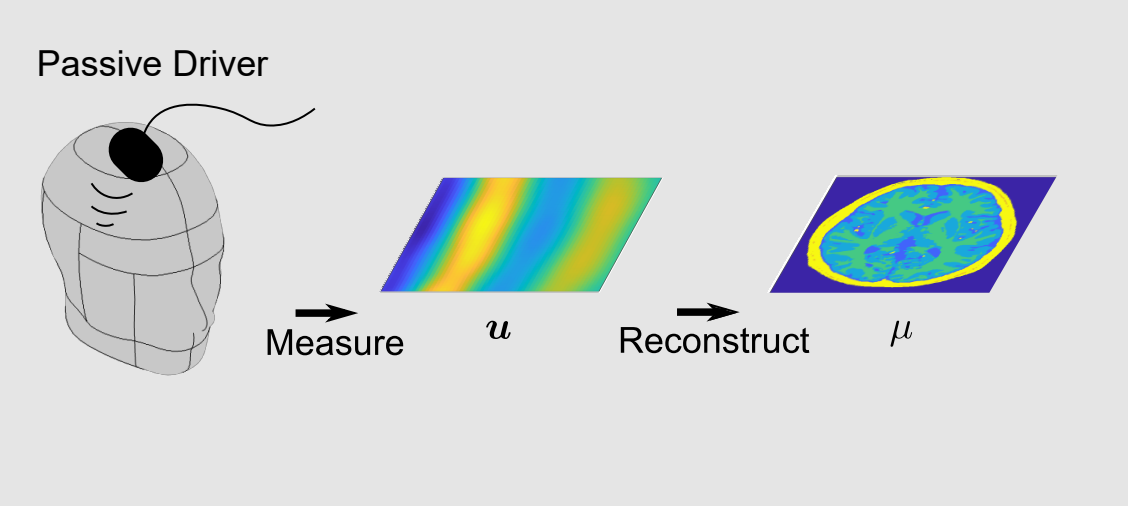

Fig. 1.3: Overview of MRE. Shear modulus and viscosity μ are reconstructed from the measured displacement field $\boldsymbol{u}$ caused by the mechanical vibration induced from an external passive driver during MRI measurement.

Thus, the governing equations are the equation of motion for the time-harmonic oscillation and Hooke's law for an isotropic linear material:

$$\nabla \cdot \boldsymbol{\sigma} = -\omega_1^2 \rho_0 \boldsymbol{u}, \tag{1.3}$$

$$\boldsymbol{\sigma} = \lambda \nabla \cdot \boldsymbol{u} \boldsymbol{I} + \mu \check{\nabla} \boldsymbol{u}, \tag{1.4}$$

where $\boldsymbol{\sigma}$ and $\boldsymbol{u}$ are the complex amplitudes of the stress and displacement fields, ρ_0 is the mass density of water, and λ and μ are Lame's first and second parameters. $\check{\nabla}\boldsymbol{u} := \nabla \boldsymbol{u} + \nabla \boldsymbol{u}^{\mathsf{T}}$ is the symmetrized gradient tensor of a vector field. Typically, the shear modulus μ is the main target of MRE because λ has less contrast among different types of tissues. The mass density is assumed to be constant and identical to ρ_0 throughout the entire body [20]. The MRE problem is to reconstruct μ and possibly λ from the measured $\boldsymbol{u}$ according to Eqs. (1.3) and (1.4).

1.2.2 Simultaneous Conductivity and Susceptibility Mapping

In MRI, a strong static magnetic field called the B0 field is applied to align the proton nuclei inside the body. Then, a tissue with magnetic susceptibility gains magnetization $\boldsymbol{M}$ and modifies the magnetic field around the tissue. The governing equations are Maxwell's equations for magnetostatics:

$$\nabla \cdot \boldsymbol{B} = 0, \tag{1.5}$$

$$\nabla \times \boldsymbol{B} = \mu_0 \nabla \times \boldsymbol{M}, \tag{1.6}$$

where $\boldsymbol{B}$ is the magnetic flux density and the magnetization $\boldsymbol{M}$ is given as follows:

$$\boldsymbol{M} = \frac{1}{\mu_0} \frac{\chi}{1+\chi} \boldsymbol{B}, \tag{1.7}$$

where χ is the magnetic susceptibility. What we probe using an MRI scanner is the microscopic local field experienced by each proton nucleus represented as $\boldsymbol{B}^{\mathrm{l}} = \boldsymbol{B} - 2/3\mu_0 \boldsymbol{M}$.

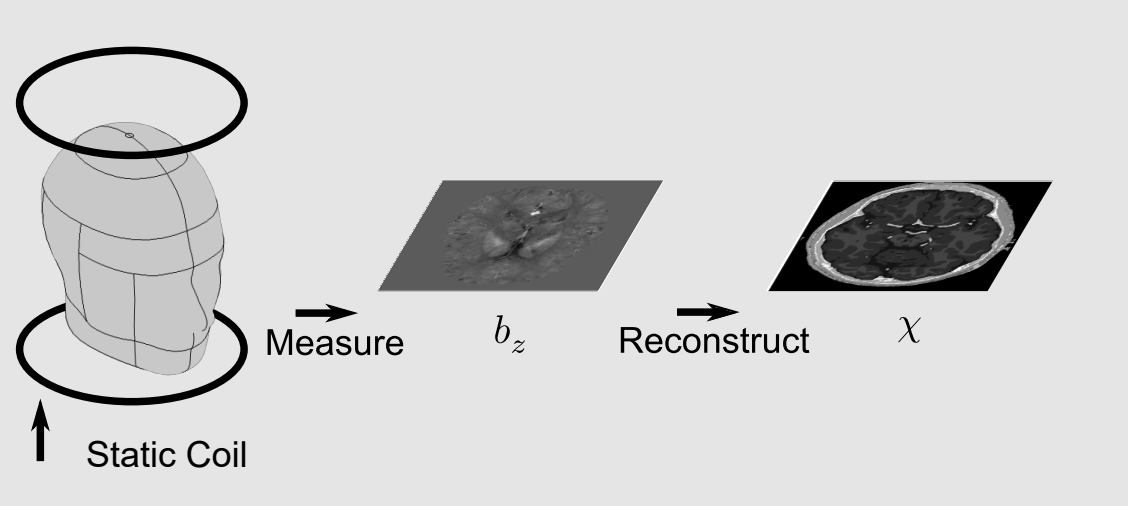

Fig. 1.4: Overview of QSM. Magnetic susceptibility χ is reconstructed from the perturbation of the static magnetic field along the body axis b_z measured using MRI.

From a gradient echo (GRE) acquisition, the z-component of the magnetic field perturbation $b_z = B_z^{\mathrm{l}} - B_z^{\mathrm{e}}$, where B_z^{e} is the homogeneous static field induced by the main magnet of the MRI scanner, can be measured. The QSM problem is to reconstruct χ from the measured b_z data according to Eqs. (1.5) and (1.6) as shown in Fig. 1.4.

While QSM is typically based on GRE acquisition to extract the B0 field inhomogeneity, QCM is based on spin echo (SE) or balanced-SSFP (bSSFP) acquisition to extract the B1 phase contribution without being affected by the B0 field. Therefore, QCM and QSM were originally developed independently. Recently, QSM was combined with QCM to beget a novel concept of simultaneous conductivity–susceptibility mapping [27] based on multiecho GRE acquisition, in which GRE signals at multiple instants are collected. This simultaneous QCM and QSM technique, which we will denote as QCM+QSM hereafter, enables us to obtain both electromagnetic property maps from a single measurement.

1.3 Objectives of This Thesis

1.3.1 Electrical and Mechanical Properties Mapping

In the previous sections, we have seen the problem formulations of three electrical and mechanical properties imaging modalities: EPT, QCM, and MRE. The conventional methods of EPT, QCM, and MRE can be divided into four groups in terms of two criteria as shown in Table 1.1. The first is whether the method is local or global and the second is whether the method is direct or iterative. Local methods are based on partial differential equations (PDEs) that relate the measured field and the material properties to be reconstructed, and global methods are based on integral equations (IEs). The limitation of local methods is that the measurement noise is amplified in the process of calculating the higher-order derivatives of the measured data, whereas the global methods can avoid the higher-order derivatives, rendering them more robust against measurement noise. Iterative methods estimate the solution by nonlinear minimization of the cost functional while linear methods can directly obtain the solution by solving a linear system. The limitation of iterative methods is that the solution depends on the initial guess due to the nonlinear formulations, which may lead to local minima. We previously proposed a direct and global method based on the so-called Dbar equation

Table 1.1: Conventional methods for electrical and mechanical properties mapping. They can be categorized as local/global methods and iterative/direct methods.

	Iterative	Direct
Local	PDE-based nonlinear method [30, 31]	PDE-based linear method [32]
Global	IE-based nonlinear method [33, 34]	Dbar equation-based linear method based on the 2D approximation [35]

derived from a two-dimensional (2D) approximation of the governing equations. Although this method can reconstruct material properties in an explicit and robust manner, it is only valid for 2D problems where the material properties are homogeneous along the body axis.

Based on the discussion so far, a global and direct method that can reconstruct three-dimensional (3D) material properties is urgently required. Therefore, the first objective of this thesis is to propose a novel method for EPT, QCM, and MRE that has the following three features:

1. The method is based on global IEs and does not use the higher-order derivatives of the measurement field, and thus is robust against measurement noise.
2. The method is formulated as a linear problem that can be solved by a direct procedure without iterative updating of the temporal estimate, and is thus free from local minima and nonconvergent results.
3. The method does not use the 2D approximation, and is thus able to reconstruct general 3D distributed material properties.

To achieve these three features, we first show that EPT, QCM, and MRE problems can all be formulated in a unified manner, which we call the divergence-constraint impedivity inverse problem. In this formulation, the problem of reconstructing material properties is defined as estimating the impedivity given as the ratio of the measured field and the concomitant field, which we refer to as the dual fields. It is shown that the divergence of the dual field can be stated in terms of the measured field. Based on this property, an IE for the impedivity is obtained by using Helmholtz's decomposition of the dual field, from which the impedivity is estimated in a global, direct, and 3D manner.

To be precise, as we will see in Chapters 2 and 3, the governing equations for EPT, QCM, and MRE can be written in the same form as shown in Table 1.2, where $\lambda := \gamma^{-1}$ and $\rho := \sigma^{-1}$, and ϕ is the transceive B1 phase measured in QCM. In all cases, the material properties to be reconstructed are given by the ratio of the measured fields $(H^+, \phi, \boldsymbol{u})$ to the corresponding dual fields $(\tilde{\boldsymbol{E}}, \boldsymbol{\psi}, \boldsymbol{\sigma})$ as shown in the top row. Hence, the targeted material properties are considered as the impedance quantities between the measured and dual fields. The divergence-constraint equations shown in the bottom row state that the divergence of the dual fields is given by the measured fields. Therefore, we refer to the EPT, QCM, and MRE problems formulated by these defining equations and divergence-constraint equations of the dual fields collectively as the divergence-constraint impedivity inverse problem.

In this study, we utilize Helmholtz's representation formula, which gives integral representations of vector and tensor fields by their divergence and curl to develop a unified reconstruction method for EPT, QCM, and MRE that is global, direct, and valid for 3D objects.

1.3.2 Simultaneous Conductivity and Susceptibility Mapping

Our second objective is to apply the proposed QCM method to the framework of simulations conductivity–susceptibility mapping to realize multi-modality imaging that reconstructs both

Table 1.2: Governing equations for EPT, QCM, and MRE formulated as the divergence-constraint impedivity inverse problem consisting of the defining equation and the divergence-constraint equation of the dual field.

	EPT	QCM	MRE
Defining equation of dual fields	$\tilde{\boldsymbol{E}} = \lambda \nabla^{\mathrm{c}} H^{+}$	$\boldsymbol{\psi} = \rho \nabla \phi$	$\boldsymbol{\sigma} = \lambda \nabla \cdot \boldsymbol{u}\boldsymbol{I} + \mu \check{\nabla} \boldsymbol{u}$
Div-constraint equation of dual fields	$\nabla \cdot \tilde{\boldsymbol{E}} = \mathrm{i}\omega_0 \mu_0 H^{+}$	$\nabla \cdot \boldsymbol{\psi} = 2\omega_0 \mu_0$	$\nabla \cdot \boldsymbol{\sigma} = -\omega_1^2 \rho_0 \boldsymbol{u}$

electromagnetic tissue properties. To achieve this, we improve the current QCM+QSM framework from two perspectives.

In QCM+QSM, the B1 phase used in QCM and the B0 field used in QSM are first separated and estimated from the multiecho GRE image, and then each QCM and QSM reconstruction procedure is applied independently. The previous method uses only the phase image of the multiecho GRE data and estimates the fields by linear least-squares fitting [27]. Specifically, the B1 phase is obtained as the intercepting value of the phase signal linearly evolving along time and the B0 field is obtained as the rate of evolution. However, unlike the in-phase and quadrature-phase MRI images whose noise behavior is well described by the Gaussian distribution, the noise distribution of the phase image deviates from normality [36], making the least-squares fitting non-optimal. Furthermore, it is known that the nonlinear phase is accumulated in the multiecho GRE signal, which hampers finding the correct offset phase value [37]. Therefore, in this thesis, pursuant of optimal estimation, we propose to utilize both the magnitude and phase images of the multiecho GRE data and estimate the fields by nonlinear least-squares on the complex signal whose noise distribution is Gaussian.

We also improve the QCM reconstruction. While QSM reconstruction has been well developed and successfully applied in clinical contexts, there is scope for improvement. Here, we apply our novel QCM reconstruction method proposed in Chapter 2 to this QCM+QSM framework. In addition, we adopt the morphology-based regularization used in the QSM literature [21] but not applied in the QCM+QSM framework, to stabilize the QCM inversion and facilitate consistent results between conductivity and susceptibility maps.

1.4 Organization of This Thesis

In Chapter 1, after describing the background of the material properties mapping of biological tissues, the problem formulations of EPT, QCM, MRE, and QSM as well as the conventional methods and their limitations are explained.

As shown in Fig. 1.5, the subsequent chapters are organized as follows. In Chapter 2, we propose novel reconstruction methods for EPT and QCM. Based on Helmholtz's representation formula for vector fields, an integral representation formula of a vector field by its divergence and itself is derived and applied to the divergence-constraint impedivity inverse problems for EPT and QCM to construct global, direct, and 3D reconstruction methods. The proposed methods are validated through numerical simulations including an anatomical brain model and phantom experiments. In Chapter 3, the integral representation formula for vector fields derived in Chapter 2 is reformulated for tensor fields. The tensor representation formula is applied to an MRE inverse problem and its validity is confirmed by numerical simulations. Chapter 4 derives an EPT reconstruction method based on the Cauchy–Pompeiu formula that reconstructs EPs in a slicewise manner. The method proposed in this chapter allows reconstruction of EPs without prior information concerning their values on the boundary of the region of interest (ROI). In Chapter 5, the framework for simultaneous conductivity

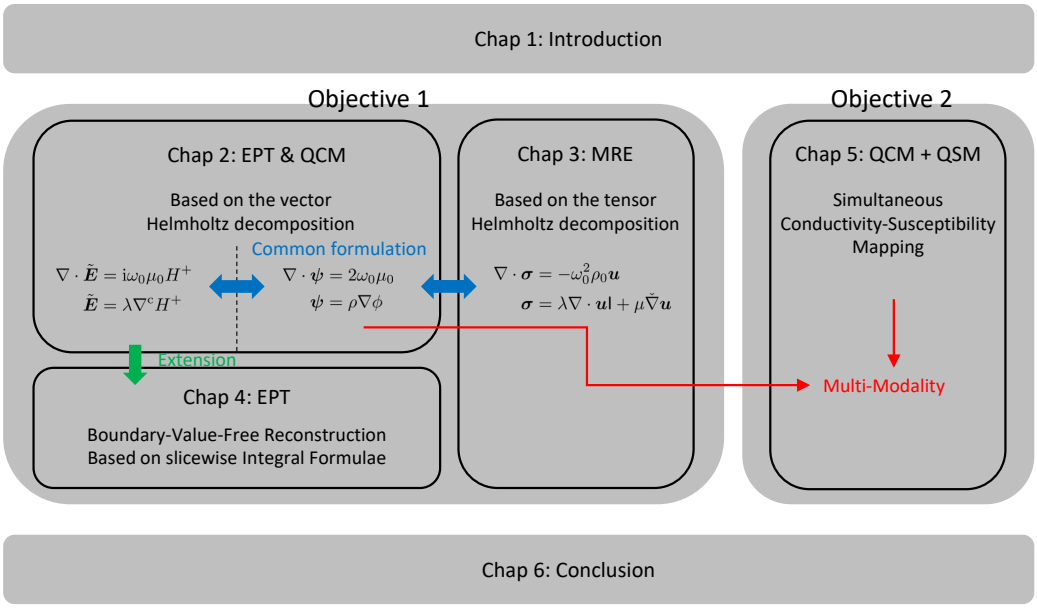

Fig. 1.5: Organization of this thesis. In Chapters 2 and 3, EPT, QCM, and MRE problems are formulated in a unified manner and novel reconstruction methods are proposed. Chapter 4 extends the EPT method in Chapter 2 to configure a boundary-value-free reconstruction method. In chapter 5, QCM+QSM are improved and applied to *in vivo* data. Finally, Chapter 6 concludes the thesis.

and susceptibility reconstruction is improved by using nonlinear least-squares fitting in the B1 phase and B0 field estimation and applying the proposed QCM reconstruction method with the morphology-based regularization to QCM reconstruction. The method is tested using *in vivo* data on healthy subjects and subjects with brain tumors. Finally, Chapter 6 concludes the thesis and suggests research directions.

Chapter 2

Conductivity and Permittivity Mapping from B1 Magnetic Field Measurements

In this chapter, we develop global and direct methods for EPT and QCM that can reconstruct 3D EPs. After explaining the background and the conventional methods in section 2.1, we introduce the notion of dual fields of the measured fields and EPT and QCM problems are formulated as impedivity inverse problems with either a divergence or curl constraint in section 2.2. Section 2.3 presents various representation formulae concerning vector fields in terms of their divergence and curl as well as themselves. The representation formulae are utilized in section 2.4 to derive IEs for the impedivity and to construct our proposed reconstruction formulae. In section 2.5, the computational procedures for solving the IEs and estimating a regularized solution of the impedivity are described in detail. The proposed methods are validated by numerical simulations in section 2.6 and phantom experiments in section 2.7. Finally, section 2.8 concludes this chapter.

2.1 Introduction of This Chapter

2.1.1 Electrical Properties of Biological Tissues

EPs of biological tissues vary strongly with frequency [38–40]. Schwan *et al.* [41] modeled human tissues as an equivalent circuit that consists of extracellular liquid, cell membrane, and intercellular liquid. Each of these has its own conductance and capacitance, exhibiting the following impedance:

$$|Z(\omega)| = \frac{1}{\sqrt{G^2 + \omega^2 C^2}}, \tag{2.1}$$

where G is the conductance and C is the capacitance. Schwan *et al.* [41] and Pethig [42] reported that conductance was around 100 S and capacitance was around 1000 nF for most membrane cells. From these values, it is expected that the impedance of tissues changes substantially around 100 kHz–10 MHz, where the capacitive property of the cell membrane becomes dominant. This is called beta-dispersion and this dispersive property of tissues is described by the Debye model and the Cole–Cole model [43, 44]. Above 100 MHz, the impedance of membrane cells becomes so small that almost all electric currents flow into cells. Therefore, the impedance of tissues is independent of their membrane cells and determined by the impedance of inter- and extra-cellular liquids. Hence, EPs of tissues in the microwave range can be described by the ion and water concentrations [41, 42, 45].

Table 2.1: Conductivity and permittivity values of various types of normal and cancerous tissues at 100 MHz. Rearranged from [52].

Tissue	Conductivity (S/m)		Permittivity (ϵ_0)	
	Normal	Cancerous	Normal	Cancerous
Colon	0.62	0.74	52.0	65.0
Kidney	0.77	0.75	72.0	68.0
Liver	0.49	0.66	62.0	66.0
Lung	0.62	0.82	77.0	69.0
Mammal	0.11	0.78	20.5	69.0

In living organisms, active mechanisms regulate the contrast of sodium ion concentration and osmotic pressure inside and outside the cell. In ischemic strokes and myocardial infarctions, the sodium–potassium pump, which uses adenosine triphosphate (ATP) as an energy source, fails to function because the supply of oxygen and nutrients through the blood circulation is cut off. As a result, intracellular sodium concentration and osmotic pressure are increased, which allows water molecules to penetrate into the cells, leading to swelling, rupture, and death of the cells [16]. It has been reported that the sodium concentration of the intracellular fluid increases whereas the extracellular fluid is maintained at a level of 140 mM due to the buffering effect of the organism, resulting in an increase in overall tissue sodium concentration [46, 47]. Therefore, imaging of EPs may be useful in the diagnosis of acute strokes and other ischemic diseases. ^{23}Na-MRI is expected to delineate the boundaries between tissues that are still viable and those that are not, based on the quantitative value of sodium concentration. However, one of the problems with ^{23}Na-MRI is its intrinsically low signal-to-noise ratio (SNR) due to the low abundance of ^{23}Na in a body compared to ^{1}H. Therefore, if we can image the EPs using an ordinary ^{1}H-MRI scanner, it will allow us to make more accurate diagnoses [16].

In cancer, as in the case of ischemic disease, angiogenesis of capillaries makes the transport of oxygen and nutrients inefficient, causing the sodium–potassium pump to malfunction and the intracellular sodium concentration increases, resulting in an increase in conductivity [48]. In addition, as a result of angiogenesis, the fraction of the extracellular space increases, which increases the water content of the tissue and causes an increase in conductivity and permittivity [49]. Indeed, invasive measurements have shown that the EPs of cancer cells are markedly different from those of healthy cells in various tissues [50–54]. Joines *et al.* [52] measured the conductivity and permittivity of healthy cells and cancerous cells in several tissues over the 50 MHz–900 MHz range using a coaxial probe. Table 2.1 shows the measured values of conductivity and permittivity at 100 MHz for each type of cell. In both tissues, there is a difference in EPs between cancerous and healthy cells. In addition to the tissues listed in Table 2.1, increased conductivity in core areas of brain tumors has also been observed [51]. Noninvasive imaging of the brain is in high demand and it is of vital importance to diagnose cancers based on the image of the EPs.

Another important application of EPT is dosimetry. The specific absorption rate (SAR) is a quantitative criterion of tissue heating against RF electromagnetic fields in high-field MRI systems [55, 56] and is calculated as

$$\mathrm{SAR} \coloneqq \sigma \frac{|\boldsymbol{E}|^2}{\rho}, \tag{2.2}$$

where ρ is the mass density of the tissue, which is often assumed to be identical to that of water. Hence, knowledge of tissues' conductivity and the induced electric field enables us to

quantitatively evaluate the SAR distribution.

2.1.2 Measurement of the B1 Magnetic Field

This section reviews methods for measuring the B1 field H^+. The amplitude and phase of H^+ are measured separately.

The technique for measuring the B1 amplitude is called B1 mapping [57–59]. The most basic approach is the double-angle method (DAM) [60–62], in which two images with different nominal flip angles are obtained and the B1 amplitude is calculated as their ratio. As presented by Hoult [63], the MR signal as a function of the nominal flip angle α without considering relaxation effect is given as

$$S_\alpha = \frac{2\omega_0}{I} \mathrm{i} M_0 \sin\alpha |B_1'^-| \exp(\mathrm{i}(\angle B_1^+ + \angle B_1'^-)), \tag{2.3}$$

where $\alpha = \gamma_0 \mu_0 |H^+| \tau$ for a hard pulse with duration τ. The derivation is found in Appendix B. Hence, the ratio of the two magnitude images with the flip angle of α and 2α is given as

$$\frac{|S_{2\alpha}|}{|S_\alpha|} = \frac{\sin 2\alpha}{\sin\alpha} = 2\cos\alpha, \tag{2.4}$$

leading to the following formula for calculating $|H^+|$:

$$|H^+| = \frac{1}{\gamma_0 \mu_0 \tau} \cos^{-1}\left(\frac{|S_{2\alpha}|}{2|S_\alpha|}\right). \tag{2.5}$$

To eliminate the relaxation effect, DAM requires a very long TR, which makes the measurement time-consuming. Another limitation of DAM that encodes the B1 field information into the magnitude of the MR signal is that it is sensitive to the RF pulse shape, slice-select gradients, off-resonance excitation, and B0 inhomogeneities [64].

Phase-based B1 mapping methods [65–67] are immune to these undesired effects, and the Bloch–Siegert shift (BSS) method [67] is reported to yield good estimates of the B1 amplitude in the EPT literature [68]. In the BSS method, an additional RF pulse is applied after the usual RF excitation pulse that tips the magnetization into the transverse plane. The career frequency of this additional pulse is shifted away from the resonance frequency $\omega_0 = \gamma_0 B_0$ by $\Delta\omega$. In the rotating frame of reference that rotates at $\omega_0 + \Delta\omega$, a residual magnetic field $B^{\mathrm{res}} = \Delta\omega/\gamma_0$ exists along the z-axis. If the frequency shift is large enough so that B^{res} is much greater than the magnitude of the additional RF pulse $|B_1^+|$, the magnitude of the total effective field is given as

$$B^{\mathrm{eff}} = \sqrt{(\Delta\omega/\gamma_0)^2 + |B_1^+|^2} \simeq \frac{\Delta\omega}{\gamma_0}\left(1 + \frac{|B_1^+|^2}{2(\Delta\omega/\gamma_0)^2}\right), \tag{2.6}$$

and the orientation is along the z-axis. In the rotating frame at ω_0 where the signal demodulation is performed, B^{eff} is given as

$$B^{\mathrm{eff}} = \frac{|B_1^+|^2}{2\Delta\omega/\gamma_0}. \tag{2.7}$$

Hence, in this frame, the phase accrual ϕ_{BSS} is represented as

$$\phi_{\mathrm{BSS}} = \int_0^T \gamma_0 B^{\mathrm{eff}}(t)\mathrm{d}t = \int_0^T \frac{(\gamma_0 |B_1^+(t)|)^2}{2\Delta\omega}\mathrm{d}t = |\hat{B}_1^+|^2 \int_0^T \frac{(\gamma_0 K(t))^2}{2\Delta\omega}\mathrm{d}t, \tag{2.8}$$

where T is duration of the pulse, $|\hat{B}_1^+|$ is the peak B1 value to be estimated and $K(t)$ is the normalized B1 profile determined by the shape of the pulse. In general, other factors such as the transmit and receive B1 phases affect the MR phase signal as described in Eq. (2.3). To cancel unwanted phase accumulations, two phase images with the opposite frequency shift $\pm\Delta\omega$ are measured and the difference between them is taken as follows:

$$\angle S_{\Delta\omega} - \angle S_{-\Delta\omega} = 2\phi_{\mathrm{BSS}} = |\hat{B}_1^+|^2 \int_0^T \frac{(\gamma_0 K(t))^2}{\Delta\omega} \mathrm{d}t, \tag{2.9}$$

leading to the following formula for calculating $|H^+|$:

$$|H^+| = \frac{1}{\mu_0} \sqrt{(\angle S_{\Delta\omega} - \angle S_{-\Delta\omega}) \Big/ \int_0^T \frac{(\gamma_0 K(t))^2}{\Delta\omega} \mathrm{d}t}. \tag{2.10}$$

The BSS method is immune to TR and B0 inhomogeneity.

The B1 phase is obtained from an SE phase image to avoid the effect of B0 field inhomogeneity. The phase signal of SE acquisition is represented as follows:

$$\angle S = \angle B_1^+ + \angle B_1'^- + \phi^{\mathrm{eddy}}. \tag{2.11}$$

We note that the phase accumulation due to the B0 field inhomogeneity is removed by the refocusing pulse in SE but the contribution of eddy currents due to the gradient switching still exists. To compensate the eddy currents, two SE acquisitions with the opposite readout gradient polarities are performed and the B1 field-related phase is extracted as the difference between them as follows [69]:

$$\angle B_1^+ + \angle B_1'^- = \angle S_\uparrow - \angle S_\downarrow, \tag{2.12}$$

where $S_\uparrow$ and $S_\downarrow$ are the MR signals when the readout direction is from anterior/right to posterior/left and from posterior/left to anterior/right, respectively.

To extract only the B1 transmit phase, we exploit the geometrical symmetry of the birdcage coil [70, 71] when driven by the quadrature mode. In the quadrature mode, the two orthogonal ports of the birdcage coil generate the transmit field B_1^+ and $\mathrm{i}B_1^+$ and have the receive sensitivity B_1^- and $\mathrm{i}B_1^-$. Hence, by multiplying the signal of the quadrature port by $-\mathrm{i}$ when transmitting and multiplying the signal of the quadrature port by i when receiving, we can make B_1^+ and $B_1'^-$ identical. Therefore, the B1 transmit phase can be calculated as half of the transceive phase. We note that this holds only at the center of the birdcage coil when the loading object is symmetric for its EP distribution. This approximation is called the transceive phased approximation (TPA) and its validity against different main magnetic field strengths has hitherto been studied by van Lier *et al.* [72].

2.1.3 Conventional EPT Reconstruction Methods

As explained in Chapter 1, most of the conventional methods eliminate the electric field $\boldsymbol{E}$ from Eqs. (1.1) and (1.2) to directly relate the measured field with EPs.

Taking the curl of Eq. (1.2) and substituting it into Eq. (1.1) gives

$$\Delta\boldsymbol{H} + \frac{\nabla\gamma}{\gamma} \times (\nabla \times \boldsymbol{H}) - \mathrm{i}\omega_0\mu_0\gamma\boldsymbol{H} = \boldsymbol{0}, \tag{2.13}$$

where we used $\nabla \cdot \boldsymbol{H} = 0$. Equation (2.13) directly relates the admittivity to the magnetic field.

A typical approach for the EPT inverse problem neglects the spatial variation of the EPs to derive the following Helmholtz equation:

$$\Delta \boldsymbol{H} - \mathrm{i}\omega_0\mu_0 \boldsymbol{H} = \boldsymbol{0}. \tag{2.14}$$

Taking the $(x + \mathrm{i}y)$-component of Eq. (2.14) yields the standard EPT formula [73, 74]:

$$\gamma = \frac{1}{\mathrm{i}\omega_0\mu_0}\frac{\Delta H^+}{H^+}. \tag{2.15}$$

Some authors proposed a stabilized version [26, 69] that avoids calculation of the Laplacian of the measured H^+ data. By integrating Eq. (2.15) over a small region in which EPs are assumed to be constant, we have the following formula [26]:

$$\gamma = -\frac{1}{\mathrm{i}\omega_0\mu_0}\frac{\oint_{\partial\Omega_r} \boldsymbol{n}\cdot\nabla H^+ \mathrm{d}S}{\int_{\Omega_r} H^+ \mathrm{d}V}, \tag{2.16}$$

where $\Omega_{\boldsymbol{r}}$ is a neighboring region of $\boldsymbol{r}$. However, these methods based on the local homogeneity assumption (LHA) fail in adjacent areas of different types of tissues where the spatial variation of EPs cannot be ignored [75, 76].

Several methods beyond LHA have been proposed, most of which can be categorized along two dimensions as described in Table 1.1: local/global methods and direct/iterative methods. Song *et al.* [30] derived the following PDE that directly relates γ and the measurable quantity H^+ without assuming $\nabla\gamma = \boldsymbol{0}$:

$$\Delta H^+ - \frac{\nabla\gamma}{\gamma}\cdot\begin{pmatrix}(\partial_x - \mathrm{i}\partial_y)H^+\\ (\mathrm{i}\partial_x + \partial_y)H^+\\ \partial_z H^+\end{pmatrix} - \mathrm{i}\omega_0\mu_0\gamma H^+ = 0, \quad \boldsymbol{r}\in\Omega. \tag{2.17}$$

Song *et al.* [30] proposed an iterative method by solving a semilinear PDE obtained by assuming $\partial_z\gamma = 0$ and later Ammari *et al.* [77] extended the method to incorporate the longitudinal variation of EPs. However, these methods are very sensitive to the initial estimate and can yield nonconvergent results due to the nonlinearity of the PDE.

Hafalir *et al.* [32] derived the following linear PDE that relates the measured H^+ and EPs by introducing the inverse of admittivity, i.e., impedivity λ:

$$\begin{pmatrix}(\partial_x - \mathrm{i}\partial_y)H^+\\ (\mathrm{i}\partial_x + \partial_y)H^+\\ \partial_z H^+\end{pmatrix}\cdot\nabla\lambda + \Delta H^+\lambda - \mathrm{i}\omega_0\mu_0 H^+ = 0. \tag{2.18}$$

They solved Eq. (2.18) by the finite element method (FEM). Equation (2.18) is the convection-diffusion-reaction equation for λ with no diffusion term. In this method, the Laplacian of the measured magnetic field data must be calculated, which amplifies the measurement noise. Moreover, as reported by Li *et al.* [78], the numerical solution of the convection-diffusion-reaction equation becomes unstable if the convection term dominates the diffusion term, and the solution will have spurious oscillations. Li *et al.* [78] proposed adding an artificial diffusion term to stabilize the inversion but the resulting image is strongly dependent on the choice of regularization parameters that determines the trade-off between the spurious oscillation and the blurring effect.

Some authors have solved the EPT problem using an IE-based approach [33, 34, 79, 80], comprising the global methods. Balidemaj *et al.* [33] solved the EPT inverse problem by solving an IE for the contrast source, which is the ratio of tissues' EPs to those of background

values based on the inverse scattering problem formulation. According to electromagnetic scattering theory [81], the following IE holds for the scattered electromagnetic fields:

$$\boldsymbol{E}_{\mathrm{s}} = \boldsymbol{G}_{\mathrm{e}}[\chi_{\mathrm{e}}\boldsymbol{E}] + \frac{1}{\mathrm{i}\omega_0\epsilon_0}\boldsymbol{G}_{\mathrm{m}}[\chi_{\mathrm{m}}\boldsymbol{H}], \tag{2.19}$$

$$\boldsymbol{H}_{\mathrm{s}} = -\frac{1}{\mathrm{i}\omega_0\mu_0}\boldsymbol{G}_{\mathrm{m}}[\chi_{\mathrm{e}}\boldsymbol{E}] + \boldsymbol{G}_{\mathrm{e}}[\chi_{\mathrm{m}}\boldsymbol{H}], \tag{2.20}$$

where $\chi_{\mathrm{e}} \coloneqq \gamma/(\mathrm{i}\omega_0\epsilon_0) - 1$ and $\chi_{\mathrm{m}} \coloneqq \mu/\mu_0 - 1$ are the electromagnetic contrast sources, and $\boldsymbol{E}_{\mathrm{s}}$ and $\boldsymbol{H}_{\mathrm{s}}$ are the scattered fields that are defined as the difference between the total fields and the incident fields $(\boldsymbol{E}_{\mathrm{i}}, \boldsymbol{H}_{\mathrm{i}})$ produced by the current source without the presence of the scatterer. $\boldsymbol{G}_{\mathrm{e}}$ and $\boldsymbol{G}_{\mathrm{m}}$ are so-called electromagnetic source-to-field operators and defined as follows:

$$\boldsymbol{G}_{\mathrm{e}}[\boldsymbol{f}] \coloneqq \int_{\Omega} (k_0^2\boldsymbol{I} + \nabla\nabla)G(\boldsymbol{r} - \boldsymbol{r}') \cdot \boldsymbol{f}(\boldsymbol{r}')\mathrm{d}V(\boldsymbol{r}'), \tag{2.21}$$

$$\boldsymbol{G}_{\mathrm{m}}[\boldsymbol{f}] \coloneqq \int_{\Omega} k_0^2\boldsymbol{I} \times \nabla G(\boldsymbol{r} - \boldsymbol{r}') \cdot \boldsymbol{f}(\boldsymbol{r}')\mathrm{d}V(\boldsymbol{r}'), \tag{2.22}$$

where G is the fundamental solution of the scalar Helmholtz equation. Since no strong magnetic object exists in the human body and only H^+ is measurable in our EPT problem, the governing equations are as follows:

$$\boldsymbol{E} = \boldsymbol{E}_{\mathrm{i}} + \boldsymbol{G}_{\mathrm{e}}[\chi_{\mathrm{e}}\boldsymbol{E}], \tag{2.23}$$

$$H^+ = H_{\mathrm{i}}^+ + G_{\mathrm{m}}^+[\chi_{\mathrm{e}}\boldsymbol{E}], \tag{2.24}$$

where $G_{\mathrm{m}}^+[\boldsymbol{f}] \coloneqq \boldsymbol{G}_{\mathrm{m}}[\boldsymbol{f}] \cdot (\boldsymbol{e}_x + \mathrm{i}\boldsymbol{e}_y)/2$.

Balidemaj *et al.* [33] proposed the contrast source inversion EPT (CSI-EPT) method, in which Eqs. (2.23) and (2.24) are solved by the CSI method [82, 83]. In CSI-EPT, an additional variable $\boldsymbol{w} \coloneqq \chi_{\mathrm{e}}\boldsymbol{E}$ called the contrast function is introduced and the following objective functional is minimized in an alternating manner:

$$J[\boldsymbol{w}, \chi_{\mathrm{e}}] = \frac{\|\chi_{\mathrm{e}}\boldsymbol{E}_{\mathrm{i}} - \boldsymbol{w} + \chi_{\mathrm{e}}\boldsymbol{G}_{\mathrm{e}}[\boldsymbol{w}]\|_{\Omega}^2}{\|\chi_{\mathrm{e}}\boldsymbol{E}_{\mathrm{i}}\|_{\Omega}^2} + \frac{\|H_{\mathrm{i}}^+ - H^+ + G_{\mathrm{m}}[\boldsymbol{w}]\|_{\Omega}^2}{\|H_{\mathrm{s}}^+\|_{\Omega}^2}, \tag{2.25}$$

$$\chi_{\mathrm{e}} = \frac{\langle \boldsymbol{E}_{\mathrm{i}} + \boldsymbol{G}_{\mathrm{e}}[\boldsymbol{w}], \boldsymbol{w}\rangle}{|\boldsymbol{E}_{\mathrm{i}} + \boldsymbol{G}_{\mathrm{e}}[\boldsymbol{w}]|^2}. \tag{2.26}$$

Specifically, Eq. (2.25) is first minimized for $\boldsymbol{w}$ with only a single iteration of the nonlinear conjugate gradient (CG) method. Then, χ is updated according to Eq. (2.26). The above procedure is repeated until the convergence criterion is satisfied. As pointed out by Arduino *et al.* [84], a linear PDE must be solved at each iteration by the FEM to adequately account for the RF shield of the MRI coil, making its computational cost very high. Guo *et al.* [80] proposed a method based on the same scattering formulation. Unlike the CSI-EPT method, Eqs. (2.23) and (2.24) are solved successively for $\boldsymbol{w}$ and χ_{e}. First, Eq. (2.24) is fully solved by the nonlinear CG method to yield the estimate of $\boldsymbol{w}$ and then χ_{e} is determined by Eq. (2.26). This method is computationally more efficient than the CSI-EPT method. Hong *et al.* [79] also proposed using the same IEs, but solved them using the variational Born iterative method (VBIM) [85].

The updating procedure is described as follows:

$$\boldsymbol{E}^{(n)} = \arg\min_{\boldsymbol{E}} \|\boldsymbol{E} - \boldsymbol{E}_{\mathrm{i}} - \boldsymbol{G}_{\mathrm{e}}[\chi_{\mathrm{e}}^{(n)}\boldsymbol{E}]\|_{\Omega}^{2} \tag{2.27}$$

$$H^{+;(n)} = H_{\mathrm{i}}^{+} + G_{\mathrm{m}}^{+}[\chi_{\mathrm{e}}^{(n)}\boldsymbol{E}^{(n)}] \tag{2.28}$$

$$\delta\chi_{\mathrm{e}}^{(n)} = \arg\min_{\delta\chi_{\mathrm{e}}} \|H^{+} - H^{+;(n)} - G_{\mathrm{m}}^{+}[\delta\chi\boldsymbol{E}^{(n)}]\|_{\Omega}^{2} \tag{2.29}$$

$$\chi_{\mathrm{e}}^{(n+1)} = \chi_{\mathrm{e}}^{(n)} + \delta\chi_{\mathrm{e}}^{(n)} \tag{2.30}$$

This method is also computationally more efficient because it does not need to recalculate Green's function in each iteration. The limitation of methods based on the scattering formulation is that the incident fields must be given, which are determined by the current source of the RF coils. Although they could be given through numerical simulations, erroneous estimation would lead to reconstruction errors.

We previously proposed an EPT method based on the complex form of Maxwell's equations [35]. By introducing the complex-differential operators defined in Eqs. (A.66) and (A.67), the $(x + \mathrm{i}y)$, $(x - \mathrm{i}y)$, and z-components of Maxwell's equations can be written as follows:

$$\begin{aligned}
\bar{\partial}E_z - \partial_z E^{+} &= \omega_0\mu_0 H^{+}, & \bar{\partial}H_z - \partial_z H^{+} &= \mathrm{i}\gamma E^{+},\\
\partial E_z - \partial_z E^{-} &= -\omega_0\mu_0 H^{-}, & \partial H_z - \partial_z H^{-} &= -\mathrm{i}\gamma E^{-},\\
\partial E^{+} - \bar{\partial}E^{-} &= \frac{\omega_0\mu_0}{2}H_z, & \partial H^{+} - \bar{\partial}H^{-} &= \frac{\mathrm{i}\gamma}{2}E_z,
\end{aligned}$$

where $E^{\pm} \coloneqq (E_x \pm \mathrm{i}E_y)/2$ and $H^{-} \coloneqq (H_x - \mathrm{i}H_y)/2$. As pointed out in [69], the magnitude of H_z generated by a birdcage coil typically used in MRI scanners is very small and can be neglected especially in the central region. In this case, the $(x + \mathrm{i}y)$-component of Faraday's and Ampère's laws and the z-component of Ampère's law can be rewritten as follows:

$$\bar{\partial}E_z = \omega\mu_0 H^{+} + \partial_z E^{+}, \tag{2.31}$$

$$\partial_z H^{+} = -\mathrm{i}\gamma E^{+}, \tag{2.32}$$

$$4\partial H^{+} = \mathrm{i}\gamma E_z. \tag{2.33}$$

Equation (2.31) can be seen as the so-called Dbar equation for E_z if E^{+} is known and its solution can be explicitly given by the Cauchy–Pompeiu formula [86] as follows:

$$E_z = \frac{1}{2\pi\mathrm{i}}\oint_{\partial D}\frac{E_z(\zeta')}{\zeta' - \zeta}\mathrm{d}\zeta' + T[\omega_0\mu_0 H^{+} + \partial_z E^{+}], \tag{2.34}$$

where the operator T is defined in Eq. (A.79). If we assume $\partial_z H^{+} \simeq 0$, which is reasonable when the loading object has homogeneous EPs along the z-axis, it holds that $E^{+} = 0$ by Eq. (2.32), and thus Eq. (2.34) gives an explicit reconstruction formula for E_z. Once E_z is reconstructed inside the ROI, it is straightforward to calculate γ according to Eq. (2.33) as follows:

$$\gamma = \frac{4\partial H^{+}}{\mathrm{i}E_z}. \tag{2.35}$$

Since this method can avoid using the Laplacian of the measured H^{+}, it is robust against measurement noise. If the loading object is also inhomogeneous along the z-axis, the following

iterative correction method can be constructed:

$$E_z^{(n+1)} = \frac{1}{2\pi \mathrm{i}} \oint_{\partial D} \frac{E_z(\zeta')}{\zeta' - \zeta} \mathrm{d}\zeta' + T[\omega_0 \mu_0 H^+ + \partial_z E^{+,(n)}], \tag{2.36}$$

$$E^{+,(n+1)} = \frac{\mathrm{i}\partial_z H^+}{\gamma^{(n)}} = -\frac{\partial_z H^+}{4\partial H^+} E_z^{(n+1)}. \tag{2.37}$$

Although this procedure is reported to successfully correct EP estimates in a numerical simulation, the error does not decrease monotonically, and the convergence has not been proven. Indeed, we illustrate a case where a nonconvergent result is produced in Chapter 4.

Lastly, methods based on the multichannel transmission MRI system have also been proposed and reported to give successful reconstruction results [87–95]. Liu *et al.* [89, 91] proposed the gradient EPT (gEPT) method in which γ and its spatial derivatives are treated as independent variables and estimated by solving a system of equations constructed from multiple data with different transmit channels. The method was extended by Wang *et al.* [93–95]. Sodickson *et al.* [87, 88] proposed Local Maxwell Tomography (LMT) and Global Maxwell Tomography (GMT), which also combine multiple data to estimate EPs. Although these methods provide good reconstruction results, the multichannel RF transmission system is not always available in practice. Therefore, in this thesis, we focus on constructing a method based on a single H^+ dataset generated by the typical birdcage coil.

2.1.4 Conventional QCM Reconstruction Methods

According to Eq. (2.15), the conductivity and permittivity reconstruction formulae of the standard EPT method can be rewritten in terms of the magnitude and phase of H^+ as follows:

$$\sigma = \frac{1}{\omega_0 \mu_0} \mathrm{Re}\left[\frac{\Delta H^+}{H^+}\right] = \frac{1}{\omega_0 \mu_0}\left(\Delta \angle H^+ + 2\frac{\nabla |H^+| \cdot \nabla \angle H^+}{|H^+|}\right), \tag{2.38}$$

$$\epsilon = -\frac{1}{\omega_0^2 \mu_0} \mathrm{Im}\left[\frac{\Delta H^+}{H^+}\right] = -\frac{1}{\omega_0^2 \mu_0}\left(\frac{\Delta |H^+|}{|H^+|} - |\nabla \angle H^+|^2\right). \tag{2.39}$$

Thus, under the assumption that $\nabla |H^+| \simeq \mathbf{0}$, the conductivity can be estimated by the formula

$$\sigma \simeq \frac{1}{\omega_0 \mu_0} \Delta \angle H^+, \tag{2.40}$$

and under the assumption that $\nabla \angle H^+ \simeq \mathbf{0}$, the permittivity can be estimated by the formula

$$\epsilon \simeq -\frac{1}{\omega_0^2 \mu_0} \frac{\Delta |H^+|}{|H^+|}. \tag{2.41}$$

One important advantage of QCM is that the conductivity can be reconstructed from the transceive phase $\phi = \angle H^+ + \angle H'^-$ instead of the transmit phase $\angle H^+$. Since Eq. (2.40) also holds for H'^- and the equation is linear for H^+ and H'^-, it holds that

$$\sigma = \frac{1}{2\omega_0 \mu_0}(\Delta \angle H^+ + \Delta \angle H'^-) = \frac{1}{2\omega_0 \mu_0} \Delta \phi. \tag{2.42}$$

We refer to Eq. (2.42) as the standard QCM formula. The following stabilized version is also proposed in [26]:

$$\sigma = \frac{1}{2\omega_0 \mu_0 |\Omega_{\boldsymbol{r}}|} \oint_{\partial \Omega_{\boldsymbol{r}}} \boldsymbol{n} \cdot \nabla \phi \mathrm{d}S. \tag{2.43}$$

Shin *et al*. [96] proposed to stabilize the solution by improving the filter to calculate the derivatives of the measured phase data. However, these methods using LHA have severe artefact in adjacent regions of different tissues.

Starting from Eq. (2.18), Gurler *et al*. [97] derived the linear PDE for ϕ that does not use LHA. By neglecting $\nabla|H^+|$ and $\nabla|H'^-|$, the real part of Eq. (2.18) reduces to

$$\nabla\phi \cdot \nabla \operatorname{Re}[\lambda] - \Delta\phi \operatorname{Re}[\lambda] + 2\omega_0\mu_0 = 0. \tag{2.44}$$

If we further assume that $\sigma^2 \gg (\omega_0\epsilon)^2$, $\operatorname{Re}[\lambda] \simeq 1/\sigma$ holds, this yields the following phase-based cr-EPT formula:

$$\nabla\phi \cdot \nabla\rho + \Delta\phi\rho = 2\omega_0\mu_0, \tag{2.45}$$

where $\rho \coloneqq 1/\sigma$ is the resistivity. Similar to the original cr-EPT method, the numerical solution of this convection-reaction equation is unstable, and an artificial diffusion term should be added to obtain a reliable estimate.

2.2 EPT and QCM as Impedivity Inverse Problems

As we have seen in the previous section, most of the conventional EPT methods [26, 30–32, 69, 73, 74, 78, 98] eliminate the electric field from Maxwell's equations to derive an equation which directly relates the measured magnetic field and the admittivity. This process yields the higher-order derivative of the measured H^+, making these methods sensitive to measurement noise. Here, we regard the electric field $\boldsymbol{E}$, as the dual field of the magnetic field $\boldsymbol{H}$ instead of eliminating it. This reformulates the EPT inverse problem as follows:

Given the measured B1 field vector $\boldsymbol{H}$ inside an ROI, reconstruct EPs $\lambda = \gamma^{-1}$ according to

$$\boldsymbol{E} = \lambda\nabla \times \boldsymbol{H}, \tag{2.46}$$

$$\nabla \times \boldsymbol{E} = -\mathrm{i}\omega_0\mu_0\boldsymbol{H}. \tag{2.47}$$

This inverse problem reconstructs the impedivity defined as the ratio of the derivative of the measured field to the dual field. In Eq. (2.47), the curl of the dual field is represented by the measured field. Therefore, we refer to this form of problem as the curl-constraint impedivity inverse problem.

We note that in the problem formulation given above, all three components of the magnetic field are assumed to be known. However, only H^+ is accessible via actual MRI measurements. Therefore, we introduce another form of impedivity inverse problem that contains only H^+. By substituting Eqs. (2.32) and (2.33) into Eq. (2.31), the $(x + \mathrm{i}y)$-component of Faraday's law can be rewritten as follows:

$$\partial_x\left(\frac{\mathrm{i}E_z}{2}\right) + \partial_y\left(-\frac{E_z}{2}\right) + \partial_z(-\mathrm{i}E^+) = \mathrm{i}\omega_0\mu_0 H^+ \tag{2.48}$$

This can be expressed as the divergence-constraint form

$$\nabla \cdot \tilde{\boldsymbol{E}} = \mathrm{i}\omega_0\mu_0 H^+, \tag{2.49}$$

where we defined a new vector field

$$\tilde{\boldsymbol{E}} \coloneqq \begin{pmatrix} \mathrm{i}E_z/2 \\ -E_z/2 \\ -\mathrm{i}E^+ \end{pmatrix} \tag{2.50}$$

that contains the $(x+\mathrm{i}y)$- and z-components of the electric field. Using Eqs. (2.32) and (2.33), these components are represented by H^+ and λ as

$$\mathrm{i}\lambda\partial_z H^+ = E^+, \tag{2.51}$$

$$4\mathrm{i}\lambda\partial H^+ = E_z. \tag{2.52}$$

Hence, the newly introduced vector field $\tilde{\boldsymbol{E}}$ can be written as

$$\tilde{\boldsymbol{E}} = \lambda\nabla^{\mathrm{c}} H^+, \tag{2.53}$$

where we define the complex-gradient operator as follows:

$$\nabla^{\mathrm{c}} := \begin{pmatrix} 2\partial \\ 2\mathrm{i}\partial \\ \partial_z \end{pmatrix} \tag{2.54}$$

Therefore, the impedivity λ, which was originally defined as the ratio of $\boldsymbol{E}$ to $\nabla\times\boldsymbol{H}$, can also be seen as the impedivity that relates $\tilde{\boldsymbol{E}}$ and $\nabla^{\mathrm{c}}H^+$. Combining Eqs. (2.49) and (2.53) enables us to formulate a novel impedivity inverse problem:

Given the measured positively rotating B1 field H^+ in an ROI, reconstruct EPs λ according to

$$\tilde{\boldsymbol{E}} = \lambda\nabla^{\mathrm{c}} H^+, \tag{2.55}$$

$$\nabla\cdot\tilde{\boldsymbol{E}} = \mathrm{i}\omega_0\mu_0 H^+. \tag{2.56}$$

Since Eq. (2.49) constraints the divergence of the dual field $\tilde{\boldsymbol{E}}$ by the measured field, we refer to the problem of this form as the divergence-constraint impedivity inverse problem.

This divergence-constraint problem can be also derived from the cr-EPT method [32] discussed in Chapter 1. Using the complex-gradient operator, Eq. (2.18) can be rewritten as

$$\lambda\Delta H^+ + \nabla\lambda\cdot\nabla^{\mathrm{c}}H^+ - \mathrm{i}\omega_0\mu_0 H^+ = 0. \tag{2.57}$$

It holds that

$$\nabla^{\mathrm{c}} = \begin{pmatrix} 2\partial \\ 2\mathrm{i}\partial \\ \partial_z \end{pmatrix} = \begin{pmatrix} \partial_x - \mathrm{i}\partial_y \\ \partial_y + \mathrm{i}\partial_x \\ \partial_z \end{pmatrix} = \nabla - \mathrm{i}\nabla\times\boldsymbol{e}_z, \tag{2.58}$$

where $\boldsymbol{e}_z$ is the unit vector along the z-axis. The second term, $\nabla\times\boldsymbol{e}_z = (\partial_y, -\partial_x, 0)$ is called the Hodge dual of ∇ and is normal to ∇ by definition. Taking advantage of this property, we can prove that

$$\nabla\cdot\nabla^{\mathrm{c}} = \nabla\cdot(\nabla - \mathrm{i}\nabla\times\boldsymbol{e}_z) = \nabla\cdot\nabla = \Delta. \tag{2.59}$$

Hence, Eq. (2.57) can be represented in the following divergence-constraint form:

$$\nabla\cdot(\lambda\nabla^{\mathrm{c}}H^+) = \mathrm{i}\omega_0\mu_0 H^+. \tag{2.60}$$

This is equivalent to the divergence-constraint impedivity inverse problem given by Eqs. (2.49) and (2.53). We note that a similar formulation can be derived for H^- by introducing the conjugate operator, $\bar{\nabla}^{\mathrm{c}} := \nabla + \mathrm{i}\nabla\times\boldsymbol{e}_z$. Specifically, it holds that

$$\nabla\cdot\tilde{\boldsymbol{E}}' = \mathrm{i}\omega_0\mu_0 H^-, \tag{2.61}$$

$$\tilde{\boldsymbol{E}}' = \lambda\bar{\nabla}^{\mathrm{c}} H^-, \tag{2.62}$$

where the vector field $\tilde{\boldsymbol{E}}'$ is defined as

$$\tilde{\boldsymbol{E}}' \coloneqq \begin{pmatrix} -\mathrm{i}E_z/2 \\ -E_z/2 \\ \mathrm{i}E^- \end{pmatrix}. \tag{2.63}$$

Next, we derive a similar formulation for the QCM inverse problem. According to the standard QCM methods [26, 99], we assume that $\nabla|H^{\pm}| \simeq \mathbf{0}$. Then, Eqs. (2.53) and (2.62) are approximated as

$$\tilde{\boldsymbol{E}} \simeq \lambda|H^+|\nabla^{\mathrm{c}} \exp(\mathrm{i}\angle H^+) = \mathrm{i}|H^+|\lambda \exp(\mathrm{i}\angle H^+)\nabla^{\mathrm{c}}\angle H^+, \tag{2.64}$$

$$\tilde{\boldsymbol{E}}' \simeq \lambda|H^-|\bar{\nabla}^{\mathrm{c}} \exp(\mathrm{i}\angle H^-) = \mathrm{i}|H^-|\lambda \exp(\mathrm{i}\angle H^-)\bar{\nabla}^{\mathrm{c}}\angle H^-. \tag{2.65}$$

Taking the divergence of both sides of the above equations leads to

$$\begin{aligned} \nabla \cdot \tilde{\boldsymbol{E}} &= \mathrm{i}|H^+|(\nabla\lambda \cdot \exp(\mathrm{i}\angle H^+)\nabla^{\mathrm{c}}\angle H^+ + \lambda\nabla \cdot (\exp(\mathrm{i}\angle H^+)\nabla^{\mathrm{c}}\angle H^+)) \\ &= \mathrm{i}H^+(\nabla\lambda \cdot \nabla^{\mathrm{c}}\angle H^+ + \lambda\Delta\angle H^+ + \mathrm{i}\lambda\nabla\angle H^+ \cdot \nabla^{\mathrm{c}}\angle H^+) \\ &= \mathrm{i}H^+(\nabla \cdot (\lambda\nabla^{\mathrm{c}}\angle H^+) + \mathrm{i}\lambda|\nabla\angle H^+|^2), \end{aligned} \tag{2.66}$$

$$\begin{aligned} \nabla \cdot \tilde{\boldsymbol{E}}' &= \mathrm{i}|H^-|(\nabla\lambda \cdot \exp(\mathrm{i}\angle H^-)\bar{\nabla}^{\mathrm{c}}\angle H^- + \lambda\nabla \cdot (\exp(\mathrm{i}\angle H^-)\bar{\nabla}^{\mathrm{c}}\angle H^-)) \\ &= \mathrm{i}H^-(\nabla\lambda \cdot \bar{\nabla}^{\mathrm{c}}\angle H^- + \lambda\Delta\angle H^- + \mathrm{i}\lambda\nabla\angle H^- \cdot \bar{\nabla}^{\mathrm{c}}\angle H^-) \\ &= \mathrm{i}H^-(\nabla \cdot (\lambda\bar{\nabla}^{\mathrm{c}}\angle H^-) + \mathrm{i}\lambda|\nabla\angle H^-|^2), \end{aligned} \tag{2.67}$$

where we used Eq. (2.59). Substituting them into Eqs. (2.49) and (2.61) and dividing them by $\mathrm{i}H^{\pm}$ yields

$$\nabla \cdot (\lambda\nabla^{\mathrm{c}}\angle H^+) + \mathrm{i}\lambda|\nabla\angle H^+|^2 = \omega_0\mu_0, \tag{2.68}$$

$$\nabla \cdot (\lambda\bar{\nabla}^{\mathrm{c}}\angle H^-) + \mathrm{i}\lambda|\nabla\angle H^-|^2 = \omega_0\mu_0. \tag{2.69}$$

According to the cr equation-based QCM method [97], we further assume that the conductive property of tissues is dominant over their dielectric property, i.e., $\mathrm{Re}[\lambda] \simeq \rho$, leading to

$$\nabla \cdot (\rho\nabla^{\mathrm{c}}\angle H^+) = \omega_0\mu_0, \tag{2.70}$$

$$\nabla \cdot (\rho\bar{\nabla}^{\mathrm{c}}\angle H^-) = \omega_0\mu_0. \tag{2.71}$$

These equations can be considered as the divergence-constraint forms for the dual fields

$$\boldsymbol{F} \coloneqq \rho\nabla^{\mathrm{c}}\angle H^+, \tag{2.72}$$

$$\boldsymbol{F}' \coloneqq \rho\bar{\nabla}^{\mathrm{c}}\angle H^- \tag{2.73}$$

of the fields $\angle H^{\pm}$. Therefore, by replacing the transmit field in Eq. (2.73) with the receive field and adding it to Eq. (2.72), it holds that

$$\nabla \cdot \boldsymbol{\psi} = 2\omega_0\mu_0, \tag{2.74}$$

$$\boldsymbol{\psi} = \rho(\nabla^{\mathrm{c}}\angle H^+ + \bar{\nabla}^{\mathrm{c}}\angle H^-). \tag{2.75}$$

As discussed by Gurler *et al.* [97], the spatial variation of $\angle H^+ - \angle H'^-$ is sufficiently small, and thus we can approximate $\boldsymbol{\psi}$ as

$$\boldsymbol{\psi} = \rho \begin{pmatrix} \partial_x\phi - \mathrm{i}\partial_y(\angle H^+ - \angle H'^-) \\ \partial_y\phi + \mathrm{i}\partial_x(\angle H^+ - \angle H'^-) \\ \partial_z\phi \end{pmatrix} \simeq \rho\nabla\phi. \tag{2.76}$$

Therefore, the QCM problem can be reformulated as follows:

Given the measured transceive B1 phase ϕ inside an ROI, reconstruct the conductivity $\sigma = \rho^{-1}$ according to

$$\boldsymbol{\psi} = \rho \nabla \phi, \tag{2.77}$$

$$\nabla \cdot \boldsymbol{\psi} = 2\omega_0 \mu_0. \tag{2.78}$$

This divergence-constraint problem can also be derived from the phase-based cr-EPT method [97] discussed in Chapter 1. By Eq. (2.45), it immediately follows that

$$\nabla \cdot (\rho \nabla \phi) = 2\omega_0 \mu_0. \tag{2.79}$$

This is equivalent to Eqs. (2.78) and (2.77).

In our newly formulated EPT and QCM problems, either the divergence or curl of the dual field is known from the measurement data. This means that the longitudinal or transverse component of the dual field is known when considering Helmholtz's decomposition. Therefore, the inverse problems are to reconstruct the other component of the field. In the next section, we derive various representation formulae of vector fields based on Helmholtz's decomposition, which is reviewed in detail in Appendix A.

2.3 Representation Formulae of Vector Fields Based on Helmholtz's Decomposition

Equation (A.54) is a representation formula of a vector field by both its divergence and curl. In other words, the operators $\boldsymbol{P}_{\mathrm{L}}$ and $\boldsymbol{P}_{\mathrm{T}}$ project a vector field onto the irrotational and solenoidal fields via its divergence or curl. Here, we modify these operators to obtain alternatives that directly project the field without computing its divergence or curl.

By the product rule of vector differentiation

$$\nabla \cdot (\boldsymbol{f} \nabla w) = \nabla w (\nabla \cdot \boldsymbol{f}) + \boldsymbol{f} \cdot \nabla \nabla w, \tag{2.80}$$

the following integration by parts holds:

$$\int_\Omega \nabla w (\nabla \cdot \boldsymbol{f}) \mathrm{d}V = \oint_{\partial\Omega} \nabla w (\boldsymbol{n} \cdot \boldsymbol{f}) \mathrm{d}S - \int_\Omega \boldsymbol{f} \cdot \nabla \nabla w \mathrm{d}V. \tag{2.81}$$

Using the above relation, the operator $\boldsymbol{P}_{\mathrm{L}}$ defined in Eq. (A.56) can be rewritten as follows:

$$\boldsymbol{P}_{\mathrm{L}}[\boldsymbol{f}](\boldsymbol{r}) = -\int_\Omega \boldsymbol{f}(\boldsymbol{r}') \cdot \nabla \nabla G(\boldsymbol{r}'; \boldsymbol{r}) \mathrm{d}V'. \tag{2.82}$$

The representation of $\boldsymbol{P}_{\mathrm{L}}$ given by Eq. (2.82) allows projection of a vector field onto its longitudinal component without giving or calculating its divergence. Using Eq. (2.82), Eq. (A.54) is modified as

$$\boldsymbol{f}(\boldsymbol{r}) = \oint_{\partial\Omega} \nabla G(\boldsymbol{r}'; \boldsymbol{r}) \times (\boldsymbol{n}(\boldsymbol{r}') \times \boldsymbol{f}(\boldsymbol{r}')) \mathrm{d}S' - \int_\Omega \nabla G(\boldsymbol{r}'; \boldsymbol{r}) \times (\nabla \times \boldsymbol{f}(\boldsymbol{r}')) \mathrm{d}V' - \int_\Omega \boldsymbol{f}(\boldsymbol{r}') \cdot \nabla \nabla G(\boldsymbol{r}'; \boldsymbol{r}) \mathrm{d}V' \tag{2.83}$$

This is a representation formula of a vector field by the field itself and its curl.

Similarly, by the vector field identity

$$\nabla w \times (\nabla \times \boldsymbol{f}) + (\boldsymbol{f} \times \nabla) \times \nabla w = \nabla(\nabla w \cdot \boldsymbol{f}) - \nabla \cdot (\nabla w \boldsymbol{f}), \tag{2.84}$$

the following integration by parts holds:

$$\int_\Omega \nabla w \times (\nabla \times \boldsymbol{f}) \mathrm{d}V + \int_\Omega (\boldsymbol{f} \times \nabla) \times \nabla w \mathrm{d}V = \oint_{\partial\Omega} \boldsymbol{n} \nabla w \cdot \boldsymbol{f} - \boldsymbol{n} \cdot \nabla w \boldsymbol{f} \mathrm{d}S. \tag{2.85}$$

Using the triplet identity

$$\boldsymbol{n} \nabla w \cdot \boldsymbol{f} - \boldsymbol{n} \cdot \nabla w \boldsymbol{f} = \nabla w \times (\boldsymbol{n} \times \boldsymbol{f}), \tag{2.86}$$

it holds that

$$\int_\Omega \nabla w \times (\nabla \times \boldsymbol{f}) \mathrm{d}V + \int_\Omega (\boldsymbol{f} \times \nabla) \times \nabla w \mathrm{d}V = \oint_{\partial\Omega} \nabla w \times (\boldsymbol{n} \times \boldsymbol{f}) \mathrm{d}S. \tag{2.87}$$

Using the above relation, the operator $\boldsymbol{P}_\mathrm{T}$ defined in Eq. (A.57) can be rewritten as follows:

$$\boldsymbol{P}_\mathrm{T}[\boldsymbol{f}](\boldsymbol{r}) = \int_\Omega (\boldsymbol{f}(\boldsymbol{r}') \times \nabla) \times \nabla G(\boldsymbol{r}'; \boldsymbol{r}) \mathrm{d}V'. \tag{2.88}$$

The representation of $\boldsymbol{P}_\mathrm{T}$ given by Eq. (2.88) allows projection of a vector field onto its transverse component without giving or calculating its curl. Using Eq. (2.88), Eq. (A.54) is modified as

$$\begin{aligned} \boldsymbol{f}(\boldsymbol{r}) = -\oint_{\partial\Omega} \nabla G(\boldsymbol{r}'; \boldsymbol{r})(\boldsymbol{n}(\boldsymbol{r}') \cdot \boldsymbol{f}(\boldsymbol{r}')) \mathrm{d}S' + \int_\Omega \nabla G(\boldsymbol{r}'; \boldsymbol{r})(\nabla \cdot \boldsymbol{f}(\boldsymbol{r}')) \mathrm{d}V' \\ + \int_\Omega (\boldsymbol{f}(\boldsymbol{r}') \times \nabla) \times \nabla G(\boldsymbol{r}'; \boldsymbol{r}) \mathrm{d}V'. \end{aligned} \tag{2.89}$$

This is a representation formula of a vector field by the field itself and its divergence.

Using both Eqs. (2.82) and (2.88), we can represent a vector field by itself as

$$\boldsymbol{f}(\boldsymbol{r}) = -\int_\Omega \boldsymbol{f}(\boldsymbol{r}') \cdot \nabla \nabla G(\boldsymbol{r}'; \boldsymbol{r}) \mathrm{d}V' + \int_\Omega (\boldsymbol{f}(\boldsymbol{r}') \times \nabla) \times \nabla G(\boldsymbol{r}'; \boldsymbol{r}) \mathrm{d}V'. \tag{2.90}$$

Although representing a field by itself might seem meaningless, the important point here is that the field is decomposed into the longitudinal and transverse fields. Therefore, Eq. (2.90) can be interpreted as Helmholtz's decomposition of a vector field. Despite the fact that Eq. (2.90) contains only volume integral terms and no surface integral appears, Eq. (2.90) is still valid for general bounded domains.

This decomposition formula can be directly derived from the identity

$$\Delta w \boldsymbol{f} = \boldsymbol{f} \cdot \nabla \nabla w - (\boldsymbol{f} \times \nabla) \times \nabla w. \tag{2.91}$$

Taking w as G and integrating both sides over Ω yields Eq. (2.90). From Eq. (2.91), it is obvious that Eq. (2.91) gives a decomposition of a vector field.

2.4 EPT and QCM Reconstruction Based on Helmholtz's Representation Formula

In this section, we derive IEs for the impedivity using the representation formulae derived in the previous section. First, we consider the case where all three components of the magnetic field are measured. As proposed in [100], by applying the representation formula of a vector field in terms of its curl and itself to $\boldsymbol{E}$, we have

$$\boldsymbol{E} = \oint_{\partial\Omega} \nabla G(\boldsymbol{r}';\boldsymbol{r}) \times (\boldsymbol{n} \times \boldsymbol{E}) \mathrm{d}S' - \int_{\Omega} \nabla G(\boldsymbol{r}';\boldsymbol{r}) \times (\nabla \times \boldsymbol{E}) \mathrm{d}V' - \int_{\Omega} \boldsymbol{E} \cdot \nabla\nabla G(\boldsymbol{r}';\boldsymbol{r}) \mathrm{d}V'. \quad (2.92)$$

If $\boldsymbol{H}$ is known, the first two terms corresponding to the transverse component of the electric field can be calculated as follows:

$$\boldsymbol{E}_{\mathrm{T}} = \oint_{\partial\Omega} \nabla G(\boldsymbol{r}';\boldsymbol{r}) \times (\boldsymbol{n} \times (\lambda\nabla \times \boldsymbol{H})) \mathrm{d}S' - \int_{\Omega} \nabla G(\boldsymbol{r}';\boldsymbol{r}) \times \mathrm{i}\omega_0\mu_0 \boldsymbol{H} \mathrm{d}V'. \quad (2.93)$$

Then, it holds that

$$\boldsymbol{E} = \boldsymbol{E}_{\mathrm{T}} - \int_{\Omega} \boldsymbol{E} \cdot \nabla\nabla G(\boldsymbol{r}';\boldsymbol{r}) \mathrm{d}V'. \quad (2.94)$$

Eda *et al*. [100] considered Eq. (2.94) as an IE for the vector field $\boldsymbol{E}$ and proposed to solve it for $\boldsymbol{E}$. However, this system of equations cannot be solved generally because of the orthogonality of Helmholtz's decomposition; the longitudinal and transverse components are completely independent and one cannot be determined from the other. Later they extended the method by adding a constraint using Ampère's law and iteratively calculating the electric field that satisfies both Eqs. (2.94) and (1.2) using the iterative projection onto convex sets [101]. Although this iteration is guaranteed to converge on an intersection of the two convex sets, its dependency of the initial guess and the rate of convergence is still unclear.

Instead of iteratively estimating the electric field, we propose to substitute Ampère's law into the IE and directly solve it for the impedivity. Specifically, substituting Eq. (2.46) into Eq. (2.94) yields

$$\lambda\nabla \times \boldsymbol{H} = \boldsymbol{E}_{\mathrm{T}} - \int_{\Omega} (\lambda\nabla \times \boldsymbol{H}) \cdot \nabla\nabla G(\boldsymbol{r}';\boldsymbol{r}) \mathrm{d}V'. \quad (2.95)$$

This equation can be seen as an IE for the scalar quantity λ. Through numerical simulations, we verify that this equation for λ is solvable, unlike the case of solving it for the vector field $\boldsymbol{E}$. Equation (2.95) is an IE relating λ with $\boldsymbol{H}$ globally and does not contain the Laplacian of the measured B1 field. Furthermore, Eq. (2.95) is linear for λ, rendering the method free from local minima. Therefore, the proposed method is global, direct, and valid for 3D mapping.

We note that only the positively rotating component H^+ can be obtained in practical situations. One simple approach to fill this gap is to approximate $\boldsymbol{H}$ using H^+ by taking advantage of the fact that $|H^-|$ and $|H_z|$ is much smaller than $|H^+|$ when the body is excited by the quadrature birdcage coil typically used in modern MRI systems. By assuming $H_z = H^- = 0$, $\boldsymbol{H}$ and $\nabla \times \boldsymbol{H}$ can be approximated as

$$\boldsymbol{H} = \begin{pmatrix} H^+ + H^- \\ -\mathrm{i}(H^+ - H^-) \\ H_z \end{pmatrix} \simeq \begin{pmatrix} H^+ \\ -\mathrm{i}H^+ \\ 0 \end{pmatrix}, \quad (2.96)$$

$$\nabla \times \boldsymbol{H} = \begin{pmatrix} \partial_y H_z - \partial_z H_y \\ \partial_z H_x - \partial_x H_z \\ -4\mathrm{i}\partial H^+ - \mathrm{i}\partial_z H_z \end{pmatrix} \simeq \begin{pmatrix} \mathrm{i}\partial_z H^+ \\ \partial_z H^+ \\ -4\mathrm{i}\partial H^+ \end{pmatrix}. \quad (2.97)$$

The error due to this approximation is investigated by numerical simulations.

Instead of neglecting H^- and H_z, we can derive a reconstruction method that only uses the measured H^+ based on Eqs. (2.49) and (2.53) that we newly derived in the previous section. By applying the representation formula of a vector field in terms of its divergence and itself to $\tilde{\boldsymbol{E}}$, we have

$$\tilde{\boldsymbol{E}} = -\oint_{\partial\Omega} \nabla G(\boldsymbol{r}';\boldsymbol{r})(\boldsymbol{n}\cdot\tilde{\boldsymbol{E}})\mathrm{d}S' + \int_{\Omega} \nabla G(\boldsymbol{r}';\boldsymbol{r})\nabla\cdot\tilde{\boldsymbol{E}}\mathrm{d}V' + \int_{\Omega} (\tilde{\boldsymbol{E}}\times\nabla)\times\nabla G(\boldsymbol{r}';\boldsymbol{r})\mathrm{d}V' \quad (2.98)$$

By Eqs. (2.49) and (2.53), the first two terms corresponding to the longitudinal component of $\tilde{\boldsymbol{E}}$ can be calculated as follows:

$$\tilde{\boldsymbol{E}}_{\mathrm{L}} = -\oint_{\partial\Omega} \nabla G(\boldsymbol{r}';\boldsymbol{r})(\boldsymbol{n}\cdot\lambda\nabla^{\mathrm{c}}H^+)\mathrm{d}S' + \int_{\Omega} \nabla G(\boldsymbol{r}';\boldsymbol{r})\mathrm{i}\omega_0\mu_0 H^+\mathrm{d}V'. \quad (2.99)$$

Substituting Eq. (2.53) into the above equation yields

$$\lambda\nabla^{\mathrm{c}}H^+ = \tilde{\boldsymbol{E}}_{\mathrm{L}} + \int_{\Omega} (\lambda\nabla^{\mathrm{c}}H^+\times\nabla)\times\nabla G(\boldsymbol{r}';\boldsymbol{r})\mathrm{d}V'. \quad (2.100)$$

As is the case with Eq. (2.95), Eq. (2.100) provides a global, direct, and 3D EPT reconstruction method. Furthermore, in contrast to Eq. (2.95), Eq. (2.100) can be solved using only H^+ measurable with the MRI scanner.

The same formula can be established for the QCM problem since it is also stated as the divergence-constraint impedivity inverse problem as given in Eqs. (2.78) and (2.77). By applying the divergence-form representation formula of a vector field to $\boldsymbol{\psi}$, we have

$$\boldsymbol{\psi} = -\oint_{\partial\Omega} \nabla G(\boldsymbol{r}';\boldsymbol{r})(\boldsymbol{n}\cdot\boldsymbol{\psi})\mathrm{d}S' + \int_{\Omega} \nabla G(\boldsymbol{r}';\boldsymbol{r})(\nabla\cdot\boldsymbol{\psi})\mathrm{d}V' + \int_{\Omega} (\boldsymbol{\psi}\times\nabla)\times\nabla G(\boldsymbol{r}';\boldsymbol{r})\mathrm{d}V' \quad (2.101)$$

By Eqs. (2.78) and (2.77), the first two terms corresponding to the longitudinal component of $\boldsymbol{\psi}$ can be calculated as follows:

$$\boldsymbol{\psi}_{\mathrm{L}} = -\oint_{\partial\Omega} \nabla G(\boldsymbol{r}';\boldsymbol{r})(\boldsymbol{n}\cdot\rho\nabla\phi)\mathrm{d}S' + \int_{\Omega} \nabla G(\boldsymbol{r}';\boldsymbol{r})2\omega_0\mu_0\mathrm{d}V'. \quad (2.102)$$

Substituting Eq. (2.77) into the above equation yields

$$\rho\nabla\phi = \boldsymbol{\psi}_{\mathrm{L}} + \int_{\Omega} (\rho\nabla\phi\times\nabla)\times\nabla G(\boldsymbol{r}';\boldsymbol{r})\mathrm{d}V'. \quad (2.103)$$

Using Eq. (2.103) QCM can be performed without calculating the higher-order derivatives of the measured B1 phase ϕ nor being trapped by local minima.

2.5 Numerical Solution of the Integral Equation

2.5.1 FFT-CG-Based Method for Solving the Integral Equation

The IEs derived in the previous section can be rewritten as

$$(\boldsymbol{I}-\boldsymbol{P}_{\mathrm{L}})[\lambda\nabla\times\boldsymbol{H}] = \boldsymbol{E}_{\mathrm{T}}, \quad (2.104)$$

$$(\boldsymbol{I}-\boldsymbol{P}_{\mathrm{T}})[\lambda\nabla^{c}H^+] = \tilde{\boldsymbol{E}}_{\mathrm{L}}, \quad (2.105)$$

$$(\boldsymbol{I}-\boldsymbol{P}_{\mathrm{T}})[\rho\nabla\phi] = \boldsymbol{\psi}_{\mathrm{L}}, \quad (2.106)$$

which will be denoted as $L[u] = f$ for simplicity, and can be efficiently solved using the CG method. In each iteration of the CG method, the forward operation must be performed, which can be accomplished using the FFT since the integral operation is the convolution. We note that the CG method can only solve the positive definite system. One approach to ensure this condition is to solve the least-squares system $L^*[L[u]] = L^*[f]$ instead of the original system, where L^* means the adjoint operator of L. Therefore, it is necessary to consider the expression of the adjoint operators. First, the adjoint operation of multiplying a function is to multiply the complex conjugate of the function. Second, the adjoint operation of convoluting a function $f(\boldsymbol{r})$ is to convolute $\bar{f}(-\boldsymbol{r})$. The Fourier transform of $\bar{f}(-\boldsymbol{r})$ is the complex conjugate of the Fourier transform of $f(\boldsymbol{r})$.

We also note that the Fourier transform of the convolution kernel becomes singular at the origin. Vico *et al.* [102] derived a modified kernel that is regular in the entire domain including the origin by exploiting the fact that the convolution is performed over a finite ROI instead of the entire domain. We used this nonsingular kernel for our FFT-CG calculation.

2.5.2 Regularization of the Impedivity Estimation

The impedivity inverse problem could be ill-posed in a region where the dual field vanishes. In EPT, it is known that the electric field becomes very low and vanishes around the center of the body inside the quadrature birdcage coil [69]. In this region, the EPs cannot be determined as the ratio of $\nabla \times \boldsymbol{H}$ or $\nabla^{\mathrm{c}} H^+$ to $\boldsymbol{E}$ or $\tilde{\boldsymbol{E}}$. The same problem also occurs in QCM; $\nabla\phi$ becomes zero near the center of the body. Therefore, it is essential to stabilize the inversion by applying regularization. We apply regularization in our proposed method using the following approach. First, we get a temporal estimate of the impedivity by solving the IEs without regularization. Then, by the estimated impedivity λ^*, ρ^*, we calculate the dual fields as follows:

$$\boldsymbol{E}^* = \lambda^* \nabla \times \boldsymbol{H} \tag{2.107}$$

$$\tilde{\boldsymbol{E}}^* = \lambda^* \nabla^{\mathrm{c}} H^+ \tag{2.108}$$

$$\boldsymbol{\psi}^* = \rho^* \nabla\phi \tag{2.109}$$

Then, the following equations hold:

$$\frac{\langle \boldsymbol{E}^*, \nabla \times \boldsymbol{H} \rangle}{|\boldsymbol{E}^*|} - |\boldsymbol{E}^*|\gamma = 0 \tag{2.110}$$

$$\frac{\langle \tilde{\boldsymbol{E}}^*, \nabla^{\mathrm{c}} H^+ \rangle}{|\tilde{\boldsymbol{E}}^*|} - |\tilde{\boldsymbol{E}}^*|\gamma = 0 \tag{2.111}$$

$$\frac{\langle \boldsymbol{\psi}^*, \nabla\phi \rangle}{|\boldsymbol{\psi}^*|} - |\boldsymbol{\psi}^*|\sigma = 0, \tag{2.112}$$

where γ, σ are the admittivity to be reconstructed. We propose to apply regularization to the above equations. Specifically, by simply denoting the above equations as $f - ku = 0$, where $u = \gamma, \sigma$, the objective functional is given as follows:

$$J[u] = \frac{1}{2} \int_\Omega |w_{\mathrm{f}}(f - ku)|^2 \mathrm{d}V + \frac{\lambda^p}{p} \int_\Omega |w_{\mathrm{r}} \nabla u|^p \mathrm{d}V, \qquad p = 1, 2 \tag{2.113}$$

where w_{f} and w_{r} are weighting functions used in the morphology-based regularization describe later. Taking p as 2 corresponds to Tikhonov regularization applied in the gradient domain and taking p as 1 corresponds to total variation (TV) regularization. The minimization of Eq. (2.113) can be performed by solving the linear system at a single time when $p = 2$

and by iteratively solving the system using the split Bregman method [103] when $p = 1$. However, solving this system of equations ts too computationally expensive when the size of the system matrix becomes large. Here, we used a method based on the variable splitting proposed by Milovic *et al.* [104] for QSM inversion. In this method, instead of directly solving the minimization of the above functional for u, we modify the functional by adding the two variables $\boldsymbol{v}_1$ and v_2, which are expected to be close to ∇u and u as follows:

$$J_{\eta_1,\eta_2}[u, \boldsymbol{v}_1, v_2] = \frac{1}{2}\int_\Omega |w_{\mathrm{f}}(f - kv_2)|^2 \mathrm{d}V + \frac{\lambda^p}{p}\int_\Omega |w_{\mathrm{r}}\boldsymbol{v}_1|^p \mathrm{d}V + \frac{\mu_2^2}{2}\int_\Omega |v_2 - u - \eta_2|^2 \mathrm{d}V + \frac{\mu_1^2}{2}\int_\Omega |\boldsymbol{v}_1 - \nabla u - \boldsymbol{\eta}_1|^2 \mathrm{d}V, \qquad p = 1, 2. \quad (2.114)$$

The new functional will be minimized in an alternating manner for u and $(\boldsymbol{v}_1, v_2)$, while the Bregman variables $(\boldsymbol{\eta}_1, \eta_2)$ are also updated in each iteration. In the following, we describe the detailed algorithm for each $p = 1, 2$.

In Tikhonov regularization, the update rule for each variable is as follows:

$$u^{(i+1)} = \arg\min_u \frac{\mu_2^2}{2}\int_\Omega |v_2^{(i)} - \eta_2^{(i)} - u|^2 \mathrm{d}V + \frac{\mu_1^2}{2}\int_\Omega |\boldsymbol{v}_1^{(i)} - \boldsymbol{\eta}_1^{(i)} - \nabla u|^2 \mathrm{d}V \quad (2.115)$$

$$\boldsymbol{v}_1^{(i+1)} = \arg\min_{\boldsymbol{v}_1} \frac{\lambda^2}{2}\int_\Omega |w_{\mathrm{r}}\boldsymbol{v}_1|^2 \mathrm{d}V + \frac{\mu_1^2}{2}\int_\Omega |\boldsymbol{v}_1 - \nabla u^{(i+1)} - \boldsymbol{\eta}_1^{(i)}|^2 \mathrm{d}V \quad (2.116)$$

$$v_2^{(i+1)} = \arg\min_{v_2} \frac{1}{2}\int_\Omega |w_{\mathrm{f}}(f - kv_2)|^2 \mathrm{d}V + \frac{\mu_2^2}{2}\int_\Omega |v_2 - u^{(i+1)} - \eta_2^{(i)}|^2 \mathrm{d}V \quad (2.117)$$

$$\boldsymbol{\eta}_1^{(i+1)} = \boldsymbol{\eta}_1^{(i)} + \nabla u^{(i+1)} - \boldsymbol{v}_1^{(i+1)} \quad (2.118)$$

$$\eta_2^{(i+1)} = \eta_2^{(i)} + u^{(i+1)} - v_2^{(i+1)} \quad (2.119)$$

The updates of u and $(\boldsymbol{v}_1, v_2)$ are computationally very efficient. Equation (2.115) can be minimized by solving the following equation:

$$(\mu_2^2 - \mu_1^2\Delta)u^{(i+1)} = \mu_2^2(v_2^{(i)} - \eta_2^{(i)}) - \mu_1^2\nabla \cdot (\boldsymbol{v}_1^{(i)} - \boldsymbol{\eta}_1^{(i)}). \quad (2.120)$$

This can be accomplished efficiently by performing a single iteration of the Gauss–Seidel sweep [103]. The solutions of Eqs. (2.116) and (2.117) can be given analytically as

$$\boldsymbol{v}_1^{(i+1)} = \frac{\mu_1^2(\nabla u^{(i+1)} + \boldsymbol{\eta}_1^{(i)})}{w_{\mathrm{r}}^2\lambda^2 + \mu_1^2} \quad (2.121)$$

$$v_2^{(i+1)} = \frac{w_{\mathrm{f}}^2\bar{k}f + \mu_2^2(u^{(i+1)} + \eta_2^{(i)})}{w_{\mathrm{f}}^2|k|^2 + \mu_2^2}. \quad (2.122)$$

Therefore, all procedures can be performed without solving a large system of equations as typically encountered in medical imaging.

In TV regularization, the update rule for each variable is as follows:

$$u^{(i+1)} = \arg\min_{u} \frac{\mu_2^2}{2} \int_{\Omega} |v_2^{(i)} - \eta_2^{(i)} - u|^2 \mathrm{d}V + \frac{\mu_1^2}{2} \int_{\Omega} |\boldsymbol{v}_1^{(i)} - \boldsymbol{\eta}_1^{(i)} - \nabla u|^2 \mathrm{d}V \tag{2.123}$$

$$\boldsymbol{v}_1^{(i+1)} = \arg\min_{\boldsymbol{v}_1} \lambda \int_{\Omega} |w_{\mathrm{r}} \boldsymbol{v}_1| \mathrm{d}V + \frac{\mu_1^2}{2} \int_{\Omega} |\boldsymbol{v}_1 - \nabla u^{(i+1)} - \boldsymbol{\eta}_1^{(i)}|^2 \mathrm{d}V \tag{2.124}$$

$$v_2^{(i+1)} = \arg\min_{v_2} \frac{1}{2} \int_{\Omega} |w_{\mathrm{f}}(f - k v_2)|^2 \mathrm{d}V + \frac{\mu_2^2}{2} \int_{\Omega} |v_2 - u^{(i+1)} - \eta_2^{(i)}|^2 \mathrm{d}V \tag{2.125}$$

$$\boldsymbol{\eta}_1^{(i+1)} = \boldsymbol{\eta}_1^{(i)} + \nabla u^{(i+1)} - \boldsymbol{v}_1^{(i+1)} \tag{2.126}$$

$$\eta_2^{(i+1)} = \eta_2^{(i)} + u^{(i+1)} - v_2^{(i+1)} \tag{2.127}$$

Only Eq. (2.124) is different from the previous section. The solution of Eq. (2.124) is also given analytically by the so-called soft threshold operation as

$$\boldsymbol{v}_1^{(i+1)} = \frac{\nabla u^{(i+1)} + \boldsymbol{\eta}_1^{(i)}}{|\nabla u^{(i+1)} + \boldsymbol{\eta}_1^{(i)}|} \max\left(|\nabla u^{(i+1)} + \boldsymbol{\eta}_1^{(i)}| - w_{\mathrm{r}} \frac{\lambda}{\mu_1^2}, 0 \right) \tag{2.128}$$

Therefore, TV regularization can also be performed without solving a large system of equations.

The iterative algorithm described above requires additional parameters (μ_1, μ_2). These parameters are known to determine the convergence speed of the algorithm without affecting the final result. We set (μ_1, μ_2) as $(\lambda, 1)$ throughout all numerical simulations and phantom experiments.

2.6 Numerical Simulations

2.6.1 Setup and Conditions

As shown in Fig. 2.1, a 16-leg high-pass shielded birdcage coil with a diameter of 240 mm and a height of 270 mm was constructed using FEM software COMSOL Multiphysics 5.5 (COMSOL Inc.). The optimal capacitance value of the birdcage coil was determined according to the method proposed by Gurler [105]. The magnetic field was excited at 123.2 MHz (corresponding to a 2.89 T MRI system) in quadrature excitation mode, in which the coil was driven by two ports 90° apart from each other and with a 90° phase difference. H^+ was obtained on a 180 mm × 180 mm × 80 mm square region centered at the origin with a matrix size of 128 × 128 × 16 (a resolution of about 1.4 mm × 1.4 mm × 5 mm).

Two models (the sphere model in Fig. 2.2(a) and the brain model in Fig. 2.2(b)) were constructed as loading objects. The sphere model consists of a cylindrical background region with a conductivity of 0.5 S/m and a relative permittivity of 80, and spherical inclusions with the conductivity 1 S/m and relative permittivity 50. The brain model was created from segmented anatomical brain data called the BrainWeb model [106, 107], in which the brain image was acquired by high-resolution MRI imaging and segmented into ten types of tissue: cerebrospinal fluid (CSF), white matter (WM), gray matter (GM), fat, dura, scalp, muscle, skull, vessel, and marrow. We simplified the model by reducing the number of tissue types to five: CSF, WM, GM, skull, and scalp as per the approach of Hafalir *et al.* [32]. These five types of tissues and their EPs are shown in Table 2.2.

The ROI was set to the 90 mm × 90 mm × 90 mm rectangular region centered at the origin. MATLAB R2020a (The MathWorks Inc.) was used for all reconstruction processes.

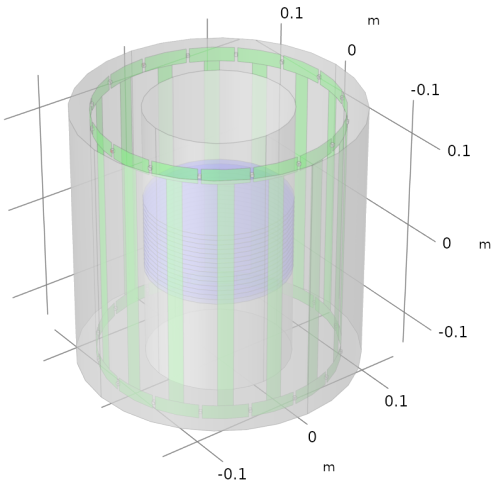

Fig. 2.1: Configuration of numerical simulations. The time-harmonic magnetic field was excited from two orthogonal ports of the birdcage coil (green) and H^+ was obtained on sixteen slices at the center (blue).

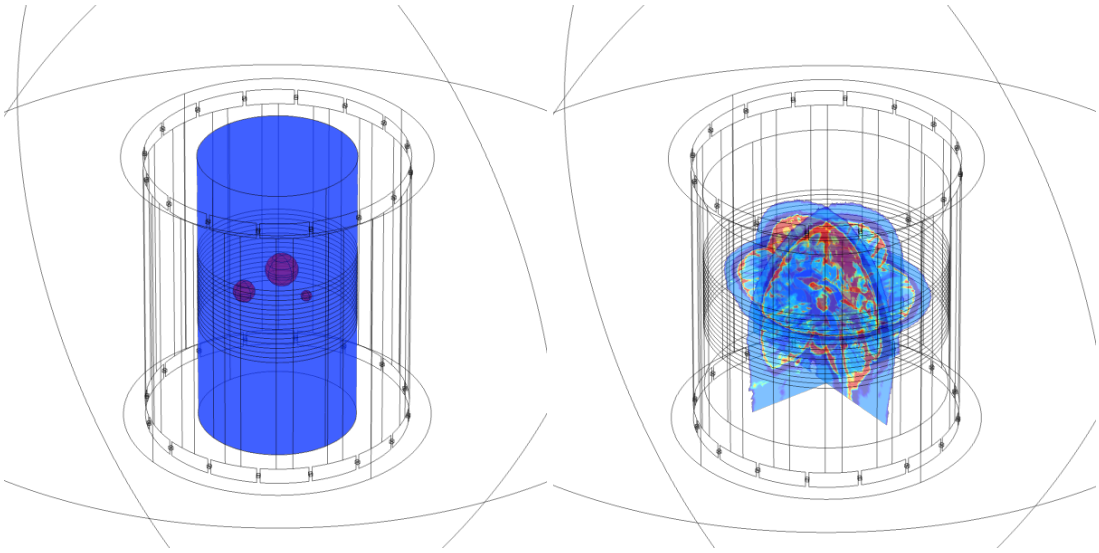

(a) Sphere model (b) Brain model

Fig. 2.2: Simulation models. The sphere model consists of a cylindrical background region and three spherical inclusions. The brain model was created from anatomical brain MRI data provided by BrainWeb [106, 107].

In the proposed methods as well as the conventional methods, the derivatives of the measured H^+ must be calculated. To mitigate noise amplification, the derivatives were calculated by applying the Savitzky–Golay filter [108, 109] in which the function is fit by a second-order polynomial in each neighboring region of the targeted voxel as

$$f(\boldsymbol{r}) \simeq c_{ijk}^{000} + c_{ijk}^{100}x + c_{ijk}^{010}y + c_{ijk}^{001}z + c_{ijk}^{110}xy + c_{ijk}^{101}xz + c_{ijk}^{011}yz + c_{ijk}^{200}x^2 + c_{ijk}^{020}y^2 + c_{ijk}^{002}z^2, \quad \boldsymbol{r} \in \Omega_{ijk}, \quad (2.129)$$

Table 2.2: Five brain tissue types and their EPs specified in the simulation.

Tissue	Conductivity (S/m)	Permittivity (ϵ_0)
CSF	2.14	84
WM	0.34	52
GM	0.59	73
Skull	0.12	21
Scalp	0.54	62

Table 2.3: Conductivity and permittivity errors of proposed methods.

Method	Given data	Conductivity error (%)	Permittivity error (%)
$\boldsymbol{H}$-based	(H^+, H^-, H_z)	5.5142	2.9007
$\boldsymbol{H}$-based	$(H^+, 0, 0)$	11.306	4.2008
H^+-based	H^+ only	5.8221	3.3563

where Ω_{ijk} includes the neighboring voxels of $\boldsymbol{r}_{ijk}$. Then, the derivatives are analytically expressed as follows:

$$\begin{aligned}
\partial_x f(\boldsymbol{r}) &= c_{ijk}^{100} + c_{ijk}^{110} y + c_{ijk}^{101} z + 2c_{ijk}^{200} x, & \partial_{xx} f(\boldsymbol{r}) &= 2c_{ijk}^{200}, & \partial_{xy} f(\boldsymbol{r}) &= c_{ijk}^{110}, \\
\partial_y f(\boldsymbol{r}) &= c_{ijk}^{010} + c_{ijk}^{110} x + c_{ijk}^{011} z + 2c_{ijk}^{020} y, & \partial_{yy} f(\boldsymbol{r}) &= 2c_{ijk}^{020}, & \partial_{xz} f(\boldsymbol{r}) &= c_{ijk}^{101}, \\
\partial_z f(\boldsymbol{r}) &= c_{ijk}^{001} + c_{ijk}^{101} x + c_{ijk}^{011} y + 2c_{ijk}^{002} z, & \partial_{zz} f(\boldsymbol{r}) &= 2c_{ijk}^{002}, & \partial_{yz} f(\boldsymbol{r}) &= c_{ijk}^{011}.
\end{aligned}$$

If the number of voxels in Ω_{ijk} is larger than the number of coefficients, i.e., 10, which is always satisfied except for the boundary voxels, the coefficients can be computed by least-squares fitting. At the boundary voxels, minimum norm estimation is applied. We also recalculated H^+ itself using Eq. (2.129) to smooth the data.

2.6.2 Results and Discussion

Figure 2.3 shows the reconstruction results for the sphere model by the conventional methods. As shown in the middle row, the results of the standard method are severely artifactual at the tissue-transition region where EPs vary spatially. This is because the spatial variation of EPs is ignored in the standard method. As shown in the bottom row, the results of the cr method exhibit spurious oscillation. This is due to the unstable nature of the convection-reaction equation with no diffusion. Figure 2.4 shows the reconstruction results when the SNR is 40 dB. As shown in the top row, the results of the standard method are very noisy. This is because the Laplacian of H^+ is used, which amplifies the noise. As shown in the bottom row, the results of the cr method are also very unstable. Therefore, both standard and cr methods are infeasible in practical situations.

Next, we tested our proposed methods. Figure 2.5 shows the reconstruction results of the proposed method based on the full $\boldsymbol{H}$ measurement. When all the components of the magnetic field are given, the proposed method yields very accurate results as shown in the top row. However, when H^- and H_z are neglected, the results are slightly distorted. Figure 2.6 shows the reconstruction results of the proposed method using only H^+. This method yields very similar results to the proposed method using all the components of the magnetic field even though it only uses H^+. From the results using the proposed method, we observe some ghosts: circular regions with higher conductivity and lower permittivity values at the end

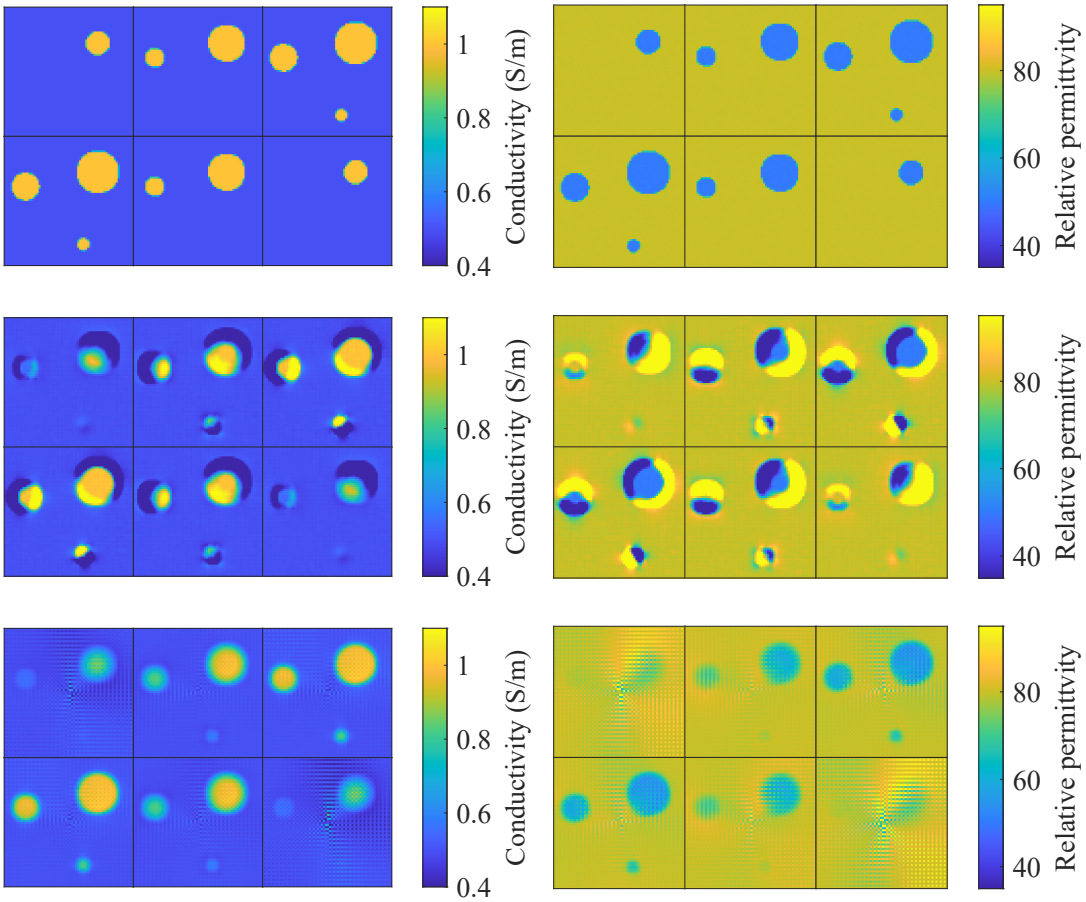

(a) Conductivity (b) Permittivity

Fig. 2.3: Reconstructed (a) conductivity and (b) permittivity maps of the conventional methods for the sphere model without noise. (top) True maps, and results of (middle) standard method and (bottom) cr method.

slices. This is because the derivatives of H^+ are computed with the Savitzky–Golay filter in which the data are smoothed to robustly calculate their derivatives. The voxel size is larger in the through-plane direction than the in-plane direction (5 mm and 1.4 mm, respectively), making the ghost more significant in the through-plane direction.

Table 2.3 shows the relative errors of the proposed methods measured using the relative L2 norm expressed as

$$E[u] = \frac{\|u - u_{\text{true}}\|_2}{\|u_{\text{true}}\|_2} = \sqrt{\frac{\int_\Omega |u(\boldsymbol{r}) - u_{\text{true}}(\boldsymbol{r})|^2 \mathrm{d}V}{\int_\Omega |u_{\text{true}}(\boldsymbol{r})|^2 \mathrm{d}V}}, \tag{2.130}$$

where $u = \sigma, \epsilon$. Although the method using full $\boldsymbol{H}$ components yields the best results when all these components are given, it has larger errors when H^- and H_z are neglected. In the H^+-based method, the error values are very close to those of the $\boldsymbol{H}$-based method using all three components of $\boldsymbol{H}$ even though it only uses H^+. Therefore, the H^+-based method is the most practical choice.

Most of the conventional methods and the proposed methods assume that $H_z = 0$. To test the validity of this assumption, we investigated the distribution of H_z exported from the FEM

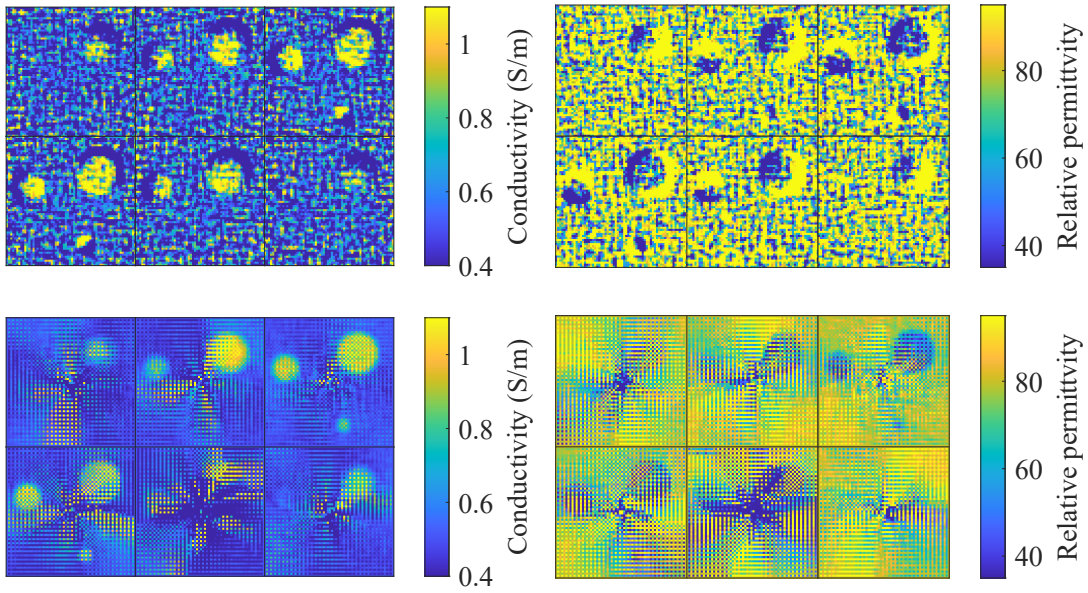

(a) Conductivity (b) Permittivity

Fig. 2.4: Reconstructed (a) conductivity and (b) permittivity maps of conventional methods for sphere model and SNR of 40 dB. Results of (top) standard method and (bottom) cr method.

simulation and compared it with H^+. Figure 2.7 shows the magnitudes of H_z and H^+ as well as their ratio on two slices at the center and the bottom. The magnitude of H_z is very low compared with that of H^+ at the center as shown in the top row. Although the magnitude of H_z is higher on the bottom slice as shown in the bottom row, the value is still lower and less than 15% compared with H^+.

Figure 2.8 shows the reconstruction results of the proposed method when the SNR is 40 dB. Without regularization, the resultant images are noisy especially near the center of the ROI. This is because the electric field vanishes at the center of the body; this is known as the low-electric field artifact of the low-convective field artifact [32]. In this region, both E_z and ∂H^+ reach zero, and thus γ cannot be determined from Ampère's law. This means that the inversion becomes ill-posed and EPs are difficult to determine in this region. To overcome this, the distribution of the electromagnetic fields inside the birdcage coil must be modified to move the zero-point of the electric field by, for example, putting a dielectric pad inside the coil [110]. We also tested the results with Tikhonov and TV regularization with manually chosen regularization parameter λ. As shown in the middle and bottom rows, the results become stable when regularization is applied. The TV regularization is better at preserving the edge of the inclusions while making the background region more homogeneous. Figure 2.9 shows the relative errors of the results of the proposed method with SNR of 30 dB–50 dB. Reconstruction was repeated 10 times for each SNR. By applying either TV or Tikhonov regularization, the stability of the reconstruction results improves. Although the results for both TV and Tikhonov regularization are associated with similar error values, TV regularization yields results that are visually preferable, as shown in Fig. 2.8.

Figure 2.10 shows the reconstruction results of the brain model. The results have an artifact at the center of the ROI, especially in the permittivity map. This is due to the zero-point of the electric field. To improve the reconstruction results, we could utilize the anatomical information available from MRI measurements as proposed in the morphology-enable dipole inversion method in QSM [111]. As anatomical information, we used the simulated

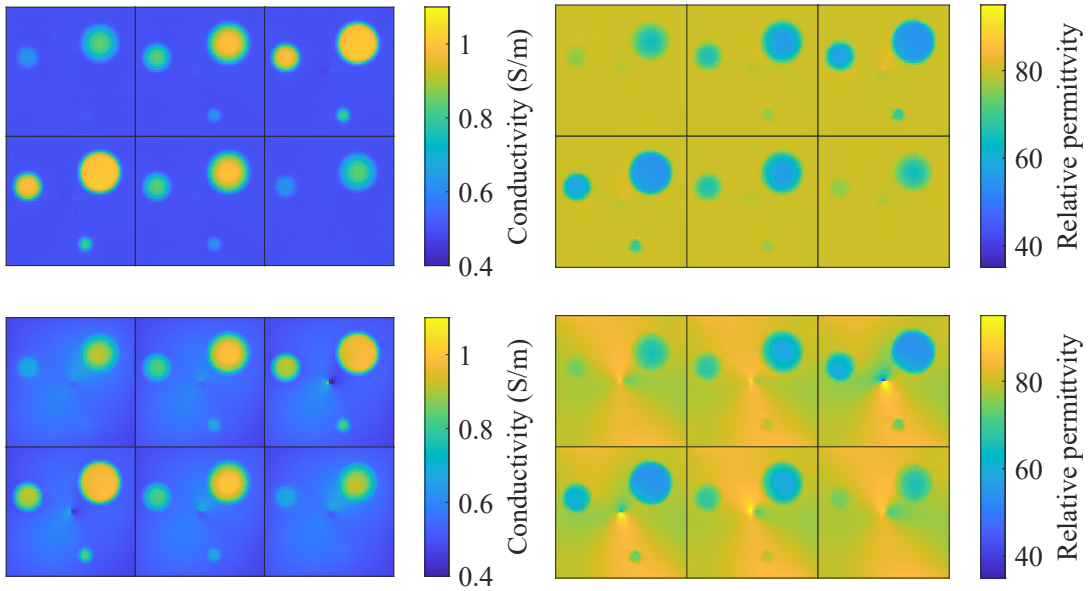

(a) Conductivity (b) Permittivity

Fig. 2.5: Reconstructed (a) conductivity and (b) permittivity maps for sphere model. Results of (top) method based on Eq. (2.95) using all components of $\boldsymbol{H}$, and (bottom) method based on Eq. (2.95) assuming $H^- = H_z = 0$.

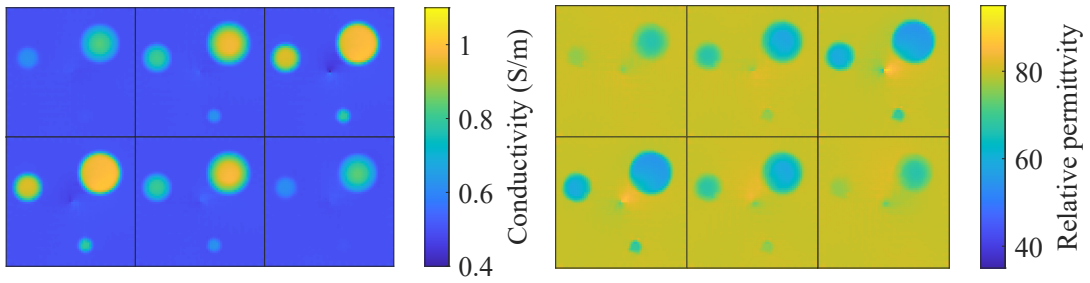

(a) Conductivity (b) Permittivity

Fig. 2.6: Reconstructed (a) conductivity and (b) permittivity maps for sphere model by proposed method using only H^+.

T1-weighted (T1w) image of the brain model provided by the BrainWeb project [106, 107]. Figure 2.11 shows the T1w image and the weighted mask created from the T1w image that excludes the transition region of different tissue types to suppress over-smoothing by regularization. Figure 2.12 shows the reconstruction results with the anatomical information incorporated. Compared to the original results, both conductivity and permittivity maps have sharper edges that coincide with the anatomical structure of the brain.

Figure 2.13 shows the reconstruction results when the SNR is 40 dB. As shown in the middle row, TV regularization makes the resultant maps overly smooth to suppress the noise contained in the image. With the anatomical information, the results became sharper while being more stable.

We also estimated the SAR distribution for the brain model. Figure 2.14 shows the es-

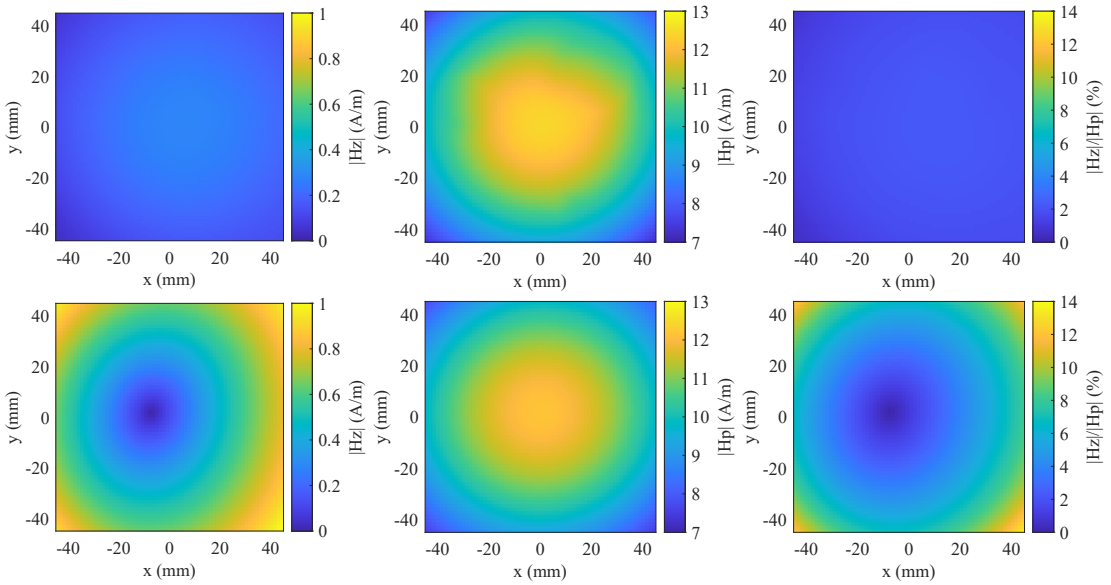

(a) $|H_z|$ (b) $|H^+|$ (c) $|H_z|/|H^+|$

Fig. 2.7: Magnitudes of (a) z- and (b) $(x+\mathrm{i}y)$-components of magnetic field and (c) their ratio for sphere model. Magnitudes at (top) central and (bottom) bottom slices.

timated SAR results by the proposed method using full $\boldsymbol{H}$ and the measured H^+ and their errors for the brain model. In both of the proposed methods, SAR is well estimated except for the boundary regions of different tissue. In practical contexts, it is important to find the local spot where the SAR value is higher than other area, and thus the resolution of the resultant SAR map is of less importance. Therefore, the results of the proposed methods are suitable. In the proposed method using only H^+, the error becomes larger especially in the central region where the conductivity estimation is poor due to the zero-point of the electric field. However, SAR is almost zero in this region because it is determined by the magnitude of the applied electric field. Therefore, this additional error in the central region does not reduce the efficacy of the method.

Figure 2.15 shows the reconstruction results of QCM. Similar to the ordinary EPT, the standard method has severe artifact in the adjacent regions of different tissue types. The cr method also generates a spurious oscillation in the whole region. The proposed method yields good reconstruction results, including the tissue-transition region.

2.7 Phantom Experiments

2.7.1 Setup and Conditions

A phantom composed of two cylindrical regions (inner and outer regions) was created. The conductivity of the phantom was modified by adding NaCl. The permittivity was constant and identical to that of water. Conducting experimental studies with phantoms with varying permittivity [112, 113] will be a focus of our future work in this domain. We added 6 and 2 g/l of NaCl in the inner and outer regions, respectively. The conductivities of the inner and outer regions were 0.94 and 0.43 S/m, as measured using a conductivity meter (Hanna Instruments, HI 8733). We further added $CuSO_4$ (1.5 g/l) to adjust the T_1 value of the phantom.

The magnitude of H^+ can be measured using the B1 mapping technique. We used the double-angle method proposed in [60]. Specifically, $|H^+|$ is calculated from two GRE images

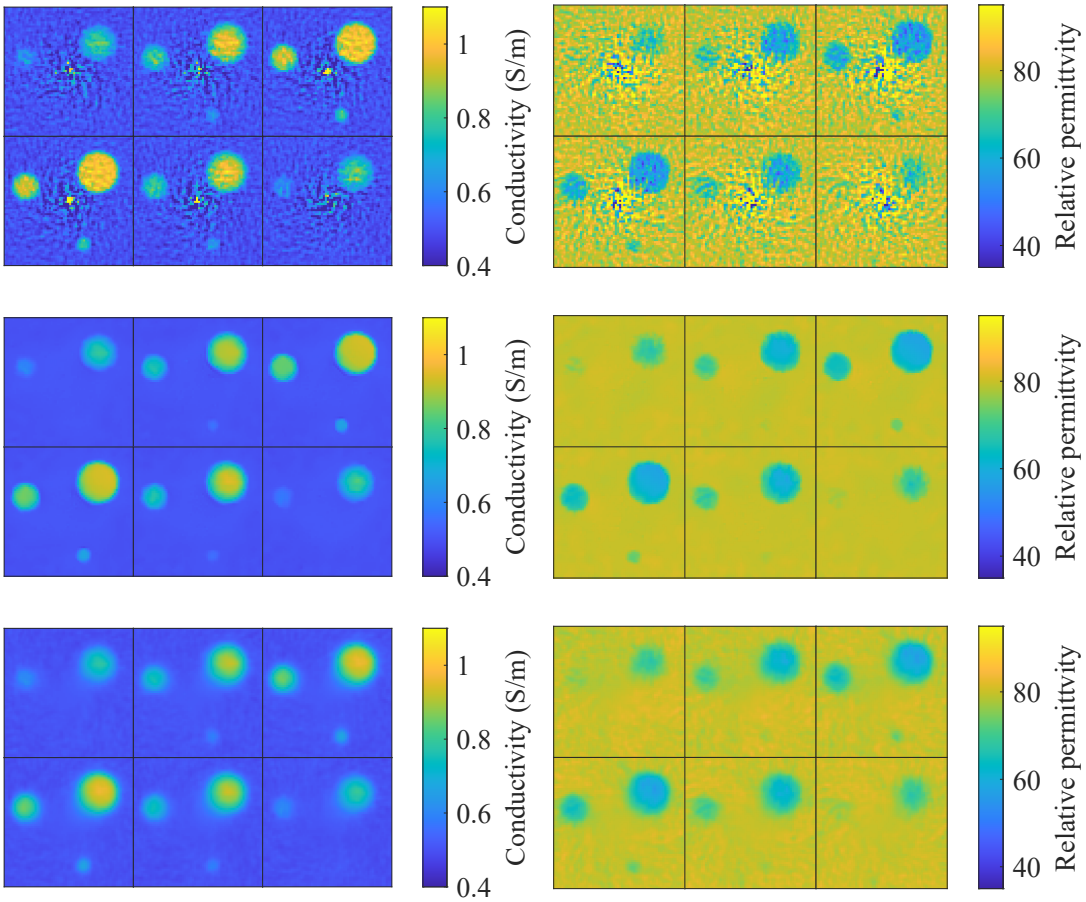

(a) Conductivity (b) Permittivity

Fig. 2.8: Reconstructed (a) conductivity and (b) permittivity maps for sphere model with SNR of 40 dB. Results with (top) no regularization, (middle) TV regularization, and (bottom) Tikhonov regularization.

with 60° and 120° flip angles as follows:

$$|H^+| = \frac{\cos^{-1}\left(|S_{\mathrm{GRE},120}|/2|S_{\mathrm{GRE},60}|\right)}{\mu_0\gamma_0\tau}, \tag{2.131}$$

where γ_0 is the gyromagnetic ratio and τ is the duration time of the RF pulse. The phase of H^+ is calculated from two spin echo images with opposite readout directions as follows:

$$\angle H^+ = \frac{(\angle S_{\mathrm{SE,AP}} + \angle S_{\mathrm{SE,PA}})/2}{2}. \tag{2.132}$$

Note that we used the transceive phase approximation [114] to separate transmit phase $\angle H^+$ from receive phase $\angle H^-$.

The experiment was conducted using a 3 T MR scanner Magnetom Prisma (Siemens) at the University of Tokyo.

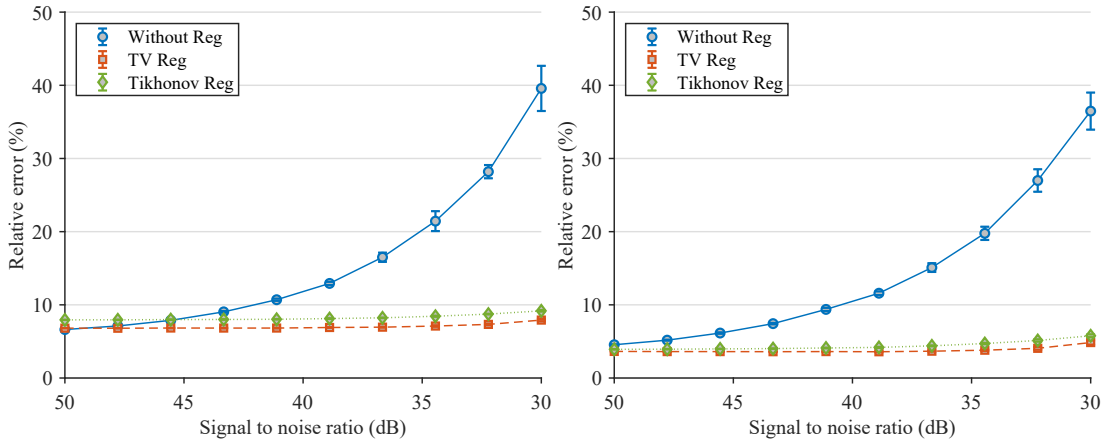

(a) Conductivity (b) Permittivity

Fig. 2.9: Relative errors of (a) conductivity and (b) permittivity maps for sphere model with SNR of 30–50 dB.

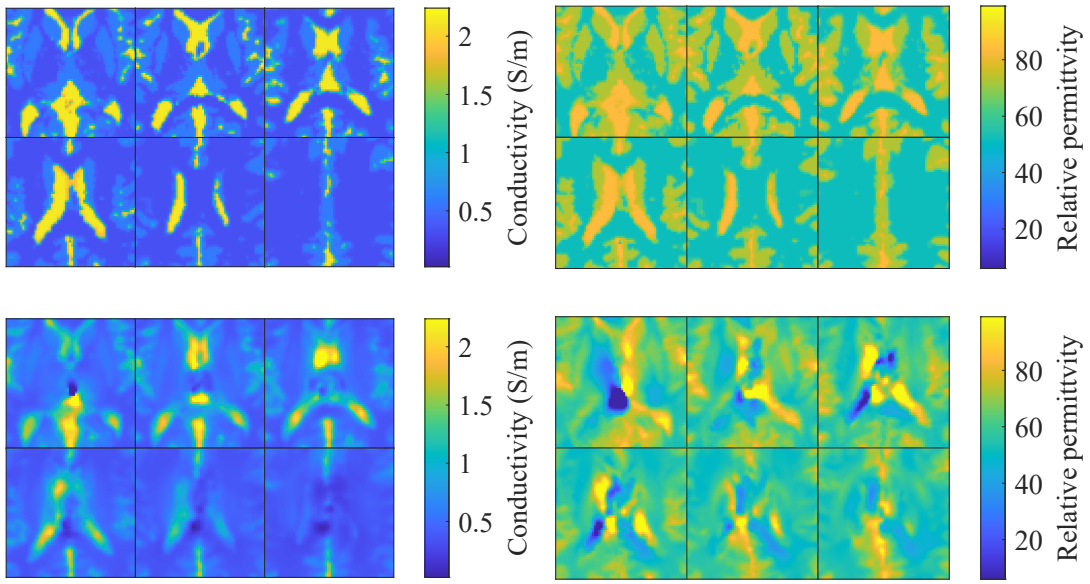

(a) Conductivity (b) Permittivity

Fig. 2.10: Reconstructed (a) conductivity and (b) permittivity maps for brain model. (top) True maps and results of (bottom) proposed method based on Helmholtz's formula.

2.7.2 Results and Discussion

Figure 2.16 shows the reconstructed conductivity of the phantom. The results of the standard method show a severe artifact at the boundary of the inner and outer cylinders, whereas the proposed method yields good results in this region, as shown in Fig. 2.16(b) and (c). In the proposed method, the conductivity maps was reconstructed using TV regularization. In Fig. 2.16(b), TV regularization is applied with no masking, whilst the results of TV regularization with morphology-based masking are shown in Fig. 2.16(c). The edge between the inner

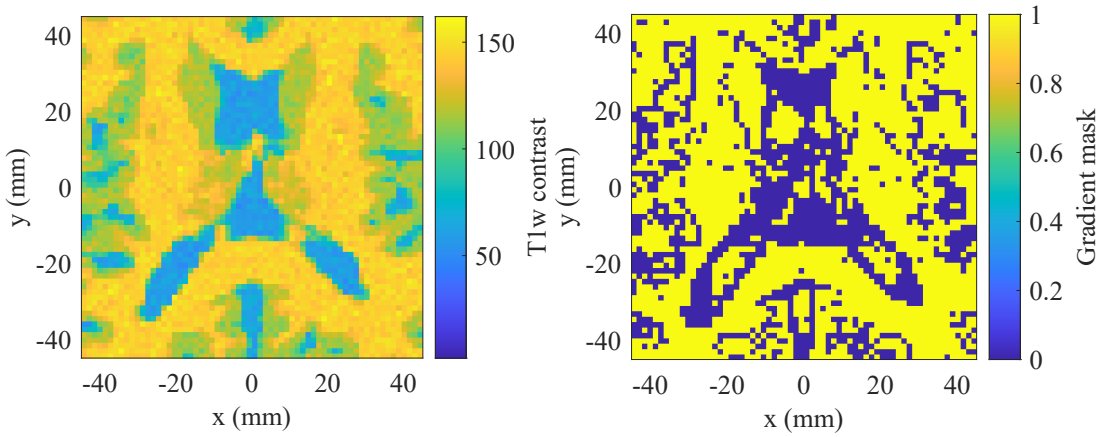

(a) T1-weighted image (b) Gradient weighting

Fig. 2.11: (a) Simulated T1-weighted image and (b) a binary mask created from the T1w image to incorporate anatomical information in regularization.

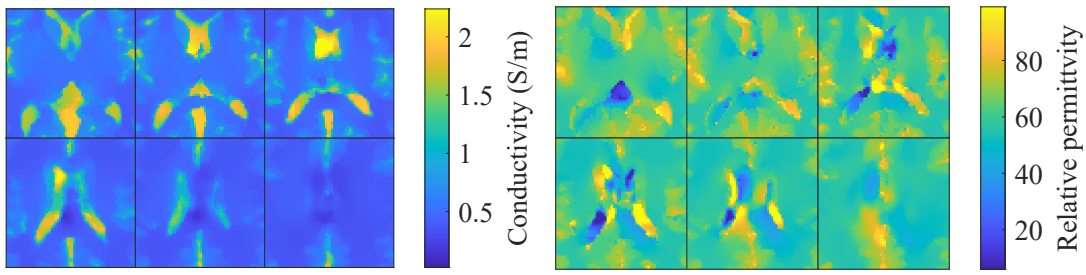

(a) Conductivity (b) Permittivity

Fig. 2.12: Reconstructed (a) conductivity and (b) permittivity maps for brain model by proposed method based on Helmholtz's formula.

and outer regions is better preserved when the regularization is applied with morphology-based masking.

Figure 2.17 shows the reconstructed conductivity of the phantom. Conductivity images are reconstructed using only the phase of H^+ field data. We applied TV regularization to get stable reconstruction results using the proposed method. As shown in Fig. 2.17 the proposed method successfully reconstructs the conductivity map from only the phase of H^+. The edge feature is better preserved when the TV regularization is applied with the morphology-based mask. Although the results deviates slightly from the results of EPT shown in Fig. 2.16 due to the assumption that $\nabla|H^+|$ is negligible, the overall structure and contrast are maintained well. Therefore, QCM is feasible for clinical applications where fast measurement is of great importance.

2.8 Conclusion of This Chapter

In this chapter, we developed novel reconstruction methods for EPT and QCM. First, we introduced the notion of dual fields of the measured fields and formulated the EPT and QCM problems as impedivity inverse problems with either a divergence or curl constraint. Then

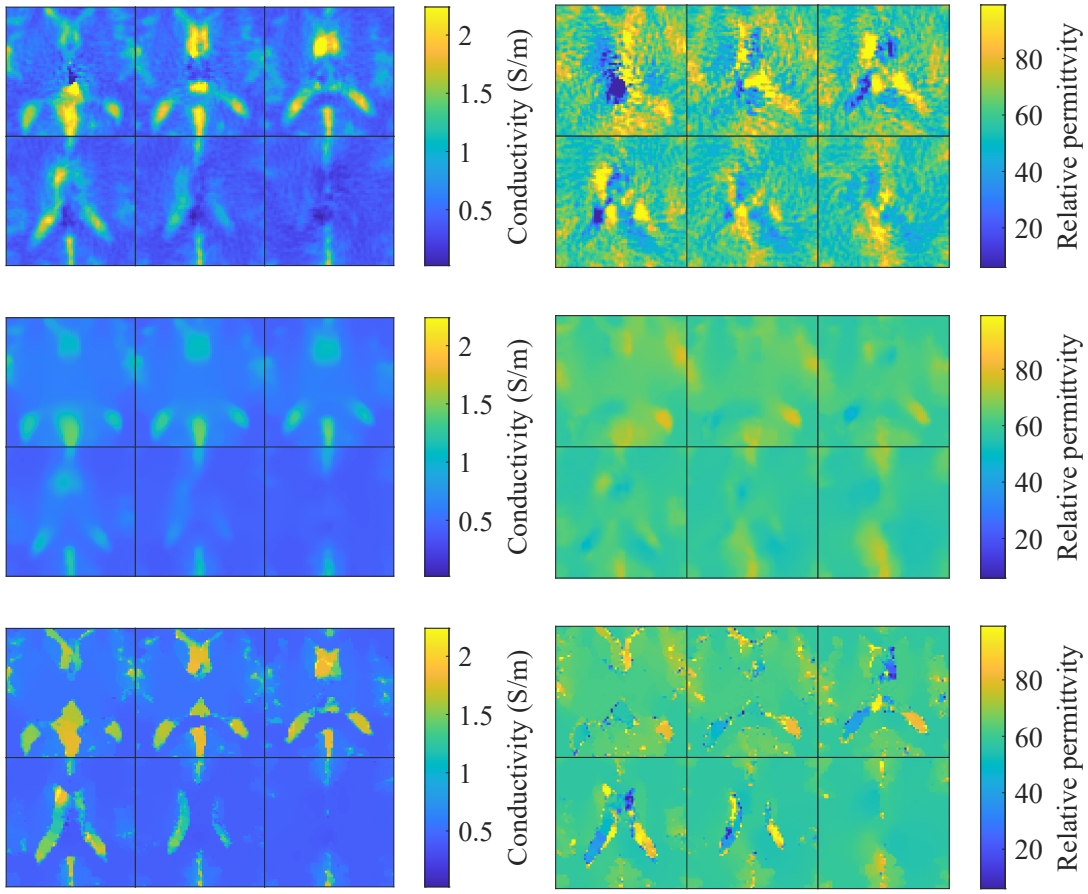

(a) Conductivity (b) Permittivity

Fig. 2.13: Reconstructed (a) conductivity and (b) permittivity maps for brain model with SNR of 40 dB. Results with (top) no regularization, (middle) ordinary TV regularization, and (bottom) morphology-based TV regularization.

representation formulae of vector fields including their divergence and curl as well as themselves were derived and used to construct global and direct EPT and QCM reconstruction methods. The proposed method was validated by numerical simulations and phantom experiments. Our proposed method successfully reconstructed EPs from only measured H^+ data in EPT and the phase of H^+ in QCM and was stable against measurement noise compared with the conventional methods. While the results of EPT, in which both the magnitude and the phase of H^+ are utilized, are slightly better than those of QCM, the latter has advantages in its applicability because it only requires the phase of H^+, which is easily obtained using fast sequences.

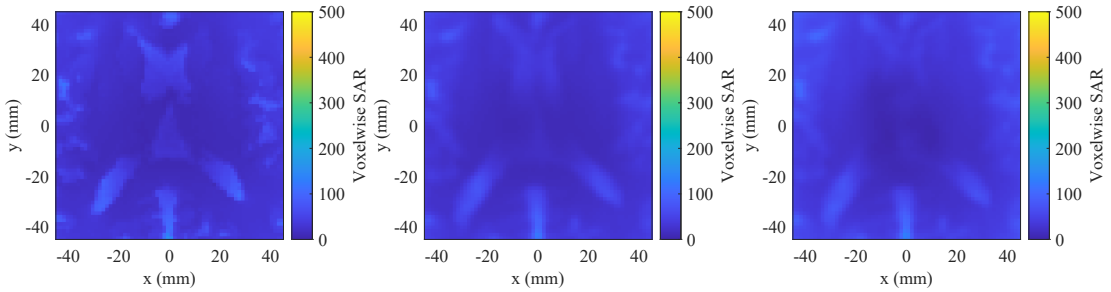

(a) True (b) $\boldsymbol{H}$-based method (c) H^+-based method

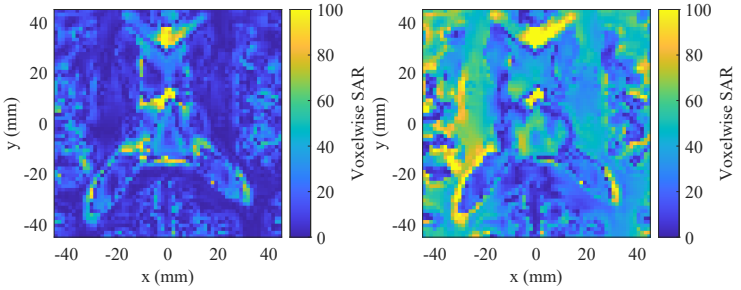

(d) Relative error of $\boldsymbol{H}$-based method (e) Relative error of H^+-based method

Fig. 2.14: Estimated SAR distributions by the proposed methods and their errors for brain model. (a) True, (b) results of $\boldsymbol{H}$-based method, (c) results of H^+-based method, (d) relative error of $\boldsymbol{H}$-based method, and (e) relative error of H^+-based method.

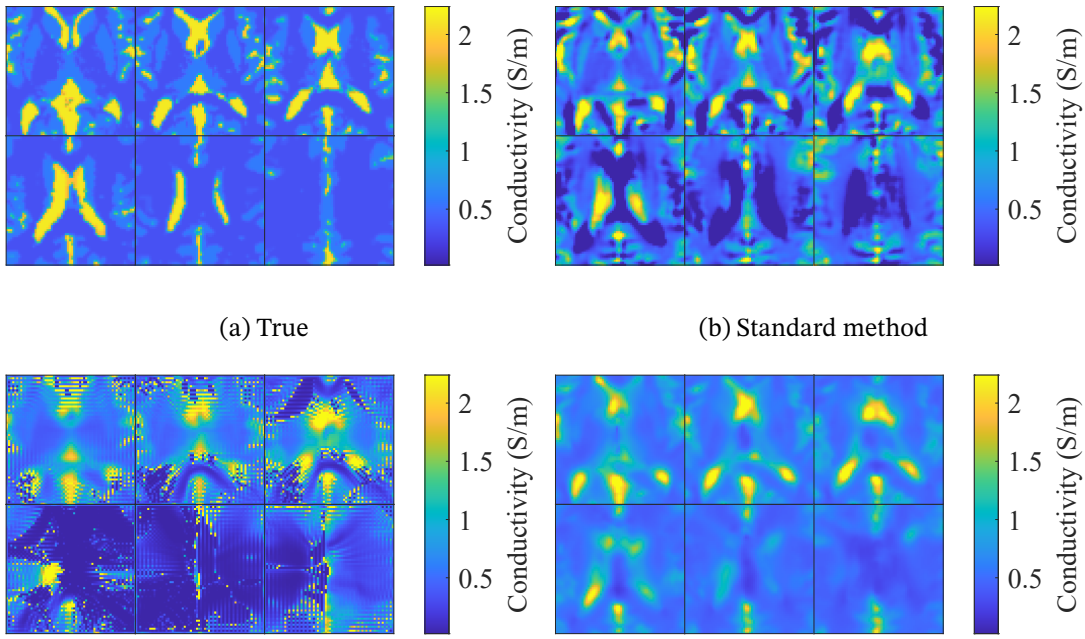

(a) True (b) Standard method

(c) Cr method (d) Proposed method

Fig. 2.15: Reconstructed conductivity maps for brain model. (a) True, (b) standard method, (c) cr method, and (d) proposed method.

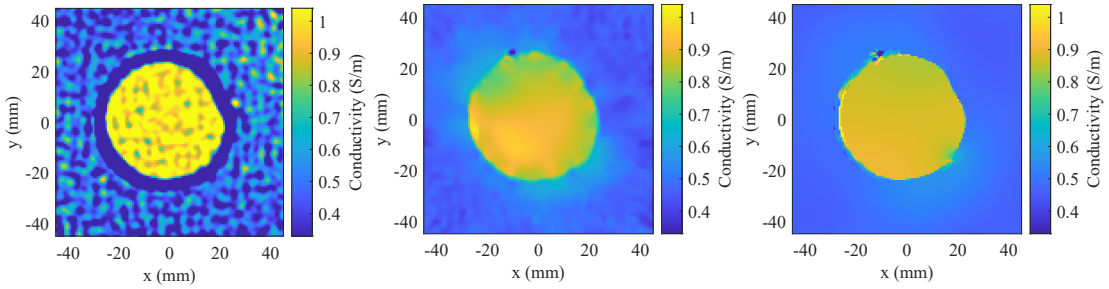

(a) Standard method

(b) Proposed method with ordinary TV reg.

(c) Proposed method with morphology-based TV reg.

Fig. 2.16: Reconstructed conductivity maps at $z = 0$ mm for experimental phantom. (a) Standard method, (b) proposed method with ordinary TV regularization, and (c) proposed method with morphology-based TV regularization.

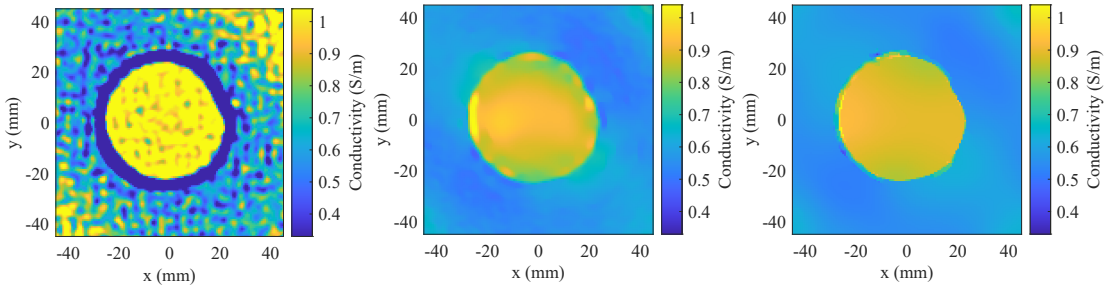

(a) Standard method

(b) Proposed method with ordinary TV reg.

(c) Proposed method with morphology-based TV reg.

Fig. 2.17: Reconstructed conductivity maps at $z = 0$ mm for experimental phantom by QCM methods. (a) Standard method and (b) proposed method with ordinary TV regularization, and (c) proposed method with morphology-based TV regularization.

Chapter 3

Shear Modulus and Viscosity Mapping from Displacement Field Measurement

In this chapter, we develop a global and direct method for MRE that can reconstruct 3D MPs. After describing the backgrounds and the conventional methods in section 3.1, we first formulate MRE as an impedivity inverse problem in section 3.2 as per the previous chapter. Unlike EPT and QCM, the dual field in MRE is a tensor field. Therefore, section 3.3 is devoted to present representation formulae of tensor fields in terms of their divergence and curl as well as themselves; this is accomplished by the same procedure as the case of vector fields. The representation formulae are utilized in section 3.4 to derive an IE for the impedivity and produce our proposed reconstruction formula. In section 3.5, we confirm that the same computational procedure as the proposed EPT and QCM method is applicable for obtaining the numerical solution of the proposed MRE method. The proposed method is validated by numerical simulations in section 3.6. Finally, section 3.7 concludes this chapter.

3.1 Introduction of This Chapter

3.1.1 Mechanical Properties of Biological Tissues

The stiffness of tissues is affected by diseases, both directly and indirectly. As tissues become fibrotic, collagen density increases in the extracellular matrix, affecting macroscopic stiffness [4]. For example, the aortic wall with an aneurysm can be significantly stiffer than the normal aortic wall due to overabundance of collagen and calcification [115–117]. Fibrosis of the liver, which is the preliminary stage of cirrhosis, occurs when cytokines generated by hepatocyte necrosis act on hepatic stellate cells to promote the production of an extracellular matrix consisting of collagen and elastin that determine the elasticity of the tissues and inhibit their degradation, leading to an abnormal increase in the extracellular matrix [118]. Therefore, in liver cirrhosis, the diseased liver becomes fibrotic and less compliant when compared with a healthy liver. In other words, the liver becomes very hard and nodular [119].

Many breast cancers are also significantly stiffer than benign tumors or normal surrounding fibroglandular tissues [120]. During tumor growth, increased cellular stiffness and compaction of surrounding tissue can combine to alter MPs of the tissues [3].

3.1.2 Conventional Reconstruction Methods

As explained in Chapter 1, the dual field $\boldsymbol{\sigma}$ is eliminated and the measured field and the impedivity are directly related in most of the conventional methods. Taking the divergence of Eq. (1.4) and substituting it into Eq. (1.3) gives Navier's equation

$$\omega_1^2 \rho_0 \boldsymbol{u} + \nabla \cdot (\mu \check{\nabla} \boldsymbol{u}) + \nabla(\lambda \nabla \cdot \boldsymbol{u}) = \boldsymbol{0}. \tag{3.1}$$

Equation (3.1) directly relates Lame's parameters and the measured displacement field.

A typical approach for the MRE inverse problem neglects the spatial variation of the MPs to derive the following algebraic equation [121]:

$$\check{\Delta} \boldsymbol{u} \mu + \nabla \nabla \cdot \boldsymbol{u} \lambda = -\omega_1^2 \rho_0 \boldsymbol{u}, \tag{3.2}$$

where $\check{\Delta} \boldsymbol{u} \coloneqq \nabla \cdot \check{\nabla} \boldsymbol{u} = \Delta \boldsymbol{u} + \nabla \nabla \cdot \boldsymbol{u}$. The pointwise least-squares solution can be directly calculated, leading to the following full-AIDE reconstruction formula:

$$\mu = -\omega_1^2 \rho_0 \frac{|\nabla \nabla \cdot \boldsymbol{u}|^2 \langle \check{\Delta} \boldsymbol{u}, \boldsymbol{u} \rangle - \langle \check{\Delta} \boldsymbol{u}, \nabla \nabla \cdot \boldsymbol{u} \rangle \langle \nabla \nabla \cdot \boldsymbol{u}, \boldsymbol{u} \rangle}{|\check{\Delta} \boldsymbol{u}|^2 |\nabla \nabla \cdot \boldsymbol{u}|^2 - |\langle \nabla \nabla \cdot \boldsymbol{u}, \check{\Delta} \boldsymbol{u} \rangle|^2}. \tag{3.3}$$

If we further assume that the media is incompressible, i.e., $\nabla \cdot \boldsymbol{u} = 0$, the following algebraic equation for μ holds:

$$\Delta \boldsymbol{u} \mu = -\omega_1^2 \rho_0 \boldsymbol{u} \tag{3.4}$$

the pointwise least-squares solution of which yields the incompressible-AIDE reconstruction formula

$$\mu = -\omega_1^2 \rho_0 \frac{\langle \Delta \boldsymbol{u}, \boldsymbol{u} \rangle}{|\Delta \boldsymbol{u}|^2}. \tag{3.5}$$

Although tissues are nearly incompressible, λ is very large and thus $p \coloneqq \lambda \nabla \cdot \boldsymbol{u}$ is not negligible. For the methods based on the incompressible assumption, it is essential to remove the contribution of the compressible wave from the measured data using a high-pass filter [122]. The compressible wave can also be removed by taking the curl of Eq. (3.1) as proposed in [123]:

$$\omega_1^2 \rho_0 \nabla \times \boldsymbol{u} + \mu \nabla \times \nabla \cdot \check{\nabla} \boldsymbol{u} = \boldsymbol{0}. \tag{3.6}$$

However, this increases the order of derivatives of the measured displacement data, making the method very sensitive to noise.

Several methods beyond LHA and the incompressibility assumption have been proposed and can be divided into iterative methods and direct methods.

Iterative methods optimize MPs so that the discrepancy between the displacement field calculated according to the forward equation and the measured data is minimized. Given the temporal estimate of MPs, the forward solution is found by solving Eq. (3.1) by FEM. Doyley *et al.* [124] and Miga *et al.* [125] solved the optimization problem by Gauss–Newton and Levenberg–Marquardt methods by assuming a nearly incompressible value of λ. Oberai *et al.* [126, 127] used the Gradient descent. They solved for both μ and p to avoid the incompressibility assumption. Van Houten *et al.* [128, 129] proposed the subzone-based method to increase the computational efficiency.

Direct methods solve Eq. (3.1) directly for μ (and p) [130, 131]. Honarvar *et al.* [132] proposed the curl-based FEM method in which the compressible term is eliminated by taking the curl of Eq. (3.1) and then the PDE is directly solved for μ. Although direct methods are usually much less computationally expensive, the main disadvantage is that second-order derivatives

must be calculated, which amplifies the noise. Sparsity-based regularization has been adopted to stabilize the estimate [133, 134].

Kojima *et al.* [135] proposed a novel MRE method based on the complex form of the equation of motion. In this method, the following quantities were introduced first:

$$\epsilon_{\mathrm{s}}^{\pm} \coloneqq \epsilon_{xz} \pm \mathrm{i}\epsilon_{yz}, \qquad \sigma_{\mathrm{s}}^{\pm} \coloneqq \sigma_{xz} \pm \mathrm{i}\sigma_{yz},$$
$$\epsilon_{\mathrm{p}}^{\pm} \coloneqq \frac{\epsilon_{xx} - \epsilon_{yy}}{2} \pm \mathrm{i}\epsilon_{xy}, \qquad \sigma_{\mathrm{p}}^{\pm} \coloneqq \frac{\sigma_{xx} - \sigma_{yy}}{2} \pm \mathrm{i}\sigma_{xy}.$$

We call $\epsilon_{\mathrm{s}}^{\pm}$ and $\sigma_{\mathrm{s}}^{\pm}$ the complex shear-strain and stress and $\epsilon_{\mathrm{p}}^{\pm}$ and $\sigma_{\mathrm{p}}^{\pm}$ the complex plane-strain and stress hereafter. Then, the following relations hold:

$$\sigma_{\mathrm{s}}^{+} = 2\mu\epsilon_{\mathrm{s}}^{+} = 2\mu(\bar{\partial}u_z + \partial_z u^{+}), \tag{3.7}$$
$$\sigma_{\mathrm{s}}^{-} = 2\mu\epsilon_{\mathrm{s}}^{-} = 2\mu(\partial u_z + \partial_z u^{-}), \tag{3.8}$$
$$\sigma_{\mathrm{p}}^{+} = 2\mu\epsilon_{\mathrm{p}}^{+} = 4\mu\bar{\partial}u^{+}, \tag{3.9}$$
$$\sigma_{\mathrm{p}}^{-} = 2\mu\epsilon_{\mathrm{p}}^{-} = 4\mu\partial u^{-}. \tag{3.10}$$

In addition, the in-plane and through-plane components of the normal strain and stress were defined as follows:

$$\epsilon_{\mathrm{n}}^{\perp} \coloneqq \epsilon_{xx} + \epsilon_{yy}, \qquad \sigma_{\mathrm{n}}^{\perp} \coloneqq \sigma_{xx} + \sigma_{yy},$$
$$\epsilon_{\mathrm{n}}^{\parallel} \coloneqq \epsilon_{zz}, \qquad \sigma_{\mathrm{n}}^{\parallel} \coloneqq \sigma_{zz}.$$

Then, the following relations hold:

$$\sigma_{\mathrm{n}}^{\perp} = 2\lambda\nabla\cdot\boldsymbol{u} + 2\mu\epsilon_{\mathrm{n}}^{\perp} = 2\lambda\nabla\cdot\boldsymbol{u} + 4\mu(\partial u^{+} + \bar{\partial}u^{-}), \tag{3.11}$$
$$\sigma_{\mathrm{n}}^{\parallel} = \lambda\nabla\cdot\boldsymbol{u} + 2\mu\epsilon_{\mathrm{n}}^{\parallel} = \lambda\nabla\cdot\boldsymbol{u} + 2\mu\partial_z u_z. \tag{3.12}$$

Using Eqs. (3.7)–(3.10) and Eqs. (3.11)–(3.12), the equation of motion can be rewritten as follows:

$$\partial\sigma_{\mathrm{p}}^{+} + \frac{1}{2}\bar{\partial}\sigma_{\mathrm{n}}^{\perp} + \frac{1}{2}\partial_z\sigma_{\mathrm{s}}^{+} = -\omega_1^2\rho_0 u^{+}, \tag{3.13}$$
$$\bar{\partial}\sigma_{\mathrm{p}}^{-} + \frac{1}{2}\partial\sigma_{\mathrm{n}}^{\perp} + \frac{1}{2}\partial_z\sigma_{\mathrm{s}}^{-} = -\omega_1^2\rho_0 u^{-}, \tag{3.14}$$
$$\partial\sigma_{\mathrm{s}}^{+} + \bar{\partial}\sigma_{\mathrm{s}}^{-} + \partial_z\sigma_{\mathrm{n}}^{\parallel} = -\omega_1^2\rho_0 u_z. \tag{3.15}$$

Eqs. (3.13) and (3.14) can be seen as the so-called Dbar equation for σ_{p}^{+} and σ_{p}^{-} if $\sigma_{\mathrm{s}}^{\pm}$ and $\sigma_{\mathrm{n}}^{\perp}$ are known and its solution can be explicitly given by the Cauchy–Pompeiu formula [86] as follows:

$$\begin{aligned}
\sigma_{\mathrm{p}}^{+}(\zeta) &= -\frac{1}{2\pi\mathrm{i}}\oint_{\partial D}\frac{\sigma_{\mathrm{p}}^{+}(\zeta')}{\bar{\zeta}' - \bar{\zeta}}\mathrm{d}\bar{\zeta}' + \bar{T}\left[-\omega_1^2\rho_0 u^{+} - \frac{1}{2}\bar{\partial}\sigma_{\mathrm{n}}^{\perp} - \frac{1}{2}\partial_z\sigma_{\mathrm{s}}^{+}\right], \\
\sigma_{\mathrm{p}}^{-}(\zeta) &= \frac{1}{2\pi\mathrm{i}}\oint_{\partial D}\frac{\sigma_{\mathrm{p}}^{-}(\zeta')}{\zeta' - \zeta}\mathrm{d}\zeta' + T\left[-\omega_1^2\rho_0 u^{-} - \frac{1}{2}\partial\sigma_{\mathrm{n}}^{\perp} - \frac{1}{2}\partial_z\sigma_{\mathrm{s}}^{-}\right].
\end{aligned} \tag{3.16}$$

If we assume $\partial_z\boldsymbol{u} \simeq \boldsymbol{0}$, which holds well when the loading object has homogeneous EPs along the z-axis, and $\nabla\cdot\boldsymbol{u} = 0$, which means that the object is incompressible, it holds that $\sigma_{\mathrm{s}}^{\pm} = \sigma_{\mathrm{n}}^{\perp} = 0$ by Eqs. (3.7)–(3.8) and (3.11), and thus Eq. (3.16) gives an explicit reconstruction

formula for $\sigma_{\mathrm{p}}^{\pm}$. Once $\sigma_{\mathrm{p}}^{\pm}$ is reconstructed inside the ROI, it is straightforward to calculate μ according to Eqs. (3.9) and (3.10) as follows:

$$\begin{aligned} \mu &= \frac{\sigma_{\mathrm{p}}^{+}}{4\bar{\partial}u^{+}}, \\ \mu &= \frac{\sigma_{\mathrm{p}}^{-}}{4\partial u^{-}}. \end{aligned} \tag{3.17}$$

Since this method can avoid using the Laplacian of the measured $u^{\pm}$, it is robust against measurement noise. If the loading object is also inhomogeneous along the z-axis, the following iterative correction method can be constructed:

$$\sigma_{\mathrm{p}}^{+,(n)} = -\frac{1}{2\pi \mathrm{i}} \oint_{\partial D} \frac{\sigma_{\mathrm{p}}^{+}}{\bar{\zeta}' - \bar{\zeta}} \mathrm{d}\bar{\zeta}' + \bar{T}\left[-\omega_1^2 \rho_0 u^{+} - \frac{1}{2}\bar{\partial}\sigma_{\mathrm{n}}^{\perp,(n)} - \frac{1}{2}\partial_z \sigma_{\mathrm{s}}^{+,(n)} \right], \tag{3.18}$$

$$\sigma_{\mathrm{s}}^{+,(n+1)} = 2\mu^{(n)}(\bar{\partial}u_z + \partial_z u^{+}) = \frac{\bar{\partial}u_z + \partial_z u^{+}}{2\bar{\partial}u^{+}} \sigma_{\mathrm{p}}^{+,(n)}, \tag{3.19}$$

$$\sigma_{\mathrm{n}}^{\perp,(n+1)} = 4\mu^{(n)}(\partial u^{+} + \bar{\partial}u^{-}) = \frac{\partial u^{+} + \bar{\partial}u^{-}}{\bar{\partial}u^{+}} \sigma_{\mathrm{p}}^{+,(n)}. \tag{3.20}$$

Although this procedure can successfully correct the estimate of MPs in a numerical simulation, the error does not decrease monotonically and convergence is not guaranteed.

3.2 MRE as an Impedivity Inverse Problem

Similar to the EPT problem in Chapter 2, the MRE problem can be formulated as the following impedivity inverse problem:

Given the measured data of $\boldsymbol{u}$ inside a ROI, reconstruct λ, μ according to the following equations:

$$\boldsymbol{\sigma} = \lambda \nabla \cdot \boldsymbol{u}\boldsymbol{I} + \mu \check{\nabla} \boldsymbol{u}, \tag{3.21}$$

$$\nabla \cdot \boldsymbol{\sigma} = -\omega_1^2 \rho_0 \boldsymbol{u}. \tag{3.22}$$

This inverse problem is to reconstruct the impedivity defined as the ratio of the derivative of the measured field to the dual field. Unlike EPT, the dual field $\boldsymbol{\sigma}$ is a tensor field, and thus the representation formulae derived in the previous chapter are extended to tensor fields in the next section based on Helmholtz's decomposition for tensor fields explained in Appendix A.

3.3 Representation Formulae of Tensor Fields Based on Helmholtz's Decomposition

Equation (A.55) is a representation formula of tensor fields by both its divergence and curl. In other words, the operators $\boldsymbol{P}_{\mathrm{L}}$ and $\boldsymbol{P}_{\mathrm{T}}$ project a tensor field onto the irrotational and solenoidal fields via its divergence or curl. Here, we modify these operators to obtain alternatives that directly project the field without computing its divergence or curl. The procedure presented in this section is analogous to the case of vector fields described in Chapter 2.

By the product rule of tensor differentiation

$$(\nabla \cdot (\boldsymbol{f} \nabla w))^{\mathsf{T}} = \nabla w (\nabla \cdot \boldsymbol{f}) + (\boldsymbol{f}^{\mathsf{T}} \cdot \nabla \nabla w)^{\mathsf{T}}, \tag{3.23}$$

the following integration by parts holds:

$$\int_\Omega \nabla w(\nabla \cdot \boldsymbol{f})\mathrm{d}V = \oint_{\partial\Omega} \nabla w(\boldsymbol{n} \cdot \boldsymbol{f})\mathrm{d}S - \int_\Omega (\boldsymbol{f}^\mathsf{T} \cdot \nabla\nabla w)^\mathsf{T}\mathrm{d}V. \tag{3.24}$$

Using the above relation, $\boldsymbol{P}_\mathrm{L}$ defined in Eq. (A.60) can be rewritten as follows:

$$\boldsymbol{P}_\mathrm{L}[\boldsymbol{f}](\boldsymbol{r}) = -\int_\Omega (\boldsymbol{f}^\mathsf{T}(\boldsymbol{r}') \cdot \nabla\nabla G(\boldsymbol{r}';\boldsymbol{r}))^\mathsf{T}\mathrm{d}V'. \tag{3.25}$$

We note that the transpose operator is required to give the proper result. This can be rewritten without the transpose symbol as

$$\boldsymbol{P}_\mathrm{L}[\boldsymbol{f}](\boldsymbol{r}) = -\int_\Omega \nabla G(\boldsymbol{r}';\boldsymbol{r})(\overleftarrow{\nabla} \cdot \boldsymbol{f}(\boldsymbol{r}'))\mathrm{d}V', \tag{3.26}$$

where the left arrow over the nabla symbol means that the differentiation applies to ∇G (and ∇G only). The representation of $\boldsymbol{P}_\mathrm{L}$ given by Eq. (3.26) allows projection of a tensor field onto its longitudinal component without giving or calculating its divergence. Using Eq. (2.82), Eq. (A.55) is modified as

$$\begin{aligned}\boldsymbol{f}(\boldsymbol{r}) = \oint_{\partial\Omega} \nabla G(\boldsymbol{r}';\boldsymbol{r}) \times (\boldsymbol{n}(\boldsymbol{r}') \times \boldsymbol{f}(\boldsymbol{r}'))\mathrm{d}S' - \int_\Omega \nabla G(\boldsymbol{r}';\boldsymbol{r}) \times (\nabla \times \boldsymbol{f}(\boldsymbol{r}'))\mathrm{d}V' \\ - \int_\Omega \nabla G(\boldsymbol{r}';\boldsymbol{r})(\overleftarrow{\nabla} \cdot \boldsymbol{f}(\boldsymbol{r}'))\mathrm{d}V'.\end{aligned} \tag{3.27}$$

This is a representation formula of a tensor fields by the field itself and its curl.

Similarly, by the tensor field identity

$$\nabla w \times (\nabla \times \boldsymbol{f}) + ((\boldsymbol{f}^\mathsf{T} \times \nabla) \times \nabla w)^\mathsf{T} = \nabla(\nabla w \cdot \boldsymbol{f}) - \nabla \cdot (\nabla w \boldsymbol{f}), \tag{3.28}$$

the following integration by parts holds:

$$\int_\Omega \nabla w \times (\nabla \times \boldsymbol{f})\mathrm{d}V + \int_\Omega ((\boldsymbol{f}^\mathsf{T} \times \nabla) \times \nabla w)^\mathsf{T}\mathrm{d}V = \oint_{\partial\Omega} \boldsymbol{n}\nabla w \cdot \boldsymbol{f} - \boldsymbol{n} \cdot \nabla w \boldsymbol{f}\mathrm{d}S. \tag{3.29}$$

Using the triplet identity

$$\boldsymbol{n}\nabla w \cdot \boldsymbol{f} - \boldsymbol{n} \cdot \nabla w \boldsymbol{f} = \nabla w \times (\boldsymbol{n} \times \boldsymbol{f}), \tag{3.30}$$

it holds that

$$\int_\Omega \nabla w \times (\nabla \times \boldsymbol{f})\mathrm{d}V + \int_\Omega ((\boldsymbol{f}^\mathsf{T} \times \nabla) \times \nabla w)^\mathsf{T}\mathrm{d}V = \oint_{\partial\Omega} \nabla w \times (\boldsymbol{n} \times \boldsymbol{f})\mathrm{d}S. \tag{3.31}$$

Using the above relation, $\boldsymbol{P}_\mathrm{T}$ can be rewritten as follows:

$$\boldsymbol{P}_\mathrm{T}[\boldsymbol{f}](\boldsymbol{r}) = \int_\Omega ((\boldsymbol{f}^\mathsf{T}(\boldsymbol{r}') \times \nabla) \times \nabla G(\boldsymbol{r}';\boldsymbol{r}))^\mathsf{T}\mathrm{d}V', \tag{3.32}$$

which can also be rewritten using the operator $\overleftarrow{\nabla}$ as

$$\boldsymbol{P}_\mathrm{T}[\boldsymbol{f}](\boldsymbol{r}) = \int_\Omega \nabla G(\boldsymbol{r}';\boldsymbol{r}) \times (\overleftarrow{\nabla} \times \boldsymbol{f}(\boldsymbol{r}'))\mathrm{d}V'. \tag{3.33}$$

The representation of $\boldsymbol{P}_{\mathrm{T}}$ given by Eq. (3.33) allows projection of a tensor field onto its transverse component without giving or calculating its curl. Using Eq. (3.33), Eq. (A.55) is modified as

$$\boldsymbol{f}(\boldsymbol{r}) = -\oint_{\partial\Omega} \nabla G(\boldsymbol{r}';\boldsymbol{r})(\boldsymbol{n}(\boldsymbol{r}')\cdot\boldsymbol{f}(\boldsymbol{r}'))\mathrm{d}S' + \int_{\Omega} \nabla G(\boldsymbol{r}';\boldsymbol{r})(\nabla\cdot\boldsymbol{f}(\boldsymbol{r}'))\mathrm{d}V' + \int_{\Omega} \nabla G(\boldsymbol{r}';\boldsymbol{r})\times(\overleftarrow{\nabla}\times\boldsymbol{f}(\boldsymbol{r}'))\mathrm{d}V'. \tag{3.34}$$

This is a representation formula of a tensor field by the field itself and its divergence.

Using both Eqs. (3.26) and (3.33), we can represent a tensor field by itself as

$$\boldsymbol{f}(\boldsymbol{r}) = -\int_{\Omega} \nabla G(\boldsymbol{r}';\boldsymbol{r})(\overleftarrow{\nabla}\cdot\boldsymbol{f}(\boldsymbol{r}'))\mathrm{d}V' + \int_{\Omega} \nabla G(\boldsymbol{r}';\boldsymbol{r})\times(\overleftarrow{\nabla}\times\boldsymbol{f}(\boldsymbol{r}'))\mathrm{d}V'. \tag{3.35}$$

This relation can be seen as Helmholtz's decomposition of a tensor field. In fact, the first term is the longitudinal component, and the second term is the transverse component of the field. This decomposition formula can be derived directly from the identity

$$\Delta w\boldsymbol{f} = \nabla w(\overleftarrow{\nabla}\cdot\boldsymbol{f}) - \nabla w\times(\overleftarrow{\nabla}\times\boldsymbol{f}). \tag{3.36}$$

Taking w as G and integrating both sides over Ω yields Eq. (3.35). From Eq. (3.36), it is obvious that Eq. (3.35) gives a decomposition of a tensor field.

3.4 MRE Reconstruction Based on Helmholtz's Representation Formula

In this section, we derive an IE for the impedivity using the representation formula derived in the previous section. By applying the representation formula of a tensor field in terms of its divergence and itself to $\boldsymbol{\sigma}$, we have

$$\boldsymbol{\sigma}(\boldsymbol{r}) = -\oint_{\partial\Omega} \nabla G(\boldsymbol{r}';\boldsymbol{r})(\boldsymbol{n}\cdot\boldsymbol{\sigma})\mathrm{d}S' + \int_{\Omega} \nabla G(\boldsymbol{r}';\boldsymbol{r})(\nabla\cdot\boldsymbol{\sigma})\mathrm{d}V' + \int_{\Omega} \nabla G(\boldsymbol{r}';\boldsymbol{r})\times(\overleftarrow{\nabla}\times\boldsymbol{\sigma})\mathrm{d}V'. \tag{3.37}$$

The longitudinal component of the stress field can be calculated as follows:

$$\boldsymbol{\sigma}_{\mathrm{L}} = -\oint_{\partial\Omega} \nabla G(\boldsymbol{r}';\boldsymbol{r})(\boldsymbol{n}\cdot\boldsymbol{\sigma})\mathrm{d}S' + \int_{\Omega} \nabla G(\boldsymbol{r}';\boldsymbol{r})(-\omega_1^2\rho_0\boldsymbol{u})\mathrm{d}V'. \tag{3.38}$$

Substituting Eq. (3.21) into the above equation yields

$$\boldsymbol{\sigma}(\boldsymbol{r}) = \boldsymbol{\sigma}_{\mathrm{L}}(\boldsymbol{r}) + \int_{\Omega} \nabla G(\boldsymbol{r}';\boldsymbol{r})\times(\overleftarrow{\nabla}\times\boldsymbol{\sigma})\mathrm{d}V'. \tag{3.39}$$

This is an IE for the tensor field $\boldsymbol{\sigma}$. However, this system cannot generally be solved because of the orthogonality of Helmholtz's decomposition, that is, because the longitudinal and transverse components of a tensor field are completely independent. To make the system solvable, we utilize Hooke's law, which relates the measured field $\boldsymbol{u}$ and the dual field $\boldsymbol{\sigma}$ via impedivity λ and μ.

$$\lambda\nabla\cdot\boldsymbol{u}\boldsymbol{I} + \mu\check{\nabla}\boldsymbol{u} = \boldsymbol{\sigma}_{\mathrm{L}} + \int_{\Omega} \nabla G(\boldsymbol{r}';\boldsymbol{r})\times(\overleftarrow{\nabla}\times(\lambda\nabla\cdot\boldsymbol{u}\boldsymbol{I} + \mu\check{\nabla}\boldsymbol{u}))\mathrm{d}V' \tag{3.40}$$

This equation can be seen as an IE for the scalar quantities λ and μ and is solvable, as will be revealed in the numerical simulations. Equation (3.40) is an IE that relates λ and μ with $\boldsymbol{u}$ globally and does not contain the Laplacian of the measured displacement field. Furthermore, Eq. (3.40) is linear for both λ and μ, making the method free from local minima. Therefore, the proposed method is global, direct, and valid for 3D mapping.

3.5 Regularized Solution of Field-to-Impedance Inversion

Similar to EPT, we apply regularization in our proposed method using the following approach. First, we get the temporal estimate of the impedivity by solving the IE without regularization. Then, by the estimated impedivity λ^*, μ^*, we calculate the temporal estimate of the stress fields as follows:

$$\boldsymbol{\sigma}^* = \lambda^* \nabla \cdot \boldsymbol{u}\boldsymbol{I} + \mu^* \check{\nabla} \boldsymbol{u}. \tag{3.41}$$

Then, the following equations hold:

$$\begin{pmatrix} |\nabla \cdot \boldsymbol{u}\boldsymbol{I}| & \frac{\langle \nabla \cdot \boldsymbol{u}\boldsymbol{I}, \check{\nabla} \boldsymbol{u} \rangle}{|\nabla \cdot \boldsymbol{u}\boldsymbol{I}|} \\ \frac{\langle \check{\nabla} \boldsymbol{u}, \nabla \cdot \boldsymbol{u}\boldsymbol{I} \rangle}{|\check{\nabla} \boldsymbol{u}|} & |\check{\nabla} \boldsymbol{u}| \end{pmatrix} \begin{pmatrix} \lambda \\ \mu \end{pmatrix} = \begin{pmatrix} \frac{\langle \nabla \cdot \boldsymbol{u}\boldsymbol{I}, \boldsymbol{\sigma}^* \rangle}{|\nabla \cdot \boldsymbol{u}\boldsymbol{I}|} \\ \frac{\langle \check{\nabla} \boldsymbol{u}, \boldsymbol{\sigma}^* \rangle}{|\check{\nabla} \boldsymbol{u}|} \end{pmatrix} \tag{3.42}$$

We propose to apply regularization to the above equations. Specifically, by simply denoting the above equations as $f - ku = 0$, where $u = (\lambda, \mu)^{\mathsf{T}}$, the objective functional is given as follows:

$$J[u] = \frac{1}{2} \int_{\Omega} |w_{\mathrm{f}}(f - ku)|^2 \mathrm{d}V + \frac{\lambda^p}{p} \int_{\Omega} |w_{\mathrm{r}} \nabla u|^p \mathrm{d}V, \qquad p = 1, 2 \tag{3.43}$$

which is exactly the same form as Eq. (2.113), and thus can be minimized by the method explained in Chapter 2.

3.6 Numerical Simulations

3.6.1 Setup and Conditions

As shown in Fig. 3.1, a 240 mm wide and 270 mm height block was constructed using FEM software COMSOL Multiphysics 5.5 (COMSOL Inc.). The viscoelastic wave was excited at 30 Hz in the y-direction from the red plane in Fig. 3.1. The green plane was set as fixed and the other four planes were free surfaces.

Two models (the cylinder model in Fig. 3.2(a) and the sphere model in Fig. 3.2(b)) were constructed as loading objects. Both models consist of a rectangular background region with constant MPs and the inclusions with higher shear modulus and viscosity.

MATLAB R2020a (The MathWorks Inc.) was used for all reconstruction processes. The derivatives of the measured data were calculated using the Savitzky–Golay filter as explained in Chapter 2.

3.6.2 Results and Discussion

Figure 3.3 shows the reconstruction results of the cylinder model. As shown in Fig. 3.3(b) and (c), both the standard method and the previous method have low estimate in the inclusions, and they are distorted in some regions. This is because of the assumption that tissues are incompressible, which is not the case in our simulation. On the other hand, the proposed method yields good reconstruction results, as shown in Fig. 3.3(d). The subtle distortion observed both in the standard and proposed methods is due to the nodes of the stationary wave

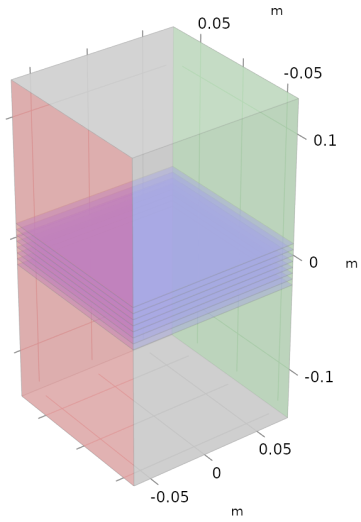

Fig. 3.1: Configuration of the numerical simulations. The mechanical vibration was excited from the red plane and the fixed boundary condition was assigned on the green plane. The displacement field was obtained on eight slices shown in blue.

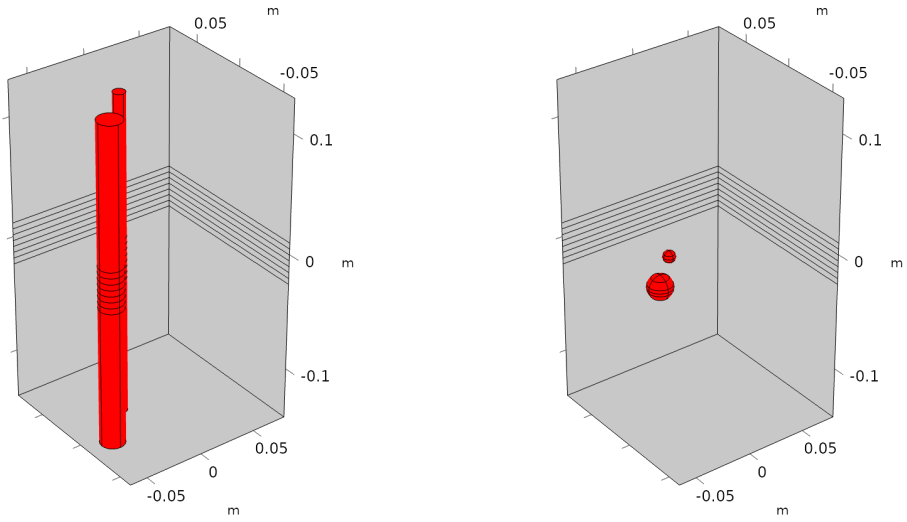

(a) Cylinder model (b) Sphere model

Fig. 3.2: Simulation models. The cylinder model has constant MPs along the z-axis whereas the sphere model has 3D structure.

formed by reflective waves. To alleviate this, post-processing filters that remove the reflected wave can be applied [136]. Multifrequency MRE [137–140] in which the displacement fields measured at different frequencies are combined also helps to stabilize the results.

Figure 3.4 shows the reconstructed shear viscosity of the cylindrical model. Note that we assume the Voigt model for viscoelastic materials; the shear viscosity is calculated as the imaginary part of the complex shear modulus divided by the angular frequency. The overall results exhibit a similar trend to that of the shear modulus. However, the results using the proposed method are also distorted. This is because with a current excitation frequency of

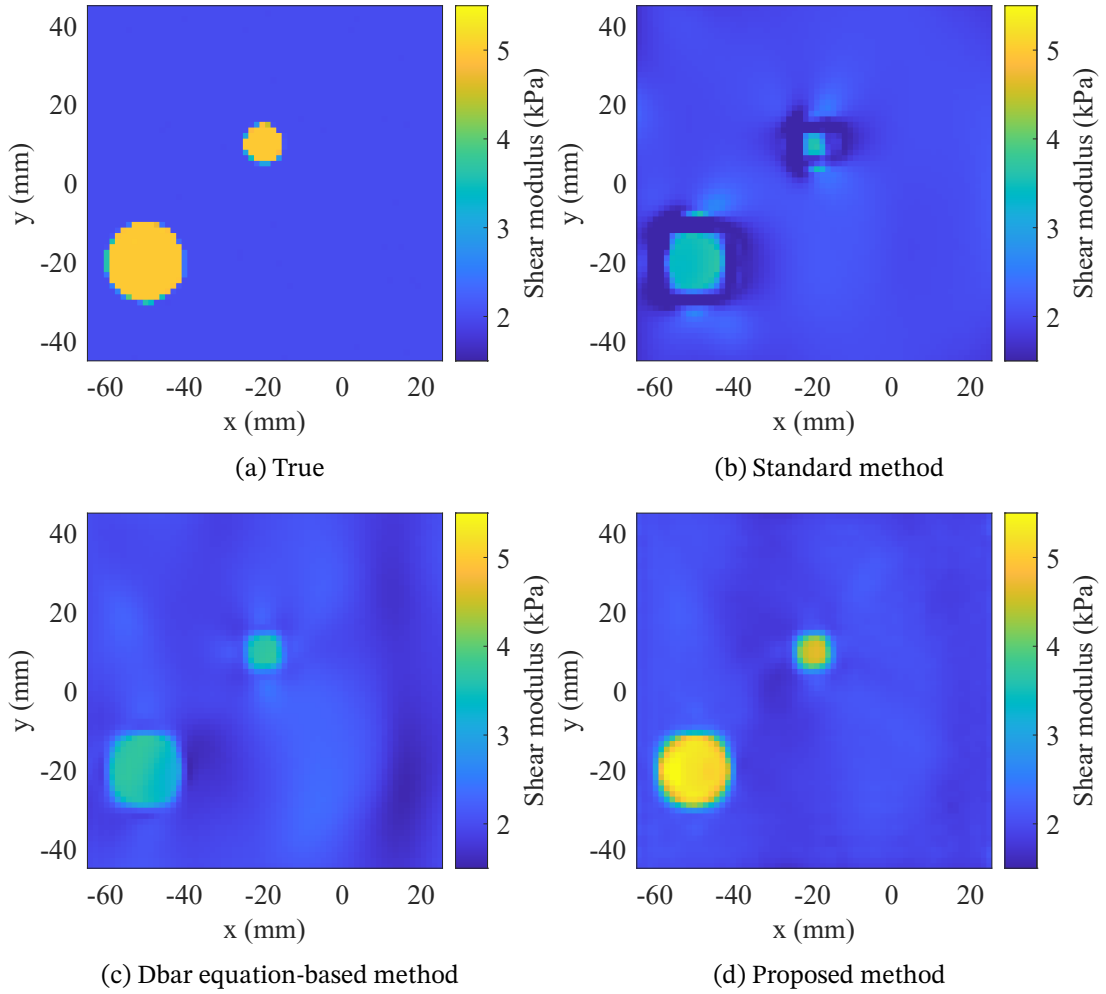

(a) True (b) Standard method

(c) Dbar equation-based method (d) Proposed method

Fig. 3.3: Reconstructed shear modulus maps at $z = 0$ mm for cylinder model. (a) True map, and results of (b) standard method, (c) Dbar equation-based method, and (d) proposed method.

30 Hz, the contribution of shear viscosity in the complex shear modulus is smaller than that of the shear modulus, and this is difficult to reconstruct. The results could be improved by using a higher frequency, but in that case, the wave would attenuate faster, making the SNR low.

Figure 3.5 shows the reconstruction results when the SNR is 40 dB. In the standard method, the resultant images are too noisy, and the inclusions are not discernible. Although the previous method yields relatively stable results, the estimated value of the shear modulus is still lower than the true value. The proposed method still provides accurate results especially in terms of the shear modulus.

In all methods, the results become noisy in the $x > 0$ region. This is because the wave emanates from the $x < 0$ direction and attenuates as x increases. Figure 3.6 shows the magnitudes of the stress tensor and the gradient of the displacement field, which are the measured and dual fields in the proposed method. The results of the proposed method becomes less stable in the region where these fields are small.

Figure 3.7 shows the reconstruction results of the proposed method when the SNR is 40 dB and TV regularization is applied to the proposed method. Due to regularization, the proposed

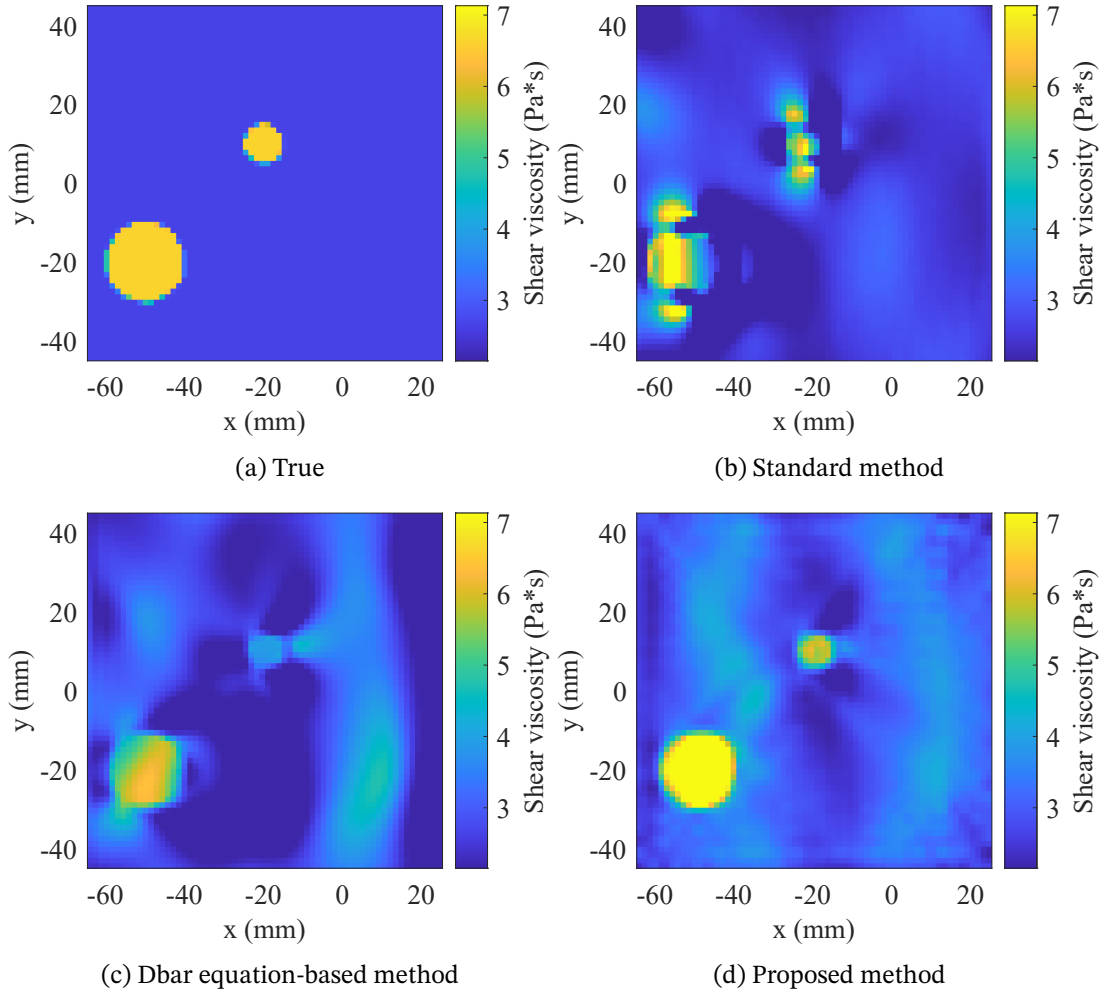

(a) True

(b) Standard method

(c) Dbar equation-based method

(d) Proposed method

Fig. 3.4: Reconstructed shear viscosity maps at $z = 0$ mm for cylinder model. (a) True map, and results of (b) standard method, (c) Dbar equation-based method, and (d) proposed method.

method yields accurate results even with the noise.

Figure 3.8 shows the reconstruction results of the sphere model. In this case, the previous method yields lower estimates because it is valid only for 2D problems. The proposed method performs well in the general 3D case.

Figure 3.9 shows the reconstruction results of the proposed method when the SNR is 40 dB and TV regularization is applied to the proposed method. With proper regularization, the proposed method yields accurate results even with the noise.

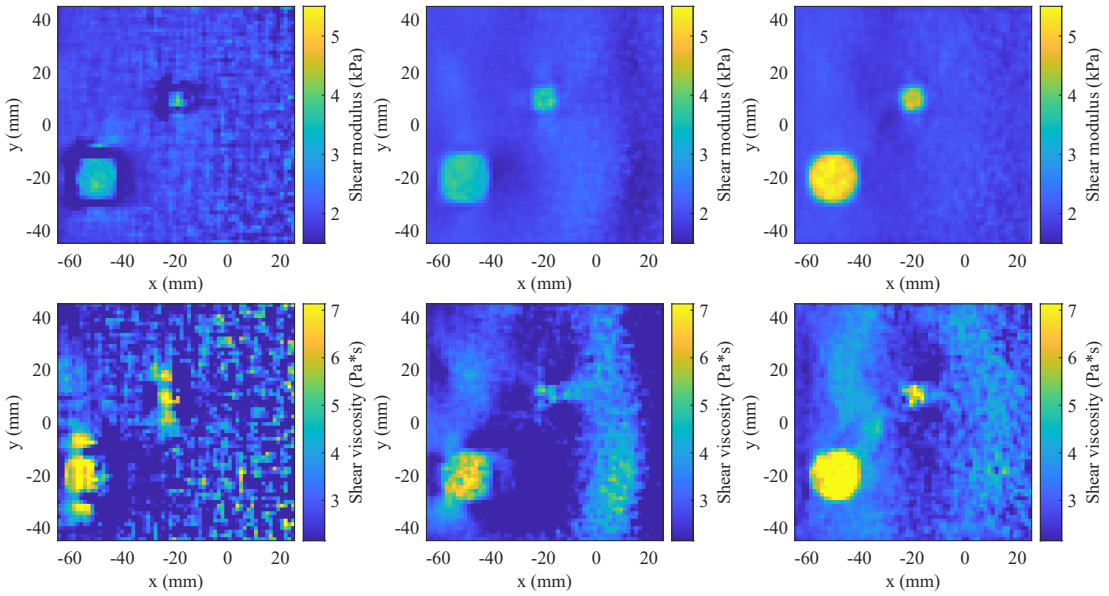

(a) Standard method (b) Dbar equation-based method (c) Proposed method

Fig. 3.5: Reconstructed (top) shear modulus and (bottom) shear viscosity maps at $z = 0$ mm for cylinder model. (a) True maps, and results of (b) Dbar equation-based method and (c) proposed method.

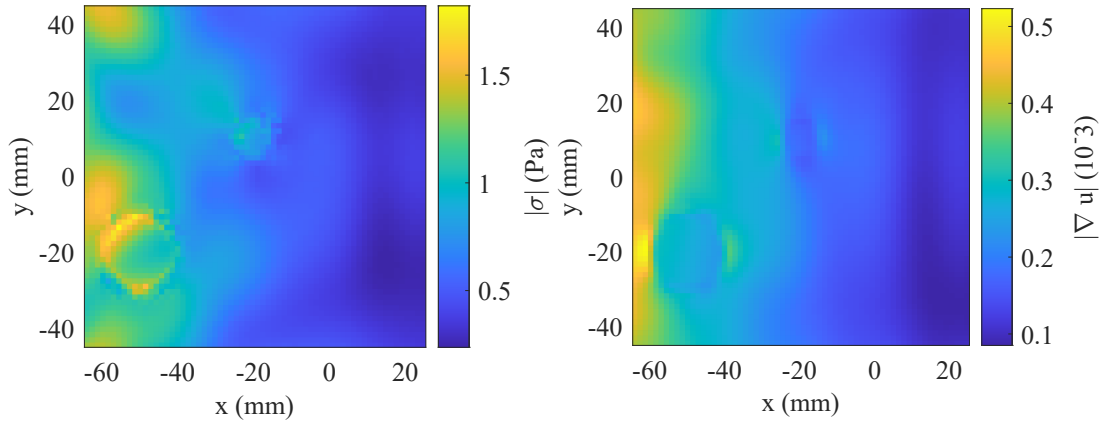

(a) $|\boldsymbol{\sigma}|$ (b) $|\nabla \boldsymbol{u}|$

Fig. 3.6: Reconstructed (top) shear modulus and (bottom) shear viscosity maps at $z = 0$ mm for cylinder model. (a) True maps, and results of (b) Dbar equation-based method and (c) proposed method.

3.7 Conclusion of This Chapter

In this chapter, we developed a novel reconstruction method for MRE. First, we formulated the MRE reconstruction as impedivity inverse problems with divergence-constraint. Then representation formulae of vector fields were extended to tensor fields and the derived formulae were used to develop an MRE reconstruction method. The proposed method was vali-

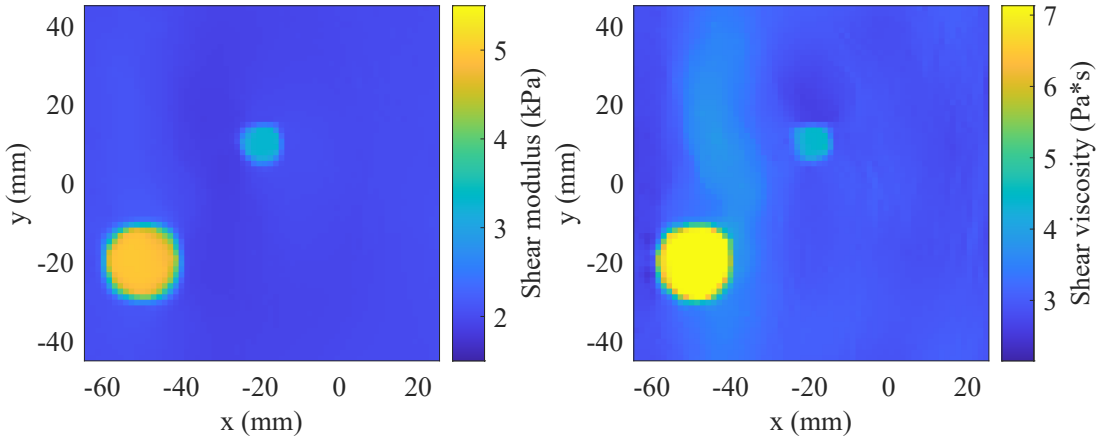

(a) Shear modulus (b) Shear viscosity

Fig. 3.7: Reconstruction results of the proposed method at $z = 0$ mm for the cylinder model with the SNR of 40 dB. Results of (a) shear modulus and (b) shear viscosity.

dated by numerical simulations; it successfully reconstructed MPs in the general 3D case and was robust against measurement noise compared with the conventional method.

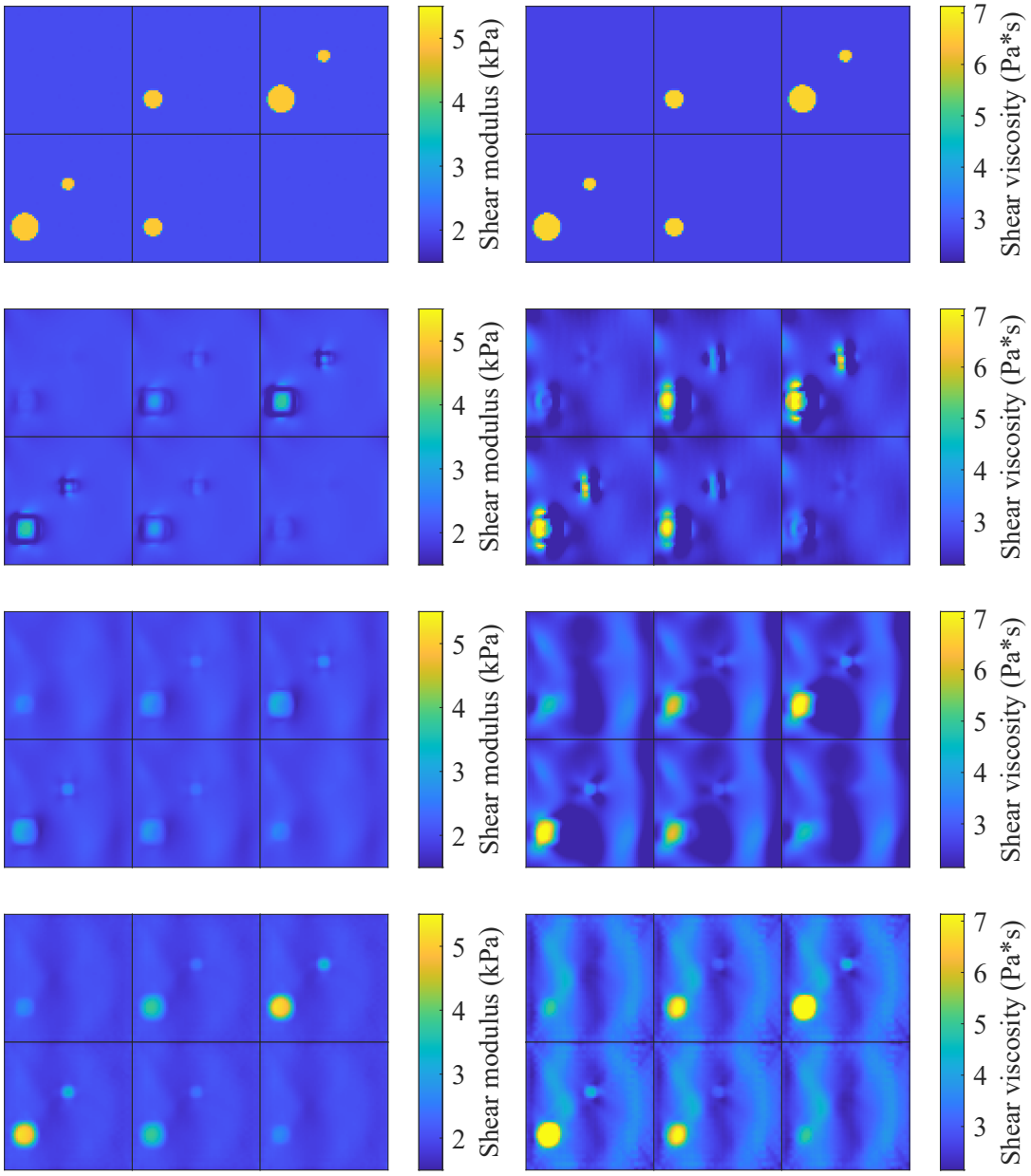

(a) Shear modulus (b) Shear viscosity

Fig. 3.8: Reconstructed (a) shear modulus and (b) shear viscosity maps for sphere model. (top) True maps, and results of (2nd row) standard method, (3rd row) 2D Dbar equation-based method, and (bottom) proposed method.

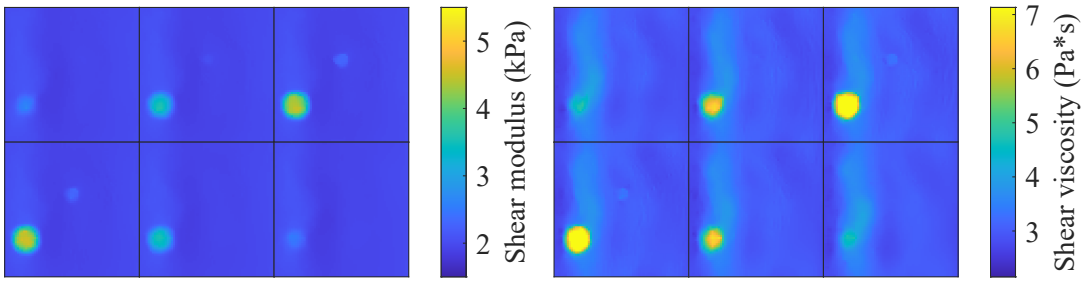

(a) Shear modulus (b) Shear viscosity

Fig. 3.9: Reconstructed (a) shear modulus and (b) shear viscosity maps of proposed method with TV regularization for sphere model with SNR of 40 dB.

Chapter 4

Electrical Properties Tomography Based on Integral Equations Derived from the Dbar Equation

In Chapter 2, we proposed an IE-based approach for 3D EPT reconstruction. The limitation of this method is that EPs must be given on the boundary of the ROI. Therefore, in this chapter, we propose a reconstruction method that does not require the information of EPs on the boundary.

First, we derive a slicewise reconstruction method based on a 2D IE in section 4.1. This method is an extension of our previous method that iteratively reconstructs 3D EPs based on the Cauchy–Pompeiu formula, and can solve 3D problems without iteration. Since this method reconstructs EPs in a slicewise manner, boundary EPs are required only on the closed curves enclosing each slice. In section 4.2, we develop another slicewise reconstruction method that is completely free from boundary EPs by deriving an explicit solution formula of the Dbar equation with the complex-derivative BC. In section 4.3, we derive a hybrid formula that uses EPs only on a fraction of the boundary of the ROI. The numerical calculation of the proposed method is discussed in section 4.4. We test the proposed method by numerical simulations in section 4.5 and phantom experiments in section 4.6. Finally, section 4.7 concludes this chapter.

4.1 Slicewise Reconstruction Based on the Cauchy–Pompeiu Formula

4.1.1 Linear Integral Equation for the Electric Field

In this section, we deduce Eq. (2.34), which was used in our previous method. It explicitly reconstructs 2D EPs and iteratively corrects the results for 3D reconstruction as explained in Chapter 1, starting from Eq. (2.100) derived from Helmholtz's representation formula.

By the relations

$$\nabla^{\mathrm{c}} H^{+} \cdot \nabla w = 4\partial H^{+}\bar{\partial} w + \partial_z H^{+}\partial_z w, \tag{4.1}$$

$$\nabla^{\mathrm{c}} H^{+} \cdot \boldsymbol{n} = 4\partial H^{+} n^{+} + \partial_z H^{+} n_z, \tag{4.2}$$

Equation (2.100) can be rewritten as follows:

$$\int_{\Omega} \lambda(4\partial H^{+}\bar{\partial} w + \partial_z H^{+}\partial_z w)\mathrm{d}V = \oint_{\partial\Omega} \lambda(4\partial H^{+} n^{+} + \partial_z H^{+} n_z) w \mathrm{d}S - \int_{\Omega} \mathrm{i}\omega_0\mu_0 H^{+} w \mathrm{d}V, \tag{4.3}$$

where $n^+ \coloneqq (n_x + \mathrm{i}n_y)/2$. Let F be the fundamental solution of the $\bar{\partial}$-operator, i.e., $\bar{\partial}F(\zeta') = -\delta(\zeta')$. If we take w as $\delta(z'-z)F(\zeta'-\zeta)$, then it holds that

$$\int_D \lambda 4\partial H^+ \bar{\partial} F \mathrm{d}\zeta' \wedge \mathrm{d}\bar{\zeta'} + \int_\Omega \lambda \partial_z H^+ F \partial_z \delta \mathrm{d}V = \oint_{\partial D} \lambda 4\partial H^+ F \mathrm{d}\zeta' - \int_D \mathrm{i}\omega_0\mu_0 H^+ F \mathrm{d}\zeta' \wedge \mathrm{d}\bar{\zeta'}. \quad (4.4)$$

By the properties of the delta function, we have

$$\int_D \lambda 4\partial H^+ \bar{\partial} F \mathrm{d}\zeta' \wedge \mathrm{d}\bar{\zeta'} = -\lambda 4\partial H^+, \quad (4.5)$$

$$\int_\Omega \lambda \partial_z H^+ F \partial_z \delta \mathrm{d}V = -\int_D \partial_z(\lambda \partial_z H^+ F)\mathrm{d}\zeta' \wedge \mathrm{d}\bar{\zeta'} = -\int_D \partial_z(\lambda \partial_z H^+) F \mathrm{d}\zeta' \wedge \mathrm{d}\bar{\zeta'}, \quad (4.6)$$

where we used the fact that F is independent of z. Hence, it holds that

$$-\lambda 4\partial H^+ - \int_D \partial_z(\lambda \partial_z H^+) F \mathrm{d}\zeta' \wedge \mathrm{d}\bar{\zeta'} = \oint_{\partial D} \lambda 4\partial H^+ F \mathrm{d}\zeta' - \int_D \mathrm{i}\omega_0\mu_0 H^+ F \mathrm{d}\zeta' \wedge \mathrm{d}\bar{\zeta'}, \quad (4.7)$$

which can be explicitly written as

$$\lambda 4\partial H^+ = \frac{1}{2\pi\mathrm{i}} \oint_{\partial D} \frac{\lambda 4\partial H^+}{\zeta' - \zeta} \mathrm{d}\zeta' + \frac{1}{2\pi\mathrm{i}} \int_D \frac{\mathrm{i}\omega_0\mu_0 H^+ - \partial_z(\lambda \partial_z H^+)}{\zeta' - \zeta} \mathrm{d}\zeta' \wedge \mathrm{d}\bar{\zeta'}. \quad (4.8)$$

Substituting Eqs. (2.32) and (2.33) gives

$$E_z = \frac{1}{2\pi\mathrm{i}} \oint_{\partial D} \frac{E_z}{\zeta' - \zeta} \mathrm{d}\zeta' + \frac{1}{2\pi\mathrm{i}} \int_D \frac{\omega_0\mu_0 H^+ + \partial_z E^+}{\zeta' - \zeta} \mathrm{d}\zeta' \wedge \mathrm{d}\bar{\zeta'}. \quad (4.9)$$

This is a linear IE for E_z and can be directly solved. Then, substituting the resultant E_z into Eq. (2.33) yields the final EP maps. This method reconstructs EPs in a slicewise manner. Therefore, the boundary ∂D of each slice D is a closed curve on this slice. This eases the need of boundary EPs in the Helmholtz's decomposition-based 3D reconstruction method.

4.1.2 Comparison with Iterative Correction Method

In this section, we compare the proposed method with our previous method that uses the 2D assumption to obtain the initial estimate given by

$$E_z^0 \coloneqq \frac{1}{2\pi\mathrm{i}} \oint_{\partial D} \frac{-4\mathrm{i}\partial H^+/\gamma}{\zeta' - \zeta} \mathrm{d}\zeta' + \frac{1}{2\pi\mathrm{i}} \int_D \frac{\omega_0\mu_0 H^+}{\zeta' - \zeta} \mathrm{d}\zeta' \wedge \mathrm{d}\bar{\zeta'}, \quad (4.10)$$

and iteratively correct the effect of $\partial_z E^+$ in Eq. (4.9).

With the current estimate of the electric field $E_z^{(n)}$, the updated estimate $E_z^{(n+1)}$ is obtained by substituting $E_z^{(n)}$ into the right-hand side of Eq. (2.34) and performing forward integral calculation. By denoting the forward operator as K, this update procedure can be written as follows:

$$E_z^{(n+1)} = E_z^0 + K[E_z^{(n)}]. \quad (4.11)$$

Iteration of this procedure can be represented as follows:

$$E_z = E_z^0 + K[E_z^0] + K[K[E_z^0]] + \cdots, \quad (4.12)$$

which corresponds to the Neumann expansion of the IE given in Eq. (4.9). Comparing Eq. (4.12) with Eq. (4.9) indicates that the n-th estimate of the iteration method corresponds

to the solution of Eq. (2.34) when $(I - K)^{-1}[E_z]$ is approximated as the first n terms of Eq. (4.12).

Note that the Neumann expansion of $(I - K)^{-1}$ is valid only when $\|K\| < 1$ holds, where $\|K\|$ represents the operator norm of K. In our case, $K[f] = -T[\partial_z(Af)]$ with A given as $-\partial_z H^+/(4\partial H^+)$. Therefore, the norm of K depends on $\partial_z H^+$ and ∂H^+. It is known that when the birdcage coil typically used in modern MR scanners is driven in quadrature mode, ∂H^+ gets very small around the center of the human body. Thus, if we include the center of the body in the ROI, $\|K\| < 1$ does not hold, resulting in a nonconvergent case of the iteration method. In contrast, our proposed method is free from such nonconvergent results because it does not use the Neumann expansion.

4.2 An Explicit Solution of the Complex-Derivative Boundary Value Problem of the Dbar Equation

In this section, we derive an explicit solution formula of the boundary value problems of the Dbar equation to propose a reconstruction method that is completely free from boundary EP values.

First, we consider the case of a holomorphic function. Let D be a domain whose boundary is a piecewise smooth Jordan curve. If ϕ is holomorphic in D and $\partial\phi \in C^0(\overline{D})$, then $\partial\phi$ is also holomorphic in D. Applying Cauchy's formula to $\partial\phi$ yields

$$\partial\phi(\zeta) = \frac{1}{2\pi\mathrm{i}} \oint_{\partial D} \frac{\partial\phi(\zeta')}{\zeta' - \zeta} \mathrm{d}\zeta', \tag{4.13}$$

where $\zeta \in D$. Integrating Eq. (4.13) gives

$$\phi(\zeta) = -\frac{1}{2\pi\mathrm{i}} \oint_{\partial D} \log\left(1 - \frac{\zeta}{\zeta'}\right) \partial\phi(\zeta')\mathrm{d}\zeta' + c, \quad \zeta \in D. \tag{4.14}$$

Equation (4.14) is a representation formula of a holomorphic function inside a domain. In contrast to the ordinary Cauchy's formula, which requires the function itself on the boundary, Eq. (4.14) uses its complex derivative on the boundary.

The constant c reflects the fact that for a function ϕ that satisfies the complex-derivative BC, the function $\tilde{\phi} \coloneqq \phi + c$ also satisfies the same BC. Therefore, the value of the function must be given for at least one point to uniquely determine the function.

Next, we extend the formula to a general function that is not necessarily holomorphic. Let us define a function ϕ as

$$\phi(\zeta) \coloneqq f(\zeta) - T[\bar{\partial} f](\zeta), \tag{4.15}$$

where $\partial f \in C^0(\overline{D})$. Differentiating both sides leads to

$$\partial\phi(\zeta) = \partial f(\zeta) - \Pi[\bar{\partial} f](\zeta), \tag{4.16}$$

where the operator Π is defined in Eq. (A.92). Since $\partial\phi$ is holomorphic, we can apply Eq. (4.14) to get

$$\phi(\zeta) = -\frac{1}{2\pi\mathrm{i}} \oint_{\partial D} \log\left(1 - \frac{\zeta}{\zeta'}\right) (\partial f(\zeta) - \Pi[\bar{\partial} f](\zeta))\mathrm{d}\zeta' + c, \quad \zeta \in D. \tag{4.17}$$

Hence, we obtain the formulae shown in the following:

Let D be a domain whose boundary is a piecewise smooth Jordan curve. If $\partial f \in C^0(\overline{D})$ and $\bar{\partial} f \in C^{0,\alpha}(\overline{D}), 0 < \alpha < 1$, then it holds that

$$f(\zeta) = -\frac{1}{2\pi \mathrm{i}} \oint_{\partial D} \log\left(1 - \frac{\zeta}{\zeta'}\right)(\partial f(\zeta) - \Pi[\bar{\partial} f](\zeta))\mathrm{d}\zeta' + T[\bar{\partial} f](\zeta) + c, \quad \zeta \in D,$$

where c is a constant. If $\bar{\partial} f \in C^0(\overline{D})$ and $\partial f \in C^{0,\alpha}(\overline{D}), 0 < \alpha < 1$, then it holds that

$$f(\zeta) = \frac{1}{2\pi \mathrm{i}} \oint_{\partial D} \log\left(1 - \frac{\bar{\zeta}}{\bar{\zeta}'}\right)(\bar{\partial} f(\zeta) - \bar{\Pi}[\partial f](\zeta))\mathrm{d}\bar{\zeta}' + \bar{T}[\partial f](\zeta) + c, \quad \zeta \in D,$$

where c is a constant.

This is a representation formula of a function f not necessarily holomorphic in terms of its complex derivative ∂f on the boundary and $\bar{\partial} f$ inside the region.

4.2.1 Reconstruction Formula without the Boundary Value of EPs

In what follows, Eq. (4.2) is applied to the EPT problem to derive the boundary-value-free reconstruction formulae of E_z, and thus γ. By taking the $(x - \mathrm{i}y)$-component of Eq. (1.1), it holds that

$$\partial E_z = -\omega_0 \mu_0 H^- + \partial_z E^- = -\omega_0 \mu_0 H^- - \frac{\partial_z H^-}{4\bar{\partial} H^-} E_z. \tag{4.18}$$

Here, we used the relations $\partial_z H^- = -\omega_0 \gamma E^-$ and $4\bar{\partial} H^- = \omega_0 \gamma E_z$, which are deduced by taking the $(x - \mathrm{i}y)$- and z-components of Eq. (2.33). Thus, under the assumption that $\partial_z H^- = 0$, we get

$$\partial E_z = -\omega_0 \mu_0 H^-. \tag{4.19}$$

Applying $f = E_z$ to Eq. (4.2), we have

$$E_z(\zeta) = -\frac{1}{2\pi \mathrm{i}} \oint_{\partial D} \log\left(1 - \frac{\zeta}{\zeta'}\right)(\omega_0 \mu_0 H^- - \Pi[\omega_0 \mu_0 H^+](\zeta'))\mathrm{d}\zeta' + \frac{1}{2\pi \mathrm{i}} \int_D \frac{\omega_0 \mu_0 H^+(\zeta')}{\zeta' - \zeta} \mathrm{d}\zeta' \wedge \mathrm{d}\bar{\zeta}' + c, \tag{4.20}$$

since $\bar{\partial} E_z$ and ∂E_z are given by Eqs (2.31) and (4.19), respectively. It is known that $|H^+| \gg |H^-|$ when the body is excited using a quadrature birdcage coil, which is commonly used in modern MRI systems [69]. Hence, substituting Eqs. (2.31) and (4.19) into Eq. (4.20) under the condition that $|H^-| \ll |\Pi[H^+]|$ gives

$$E_z(\zeta) = \frac{1}{2\pi \mathrm{i}} \oint_{\partial D} \log\left(1 - \frac{\zeta}{\zeta'}\right)\Pi[\omega_0 \mu_0 H^+](\zeta')\mathrm{d}\zeta' + \frac{1}{2\pi \mathrm{i}} \int_D \frac{\omega_0 \mu_0 H^+(\zeta')}{\zeta' - \zeta} \mathrm{d}\zeta' \wedge \mathrm{d}\bar{\zeta}' + c. \tag{4.21}$$

The validity of the assumption $|H^-| \ll |\Pi[H^+]|$ is shown using numerical simulations in section 4.4. Equation (4.21) gives E_z using only H^+ up to a constant c.

The constant c can be determined as described in the following. It is known that in the quadrature birdcage coil setting, the zero-point of E_z appears around the center of the body [32]. Accordingly, from Eq. (2.33), $\partial H^+ = 0$ here. From this fact, we determine the zero point ζ^* of E_z as the point where ∂H^+, which is computed from the measured H^+, is minimal as follows:

$$\zeta^* = \arg\min_{\zeta \in D} |\partial H^+(\zeta)|. \tag{4.22}$$

Then, c is obtained from

$$E_z(\zeta^*) = -\frac{1}{2\pi \mathrm{i}} \oint_{\partial D} \log\left(1 - \frac{\zeta^*}{\zeta'}\right)(\omega_0\mu_0 H^-(\zeta') + \Pi[\omega_0\mu_0 H^+](\zeta'))\mathrm{d}\zeta' + \frac{1}{2\pi \mathrm{i}} \int_D \frac{\omega_0\mu_0 H^+(\zeta')}{\zeta' - \zeta^*}\mathrm{d}\zeta' \wedge \mathrm{d}\bar{\zeta}' + c = 0. \quad (4.23)$$

Using this c, E_z can be determined uniquely by Eq. (4.21). Once E_z is obtained, γ can be directly calculated as the ratio of $4\partial H^+$ to $\mathrm{i}E_z$ according to Eq. (2.33). Here, we estimate γ using the total variation regularization by minimizing the functional

$$J[\gamma] = \int_D |4\partial H^+(\zeta) - \mathrm{i}\gamma E_z(\zeta)|^2 \mathrm{d}\zeta \wedge \mathrm{d}\bar{\zeta} + \frac{\lambda^p}{p} \int_D |\nabla\gamma(\zeta)|^p \mathrm{d}\zeta \wedge \mathrm{d}\bar{\zeta}, \quad (4.24)$$

where we chose p as 1 to suppress the artifact caused by the zero point of E_z [32].

4.3 An Explicit Solution of the Mixed Boundary Value Problem of the Dbar Equation

In this section, we derive an explicit solution formula of the mixed boundary value problems of the Dbar equation to propose a hybrid method that requires boundary EP values only on the fraction of the boundary of the ROI. This will reduce the reconstruction error due to neglecting H^- when EPs are known in a part of the boundary. Specifically, the mixed BC we consider here is stated as follows:

- C: Dirichlet BC
- $\partial D \setminus C$: Complex-derivative BC

First, we rewrite Eq. (4.14) by dividing the boundary ∂D into C and $\partial D \setminus C$ as follows:

$$\phi(\zeta) = -\frac{1}{2\pi \mathrm{i}} \int_C \log\left(1 - \frac{\zeta}{\zeta'}\right)\partial\phi(\zeta')\mathrm{d}\zeta' - \frac{1}{2\pi \mathrm{i}} \int_{\partial D\setminus C} \log\left(1 - \frac{\zeta}{\zeta'}\right)\partial\phi(\zeta')\mathrm{d}\zeta' + c \quad (4.25)$$

Replacing the first term by integrating by parts gives

$$\phi(\zeta) = \frac{1}{2\pi \mathrm{i}} \int_C \frac{\phi(\zeta')}{\zeta' - \zeta}\mathrm{d}\zeta' - \frac{1}{2\pi \mathrm{i}} \left[\log\left(1 - \frac{\zeta}{\zeta'}\right)\phi(\zeta')\right]_a^b - \frac{1}{2\pi \mathrm{i}} \int_{\partial D\setminus C} \log\left(1 - \frac{\zeta}{\zeta'}\right)\partial\phi(\zeta')\mathrm{d}\zeta' + c' \quad (4.26)$$

This is an integral formula that represents ϕ in D in terms of ϕ on $\partial D \setminus C$ and $\partial\phi$ on C. If we consider the limit of $C \to \partial D$, this reduces to the original Cauchy integral formula, and if we consider the limit of $C \to \varnothing$, it reduces to Eq. (4.14).

Next, we extend the formula to the general case of not necessarily holomorphic functions. Let us define the function ϕ as $f(\zeta) - T[\bar{\partial} f](\zeta)$. Then it holds that

$$\partial\phi(\zeta) = \partial f(\zeta) - \Pi[\bar{\partial} f](\zeta), \quad (4.27)$$

$$\bar{\partial}\phi(\zeta) = \bar{\partial} f(\zeta) - \bar{\partial} f(\zeta) = 0. \quad (4.28)$$

Since $\bar{\partial}\phi = 0$, ϕ is holomorphic, and we obtain the formulae shown in the following:

Let D be a domain whose boundary is a piecewise smooth Jordan curve. If $\partial f \in C^0(\overline{D})$

and $\bar{\partial} f \in C^{0,\alpha}(\overline{D}), 0 < \alpha < 1$, then it holds that

$$f(\zeta) = \frac{1}{2\pi \mathrm{i}} \int_C \frac{f(\zeta') - T[\bar{\partial} f](\zeta')}{\zeta' - \zeta} \mathrm{d}\zeta' - \frac{1}{2\pi \mathrm{i}} \left[\log\left(1 - \frac{\zeta}{\zeta'}\right) (f(\zeta') - T[\bar{\partial} f](\zeta')) \right]_a^b - \frac{1}{2\pi \mathrm{i}} \int_{\partial D \setminus C} \log\left(1 - \frac{\zeta}{\zeta'}\right) (\partial f(\zeta') - \Pi[\bar{\partial} f](\zeta')) \mathrm{d}\zeta' + T[\bar{\partial} f](\zeta) + c' \quad (4.29)$$

and if $\partial f \in C^0(\overline{D})$ and $\bar{\partial} f \in C^{0,\alpha}(\overline{D}), 0 < \alpha < 1$, then it holds that

$$f(\zeta) = -\frac{1}{2\pi \mathrm{i}} \int_C \frac{f(\zeta') - \bar{T}[\partial f](\zeta')}{\bar{\zeta}' - \bar{\zeta}} \mathrm{d}\bar{\zeta}' + \frac{1}{2\pi \mathrm{i}} \left[\log\left(1 - \frac{\bar{\zeta}}{\bar{\zeta}'}\right) (f(\zeta') - \bar{T}[\partial f](\zeta')) \right]_a^b + \frac{1}{2\pi \mathrm{i}} \int_{\partial D \setminus C} \log\left(1 - \frac{\bar{\zeta}}{\bar{\zeta}'}\right) (\bar{\partial} f(\zeta') - \bar{\Pi}[\partial f](\zeta')) \mathrm{d}\zeta' + \bar{T}[\partial f](\zeta) + c' \quad (4.30)$$

where c is a constant.

The above represents f in D by f in C and ∂f on $\partial D \setminus C$. If we consider the limit of $C \to \partial D$, this reduces to the original Cauchy-Pompeiu formula, and if we consider the limit of $C \to \varnothing$, it reduces to Eq. (4.2). By using Eq. (4.29) instead of Eq. (4.2), E_z is reconstructed from the mixed BC.

4.4 Numerical Calculation

4.4.1 FFT-Based Calculation of the Convolution over a Bounded Domain

In the method described above, 2D IEs must be solved. This can be accomplished using the CG method. In the CG method, the forward operation must be calculated for each iteration. In our case, the operator T is defined as a convolution and thus can be efficiently calculated using the FFT. Note that the convolution is executed in a finite domain D, instead of the whole complex plane. As we mentioned in Chapter 2, the nonsingular kernel that can calculate the convolution over a finite domain was derived by Vico *et al.* [102] for the Laplace kernel. Here, we derive the nonsingular kernel associated with the Cauchy kernel used in our 2D IE.

By extending the integrand f with zero-padding, the operation $T[f]$ can be regarded as a convolution of f with the Cauchy kernel as follows:

$$T[f](\zeta) = \frac{1}{\pi} \iint_{\mathbb{R}^2} \frac{\tilde{f}(\zeta')}{\zeta - \zeta'} \mathrm{d}x' \mathrm{d}y' = \tilde{f}(\zeta) * \frac{1}{\pi\zeta}, \quad (4.31)$$

where

$$\tilde{f}(\zeta) = \begin{cases} f(\zeta) & \zeta \in D, \\ 0 & \zeta \in \mathbb{R}^2 \setminus \overline{D}. \end{cases} \quad (4.32)$$

To realize this convolution as a pointwise product in the Fourier domain, we derive the Fourier-domain representation of $G(x, y) = 1/(\pi(x + \mathrm{i}y))$. Given that $G(x, y)$ is a fundamental solution of the Dbar equation, it holds that

$$\frac{1}{2}(\partial_x + \mathrm{i}\partial_y) G(x, y) = \delta(x)\delta(y). \quad (4.33)$$

Applying the Fourier transform to both sides of Eq. (4.33) yields

$$\mathcal{F}[G] = \frac{1}{\pi \mathrm{i}} \frac{1}{u + \mathrm{i}v}. \tag{4.34}$$

Note that this function is singular at the origin. Following Vico [102], we modify the function to derive a nonsingular version without any approximation.

Because $\tilde{f}$ has a finite support D by definition and thus the range that the convolution has nonzero value is bounded, it holds that

$$I(\zeta) = \tilde{f}(\zeta) * \frac{\chi_R(\zeta)}{\pi\zeta} \tag{4.35}$$

without any approximation, where χ_R is the characteristic function of the region R. R can be taken as a circle with radius a, where a is determined according to D. In this case, $\chi_R = U(a - r)$ holds, where U is the step function and $r = \sqrt{x^2 + y^2}$. Then, the Dbar derivative of $\chi_R G$ can be calculated as follows:

$$\begin{aligned} \frac{1}{2}(\partial_x + \mathrm{i}\partial_y)(\chi_R(x,y)G(x,y)) &= U(a-r)\delta(x)\delta(y) - \frac{\exp(\mathrm{i}\theta)\delta(r-a)}{2}\frac{1}{\pi\zeta} \\ &= \delta(x)\delta(y) - \frac{\delta(r-a)}{2\pi r}, \end{aligned} \tag{4.36}$$

where $\theta = \tan^{-1}(y/x)$. Compared to Eq. (4.33), Eq. (4.36) has an additional term, namely the delta function at $r = a$, reflecting the effect of $U(a - r)$. The Fourier spectrum of the second term on the right-hand side is given as follows:

$$\begin{aligned} \mathcal{F}\left[-\frac{\delta(r-a)}{2\pi r}\right] &= -\frac{1}{2\pi}\iint_{\mathbb{R}^2} \frac{\delta(r-a)}{r}\exp(-2\pi\mathrm{i}(ux+vy))\mathrm{d}x\mathrm{d}y \\ &= -J_0(2\pi a\rho), \end{aligned} \tag{4.37}$$

where $\rho = \sqrt{u^2 + v^2}$ and J_0 is the zeroth-order Bessel function of the first kind. By applying the Fourier transform to Eq. (4.36) and substituting Eq. (4.37), it holds that

$$\mathcal{F}\left[\frac{\chi_R(x,y)}{\pi(x+\mathrm{i}y)}\right] = \frac{1}{\pi\mathrm{i}}\frac{1 - J_0(2\pi a\rho)}{u + \mathrm{i}v}. \tag{4.38}$$

This function can be used to calculate the convolution with the Cauchy kernel in a finite domain and is not singular at the origin.

4.4.2 CG-FFT-Based Efficient Method for Solving the Integral Equation

Similar to the 3D IEs derived in Chapters 2 and 3, the slicewise IEs derived in this chapter can be efficiently solved by the CG method. Here we briefly describe the adjoint operators required for solving the least-squares system. The adjoint operator of the differentiation ∂_z is $-\partial_z$. Here, the original operation is performed by the forward difference scheme with the Neumann BC, while the adjoint operation is executed by the backward difference scheme with the Dirichlet BC. Therefore, if the forward operation is described as

$$L = I - \Pi B - T\partial_z A, \tag{4.39}$$

then the adjoint operator is given as

$$L^* = I - \bar{B}\Pi^* - \bar{A}\partial_z^* T^*, \tag{4.40}$$

and the least-squares system $L^*[L[u]] = L^*[f]$ is solved.

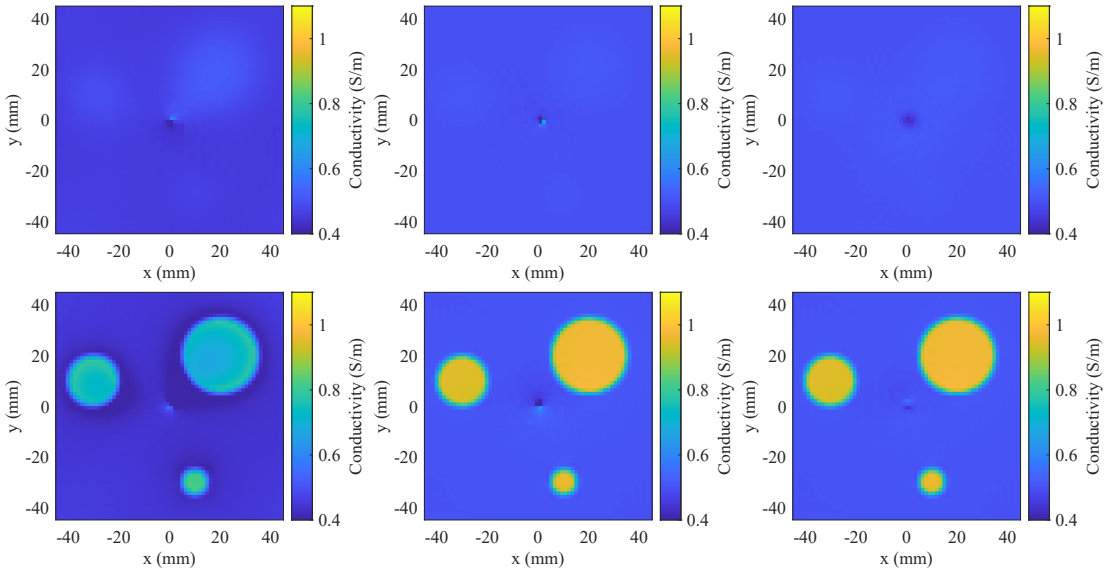

(a) No iteration (b) 5 iterations (c) Proposed method

Fig. 4.1: Reconstructed conductivity maps at (top) $z = 12.5$ mm and (bottom) $z = -12.5$ mm for short cylinder model. (a) Previous method with no iteration, (b) previous method with five iterations, and (c) proposed method.

4.5 Numerical Simulations

Numerical simulations were performed with the same conditions as explained in Chapter 2 except for the loading objects. In this section, we construct two cylinder models (a short-cylinder model and a long-cylinder model) as well as the brain model described in Chapter 2. Cylinder models consist of a large cylindrical background region with a conductivity of 0.5 S/m and a relative permittivity of 80, and small cylindrical inclusions with the conductivity 1 S/m and relative permittivity 50. The lengths of inclusions in the short-cylinder model and the long-cylinder model are 25 mm and 240 mm, respectively.

First, we compare the results of our previous method that iteratively reconstructs 3D EPs with the IE-based direct method proposed in this chapter. Then, we test the results of the boundary-value-free method by comparing the results with the case where boundary EPs were given.

Figures 4.1 and 4.2 show the reconstruction results for the cylindrical phantom by our previous and proposed methods. As shown in Figs. 4.1 and 4.2(a), in the previous method with no iteration, both conductivity and relative permittivity have lower values than those in the true maps. This is because the z derivative of the magnetic field is ignored in the previous method with no iteration. The effect of $\partial_z H^+$ is properly corrected for in the previous method after five iterations, as shown in Figs. 4.1 and 4.2(b). The proposed method also accurately estimated the conductivity and relative permittivity maps without iteration, as shown in Figs. 4.1 and 4.2(c).

Figure 4.3 shows relative errors after each iteration measured using the relative L2 norm expressed as

$$E[u] = \frac{\|u - u_{\text{true}}\|_2}{\|u_{\text{true}}\|_2} = \sqrt{\frac{\int_D |u(\zeta) - u_{\text{true}}(\zeta)|^2 \mathrm{d}\zeta \wedge \mathrm{d}\bar{\zeta}}{\int_D |u_{\text{true}}(\zeta)|^2 \mathrm{d}\zeta \wedge \mathrm{d}\bar{\zeta}}}, \tag{4.41}$$

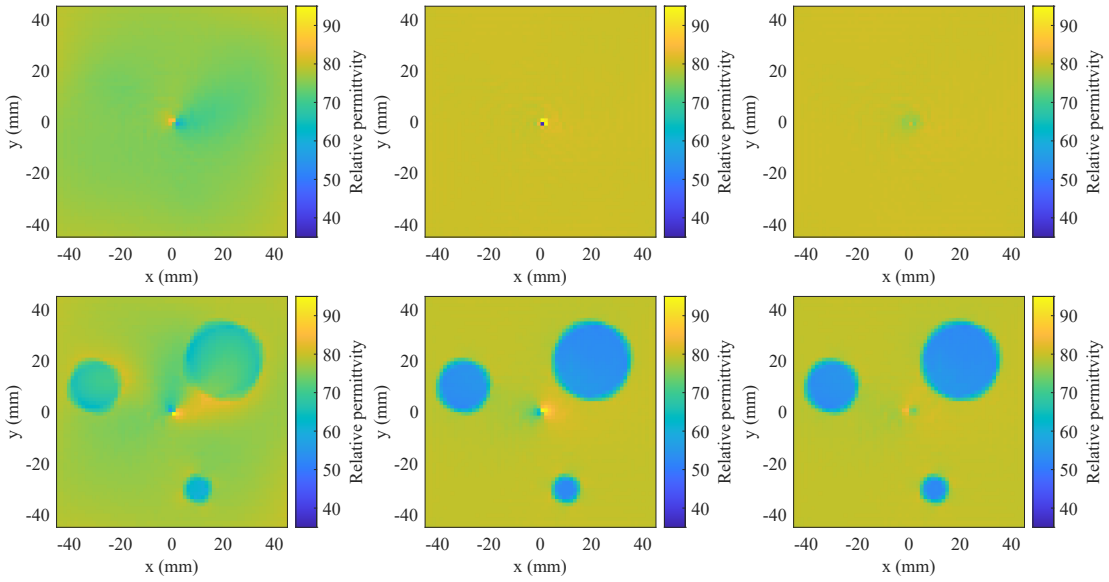

(a) No iteration (b) 5 iterations (c) Proposed method

Fig. 4.2: Reconstructed permittivity maps at (top) $z = 12.5$ mm and (bottom) $z = -12.5$ mm for short cylinder model. (a) Previous method with no iteration, (b) previous method with five iterations, and (c) proposed method.

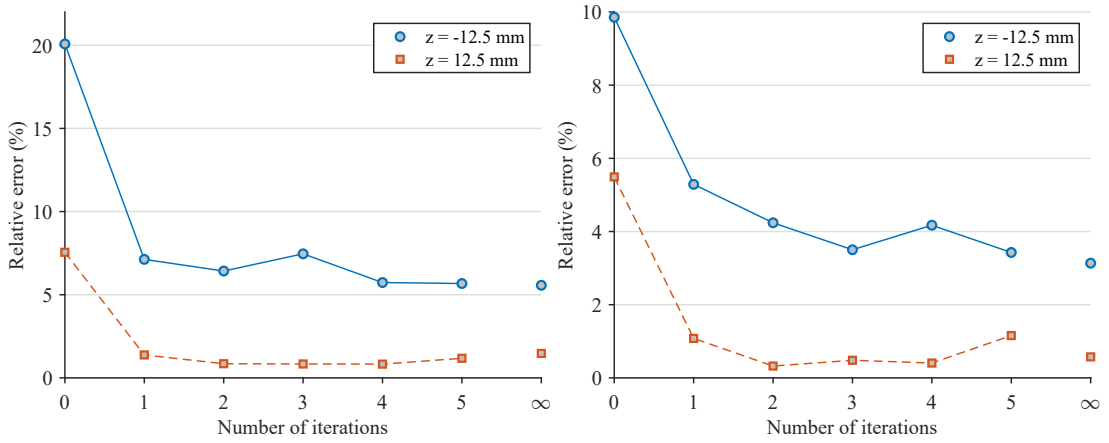

(a) Conductivity (b) Relative Permittivity

Fig. 4.3: Relative errors of (a) conductivity and (b) permittivity maps at each iteration of previous method and for proposed method (shown as ∞).

where $u = \sigma, \epsilon$. The difference from Eq. (2.130) is that the error is calculated for each slice instead of the entire volume. As shown in Fig. 4.3, both conductivity and relative permittivity converged after a single iteration. The relative errors of the proposed method are lower than those of the previous method after five iterations.

Figure 4.4 shows the reconstruction results for the human brain model when no noise was added. As shown in Fig. 4.4(a), both conductivity and relative permittivity have lower values than those in the true maps. This brain model has EPs varying along the z-axis and thus the effect of $\partial_z H^+$ is more prominent here than in the cylindrical model. The results of the previous method after five iterations have serious errors as shown in Fig. 4.4(b). This is

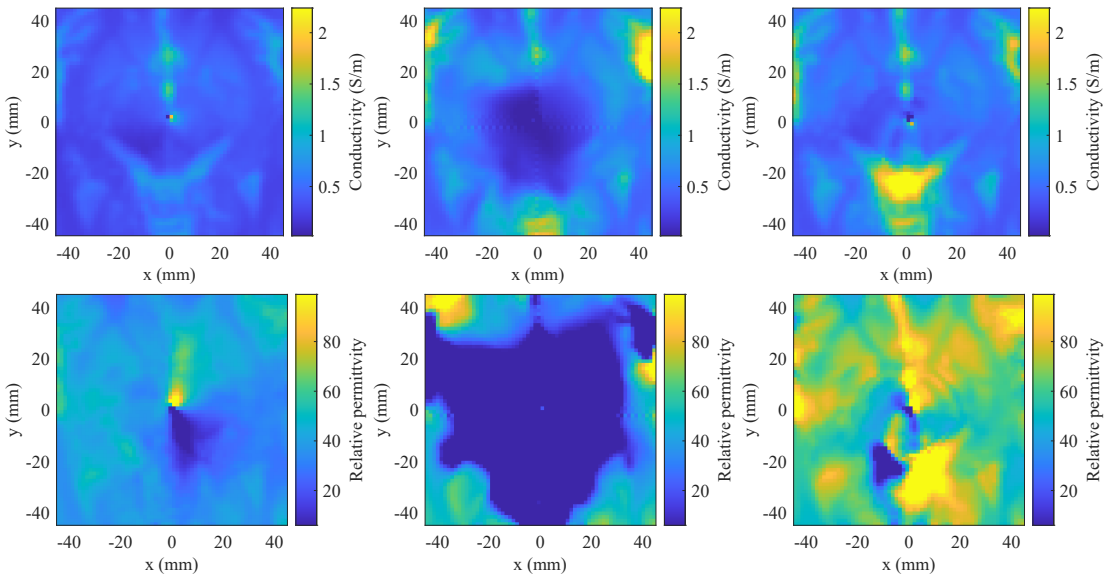

(a) No iteration (b) 5 iterations (c) Proposed method

Fig. 4.4: Reconstructed (top) conductivity and (bottom) permittivity maps at $z = -22.5$ mm for brain model. Results of (a) previous method with no iteration, (b) previous method with five iterations, and (c) proposed method.

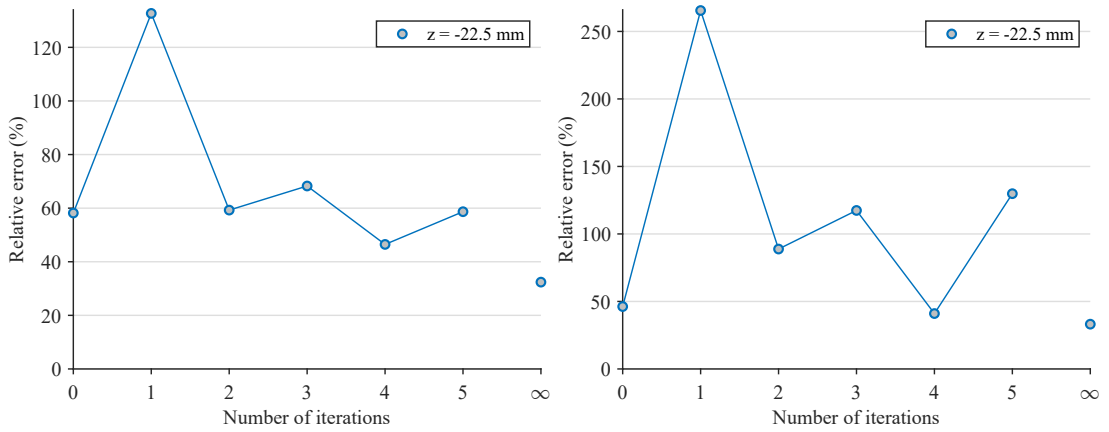

(a) Conductivity (b) Relative Permittivity

Fig. 4.5: Relative errors of (a) conductivity and (b) permittivity maps at each iteration of previous method and for proposed method (shown as ∞).

because the zero-point artifact is severe in this model and convergence is not guaranteed in this case. The proposed method correctly incorporates the effect of $\partial_z H^+$ and gives relatively stable results, as shown in Fig. 4.4(c). This is confirmed in Fig. 4.5. The relative errors of the previous method do not decrease as the number of iterations increases. The proposed method yields the lowest errors in both conductivity and relative permittivity results.

The difference between the results of the two models is explained below. For the cylindrical model, the iterative correction was successful and only a single iteration was needed to obtain converged results. This is because the zero-point artifact is not severe in the cylindrical model and thus the condition $\|K\| < 1$ may be satisfied when sufficient regularization is ap-

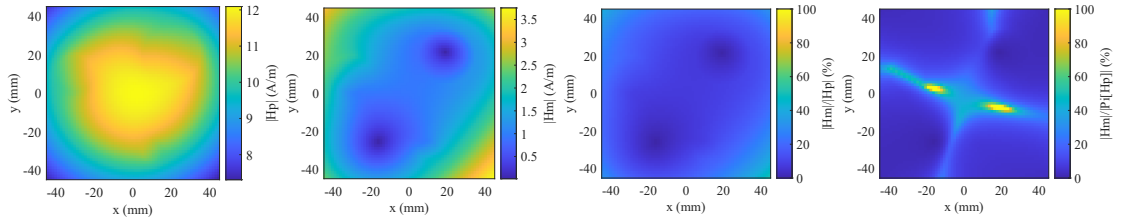

(a) $|H^+|$ (b) $|H^-|$ (c) $|H^-|/|H^+|$ (d) $|H^-|/|\Pi[H^+]|$

Fig. 4.6: Magnitude of magnetic field maps and their ratio for cylindrical phantom. (a) $|H^+|$, (b) $|H^-|$, (c) $|H^-|/|H^+|$, and (d) $|H^-|/|\Pi[H^+]|$.

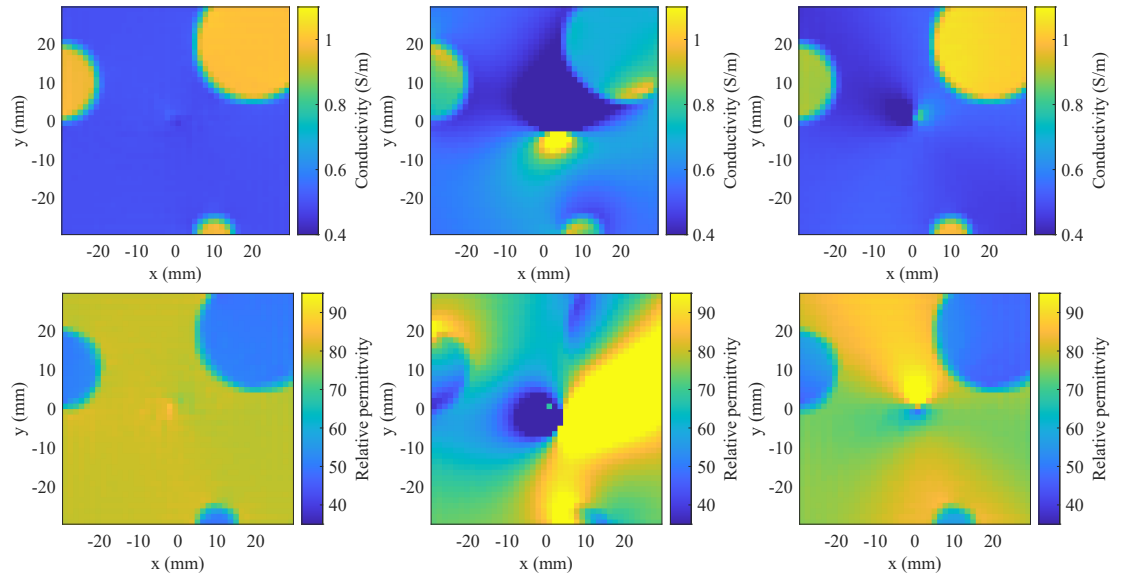

(a) Previous method with true BC (b) Previous method with background BC (c) Proposed method

Fig. 4.7: Reconstructed (top) conductivity and (bottom) permittivity results for cylindrical phantom and SNR of 40 dB. Results of (a) previous method with true BC, (b) previous method with background BC, and (c) proposed method.

plied to calculate the inverse of ∂H^+. For the human brain model, in contrast, the iteration did not converge. This is because the zero-point artifact is severe in this model and the condition $\|K\| < 1$ may not be satisfied even when the inversion of ∂H^+ is regularized.

Figure 4.6 shows the H^+ and H^- maps obtained from the FEM calculation. As shown in Fig. 4.6(c) and (d), $|H^-| \ll |H^+|$ and $|H^-| \ll |\Pi[H^+]|$ hold well. Note that the assumption $|H^-| \ll |\Pi[H^+]|$ only needs to hold on the boundary of the ROI.

Figure 4.7 shows the reconstruction results for the cylindrical phantom when Gaussian noise was added to make the SNR 40 dB. As shown in Fig. 4.7(a), the previous method with the true boundary EP values yields accurate results throughout the ROI. However, when the BC was specified as the background value of the true EPs on the boundary, which would be the most natural choice, the reconstructed images were distorted, as shown in Fig. 4.7(b). In contrast, the proposed method keeps the image quality as shown in Fig. 4.7(c). Table 4.1 shows the relative L2 error of each result. We observe that the proposed method has smaller error for both conductivity and permittivity, which means that the proposed method yielded

Table 4.1: Relative errors for cylindrical phantom.

Method	Conductivity error (%)	Permittivity error (%)
Dirichlet with true BC	3.33	2.85
Dirichlet with background BC	23.41	24.12
Complex-Derivative BC	7.52	8.65

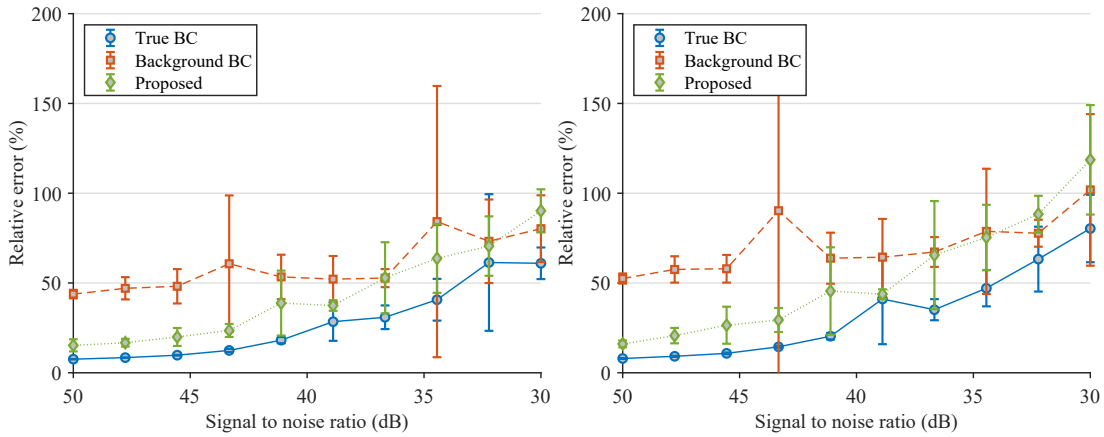

(a) Conductivity (b) Permittivity

Fig. 4.8: Reconstruction errors of (a) conductivity and (b) permittivity maps for cylindrical phantom with SNR of 20 dB–40 dB.

Table 4.2: Relative errors for cylindrical phantom.

Method	Conductivity error (%)	Permittivity error (%)
1/4 Dirichlet BC	7.21	8.01
2/4 Dirichlet BC	7.02	7.93
3/4 Dirichlet BC	5.38	5.48

better results.

We also tested the proposed method on the cylindrical phantom with different SNR between 20 dB and 40 dB. Figure 4.8 shows the relative L2 error of the conductivity and the relative permittivity. The proposed method has consistently lower errors than the previous method with the background BC. It should be emphasized that the reconstruction results of our proposed method are comparable to those of the previous method with the unpractical assumption that the true boundary values of EPs are available. In contrast to the previous method, the proposed method does not use any prior information concerning the boundary EP values, which means that the proposed method greatly enhances the applicability of EPT to practical situations.

Figure 4.9 shows the reconstruction results when the Dbar equation is solved with the mixed BC. In this case, we prescribe the Dirichlet BC to 1, 2, or 3 out of 4 sides of the rectangular boundary. The rest are given the complex-derivative BC. As shown in Fig. 4.9, the results gradually improved as more sides of the boundary were given the Dirichlet BC. Table 4.2 shows the relative error of each method. As expected from Fig. 4.9, the error reduces as more sides of the boundary are given the Dirichlet BC. Although the proposed method

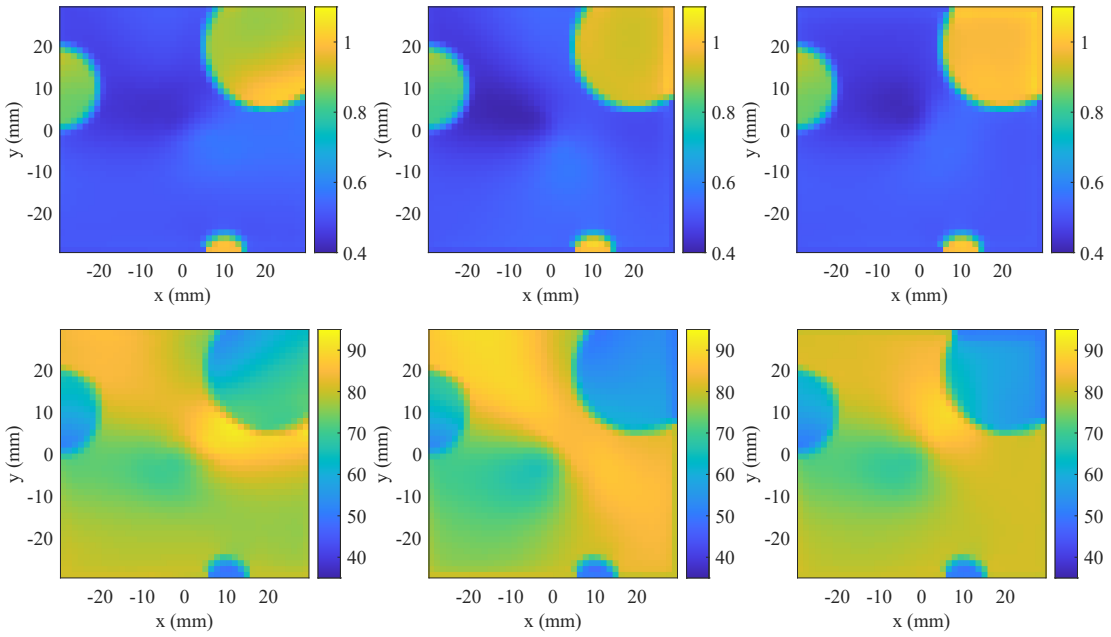

(a) 1/4 Dirichlet (b) 2/4 Dirichlet (c) 3/4 Dirichlet

Fig. 4.9: Reconstructed results of (top) conductivity and (bottom) permittivity maps for cylindrical phantom by giving mixed BC. (a) 1/4 Dirichlet and 3/4 complex-derivative BC, (b) 2/4 Dirichlet and 2/4 complex-derivative BC, and (c) 3/4 Dirichlet and 1/4 complex-derivative BC.

based on the complex-derivative BC gives fair results, combining available information about boundary EPs using the method based on the mixed BC will enhance the flexibility of the proposed method.

4.6 Phantom Experiments

Figure 4.10 shows the reconstructed conductivities of the experimental phantom. The results of the standard EPT method are also shown in Fig. 4.10(a) because standard EPT is free from 2D approximation and, with sufficient smoothing filtering, it yields accurate results except at tissue-transition regions. The conductivity values obtained using the previous method are lower than those of the standard method, whereas those of the proposed method are very close in both the inner and outer cylindrical regions. These values also match those measured using an electric probe.

Figure 4.11 shows the reconstructed conductivities of the experimental phantom. As shown in Fig. 4.11(b), large error appears in the inner regions when the boundary EP values are given as the background value. The proposed method yields a less distorted map even when no information concerning the EP values on the boundary is given.

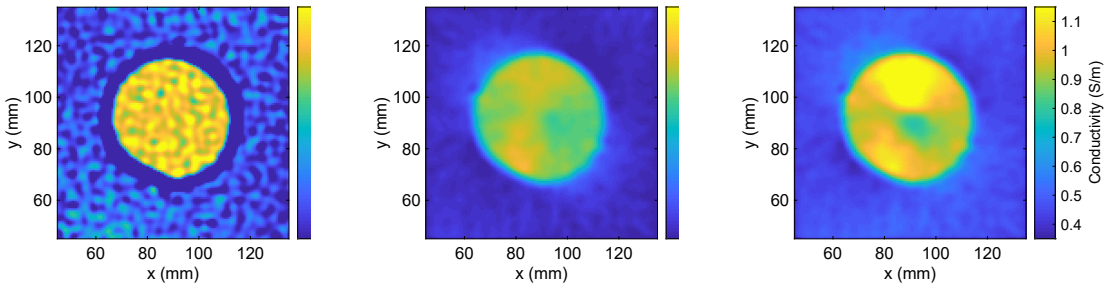

(a) Standard method (b) Previous method with no iteration (c) Proposed method

Fig. 4.10: Reconstructed (top) conductivity and (bottom) permittivity maps for phantom experiment. (a) Standard method, (b) previous method with no iteration, and (c) proposed method.

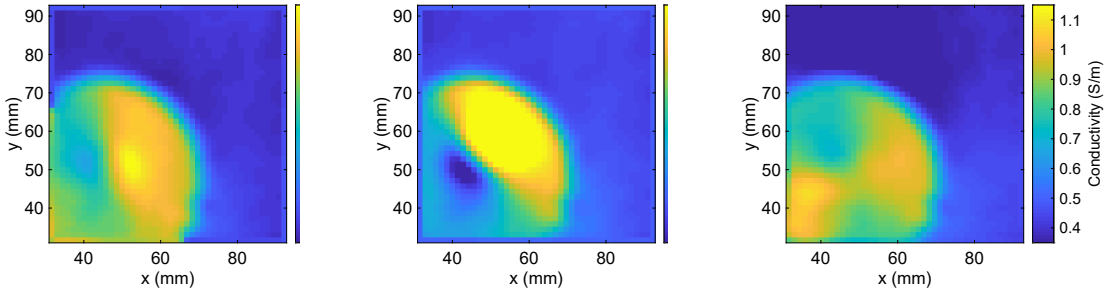

(a) Previous method wit true BC (b) Previous method wit background BC (c) Proposed method

Fig. 4.11: Reconstructed conductivity maps for phantom experiment. (a) Previous method with true BC, (b) previous method with background BC, and (c) proposed method.

4.7 Conclusion of This Chapter

In this chapter, we proposed an explicit reconstruction method for EPT that does not require prior information concerning EPs on the boundary of the ROI. The proposed method solves the Dbar equation with the novel complex-derivative BC instead of the Dirichlet BC. By assuming that $|H^+| \gg |\Pi[H^-]|$, EPs were reconstructed from only the measurable quantity, H^+ without the prior information concerning the EP values on the boundary of the ROI. We also proposed a hybrid method that requires EPs on only a part of the boundary to reduce the reconstruction error arising from the approximation of H^-. Numerical simulations and phantom experiments showed that the proposed method can reconstruct EPs without prior information concerning EPs on the boundary on the ROI.

Chapter 5

Simultaneous Conductivity and Susceptibility Mapping Using Multiecho Gradient Echo Acquisition

For studying electromagnetic tissue properties [26], QCM [69] reconstructs conductivity from transceive B1 phase data without B1 magnitude mapping, and QSM [21] retrieves the magnetic susceptibility of tissues from B0 field data typically estimated from a multiecho GRE signal. In a traditional QCM, the transceive B1 phase is obtained from spin echo (SE) acquisition, which is free from the B0 inhomogeneity effect and reflects only the B1-related phase. Several studies show that the transceiver B1 phase can also be estimated from a multiecho GRE signal by extrapolating phase evolution along echo time [27]. In this chapter, we estimate the B1 phase and B0 field distributions simultaneously from a multiecho GRE signal by applying nonlinear least squares on the complex signal equation, which can achieve the maximum likelihood estimation. This enables us to combine QCM and QSM to simultaneously map both electromagnetic properties of tissues.

5.1 Introduction of This Chapter

5.1.1 Magnetic Properties of Biological Tissues

The susceptibility of most biological tissues is in a range of about $\pm 20\%$ of that of water [25]. The dominant determinants of tissue magnetic susceptibility are iron and calcium due to their higher abundance.

Iron can be both the donor and acceptor of an electron by converting between ferrous and ferric forms; as such, iron compounds play key roles in physiological processes. Iron in tissues exists as storage iron such as ferritin and hemosiderin, or is bound to heme proteins in hemoglobin. More than 60% of iron in the human body is in the ferrous form bound to the hemoglobin in red blood cells (RBCs) and is involved in oxygen binding and transportation. Oxyhemoglobin is weakly diamagnetic, whereas ferrous iron in deoxyhemoglobin is strongly paramagnetic [141]. Following the onset of a hemorrhage, some RBCs may be endocytosed by microglia or macrophages. Most RBCs undergo cell lysis and hemoglobin degradation from deoxyhemoglobin into methemoglobin and hemosiderin.

Beyond iron in RBCs, there is also a tiny labile iron pool. Labile iron actively participates in energy metabolism, mitochondrial respiration, lipid and DNA syntheses, and many other

important functions [142]. Although labile iron is contained in various shielding metalloproteins, it still exhibits the redox property, being harmful to nucleic acids, proteins, and lipid membranes [142]. Therefore, iron uptake, transport, and storage are highly regulated to maintain homeostasis and iron overload can cause extensive tissue damage. Most of the iron is stored as ferritin and is readily available for conversion into the labile iron pool. In pathological conditions, the amount of iron can exceed the storage capability of cellular ferritin. The excessive iron may be stored in ferric form in other proteins such as neuromelanin, hemosiderin, and hemosiderin [143, 144]. Ferric iron also accumulates as magnetite in the characteristic amyloid plaque in Alzheimer's disease [5].

Calcium in tissues has substantially lower magnetic susceptibility than water. Compared to iron, calcium is much more abundant in the human body with a small fraction in the labile calcium pool and the vast majority stored in bones. Sufficient labile calcium ions are needed for important cellular functions including signal transduction, muscle contraction, and cell membrane potential. On the other hand, excess labile calcium can cause cellular damage such as neurodegeneration and apoptosis. The concentration of labile calcium is in equilibrium with bone calcium through release and reabsorption processes that are strictly regulated by homeostasis. Calcium homeostasis also controls calcium absorption and secretion in the intestines and calcium filtration and reabsorption in the kidneys.

Disruption in calcium homeostasis can result in several pathologic conditions including osteoporosis resulting from decreased bone mass and strength, calcification in atherosclerotic plaques, and calcification in tumors. Osteoporosis is a highly prevalent disorder among the older population, causing fractures [7] and impaired mobility. Although hemorrhages from leaky blood vessels or angiogenesis are specifically found in high-grade tumors, calcification can be found in various low-grade tumors. However, the mechanisms of tumor calcification have yet to be fully investigated [145, 146].

5.1.2 Conventional Reconstruction Methods

According to Choi *et al.* [147], we first review the derivation of the QSM forward equation given as a convolution [148].

If we use $1 \pm \chi(\boldsymbol{r}) \simeq 1$ as an approximation, the perturbed magnetic field is expressed as follows:

$$\nabla \cdot \boldsymbol{B}^{\mathrm{m}}(\boldsymbol{r}) = -\frac{2}{3}\nabla\chi(\boldsymbol{r}) \cdot \boldsymbol{B}^{\mathrm{e}}, \tag{5.1}$$

$$\nabla \times \boldsymbol{B}^{\mathrm{m}}(\boldsymbol{r}) = \frac{1}{3}\nabla\chi(\boldsymbol{r}) \times \boldsymbol{B}^{\mathrm{e}}, \tag{5.2}$$

where $\boldsymbol{B}^{\mathrm{e}}$ is the constant magnetic field generated by the MRI scanner and $\boldsymbol{B}^{\mathrm{m}}$ is the perturbation caused by tissues. Taking the gradient of Eq. (5.1) and the curl of Eq. (5.2) and summing them gives

$$\Delta\boldsymbol{B}^{\mathrm{m}}(\boldsymbol{r}) = \frac{1}{3}\Delta\chi(\boldsymbol{r})\boldsymbol{B}^{\mathrm{e}} - \nabla\nabla\chi(\boldsymbol{r}) \cdot \boldsymbol{B}^{\mathrm{e}}, \tag{5.3}$$

which directly relates the magnetic field perturbation and the susceptibility. Taking the z-component of Eq. (5.3) and substituting $\boldsymbol{B}^{\mathrm{e}} = (B_z^{\mathrm{e}}, 0, 0)$ gives

$$\Delta b_z = \left(\frac{1}{3}\Delta - \partial_z^2\right)\chi, \tag{5.4}$$

where $b_z \coloneqq B_z^{\mathrm{m}}/B_z^{\mathrm{e}}$ is the normalized magnetic field. This is the Poisson equation for B_z^{m} and its solution can be represented as follows:

$$b_z(\boldsymbol{r}) = \int_{\mathbb{R}^3} \frac{1}{4\pi|\boldsymbol{r} - \boldsymbol{r}'|}\left(-\frac{1}{3}\Delta' + \partial_{z'}^2\right)\chi \mathrm{d}V'. \tag{5.5}$$

By integrating by parts, it holds that

$$b_z(\boldsymbol{r}) = \int_{\mathbb{R}^3} \left(\frac{3(z-z')^2}{4\pi|\boldsymbol{r}-\boldsymbol{r}'|^5} - \frac{1}{4\pi|\boldsymbol{r}-\boldsymbol{r}'|^3} \right) \chi \mathrm{d}V'. \tag{5.6}$$

The integral kernel

$$d(\boldsymbol{r}) = \frac{3(z-z')^2}{4\pi|\boldsymbol{r}-\boldsymbol{r}'|^5} - \frac{1}{4\pi|\boldsymbol{r}-\boldsymbol{r}'|^3} \tag{5.7}$$

is called the dipole kernel [21] and its frequency spectrum is represented as follows:

$$\mathcal{F}[d](\boldsymbol{k}) = \frac{1}{3} - \frac{w^2}{|\boldsymbol{k}|^2}, \tag{5.8}$$

where $\boldsymbol{k} = (u, v, w)$.

The total B0 field can be divided into two contributions: the local and background fields. The local field is generated by the tissues of interest, while the background field is generated by the sources outside the ROI. This background field must first be removed. This is called background field removal and several methods have been proposed to accomplish this [149]. Then Eq. (5.6) is deconvolved to yield the susceptibility map.

A primitive approach is to perform the deconvolution in k-space as follows:

$$\chi = \mathcal{F}^{-1}\left[\frac{\mathcal{F}[b_z]}{\mathcal{F}[d]} \right]. \tag{5.9}$$

However, this method produces a streaking artifact due to the zero cone of the dipole kernel given as $u^2 + v^2 - 2w^2 = 0$. Therefore, regularization must be adopted to obtain feasible reconstruction results. Shmueli *et al.* [150] proposed the truncated k-space division (TKD) method in which the dipole kernel is truncated to avoid the division of small values as follows:

$$\chi = \mathcal{F}^{-1}\left[\frac{\operatorname{sign} \mathcal{F}[d]}{\max(\mathcal{F}[d], \lambda)} \mathcal{F}[b_z] \right], \tag{5.10}$$

where λ is a threshold that determines the trade-off between the streaking artifact and the distortion in the resultant image. Similar methods using truncated singular value decomposition (SVD) and Tikhonov regularization have also been proposed [151, 152].

A more sophisticated approach is to utilize anatomical information available from MRI images [153–155]. The rationale is that the edges in the desired susceptibility map are likely to be collocated with edges in known anatomical images since they reflect the same anatomy. The morphology enabled dipole inversion (MEDI) method [154–156] is formulated as

$$\chi = \arg\min_{\chi} \|W(b_z - d * \chi)\|_2^2 + \lambda \|M \nabla \chi\|_1, \tag{5.11}$$

where W is a weight that reflects the variance of errors in b_z data and M is the binary mask defined using the anatomical MR image I as

$$M(\boldsymbol{r}) = \begin{cases} 1 & |\nabla I(\boldsymbol{r})| < \text{threshold}, \\ 0 & \text{otherwise}. \end{cases} \tag{5.12}$$

MEDI has produced promising results in *in vivo* experiments [157] and has been applied to various anatomical regions such as the brain [158], bone [159, 160], liver [161], and cardiac MRI [162], and various diseases such as Alzheimer's disease [163], and multiple sclerosis [164, 165].

5.2 B0 and B1 Field Estimation from multiecho GRE Data Using Nonlinear Regression

The governing equation of the multiecho GRE signal can be modeled as follows:

$$d(t) = s(t) + n(t) = \rho \exp(-R_2^* t) \exp(\mathrm{i}\varphi) \exp(-\mathrm{i}\gamma \Delta B_0 t) + n(t), \qquad t = t_1, t_2, \dots, t_N, \quad (5.13)$$

where ρ is the proton density, φ is the B1 transceive phase, $R_2^* = 1/T_2^*$ is the apparent T2 relaxation ratio, and ΔB_0 is the B0 field variation. QCM is a technique that reconstructs a conductivity map from the information of φ and QSM is a technique that reconstructs a susceptibility map from the information of ΔB_0. Here, we consider the full complex signal of GRE, while only the phase of the GRE signal was considered in the conventional method. Unlike the phase signal, both real and imaginary parts of the noise $n(t)$ can be regarded as Gaussian.

For simplicity, we denote the multiecho GRE signal at $t = t_j$ as

$$d_j = c \exp(s t_j), \quad (5.14)$$

where $c = \rho \exp(\mathrm{i}\phi)$ and $s = -(R_2^* + \mathrm{i}\gamma \Delta B_0)$.

5.2.1 Initial Estimation Based on the AR Model

An initial guess of the nonlinear iteration can be given by, for example, the AR model-based approach proposed in [166, 167]. In multiecho GRE acquisition for QSM, the initial echo time is minimized as much as possible, and subsequent measurement intervals are often kept constant. In such cases, the j-th echo time t_j is represented as $t_j = t_I + (j-1)\Delta t$, and thus the signal is written as

$$d_j = c \exp(s t_I) \exp((j-1)\Delta t) + n_j, \quad j = 1, 2, \dots, N. \quad (5.15)$$

By defining $\tilde{c}_1 \coloneqq c \exp(s t_I)$ and $z_1 \coloneqq \exp(s \Delta t)$, it follows that

$$d_j = \tilde{c}_1 z_1^{j-1} + n_j, \quad j = 1, 2, \dots, N. \quad (5.16)$$

Then z_1 and $\tilde{c}_1$ can be estimated as parameters of the first-order auto regression model (a_1, b_0), where

$$\frac{\tilde{c}_1}{1 - z_1 z^{-1}} = \frac{b_0}{1 + a_1 z^{-1}}, \quad (5.17)$$

i.e., $z_1 = -a_1, \tilde{c}_1 = b_0$. The AR parameters can be estimated by the Prony method [167].

Once the estimates $\hat{c}, \hat{s}$ are obtained, ϕ and ΔB_0 are calculated as

$$\varphi = \angle \hat{c}_1, \quad (5.18)$$

$$\Delta B_0 = -\operatorname{Im}[\hat{s}]/\gamma. \quad (5.19)$$

5.2.2 Optional Estimation Based on Nonlinear Regression

Using the initial guess given in the previous section, the B1 phase ϕ and the B0 field B_0^{m} were estimated according to a Gaussian noise model in complex multiecho GRE data by nonlinear regression of the following function:

$$\hat{c}, \hat{s} = \arg\min_{c,s} \sum_{j=1}^{N} |d_j - c \exp(s t_j)|^2 = \arg\min_{c,s} \|\mathbf{d} - \mathbf{f}(c, s)\|_2^2 \quad (5.20)$$

The minimization is performed using the Levenberg–Marquardt method [168, 169]. The update formula is written as follows:

$$\begin{pmatrix} c^{(i+1)} \\ s^{(i+1)} \end{pmatrix} = \begin{pmatrix} c^{(i)} \\ s^{(i)} \end{pmatrix} + \begin{pmatrix} \Delta c \\ \Delta s \end{pmatrix}, \quad \text{where } (\mathbf{J}^*\mathbf{J} + \lambda \operatorname{diag}(\mathbf{J}^*\mathbf{J})) \begin{pmatrix} \Delta c \\ \Delta s \end{pmatrix} = \mathbf{J}^*(\mathbf{d} - \mathbf{f}(c^{(i)}, s^{(i)})), \tag{5.21}$$

where $\mathbf{J}$ is the Jacobian of the function and is explicitly given as

$$\mathbf{J} = \begin{pmatrix} \exp(st_1) & ct_1 \exp(st_1) \\ \exp(st_2) & ct_2 \exp(st_2) \\ \vdots & \vdots \\ \exp(st_N) & ct_N \exp(st_N) \end{pmatrix} \tag{5.22}$$

Hence, the update formula can be explicitly written as

$$\begin{pmatrix} (1+\lambda)\sum t_j^2 |c|^2 \exp(2\,\mathrm{Re}[s]t_j) & \sum t_j \bar{c} \exp(2\,\mathrm{Re}[s]t_j) \\ \sum t_j c \exp(2\,\mathrm{Re}[s]t_j) & (1+\lambda)\sum \exp(2\,\mathrm{Re}[s]t_j) \end{pmatrix} \begin{pmatrix} \Delta s \\ \Delta c \end{pmatrix} = \begin{pmatrix} \sum \exp(\bar{s}t_j)(d_j - c\exp(st_j)) \\ \sum \bar{c}t_j \exp(\bar{s}t_j)(d_j - c\exp(st_j)) \end{pmatrix} \tag{5.23}$$

Because the estimation is conducted in a voxelwise manner, the estimated B0 field and B1 phase must first be spatially unwrapped. We used the FFT-based fast unwrapping method [170, 171] typically used in the QSM literature.

5.3 Morphology Enabled Conductivity and Susceptibility Reconstruction

Once the unwrapped B1 phase image ϕ was obtained, its Laplacian was calculated using the Savitzky–Golay filter, which is based on second-order weighted polynomial fitting in each local region around the voxel of interest. The kernel size was $15 \times 15 \times 5$ voxels and the weighting factor was determined from magnitude image I as follows: $w(\boldsymbol{r}) = G(|I(\boldsymbol{r}) - I(\boldsymbol{r}_0)|)$, where G represents Gaussian function. Finally, conductivity σ was reconstructed by our proposed IE-based QCM method presented in Chapter 2. For the boundary EP values required in Eq. (2.103), we use the result of the standard QCM method with the morphology-based regularization given as

$$\hat{\sigma} = \arg\min_{\sigma} \|\sigma - \Delta\phi/(2\omega_0\mu_0)\|_2^2 + \lambda \|M\nabla\sigma\|_1, \tag{5.24}$$

where M represents the mask that removes boundaries of different anatomical regions and is used in the MEDI method [172] in QSM. Then, Eq. (2.103) was solved using the CG method and from the temporal estimate of ρ^* the dual field $\boldsymbol{\psi}^* = \rho^*\nabla\phi$ was calculated and the morphology-based regularization was again applied to give the final result of QCM.

QSM was also reconstructed using nonlinear MEDI [172] with automatic uniform cerebrospinal fluid zero reference (MEDI+0) [111]. This electromagnetic tissue property estimation from a multiecho GRE complex signal is referred to as QCM+QSM hereafter.

5.4 In-vivo Experiments

5.4.1 Setup and Conditions

MRI acquisitions were performed on 5 healthy human subjects and brain data were obtained using 2D FSE and 3D multiecho GRE in a 3 T clinical scanner (MR750, GE Healthcare,

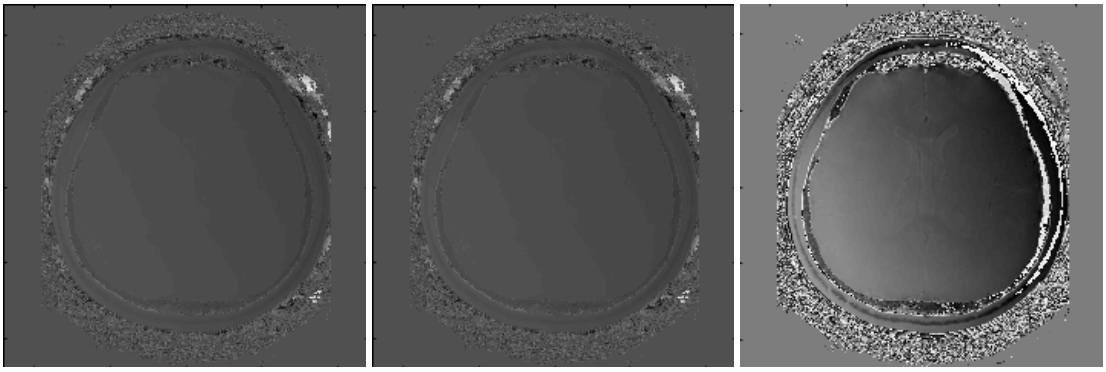

Fig. 5.1: Transceive B1 phase maps estimated from multiecho GRE data by (left) linear extrapolation method, (center) proposed nonlinear least-squares method, and (right) transceive B1 phase map directly measured by FSE acquisition.

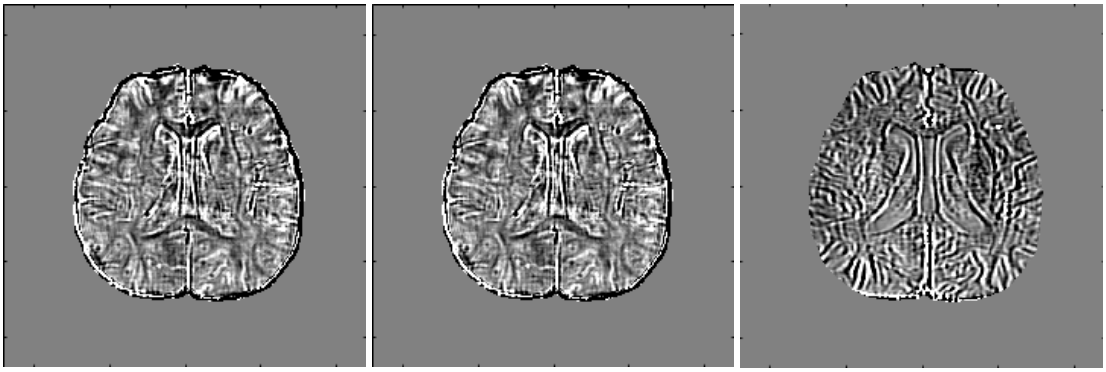

Fig. 5.2: Laplacian of transceive B1 phase maps estimated from multiecho GRE data by (left) linear extrapolation method, (center) proposed nonlinear least-squares method, and (right) transceive B1 phase map directly measured by FSE acquisition.

Waukesha, WI). A 32-channel head receiver coil was used. The imaging parameters for multiecho GRE were as follows: TR: 53.2 ms, first TE: 4.4 ms, echo spacing: 4.9 ms, flip angle: 15 deg; and for FSE: TR: 5350 ms, eff. TE: 87.9 ms, echo train length: 24, flip angle: 111 deg, NEX: 2. FOV was 240 mm $\times$ 240 mm $\times$ 144 mm and voxel size was 0.4688 mm $\times$ 0.4688 mm $\times$ 3 mm for both sequences. We then tested the proposed QCM+QSM method using these multiecho GRE data.

5.4.2 Results and Discussion

Figures 5.1 and 5.2 show the estimated transceiver B1 phase of one representative subject and its Laplacian. The estimated B1 phase maps were similar in both the linear extrapolation method (left) and the proposed nonlinear least-squares method (center). Although the B1 phase is less smooth compared with the SE phase in both linear and nonlinear methods, the proposed method yielded relatively stable results compared with the linear extrapolation method. This is because the proposed method correctly accounted for the noise distribution and achieves maximum likelihood estimation. Figure 5.3 shows the conductivity maps reconstructed from the B1 phase estimated by the nonlinear least-squares method. We varied the regularization parameter and chose the value that maximizes the curvature of the L-curve plot as shown in Fig. 5.4. When no regularization is adopted (middle), the conductivity map is very noisy. When the anatomical image is utilized as a regularizer (top), the conductivity

results are less noisy and anatomical structures are discernible. Simultaneously, we obtained B0 field map by solving Eq. 5.2 and reconstructed QSM (Fig. 5.5). This means that electromagnetic tissue properties can be successfully obtained from a single multiecho GRE acquisition. Figure 5.6 shows the reconstructed conductivity and susceptibility maps along with T1w (3rd row) and T2w (4th row) images for data spanning five tumor patients. Lesion structures are consistent between the conductivity and susceptibility maps, but the conductivity maps have higher values in all cases. Therefore, conductivity maps can give additional pathological information.

5.5 Conclusion of This Chapter

We describe a simultaneous quantitative conductivity and susceptibility mapping (QCM+QSM) method by estimating B1 phase and B0 field distributions from multiecho gradient echo signal. B1 phase and B0 filed maps are simultaneously estimated by applying a nonlinear least-squares method on the complex signal equation of the multiecho GRE signal. Then, conductivity and susceptibility are reconstructed by incorporating anatomical information as a regularizer. QCM+QSM is feasible and promising for studying electromagnetic tissue properties in healthy brains and in brains with tumors using a single multiecho GRE acquisition.

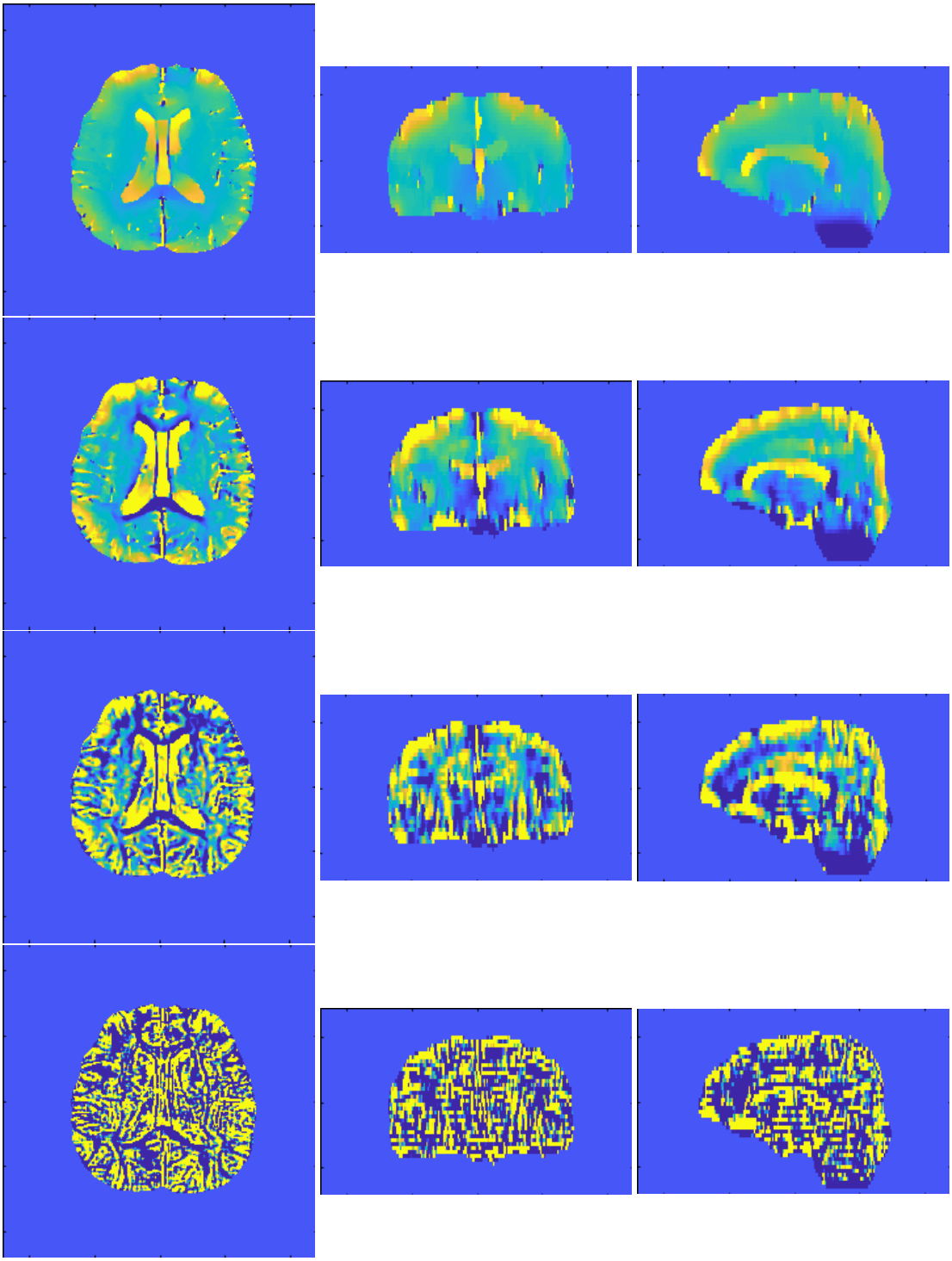

Fig. 5.3: Conductivity maps reconstructed by proposed method with three different values of morphology-based regularization parameter (1st, 2nd, and 3rd rows) and without (bottom) morphology-based regularization.

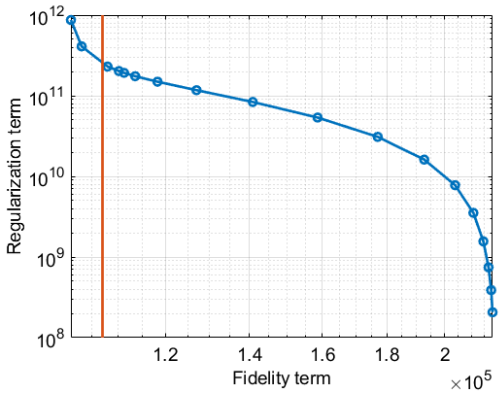

Fig. 5.4: L-curve plot to determine optimal regularization parameter in conductivity reconstruction.

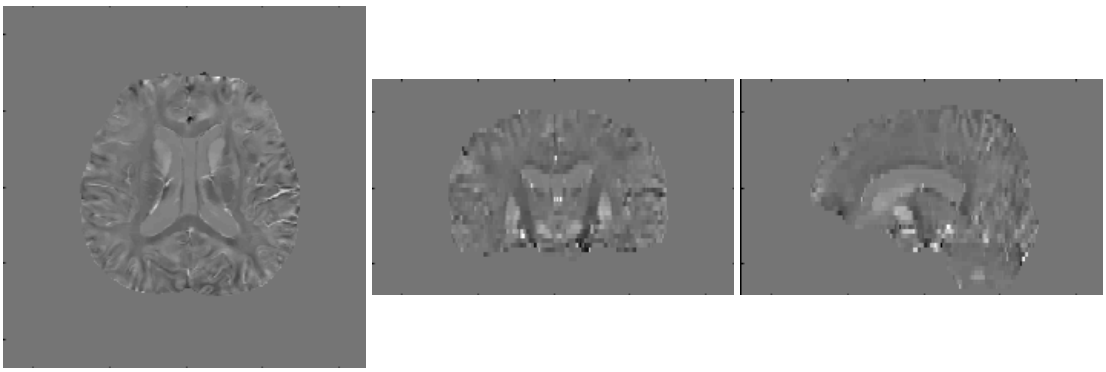

Fig. 5.5: Susceptibility map reconstructed from B0 field map simultaneously estimated from multiecho GRE data.

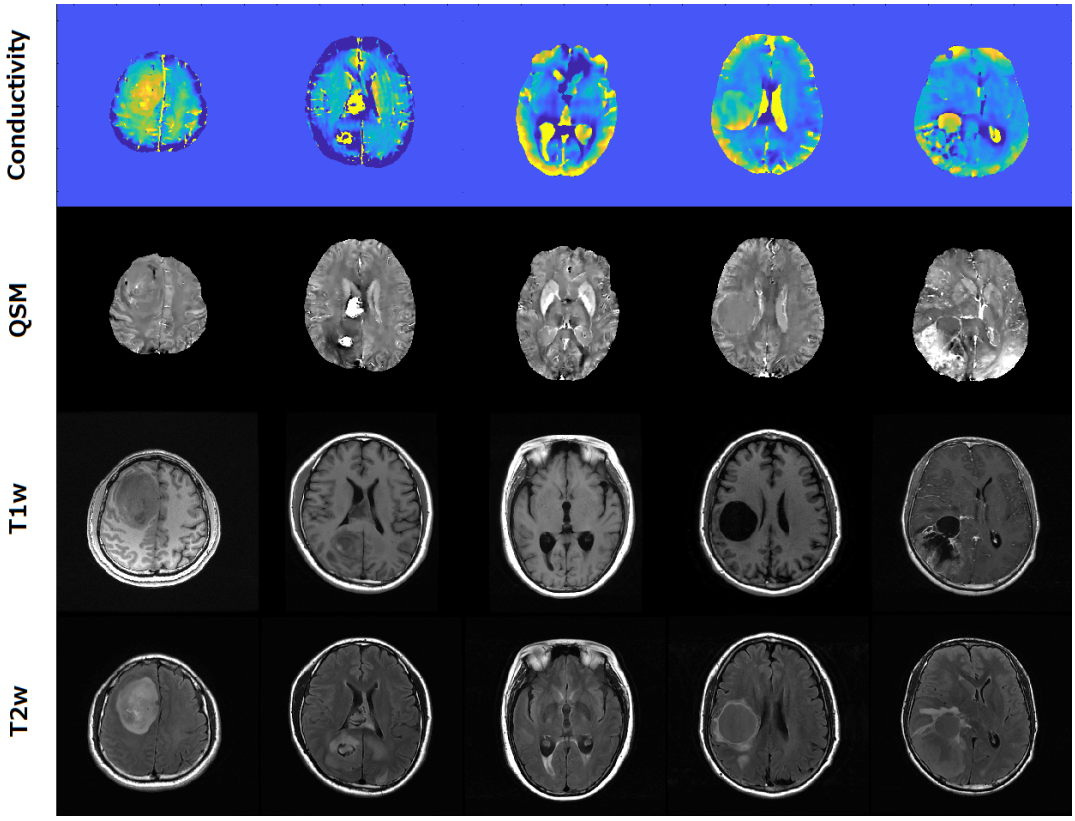

Fig. 5.6: Conductivity (top) and susceptibility (2nd row) results for 5 tumor patients. T1w (3rd row) and T2w (bottom) images are included for reference. Lesion structures are consistent between the conductivity and susceptibility maps, but the conductivity maps have higher values in all cases.

Chapter 6

Conclusion

This thesis explored EPT, QCM, MRE, and QSM, which are noninvasive modalities to reconstruct electrical, mechanical, and magnetic properties of biological tissues using MRI. The material properties of biological tissues reflect physiological and pathological conditions. Therefore, an early diagnosis of a lesion is expected by detecting changes in these material properties. EPT, QCM, and MRE were originally studied independently but they have some similarities in their governing equations and measurement methods. First, this thesis showed that EPT, QCM, and MRE can be formulated in a common framework of the impedance estimation inverse problem. Then, a global and direct method was proposed that can reconstruct 3D material properties; this has not been achieved using conventional methods. Second, we improved the conductivity reconstruction in the framework of the simultaneous reconstruction of electromagnetic properties, i.e., QCM and QSM, by applying our proposed QCM reconstruction method. Its effectiveness was then shown in vivo.

In Chapter 2, a new formulation of the EPT problem was described, which considers the impedance estimation problem. Then, a method was put forward to reconstruct the electrical properties by solving the IEs derived from Helmholtz's decomposition of the vector field. The proposed method achieved accurate reconstruction at different tissue boundaries and was robust against noise. Its effectiveness was confirmed by numerical simulations and verified by phantom experiments.

In Chapter 3, we discussed how the MRE problem can be described in a common framework with the EPT problem. However, in the case of MRE, since the system is described by a tensor field, the expression of the tensor field is derived based on Helmholtz's decomposition of the tensor field, and the IE for the mechanical properties was derived. Numerical simulations showed that the proposed method can reconstruct the general 3D distribution without making the assumptions about compressibility that characterize many of the previous methods.

In Chapter 4, we proposed a boundary-value-free reconstruction method for EPT that does not require EPs on the boundary of the ROI. This was accomplished by modifying our previous method that reconstructs EPs in a slicewise manner. In addition, a hybrid reconstruction formula was derived that uses the values of the EPs only on a fraction of the boundary of the ROI to reduce the artifact when EP values are available on a fraction of the boundary. In future research we intend to extend this method to Helmholtz's decomposition-based reconstruction method proposed in Chapter 2.

In Chapter 5, conductivity and susceptibility reconstruction were performed simultaneously from a single image acquisition. A method for maximum likelihood estimation of the phase of the B1 field and the B0 field required for each reconstruction was proposed by considering the nonlinearity of the MRI signal equation; this has not been taken into account by the conventional methods. In addition, we applied the proposed QCM method presented in Chapter 2 with regularization based on morphological information used in the susceptibil-

ity reconstruction to stabilize the B1 field to conductivity inversion. While conductivity and susceptibility images have a consistent structure, they gave different contrasts as shown in the analysis of in vivo data. Therefore, further information may be provided by performing conductivity reconstruction in addition to susceptibility reconstruction.

List of References

[1] K. R. Thulborn, T. S. Gindin, D. Davis, and P. Erb, "Comprehensive MR Imaging Protocol for Stroke Management: Tissue Sodium Concentration as a Measure of Tissue Viability in Nonhuman Primate Studies and in Clinical Studies," *Radiology*, vol. 213, no. 1, pp. 156–166, 1999, DOI: 10.1148/radiology.213.1.r99se15156.

[2] M. S. Hussain, R. W. Stobbe, Y. A. Bhagat, D. Emery, K. S. Butcher, D. Manawadu, N. Rizvi, P. Maheshwari, J. Scozzafava, A. Shuaib, and C. Beaulieu, "Sodium imaging intensity increases with time after human ischemic stroke," *Ann. Neurol.*, vol. 66, no. 1, pp. 55–62, 2009, DOI: 10.1002/ana.21648.

[3] M. J. Paszek, N. Zahir, K. R. Johnson, J. N. Lakins, G. I. Rozenberg, A. Gefen, C. A. Reinhart-King, S. S. Margulies, M. Dembo, D. Boettiger, V. M. Weaver, and D. A. Hammer, "Tensional homeostasis and the malignant phenotype," *Cancer Cell*, vol. 8, no. 3, pp. 241–254, 2005, DOI: 10.1016/j.ccr.2005.08.010.

[4] W.-C. Yeh, P.-C. Li, Y.-M. Jeng, H.-C. Hsu, P.-L. Kuo, M.-L. Li, P.-M. Yang, and P. H. Lee, "Elastic modulus measurements of human liver and correlation with pathology," *Ultrasound Med. Biol.*, vol. 28, no. 4, pp. 467–474, 2002, DOI: 10.1016/S0301-5629(02)00489-1.

[5] G. Plascencia-Villa, A. Ponce, J. F. Collingwood, M. J. Arellano-Jiménez, X. Zhu, J. T. Rogers, I. Betancourt, M. José-Yacamán, and G. Perry, "High-resolution analytical imaging and electron holography of magnetite particles in amyloid cores of Alzheimer's disease," *Sci. Rep. UK*, vol. 6, no. 1, p. 24873, 2016, DOI: 10.1038/srep24873.

[6] T. A. Rouault, "Iron metabolism in the CNS: implications for neurodegenerative diseases," *Nat. Rev. Neurosci.*, vol. 14, no. 8, pp. 551–564, 2013, DOI: 10.1038/nrn3453.

[7] L. G. Raisz, "Pathogenesis of osteoporosis: concepts, conflicts, and prospects," *J. Clin. Invest.*, vol. 115, no. 12, pp. 3318–3325, 2005, DOI: 10.1172/JCI27071.

[8] K. K. Tha, U. Katscher, S. Yamaguchi, C. Stehning, S. Terasaka, N. Fujima, K. Kudo, K. Kazumata, T. Yamamoto, M. V. Cauteren, and H. Shirato, "Noninvasive electrical conductivity measurement by MRI: a test of its validity and the electrical conductivity characteristics of glioma," *Eur. Radiol.*, vol. 28, no. 1, pp. 348–355, 2018, DOI: 10.1007/s00330-017-4942-5.

[9] Y. Zou and Z. Guo, "A review of electrical impedance techniques for breast cancer detection," *Med. Eng. Phys.*, vol. 25, no. 2, pp. 79–90, 2003, DOI: 10.1016/S1350-4533(02)00194-7.

[10] J. F. Greenleaf, M. Fatemi, and M. Insana, "Selected Methods for Imaging Elastic Properties of Biological Tissues," *Annu. Rev. Biomed. Eng.*, vol. 5, no. 1, pp. 57–78, 2003, DOI: 10.1146/annurev.bioeng.5.040202.121623.

[11] T. A. Krouskop, D. R. Dougherty, and F. S. Vinson, "A pulsed Doppler ultrasonic system for making noninvasive measurements of the mechanical properties of soft tissue," *J. Rehabil. Res. Dev.*, vol. 24, no. 2, pp. 1–8, 1987.

[12] N. G. Sepúlveda, I. M. Thomas, and J. P. Wikswo, "Magnetic susceptibility tomography for three-dimensional imaging of diamagnetic and paramagnetic objects," *IEEE Trans. Magn.*, vol. 30, no. 6, pp. 5062–5069, 1994, DOI: 10.1109/20.334296.

[13] J. K. Seo, J.-R. Yoon, E. J. Woo, and O. Kwon, "Reconstruction of conductivity and current density images using only one component of magnetic field measurements," *IEEE Trans. Biomed. Eng.*, vol. 50, no. 9, pp. 1121–1124, 2003, DOI: 10.1109/TBME.2003.816080.

[14] E. J. Woo and J. K. Seo, "Magnetic resonance electrical impedance tomography (MREIT) for high-resolution conductivity imaging," *Physiological Measurement*, vol. 29, no. 10, pp. 1–26, 2008, DOI: 10.1088/0967-3334/29/10/r01.

[15] U. Katscher and C. A. T. van den Berg, "Electric properties tomography: Biochemical, physical and technical background, evaluation and clinical applications," *NMR Biomed.*, vol. 30, no. 8, pp. 1–15, 2017, DOI: 10.1002/nbm.3729.

[16] J. Liu, Y. Wang, U. Katscher, and B. He, "Electrical Properties Tomography Based on B_1 Maps in MRI: Principles, Applications, and Challenges," *IEEE Trans. Biomed. Eng.*, vol. 64, no. 11, pp. 2515–2530, 2017, DOI: 10.1109/TBME.2017.2725140.

[17] I. Hancu, J. Liu, Y. Hua, and S.-K. Lee, "Electrical properties tomography: Available contrast and reconstruction capabilities," *Magn. Reson. Med.*, vol. 81, no. 2, pp. 803–810, 2019, DOI: 10.1002/mrm.27453.

[18] M. M. Doyley, "Model-based elastography: a survey of approaches to the inverse elasticity problem," *Phys. Med. Biol.*, vol. 57, no. 3, R35–R73, 2012, DOI: 10.1088/0031-9155/57/3/r35.

[19] H. Dong, R. D. White, and A. Kolipaka, "Advances and Future Direction of Magnetic Resonance Elastography," *Topics in Magn. Reson. Imaging*, vol. 27, no. 5, pp. 363–384, 2018, DOI: 10.1097/RMR.0000000000000179.

[20] D. Fovargue, D. Nordsletten, and R. Sinkus, "Stiffness reconstruction methods for MR elastography," *NMR Biomed.*, vol. 31, no. 10, e3935, 2018, DOI: 10.1002/nbm.3935.

[21] Y. Wang and T. Liu, "Quantitative susceptibility mapping (QSM): Decoding MRI data for a tissue magnetic biomarker," *Magn. Reson. Med.*, vol. 73, no. 1, pp. 82–101, 2015, DOI: 10.1002/mrm.25358.

[22] E. M. Haacke, S. Liu, S. Buch, W. Zheng, D. Wu, and Y. Ye, "Quantitative susceptibility mapping: current status and future directions," *Magn. Reson. Imaging*, vol. 33, no. 1, pp. 1–25, 2015, DOI: 10.1016/j.mri.2014.09.004.

[23] A. Deistung, F. Schweser, and J. R. Reichenbach, "Overview of quantitative susceptibility mapping," *NMR Biomed.*, vol. 30, no. 4, e3569, 2017, DOI: 10.1002/nbm.3569.

[24] Y. Kee, K. Deh, A. Dimov, P. Spincemaille, and Y. Wang, "Primal-dual and forward gradient implementation for quantitative susceptibility mapping," *Magn. Reson. Med.*, vol. 78, no. 6, pp. 2416–2427, 2017, DOI: 10.1002/mrm.26627.

[25] J. F. Schenck, "The role of magnetic susceptibility in magnetic resonance imaging: MRI magnetic compatibility of the first and second kinds," *Med. Phys.*, vol. 23, no. 6, pp. 815–850, 1996, DOI: 10.1118/1.597854.

[26] T. Voigt, U. Katscher, and O. Dössel, "Quantitative Conductivity and Permittivity Imaging of the Human Brain Using Electric Properties Tomography," *Magn. Reson. Med.*, vol. 66, no. 2, pp. 456–466, 2011, DOI: 10.1002/mrm.22832.

[27] D.-H. Kim, N. Choi, S.-M. Gho, J. Shin, and C. Liu, "Simultaneous imaging of in vivo conductivity and susceptibility," *Magn. Reson. Med.*, vol. 71, no. 3, pp. 1144–1150, 2014, DOI: 10.1002/mrm.24759.

[28] R. Muthupillai, D. J. Lomas, P. J. Rossman, J. F. Greenleaf, A. Manduca, and R. L. Ehman, "Magnetic resonance elastography by direct visualization of propagating acoustic strain waves," *Science*, vol. 269, no. 5232, pp. 1854–1857, 1995, DOI: 10.1126/science.7569924.

[29] R. Muthupillai, P. J. Rossman, D. J. Lomas, J. F. Greenleaf, S. J. Riederer, and R. L. Ehman, "Magnetic resonance imaging of transverse acoustic strain waves," *Magn. Reson. Med.*, vol. 36, no. 2, pp. 266–274, 1996, DOI: 10.1002/mrm.1910360214.

[30] Y. Song and J. K. Seo, "Conductivity and Permittivity Image Reconstruction at the Larmor Frequency Using MRI," *SIAM J. Appl. Math.*, vol. 73, no. 6, pp. 2262–2280, 2013.

[31] H. Ammari, J. K. Seo, and L. Zhou, "Viscoelastic Modulus Reconstruction Using Time Harmonic Vibrations. Mathematical Modelling and Analysis," *Math. Model Anal.*, vol. 20, no. 6, pp. 836–851, 2015, DOI: 10.3846/13926292.2015.1117531.

[32] F. S. Hafalir, O. F. Oran, N. Gurler, and Y. Z. Ider, "Convection-Reaction Equation Based Magnetic Resonance Electrical Properties Tomography (cr-MREPT)," *IEEE Trans. Med. Imag.*, vol. 33, no. 3, pp. 777–793, 2014, DOI: 10.1109/TMI.2013.2296715.

[33] E. Balidemaj, C. A. T. van den Berg, J. Trinks, A. L. H. M. W. van Lier, A. J. Nederveen, L. J. A. Stalpers, H. Crezee, and R. F. Remis, "CSI-EPT: A Contrast Source Inversion Approach for Improved MRI-Based Electric Properties Tomography," *IEEE Trans. Med. Imag.*, vol. 34, no. 9, pp. 1788–1796, 2015, DOI: 10.1109/TMI.2015.2404944.

[34] R. L. Leijsen, W. M. Brink, C. A. T. van den Berg, A. G. Webb, and R. F. Remis, "3-D Contrast Source Inversion-Electrical Properties Tomography," *IEEE Trans. Med. Imag.*, vol. 37, no. 9, pp. 2080–2089, 2018, DOI: 10.1109/TMI.2018.2816125.

[35] T. Nara, T. Furuichi, and M. Fushimi, "An explicit reconstruction method for magnetic resonance electrical property tomography base on the generalized Cauchy formula," *Inverse Probl.*, vol. 33, no. 10, p. 105005, 2017, DOI: 10.1088/1361-6420/aa8414.

[36] H. Gudbjartsson and S. Patz, "The Rician Distribution of Noisy MRI Data," *Magn. Reson. Med.*, vol. 34, no. 6, pp. 910–914, 1995, DOI: 10.1002/mrm.1910340618.

[37] K. Ryu, J. Shin, H. Lee, J.-H. Kim, and D.-H. Kim, "Multi-echo GRE-based conductivity imaging using Kalman phase estimation method," *Magn. Reson. Med.*, vol. 81, no. 1, pp. 702–710, 2019, DOI: 10.1002/mrm.27376.

[38] C. Gabriel, S. Gabriel, and E. Corthout, "The dielectric properties of biological tissues: I. Literature survey," *Phys. Med. Biol.*, vol. 41, no. 11, pp. 2231–2249, 1996, DOI: 10.1088/0031-9155/41/11/001.

[39] S. Gabriel, R. W. Lau, and C. Gabriel, "The dielectric properties of biological tissues: II. Measurements in the frequency range 10 Hz to 20 GHz," *Phys. Med. Biol.*, vol. 41, no. 11, pp. 2251–2269, 1996, DOI: 10.1088/0031-9155/41/11/002.

[40] S. Gabriel, R. W. Lau, and C. Gabriel, "The dielectric properties of biological tissues: III. Parametric models for the dielectric spectrum of tissues," *Phys. Med. Biol.*, vol. 41, no. 11, pp. 2271–2293, 1996, DOI: 10.1088/0031-9155/41/11/003.

[41] H. P. Schwan and K. R. Foster, "Microwave dielectric properties of tissue: Some comments on the rotational mobility of tissue water," *Biophys. J.*, vol. 17, no. 2, pp. 193–197, 1977, DOI: 10.1016/S0006-3495(77)85637-3.

[42] R. Pethig, "Dielectric Properties of Biological Materials: Biophysical and Medical Applications," *IEEE Trans. Electr. Insul.*, vol. EI-19, no. 5, pp. 453–474, 1984, DOI: 10.1109/TEI.1984.298769.

[43] K. S. Cole and R. H. Cole, "Dispersion and Absorption in Dielectrics I. Alternating Current Characteristics," *J. Chem. Phys.*, vol. 9, no. 4, pp. 341–351, 1941, DOI: 10.1063/1.1750906.

[44] K. S. Cole and R. H. Cole, "Dispersion and Absorption in Dielectrics II. Direct Current Characteristics," *J. Chem. Phys.*, vol. 10, no. 2, pp. 98–105, 1942, DOI: 10.1063/1.1723677.

[45] K. R. Foster, J. L. Schepps, R. D. Stoy, and H. P. Schwan, "Dielectric Properties of Brain Tissue between 0.01 and 10 GHz," *Phys. Med. Biol.*, vol. 24, no. 6, pp. 1177–1187, 1979, DOI: 10.1088/0031-9155/24/6/008.

[46] G. Madelin and R. R. Regatte, "Biomedical applications of sodium MRI in vivo," *J. Magn. Reson. Imaging*, vol. 38, no. 3, pp. 511–529, 2013, DOI: 10.1002/jmri.24168.

[47] G. Madelin, J.-S. Lee, R. R. Regatte, and A. Jerschow, "Sodium MRI: Methods and applications," *Prog. Nucl. Mag. Res. Sp.*, vol. 79, pp. 14–47, 2014, DOI: 10.1016/j.pnmrs.2014.02.001.

[48] E. J. Ambrose, A. M. James, and J. H. B. Lowick, "Differences between the Electrical Charge carried by Normal and Homologous Tumour Cells," *Nature*, vol. 177, pp. 576–577, 1956, DOI: 10.1038/177576a0.

[49] J. L. Schepps and K. R. Foster, "The UHF and microwave dielectric properties of normal and tumour tissues: variation in dielectric properties with tissue water content," *Phys. Med. Biol.*, vol. 25, no. 6, pp. 1149–1159, 1980, DOI: 10.1088/0031-9155/25/6/012.

[50] A. J. Surowiec, S. S. Stuchly, J. R. Barr, and A. Swarup, "Dielectric Properties of Breast Carcinoma and the Surrounding Tissues," *IEEE Trans. Biomed. Eng.*, vol. 35, no. 4, pp. 257–263, 1988, DOI: 10.1109/10.1374.

[51] Y. Lu, B. Li, J. Xu, and J. Yu, "Dielectric properties of human glioma and surrounding tissue," *Int. J. Hyperther.*, vol. 8, no. 6, pp. 755–760, 1992, DOI: 10.3109/02656739209005023.

[52] W. T. Joines, Y. Zhang, C. Li, and R. L. Jirtle, "The measured electrical properties of normal and malignant human tissues from 50 to 900 MHz," *Med. Phys.*, vol. 21, no. 4, pp. 547–550, 1994, DOI: 10.1118/1.597312.

[53] M. Lazebnik, D. Popovic, L. McCartney, C. BWatkins, M. J. Lindstrom, J. Harter, S. Sewall, T. Ogilvie, A. Magliocco, T. M. Breslin, W. Temple, D. Mew, J. H. Booske, M. Okoniewski, and S. C. Hagness, "A large-scale study of the ultrawideband microwave dielectric properties of normal, benign and malignant breast tissues obtained from cancer surgeries," *Phys. Med. Biol.*, vol. 52, no. 20, pp. 6093–6115, 2007, DOI: 10.1088/0031-9155/52/20/002.

[54] Z. Li, W. Wang, Z. Cai, S. Han, S. Lin, L. He, M. Chen, D. Pan, G. Deng, S. Duan, and S. X. Xin, "Variation in the Dielectric Properties of Freshly Excised Colorectal Cancerous Tissues at Different Tumor Stages," *Bioelectromagnetics*, vol. 38, no. 7, pp. 522–532, 2017, DOI: 10.1002/bem.22066.

[55] D. L. Collins, A. P. Zijdenbos, V. Kollokian, J. G. Sled, N. J. Kabani, C. J. Holmes, and A. C. Evans, "Design and construction of a realistic digital brain phantom," *IEEE Trans. Med. Imag.*, vol. 17, no. 3, pp. 463–468, 1998, DOI: 10.1109/42.712135.

[56] C. M. Collins, W. Liu, J. Wang, R. Gruetter, J. T. Vaughan, K. Ugurbil, and M. B. Smith, "Temperature and SAR Calculations for a Human Head Within Volume and Surface Coils at 64 and 300 MHz," *J. Magn. Reson. Imaging*, vol. 19, no. 5, pp. 650–656, 2004, DOI: 10.1002/jmri.20041.

[57] G. R. Morrell and M. C. Schabel, "An analysis of the accuracy of magnetic resonance flip angle measurement methods," *Phys. Med. Biol.*, vol. 55, no. 20, pp. 6157–6174, 2010, DOI: 10.1088/0031-9155/55/20/008.

[58] D. J. Park, N. K. Bangerter, A. Javed, J. Kaggie, M. M. Khalighi, and G. R. Morrell, "A statistical analysis of the Bloch–Siegert B_1 mapping technique," *Phys. Med. Biol.*, vol. 58, no. 16, pp. 5673–5691, 2013, DOI: 10.1088/0031-9155/58/16/5673.

[59] R. Pohmann and K. Scheffler, "A theoretical and experimental comparison of different techniques for B_1 mapping at very high fields," *NMR Biomed.*, vol. 26, no. 3, pp. 265–275, 2013, DOI: 10.1002/nbm.2844.

[60] E. K. Insko and L. Bolinger, "Mapping of the Radiofrequency Field," *J. Magn. Reson.: Series A*, vol. 103, no. 1, pp. 82–85, 1993, DOI: 10.1006/jmra.1993.1133.

[61] S. Akoka, F. Franconi, F. Seguin, and A. le Pape, "Radiofrequency map of an NMR coil by imaging," *Magn. Reson. Imaging*, vol. 11, no. 3, pp. 437–441, 1993, DOI: 10.1016/0730-725X(93)90078-R.

[62] R. Stollberger and P. Wach, "Imaging of the active B_1 field in vivo," *Magn. Reson. Med.*, vol. 35, no. 2, pp. 246–251, 1996, DOI: 10.1002/mrm.1910350217.

[63] D. I. Hoult, "The principle of reciprocity in signal strength calculations—A mathematical guide," *Concept. Magnetic Res.*, vol. 12, no. 4, pp. 173–187, 2000, DOI: 10.1002/1099-0534(2000)12:4<173::AID-CMR1>3.0.CO;2-Q.

[64] J. Wang, W. Mao, M. Qiu, M. B. Smith, and R. T. Constable, "Factors influencing flip angle mapping in MRI: RF pulse shape, slice-select gradients, off-resonance excitation, and B0 inhomogeneities," *Magn. Reson. Med.*, vol. 56, no. 2, pp. 463–468, 2006, DOI: 10.1002/mrm.20947.

[65] V. L. Yarnykh, "Actual flip-angle imaging in the pulsed steady state: A method for rapid three-dimensional mapping of the transmitted radiofrequency field," *Magn. Reson. Med.*, vol. 57, no. 1, pp. 192–200, 2007, DOI: 10.1002/mrm.21120.

[66] G. R. Morrell, "A phase-sensitive method of flip angle mapping," *Magn. Reson. Med.*, vol. 60, no. 4, pp. 889–894, 2008, DOI: 10.1002/mrm.21729.

[67] L. I. Sacolick, F. Wiesinger, I. Hancu, and M. W. Vogel, "B_1 mapping by Bloch–Siegert shift," *Magn. Reson. Med.*, vol. 63, no. 5, pp. 1315–1322, 2010, DOI: 10.1002/mrm.22357.

[68] S. Gavazzi, C. A. T. van den Berg, A. Sbrizzi, H. P. Kok, L. J. A. Stalpers, J. J. W. Lagendijk, H. Crezee, and A. L. H. M. W. van Lier, "Accuracy and precision of electrical permittivity mapping at 3T: the impact of three B_1^+ mapping techniques," *Magn. Reson. Med.*, vol. 81, no. 6, pp. 3628–3642, 2019, DOI: 10.1002/mrm.27675.

[69] U. Katscher, T. Voigt, C. Findeklee, P. Vernickel, K. Nehrke, and O. Dössel, "Determination of Electric Conductivity and Local SAR Via B1 Mapping," *IEEE Trans. Med. Imag.*, vol. 28, no. 9, pp. 1365–1374, 2009, DOI: 10.1109/TMI.2009.2015757.

[70] C. E. Hayes, W. A. Edelstein, J. F. Schenck, O. M. Mueller, and M. Eash, "An Efficient, Highly Homogeneous Radiofrequency Coil for Whole-Body NMR Imaging at 1.5T," *J. Magn. Reson.*, vol. 63, no. 3, pp. 622–628, 1985, DOI: 10.1016/0022-2364(85)90257-4.

[71] W. R. Overall, J. M. Pauly, P. P. Stang, and G. C. Scott, "Ensuring safety of implanted devices under MRI using reversed RF polarization," *Magn. Reson. Med.*, vol. 64, no. 3, pp. 823–833, 2010, DOI: 10.1002/mrm.22468.

[72] A. L. H. M. W. van Lier, A. Raaijmakers, T. Voigt, J. J. W. Lagendijk, P. R. Luijten, U. Katscher, and C. A. T. van den Berg, "Electrical Properties Tomography in the Human Brain at 1.5, 3, and 7T: A Comparison Study," *Magn. Reson. Med.*, vol. 71, no. 1, pp. 354–363, 2014, DOI: 10.1002/mrm.24637.

[73] E. M. Haacke, L. S. Petropoulos, E. W. Nilges, and D. H. Wu, "Extraction of conductivity and permittivity using magnetic resonance imaging," *Phys. Med. Biol.*, vol. 36, no. 6, pp. 723–734, 1991, DOI: 10.1088/0031-9155/36/6/002.

[74] H. Wen, "Noninvasive quantitative mapping of conductivity and dielectric distributions using RF wave propagation effects in high-field MRI," *Proc. SPIE Medical Imaging 2003*, vol. 5030, pp. 471–477, San Diego, CA, USA, DOI: 10.1117/12.480000.

[75] J. K. Seo, M.-O. Kim, J. Lee, N. Choi, E. J. Woo, H. J. Kim, O. I. Kwon, and D.-H. Kim, "Error Analysis of Nonconstant Admittivity for MR-Based Electric Property Imaging," *IEEE Trans. Med. Imag.*, vol. 31, no. 2, pp. 430–437, 2012, DOI: 10.1109/TMI.2011.2171000.

[76] S. Duan, C. Xu, G. Deng, J. Wang, F. Liu, and S. X. Xin, "Quantitative analysis of the reconstruction errors of the currently popular algorithm of magnetic resonance electrical property tomography at the interfaces of adjacent tissues," *NMR Biomed.*, vol. 29, no. 6, pp. 744–750, 2016, DOI: 10.1002/nbm.3522.

[77] H. Ammari, H. Kwon, Y. Lee, K. Kang, and J. K. Seo, "Magnetic-resonance-based reconstruction method of conductivity and permittivity distribution at Larmor frequency," *Inverse Probl.*, vol. 31, no. 10, p. 105001, 2015, DOI: 10.1088/0266-5611/31/10/105001.

[78] C. Li, W. Yu, and S. Y. Huang, "An MR-Based Viscosity-Type Regularization Method for Electrical Property Tomography," *Tomography*, vol. 3, no. 1, pp. 50–59, 2017, DOI: 10.18383/j.tom.2016.00283.

[79] R. Hong, S. Li, J. Zhang, Y. Zhang, N. Liu, Z. Yu, and Q. H. Liu, "3-D MRI-Based Electrical Properties Tomography Using the Volume Integral Equation Method," *IEEE Trans. Microw. Theory Techn.*, vol. 65, no. 12, pp. 4802–4811, 2017, DOI: 10.1109/TMTT.2017.2725830.

[80] L. Guo, J. Jin, C. Liu, F. Liu, and S. Crozier, "An Efficient Integral-Based Method for Three-Dimensional MR-EPT and the Calculation of the RF-Coil-Induced B_z Field," *IEEE Trans. Biomed. Eng.*, vol. 65, no. 2, pp. 282–293, 2018, DOI: 10.1109/TBME.2017.2763590.

[81] E. J. Rothwell and M. J. Cloud, *Electromagnetics*, CRC Press, ISBN: 9781498796569.

[82] P. M. van den Berg and R. E. Kleinman, "A contrast source inversion method," *Inverse Probl.*, vol. 13, no. 6, pp. 1607–1620, 1997, DOI: 10.1088/0266-5611/13/6/013.

[83] A. Abubakar, W. Hu, P. M. van den Berg, and T. M. Habashy, "A finite-difference contrast source inversion method," *Inverse Probl.*, vol. 24, no. 6, p. 065004, 2008, DOI: 10.1088/0266-5611/24/6/065004.

[84] A. Arduino, L. Zilberti, M. Chiampi, and O. Bottauscio, "CSI-EPT in Presence of RF-Shield for MR-Coils," *IEEE Trans. Med. Imag.*, vol. 36, no. 7, pp. 1396–1404, 2017, DOI: 10.1109/TMI.2017.2665688.

[85] W. Zhang and Q. H. Liu, "Three-Dimensional Scattering and Inverse Scattering from Objects With Simultaneous Permittivity and Permeability Contrasts," *IEEE Trans. Geosci. Remote Sens.*, vol. 53, no. 1, pp. 429–439, 2015, DOI: 10.1109/TGRS.2014.2322954.

[86] M. J. Ablowitz and A. S. Fokas, *Complex Variables: Introduction and Applications*, Second, Cambridge University Press, ISBN: 9780521534291.

[87] D. K. Sodickson, L. Alon, C. M. Deniz, R. Brown, B. Zhang, G. C. Wiggins, G. Y. Cho, N. B. Eliezer, D. S. Novikov, R. Lattanzi, Q. Duan, L. A. Sodickson, and Y. Zhu, "Local Maxwell Tomography Using Transmit-Receive Coil Arrays for Contact-Free Mapping of Tissue Electrical Properties and Determination of Absolute RF Phase," *Proceedings of the ISMRM 20th Annual Meeting*, p. 387, Melbourne, VIC, Australia.

[88] D. K. Sodickson, L. Alon, C. M. Deniz, N. B. Eliezer, L. A. Sodickson, C. M. Collins, G. C. Wiggins, and D. S. Novikov, "Generalized Local Maxwell Tomography for Mapping of Electrical Property Gradients and Tensors," *Proceedings of the ISMRM 21st Annual Meeting*, p. 4175, Salt Lake City, UT, USA.

[89] J. Liu, X. Zhang, P.-F. van de Moortele, S. Schmitter, and B. He, "Determining electrical properties based on B_1 fields measured in an MR scanner using a multi-channel transmit/receive coil: a general approach," *Phys. Med. Biol.*, vol. 58, no. 13, pp. 4395–4408, 2013, DOI: 10.1088/0031-9155/58/13/4395.

[90] X. Zhang, S. Schmitter, P.-F. van de Moortele, J. liu, and B. He, "From Complex B_1 Mapping and to Local SAR Estimation for Human Brain MR Imaging Using Multi-Channel Transceiver Coil at 7T," *IEEE Trans. Med. Imag.*, vol. 32, no. 6, pp. 1058–1067, 2013, DOI: 10.1109/TMI.2013.2251653.

[91] J. Liu, X. Zhang, S. Schmitter, P.-F. van de Moortele, and B. He, "Gradient-Based Electrical Properties Tomography (gEPT): A Robust Method for Mapping Electrical Properties of Biological Tissues In Vivo Using Magnetic Resonance Imaging," *Magn. Reson. Med.*, vol. 74, no. 3, pp. 634–646, 2015, DOI: 10.1002/mrm.25434.

[92] J. Liu, P.-F. van de Moortele, X. Zhang, Y. Wang, and B. He, "Simultaneous Quantitative Imaging of Electrical Properties and Proton Density From B_1 Maps Using MRI," *IEEE Trans. Med. Imag.*, vol. 35, no. 9, pp. 2064–2073, 2016, DOI: 10.1109/TMI.2016.2547988.

[93] Y. Wang, P.-F. van de Moortele, and B. He, "Automated gradient-based electrical properties tomography in the human brain using 7 Tesla MRI," *Magn. Reson. Imaging*, vol. 63, pp. 258–266, 2019, DOI: 10.1016/j.mri.2019.08.003.

[94] Y. Wang, Q. Shao, P.-F. van de Moortele, E. Racila, J. Liu, J. Bischof, and B. He, "Mapping electrical properties heterogeneity of tumor using boundary informed electrical properties tomography (BIEPT) at 7T," *Magn. Reson. Med.*, vol. 81, no. 1, pp. 393–409, 2019, DOI: 10.1002/mrm.27414.

[95] Y. Wang, P. van de Moortele, and B. He, "CONtrast Conformed Electrical Properties Tomography (CONCEPT) Based on Multi-Channel Transmission and Alternating Direction Method of Multipliers," *IEEE Trans. Med. Imag.*, vol. 38, no. 2, pp. 349–359, 2019, DOI: 10.1109/TMI.2018.2865121.

[96] J. Shin, J.-H. Kim, and D.-H. Kim, "Redesign of the Laplacian kernel for improvements in conductivity imaging using MRI," *Magn. Reson. Med.*, vol. 81, no. 3, pp. 2167–2175, 2019, DOI: 10.1002/mrm.27528.

[97] N. Gurler and Y. Z. Ider, "Gradient-Based Electrical Conductivity Imaging Using MR Phase," *Magn. Reson. Med.*, vol. 77, no. 1, pp. 137–150, 2017, DOI: 10.1002/mrm.26097.

[98] A. Nachman, D. Wang, W. Ma, and M. Joy, "A Local Formula for Inhomogeneous Complex Conductivity as a Function of the RF Magnetic Field," *Proc. ISMRM 15th Annual Meeting*, p. 15, Berlin, Germany.

[99] A. L. H. M. W. van Lier, D. O. Brunner, K. P. Pruessmann, D. W. J. Klomp, P. R. Luijten, J. J. W. Lagendijk, and C. A. T. van den Berg, "B_1^+ Phase Mapping at 7 T and its Application for In Vivo Electrical Conductivity Mapping," *Magn. Reson. Med.*, vol. 67, no. 2, pp. 552–561, 2012, DOI: 10.1002/mrm.22995.

[100] N. Eda, M. Fushimi, K. Hasegawa, and T. Nara, "Noniterative Electrical Properties Tomography Reconstruction Method Based on Three-Dimensional Integral Equation for the Electric Field," *Proc. ISMRM 28th Annual Meeting*, Online.

[101] N. Eda, M. Fushimi, and T. Nara, "An Iterative Reconstruction Method for the Electric Field and Electrical Properties Using MRI Based on the Helmholtz Identity," *Proc. SICE 37th Sensing Forum*, Online (In Japanese).

[102] F. Vico, L. Greengard, and M. Ferrando, "Fast convolution with free-space Green's functions," *J. Comput. Phys.*, vol. 323, pp. 191–203, 2016, DOI: 10.1016/j.jcp.2016.07.028.

[103] T. Goldstein and S. Osher, "The Split Bregman Method for L1-Regularized Problems," *SIAM J. Imaging Sci.*, vol. 2, no. 2, pp. 323–343, 2009, DOI: 10.1137/080725891.

[104] C. Milovic, B. Bilgic, B. Zhao, J. Acosta-Cabronero, and C. Tejos, "Fast nonlinear susceptibility inversion with variational regularization," *Magn. Reson. Med.*, vol. 80, no. 2, pp. 814–821, 2018, DOI: 10.1002/mrm.27073.

[105] N. Gurler and Y. Z. Ider, "Numerical Methods and Software Tools for Simulation, Design, and Resonant Mode Analysis of Radio Frequency Birdcage Coils Used in MRI," *Concept. Magnetic Res. Part B*, vol. 45, no. 1, pp. 13–32, 2015.

[106] B. Aubert-Broche, A. C. Evans, and D. L. Collins, "A new improved version of the realistic digital brain phantom," *NeuroImage*, vol. 32, no. 1, pp. 138–145, 2006, DOI: 10.1016/j.neuroimage.2006.03.052.

[107] B. Aubert-Broche, M. Griffin, G. B. Pike, A. C. Evans, and D. L. Collins, "Twenty New Digital Brain Phantoms for Creation of Validation Image Data Bases," *IEEE Trans. Med. Imag.*, vol. 25, no. 11, pp. 1410–1416, 2006, DOI: 10.1109/TMI.2006.883453.

[108] A. Savitzky and M. J. E. Golay, "Smoothing and Differentiation of Data by Simplified Least Squares Procedures," *Anal. Chem.*, vol. 36, no. 8, pp. 1627–1639, 1964, DOI: 10.1021/ac60214a047.

[109] S. Rajagopalan and R. A. Robb, "Image smoothing with Savitzky–Golay filters," *Proc. SPIE Medical Imaging 2003*, vol. 5029, pp. 773–781, San Diego, CA, USA, DOI: 10.1117/12.479596.

[110] G. Yildiz and Y. Z. Ider, "Use of dielectric padding to eliminate low convective field artifact in cr-MREPT conductivity images," *Magn. Reson. Med.*, vol. 81, no. 5, pp. 3168–3184, 2019, DOI: 10.1002/mrm.27648.

[111] Z. Liu, P. Spincemaille, Y. Yao, Y. Zhang, and Y. Wang, "MEDI+0: Morphology enabled dipole inversion with automatic uniform cerebrospinal fluid zero reference for quantitative susceptibility mapping," *Magn. Reson. Med.*, vol. 79, no. 5, pp. 2795–2803, 2018, DOI: 10.1002/mrm.26946.

[112] C. Ianniello, J. A. de Zwart, Q. Duan, C. M. Deniz, L. Alon, J.-S. Lee, R. Lattanzi, and R. Brown, "Synthesized tissue-equivalent dielectric phantoms using salt and polyvinylpyrrolidone solutions," *Magn. Reson. Med.*, vol. 80, no. 1, pp. 413–419, 2018, DOI: 10.1002/mrm.27005.

[113] N. Arteaga-Marrero, E. Villa, J. González-Fernández, Y. Martín, and J. Ruiz-Alzola, "Polyvinyl alcohol cryogel phantoms of biological tissues for wideband operation at microwave frequencies," *PLOS ONE*, vol. 14, no. 7, pp. 1–17, 2019, DOI: 10 . 1371 / journal.pone.0219997.

[114] A. L. H. M. W. van Lier, J. M. Hoogduin, D. L. Polders, V. O. Boer, J. Hendrikse, P. A. Robe, P. A. Woerdeman, J. J. Lagendijk, P. R. Luijten, and C. A. van den Berg, "Electrical conductivity imaging of brain tumours," *Proc. ISMRM 19th Annual Meeting*, p. 4464, Montréal, QC, Canada.

[115] J. Satta, T. Juvonen, K. Haukipuro, M. Juvonen, and M. I. Kairaluoma, "Increased turnover of collagen in abdominal aortic aneurysms, demonstrated by measuring the concentration of the aminoterminal propeptide of type III procollagen in peripheral and aortal blood samples," *J. Vasc. Surg.*, vol. 22, no. 2, pp. 155–160, 1995, DOI: 10.1016/S0741-5214(95)70110-9.

[116] M. L. Raghavan, M. W. Webster, and D. A. Vorp, "Ex vivo biomechanical behavior of abdominal aortic aneurysm: Assessment using a new mathematical model," *Ann. Biomed. Eng.*, vol. 24, no. 5, pp. 573–582, 1996, DOI: 10.1007/BF02684226.

[117] D. A. Vorp and J. P. Vande Geest, "Biomechanical Determinants of Abdominal Aortic Aneurysm Rupture," *Arterioscl. Throm. Vas.*, vol. 25, no. 8, pp. 1558–1566, 2005, DOI: 10.1161/01.ATV.0000174129.77391.55.

[118] S. L. Friedman, "Liver fibrosis—from bench to bedside," *J. Hepatol.*, vol. 38, pp. 38–53, 2003, DOI: 10.1016/S0168-8278(02)00429-4.

[119] S. K. Venkatesh, M. Yin, J. F. Glockner, N. Takahashi, P. A. Araoz, J. A. Talwalkar, and R. L. Ehman, "MR Elastography of Liver Tumors: Preliminary Results," *Am. J. Roentgenol.*, vol. 190, no. 6, pp. 1534–1540, 2008, DOI: 10.2214/AJR.07.3123.

[120] T. A. Krouskop, T. M. Wheeler, F. Kallel, B. S. Garra, and T. Hall, "Elastic Moduli of Breast and Prostate Tissues under Compression," *Ultrasonic Imaging*, vol. 20, no. 4, pp. 260–274, 1998, DOI: 10.1177/016173469802000403.

[121] T. E. Oliphant, A. Manduca, R. L. Ehman, and J. F. Greenleaf, "Complex-valued stiffness reconstruction for magnetic resonance elastography by algebraic inversion of the differential equation," *Magn. Reson. Med.*, vol. 45, no. 2, pp. 299–310, 2001, DOI: 10.1002/1522-2594(200102)45:2<299::AID-MRM1039>3.0.CO;2-O.

[122] A. Manduca, T. E. Oliphant, M. A. Dresner, J. L. Mahowald, S. A. Kruse, E. Amromin, J. P. Felmlee, J. F. Greenleaf, and R. L. Ehman, "Magnetic resonance elastography: Non-invasive mapping of tissue elasticity," *Med. Image Anal.*, vol. 5, no. 4, pp. 237–254, 2001, DOI: 10.1016/S1361-8415(00)00039-6.

[123] R. Sinkus, M. Tanter, S. Catheline, J. Lorenzen, C. Kuhl, E. Sondermann, and M. Fink, "Imaging Anisotropic and Viscous Properties of Breast Tissue by Magnetic Resonance-

Elastography," *Magn. Reson. Med.*, vol. 53, no. 2, pp. 372–387, 2005, DOI: 10.1002/mrm.20355.

[124] M. M. Doyley, P. M. Meaney, and J. C. Bamber, "Evaluation of an iterative reconstruction method for quantitative elastography," *Phys. Med. Biol.*, vol. 45, no. 6, pp. 1521–1540, 2000, DOI: 10.1088/0031-9155/45/6/309.

[125] M. I. Miga, "A new approach to elastography using mutual information and finite elements," *Phys. Med. Biol.*, vol. 48, no. 4, pp. 467–480, 2003, DOI: 10.1088/0031-9155/48/4/304.

[126] A. A. Oberai, N. H. Gokhale, and G. R. Feijóo, "Solution of inverse problems in elasticity imaging using the adjoint method," *Inverse Probl.*, vol. 19, no. 2, pp. 297–313, 2003, DOI: 10.1088/0266-5611/19/2/304.

[127] A. A. Oberai, N. H. Gokhale, M. M. Doyley, and J. C. Bamber, "Evaluation of the adjoint equation based algorithm for elasticity imaging," *Phys. Med. Biol.*, vol. 49, no. 13, pp. 2955–2974, 2004, DOI: 10.1088/0031-9155/49/13/013.

[128] E. E. W. Van Houten, K. D. Paulsen, M. I. Miga, F. E. Kennedy, and J. B. Weaver, "An overlapping subzone technique for MR-based elastic property reconstruction," *Magn. Reson. Med.*, vol. 42, no. 4, pp. 779–786, 1999, DOI: 10.1002/(SICI)1522-2594(199910)42:4<779::AID-MRM21>3.0.CO;2-Z.

[129] E. E. W. Van Houten, M. I. Miga, J. B. Weaver, F. E. Kennedy, and K. D. Paulsen, "Three-dimensional subzone-based reconstruction algorithm for MR elastography," *Magn. Reson. Med.*, vol. 45, no. 5, pp. 827–837, 2001, DOI: 10.1002/mrm.1111.

[130] E. Park and A. M. Maniatty, "Shear modulus reconstruction in dynamic elastography: time harmonic case," *Phys. Med. Biol.*, vol. 51, no. 15, pp. 3697–3721, 2006, DOI: 10.1088/0031-9155/51/15/007.

[131] M. Honarvar, R. Rohling, and S. E. Salcudean, "A comparison of direct and iterative finite element inversion techniques in dynamic elastography," *Phys. Med. Biol.*, vol. 61, no. 8, pp. 3026–3048, 2016, DOI: 10.1088/0031-9155/61/8/3026.

[132] M. Honarvar, R. Sahebjavaher, R. Sinkus, R. Rohling, and S. E. Salcudean, "Curl-Based Finite Element Reconstruction of the Shear Modulus Without Assuming Local Homogeneity: Time Harmonic Case," *IEEE Trans. Med. Imag.*, vol. 32, no. 12, pp. 2189–2199, 2013, DOI: 10.1109/TMI.2013.2276060.

[133] M. Honarvar, R. S. Sahebjavaher, S. E. Salcudean, and R. Rohling, "Sparsity regularization in dynamic elastography," *Phys. Med. Biol.*, vol. 57, no. 19, pp. 5909–5927, 2012, DOI: 10.1088/0031-9155/57/19/5909.

[134] Y. Zhang, A. A. Oberai, P. E. Barbone, and I. Harari, "Solution of the time-harmonic viscoelastic inverse problem with interior data in two dimensions," *Int. J. Numer. Meth. Eng.*, vol. 92, no. 13, pp. 1100–1116, 2012, DOI: 10.1002/nme.4372.

[135] O. Kojima and T. Nara, "Estimation of inhomogeneous shear modulus distribution under the effects of compressibility on the basis of measurements of the displacement field," *Proc. SICE 36th Sensing Forum*, Kanagawa (In Japanese).

[136] A. Manduca, D. S. Lake, S. A. Kruse, and R. L. Ehman, "Spatio-temporal directional filtering for improved inversion of MR elastography images," *Med. Image Anal.*, vol. 7, no. 4, pp. 465–473, 2003, DOI: 10.1016/S1361-8415(03)00038-0.

[137] P. R. Perriñez, F. E. Kennedy, E. E. W. V. Houten, J. B. Weaver, and K. D. Paulsen, "Modeling of Soft Poroelastic Tissue in Time-Harmonic MR Elastography," *IEEE Trans. Biomed. Eng.*, vol. 56, no. 3, pp. 598–608, 2009, DOI: 10.1109/TBME.2008.2009928.

[138] A. J. Pattison, M. McGarry, J. B. Weaver, and K. D. Paulsen, "Spatially-Resolved Hydraulic Conductivity Estimation Via Poroelastic Magnetic Resonance Elastography," *IEEE Trans. Med. Imag.*, vol. 33, no. 6, pp. 1373–1380, 2014, DOI: 10.1109/TMI.2014.2311456.

[139] H. Tzschätzsch, J. Guo, F. Dittmann, S. Hirsch, E. Barnhill, K. Jöhrens, J. Braun, and I. Sack, "Tomoelastography by multifrequency wave number recovery from time-harmonic propagating shear waves," *Med. Image Anal.*, vol. 30, pp. 1–10, 2016, DOI: 10.1016/j.media.2016.01.001.

[140] E. Barnhill, P. J. Davies, C. Ariyurek, A. Fehlner, J. Braun, and I. Sack, "Heterogeneous Multifrequency Direct Inversion (HMDI) for magnetic resonance elastography with application to a clinical brain exam," *Med. Image Anal.*, vol. 46, pp. 180–188, 2018, DOI: 10.1016/j.media.2018.03.003.

[141] L. Pauling and C. D. Coryell, "The Magnetic Properties and Structure of Hemoglobin, Oxyhemoglobin and Carbonmonoxyhemoglobin," *P. Natl. Acad. Sci. USA*, vol. 22, no. 4, pp. 210–216, 1936, DOI: 10.1073/pnas.22.4.210.

[142] M. W. Hentze, M. U. Muckenthaler, and N. C. Andrews, "Balancing Acts: Molecular Control of Mammalian Iron Metabolism," *Cell*, vol. 117, no. 3, pp. 285–297, 2004, DOI: 10.1016/S0092-8674(04)00343-5.

[143] F. A. Fischbach, D. W. Gregory, P. M. Harrison, T. G. Hoy, and J. M. Williams, "On the structure of hemosiderin and its relationship to ferritin," *J. Ultra. Struct. R.*, vol. 37, no. 5, pp. 495–503, 1971, DOI: 10.1016/S0022-5320(71)80020-5.

[144] E. Miyazaki, J. Kato, M. Kobune, K. Okumura, K. Sasaki, N. Shintani, P. Arosio, and Y. Niitsu, "Denatured H-ferritin subunit is a major constituent of haemosiderin in the liver of patients with iron overload," *Gut*, vol. 50, no. 3, pp. 413–419, 2002, DOI: 10.1136/gut.50.3.413.

[145] D. Proudfoot, J. N. Skepper, L. Hegyi, M. R. Bennett, C. M. Shanahan, and P. L. Weissberg, "Apoptosis Regulates Human Vascular Calcification In Vitro," *Circ. Res.*, vol. 87, no. 11, pp. 1055–1062, 2000, DOI: 10.1161/01.RES.87.11.1055.

[146] M. Scimeca, E. Giannini, C. Antonacci, C. A. Pistolese, L. G. Spagnoli, and E. Bonanno, "Microcalcifications in breast cancer: an active phenomenon mediated by epithelial cells with mesenchymal characteristics," *BMC Cancer*, vol. 14, no. 1, p. 286, 2014, DOI: 10.1186/1471-2407-14-286.

[147] N. Choi, J. Lee, M.-O. Kim, J. Shin, and D.-H. Kim, "A modified multi-echo AFI for simultaneous B_1^+ magnitude and phase mapping," *Magn. Reson. Imaging*, vol. 32, no. 4, pp. 314–320, 2014, DOI: 10.1016/j.mri.2013.12.005.

[148] L. Li and J. S. Leigh, "Quantifying arbitrary magnetic susceptibility distributions with MR," *Magn. Reson. Med.*, vol. 51, no. 5, pp. 1077–1082, 2004, DOI: 10.1002/mrm.20054.

[149] F. Schweser, S. D. Robinson, L. de Rochefort, W. Li, and K. Bredies, "An illustrated comparison of processing methods for phase MRI and QSM: removal of background field contributions from sources outside the region of interest," *NMR Biomed.*, vol. 30, no. 4, e3604, 2017, DOI: 10.1002/nbm.3604.

[150] K. Shmueli, J. A. de Zwart, P. van Gelderen, T.-Q. Li, S. J. Dodd, and J. H. Duyn, "Magnetic susceptibility mapping of brain tissue in vivo using MRI phase data," *Magn. Reson. Med.*, vol. 62, no. 6, pp. 1510–1522, 2009, DOI: 10.1002/mrm.22135.

[151] B. Kressler, L. de Rochefort, T. Liu, P. Spincemaille, Q. Jiang, and Y. Wang, "Nonlinear Regularization for Per Voxel Estimation of Magnetic Susceptibility Distributions From MRI Field Maps," *IEEE Trans. Med. Imag.*, vol. 29, no. 2, pp. 273–281, 2010, DOI: 10.1109/TMI.2009.2023787.

[152] S. Wharton, A. Schäfer, and R. Bowtell, "Susceptibility mapping in the human brain using threshold-based k-space division," *Magn. Reson. Med.*, vol. 63, no. 5, pp. 1292–1304, 2010, DOI: 10.1002/mrm.22334.

[153] L. de Rochefort, T. Liu, B. Kressler, J. Liu, P. Spincemaille, V. Lebon, J. Wu, and Y. Wang, "Quantitative susceptibility map reconstruction from MR phase data using bayesian regularization: Validation and application to brain imaging," *Magn. Reson. Med.*, vol. 63, no. 1, pp. 194–206, 2018, DOI: 10.1002/mrm.22187.

[154] T. Liu, J. Liu, L. de Rochefort, P. Spincemaille, I. Khalidov, J. R. Ledoux, and Y. Wang, "Morphology enabled dipole inversion (MEDI) from a single-angle acquisition: Comparison with COSMOS in human brain imaging," *Magn. Reson. Med.*, vol. 66, no. 3, pp. 777–783, 2011, DOI: 10.1002/mrm.22816.

[155] J. Liu, T. Liu, L. de Rochefort, J. Ledoux, I. Khalidov, W. Chen, A. J. Tsiouris, C. Wisnieff, P. Spincemaille, M. R. Prince, and Y. Wang, "Morphology enabled dipole inversion for quantitative susceptibility mapping using structural consistency between the magnitude image and the susceptibility map," *NeuroImage*, vol. 59, no. 3, pp. 2560–2568, 2012, DOI: 10.1016/j.neuroimage.2011.08.082.

[156] T. Liu, W. Xu, P. Spincemaille, A. S. Avestimehr, and Y. Wang, "Accuracy of the Morphology Enabled Dipole Inversion (MEDI) Algorithm for Quantitative Susceptibility Mapping in MRI," *IEEE Trans. Med. Imag.*, vol. 31, no. 3, pp. 816–824, 2012, DOI: 10.1109/TMI.2011.2182523.

[157] Y. Wang, P. Spincemaille, Z. Liu, A. Dimov, K. Deh, J. Li, Y. Zhang, Y. Yao, K. M. Gillen, A. H. Wilman, A. Gupta, A. J. Tsiouris, I. Kovanlikaya, G. C.-Y. Chiang, J. W. Weinsaft, L. Tanenbaum, W. Chen, W. Zhu, S. Chang, M. Lou, B. H. Kopell, M. G. Kaplitt, D. Devos, T. Hirai, X. Huang, Y. Korogi, A. Shtilbans, G.-H. Jahng, D. Pelletier, S. A. Gauthier, D. Pitt, A. I. Bush, G. M. Brittenham, and M. R. Prince, "Clinical quantitative susceptibility mapping (QSM): Biometal imaging and its emerging roles in patient care," *J. Magn. Reson. Imaging*, vol. 46, no. 4, pp. 951–971, 2017, DOI: 10.1002/jmri.25693.

[158] J. Cho, Y. Kee, P. Spincemaille, T. D. Nguyen, J. Zhang, A. Gupta, S. Zhang, and Y. Wang, "Cerebral metabolic rate of oxygen (CMRO2) mapping by combining quantitative susceptibility mapping (QSM) and quantitative blood oxygenation level-dependent imaging (qBOLD)," *Magn. Reson. Med.*, vol. 80, no. 4, pp. 1595–1604, 2018, DOI: 10.1002/mrm.27135.

[159] J. Zhang, D. Zhou, T. D. Nguyen, P. Spincemaille, A. Gupta, and Y. Wang, "Cerebral metabolic rate of oxygen (CMRO2) mapping with hyperventilation challenge using quantitative susceptibility mapping (QSM)," *Magn. Reson. Med.*, vol. 77, no. 5, pp. 1762–1773, 2017, DOI: 10.1002/mrm.26253.

[160] A. V. Dimov, Z. Liu, P. Spincemaille, M. R. Prince, J. Du, and Y. Wang, "Bone quantitative susceptibility mapping using a chemical species-specific signal model with ultrashort and conventional echo data," *Magn. Reson. Med.*, vol. 79, no. 1, pp. 121–128, 2018, DOI: 10.1002/mrm.26648.

[161] J. Li, H. Lin, T. Liu, Z. Zhang, M. R. Prince, K. Gillen, X. Yan, Q. Song, T. Hua, X. Zhao, M. Zhang, Y. Zhao, G. Li, G. Tang, G. Yang, G. M. Brittenham, and Y. Wang, "Quantitative susceptibility mapping (QSM) minimizes interference from cellular pathology in R2* estimation of liver iron concentration," *J. Magn. Reson. Imaging*, vol. 48, no. 4, pp. 1069–1079, 2018, DOI: 10.1002/jmri.26019.

[162] Y. Wen, T. D. Nguyen, Z. Liu, P. Spincemaille, D. Zhou, A. Dimov, Y. Kee, K. Deh, J. Kim, J. W. Weinsaft, and Y. Wang, "Cardiac quantitative susceptibility mapping (QSM) for heart chamber oxygenation," *Magn. Reson. Med.*, vol. 79, no. 3, pp. 1545–1552, 2018, DOI: 10.1002/mrm.26808.

[163] H.-G. Kim, S. Park, H. Y. Rhee, K. M. Lee, C.-W. Ryu, S. J. Rhee, S. Y. Lee, Y. Wang, and G.-H. Jahng, "Quantitative susceptibility mapping to evaluate the early stage of Alzheimer's disease," *NeuroImage Clin.*, vol. 16, pp. 429–438, 2017, DOI: 10.1016/j.nicl.2017.08.019.

[164] K. Deh, G. D. Ponath, Z. Molvi, G.-C. T. Parel, K. M. Gillen, S. Zhang, T. D. Nguyen, P. Spincemaille, Y. Ma, A. Gupta, S. A. Gauthier, D. Pitt, and Y. Wang, "Magnetic susceptibility increases as diamagnetic molecules breakdown: Myelin digestion during multiple sclerosis lesion formation contributes to increase on QSM," *J. Magn. Reson. Imaging*, vol. 48, no. 5, pp. 1281–1287, 2018, DOI: 10.1002/jmri.25997.

[165] Y. Yao, T. D. Nguyen, S. Pandya, Y. Zhang, S. Hurtado-Rúa, I. Kovanlikaya, A. Kuceyeski, Z. Liu, Y. Wang, and S. A. Gauthier, "Combining Quantitative Susceptibility Mapping with Automatic Zero Reference (QSM0) and Myelin Water Fraction Imaging to Quantify Iron-Related Myelin Damage in Chronic Active MS Lesions," *Am. J. Neuroradiol.*, vol. 39, no. 2, pp. 303–310, 2018, DOI: 10.3174/ajnr.A5482.

[166] B. A. Taylor, K.-P. Hwang, A. M. Elliott, A. Shetty, J. D. Hazle, and R. J. Stafford, "Dynamic chemical shift imaging for image-guided thermal therapy: Analysis of feasibility and potential," *Med. Phys.*, vol. 35, no. 2, pp. 793–803, 2008, DOI: 10.1118/1.2831915.

[167] B. A. Taylor, K.-P. Hwang, J. D. Hazle, and R. J. Stafford, "Autoregressive moving average modeling for spectral parameter estimation from a multigradient echo chemical shift acquisition," *Med. Phys.*, vol. 36, no. 3, pp. 753–764, 2009, DOI: 10.1118/1.3075819.

[168] K. Levenberg, "A Method for the Solution of Certain Non-Linear Problems in Least Squares," *Quart. Appl. Math.*, vol. 2, pp. 164–168, 1944, DOI: 10.1090/qam/10666.

[169] D. W. Marquardt, "An Argorithm for Least-Squares Estimation of Nonlinear Parameters," *J. Soc. Ind. Appl. Math*, vol. 11, no. 2, pp. 431–441, 1963, DOI: 10.1137/0111030.

[170] M. A. Schofield and Y. Zhu, "Fast phase unwrapping algorithm for interferometric applications," *Opt. Lett.*, vol. 28, no. 14, pp. 1194–1196, 2003, DOI: 10.1364/OL.28.001194.

[171] V. V. Volkov and Y. Zhu, "Deterministic phase unwrapping in the presence of noise," *Opt. Lett.*, vol. 28, no. 22, pp. 2156–2158, 2003, DOI: 10.1364/OL.28.002156.

[172] T. Liu, C. Wisnieff, M. Lou, W. Chen, P. Spincemaille, and Y. Wang, "Nonlinear formulation of the magnetic field to source relationship for robust quantitative susceptibility mapping," *Magn. Reson. Med.*, vol. 69, no. 2, pp. 467–476, 2013, DOI: 10.1002/mrm.24272.

[173] Y. F. Gui and W.-B. Dou, "A Rigorous and Completed Statement on Helmholtz Theorem," *PIER*, vol. 69, pp. 287–304, 2007, DOI: 10.2528/PIER06123101.

[174] T. McGraw, T. Kawai, I. Yassine, and L. Zhu, "Visualizing High-Order Symmetric Tensor Field Structure with Differential Operators," *J. Appl. Math*, vol. 2011, no. 142923, pp. 1–27, 2011, DOI: 10.1155/2011/142923.

[175] X. Zhou, "On Uniqueness Theorem of a Vector Function," *PIER*, vol. 65, pp. 93–102, 2006, DOI: 10.2528/PIER06081202.

[176] K. Kodaira, *Complex Analysis*, Cambridge University Press, ISBN: 9780521809375.

[177] A. P. Calderón and A. Zygmund, "On The Existence of Certain Singular Integrals," *Acta Math.*, vol. 88, pp. 85–139, 1952, DOI: doi.org/10.1007/BF02392130.

[178] I. N. Vekua, *Generalized Analytic Functions*, Pergamon Press, ISBN: 9781614276111.

[179] M. Fushimi, "Principles of Magnetic Resonance Imaging," *Journal of The Society of Instrument and Control Engineers*, vol. 58, no. 7, pp. 520–524, 2019, DOI: 10.11499/sicejl.58.520.

[180] Z.-P. Liang and P. C. Lauterbur, *Principles of Magnetic Resonance Imaging: A Signal Processing Perspective*, IEEE Press, ISBN: 9780819435163.

[181] Y. Wang, *Principles of Magnetic Resonance Imaging: Physics Concepts, Pulse Sequences, & Biomedical Applications*, CreateSpace Independent Publishing Platform, ISBN: 9781479350414.

[182] R. W. Brown, Y.-C. N. Cheng, E. M. Haacke, M. R. Thompson, and R. Venkatesan, *Magnetic Resonance Imaging: Physical Principles and Sequence Design*, John Wiley & Sons, ISBN: 9780471720850.

[183] A. Abragam, *The principles of nuclear magnetism*, Oxford university press, ISBN: 9780198520146.

List of Publications

Original Articles

[1] **M. Fushimi**, and T. Nara, "Three-Dimensional Magnetic Resonance Electrical Properties Tomography Based on Linear Integral Equation Derived from the Generalized Cauchy Formula," *Progress In Electromagnetics Research C*, vol. 105, pp. 147–159, 2020, doi:10.2528/PIERC20052101.

[2] **M. Fushimi**, and T. Nara, "Boundary Value-Free Magnetic Resonance Electrical Properties Tomography Based on the Generalized Cauchy Formula with the Complex-Derivative Boundary Condition," *Progress In Electromagnetics Research M*, vol. 96, pp. 1–8, 2020, doi:10.2528/PIERM20062202.

[3] **M. Fushimi**, and T. Nara, "A Boundary-Value-Free Reconstruction Method for Magnetic Resonance Electrical Properties Tomography Based on the Neumann-Type Integral Formula over a Circular Region," *Journal of Control, Measurement, and System Integration*, vol. 10, no. 6, pp. 571–578, 2017, doi:10.9746/jcmsi.10.571.

[4] T. Nara, T. Furuichi, and **M. Fushimi**, "An explicit reconstruction method for magnetic resonance electrical property tomography based on the generalized Cauchy formula," *Inverse Problems*, vol. 33, no. 10, p. 105005, 2017, doi:10.1088/1361-6420/aa8414.

Review Articles

[1] T. Nara, and **M. Fushimi**, "Imaging the Electric Properties of Human Tissue with MRI," *Medical Imaging Technology*, vol. 38, no. 3, pp. 85–90, 2020, doi:10.11409/mit.38.85. (In Japanese)

[2] **M. Fushimi**, "Principles of Magnetic Resonance Imaging," *Journal of The Society of Instrument and Control Engineers*, vol. 58, no. 7, pp. 520–524, 2019, doi:10.11499/sicejl.58.520. (In Japanese)

Presentations at International Conferences

[1] N. Eda, **M. Fushimi**, K. Hasegawa, and T. Nara, "A Noniterative Three-Dimensional Electrical Property Tomography Reconstruction Method Based on an Integral Equation for the Electric Field," *Proc. SICE 59th Annual Conference*, p. FrAT13.2, Online, Sep. 2020.

[2] **M. Fushimi**, T. Nguyen, and Y. Wang, "Morphology Enabled Quantitative Conductivity Susceptibility Mapping with B1 and B0 Estimation from Complex Multi-echo Gradient Echo Signal," *Proc. ISMRM 28th Annual Meeting*, Online, Aug. 2020.

[3] T. Nara, and **M. Fushimi**, "Computation of H^- from H^+ and its application to regularization for Magnetic Resonance Electrical Properties Tomography (MREPT)," *Proc. ISMRM 28th Annual Meeting*, Online, Aug. 2020.

[4] N. Eda, **M. Fushimi**, K. Hasegawa, and T. Nara, "Noniterative Electrical Properties

Tomography Reconstruction Method Based on Three-Dimensional Integral Equation for the Electric Field," *Proc. ISMRM 28th Annual Meeting*, Online, Aug. 2020.

[5] **M. Fushimi**, P. Spincemaille, and Y. Wang, "Simultaneous Conductivity and Susceptibility Mapping from Multi-echo GRE Data by the Nonlinear Least Square Field Estimation on the Complex Signal Equation", *Proc. 5th International Workshop on MRI Phase Contrast & QSM*, Seoul, Korea, Sep. 2019.

[6] **M. Fushimi**, and T. Nara, "An Explicit EPT Reconstruction Method Based on the Dbar Equation Incorporating Longitudinal Magnetic Field Variations," *Proc. ISMRM 27th Annual Meeting*, Montreal, QC, Canada, May. 2019.

[7] **M. Fushimi**, and T. Nara, "A suppression method of a spread of the spot-like artifact for EPT by zero-point adjusting of the electric field," *Proc. 2nd International Workshop on MR-based Electrical Properties Tomography (IMEP2019)*, Utrecht, Netherlands, Mar. 2019.

[8] T. Nara, **M. Fushimi**, and K. Ariga, "A Series Expansion Method for Reconstruction of the Admittivity Around the Zero Point of the Electric Field in Magnetic Resonance Electrical Property Tomography," *Proc. SICE 57th Annual Conference*, p. FrA03.3, Nara, Japan, Sep. 2018.

[9] **M. Fushimi**, and T. Nara, "Magnetic Resonance Based Electrical Properties Reconstruction with Total Variation Regularization and Zero-point Control of Electric Fields," *Proc. PIERS 2018*, p. 49, Toyama, Japan, Aug. 2018.

[10] **M. Fushimi**, and T. Nara, "An Explicit Method for MR-Based Electrical Properties Reconstruction Free from Their Boundary Values," *Proc. ISMRM 26th Annual Meeting*, Paris, France, Jun. 2018.

[11] **M. Fushimi**, and T. Nara, "A Boundary-Value-Free Method for Reconstructing Electrical Properties Using MRI Based on the Neumann-Type Integral Formula," *Proc. SICE 56th Annual Conference*, p. ThA08.2, Ishikawa, Japan, Sep. 2017.

[12] T. Nara, T. Furuichi, and **M. Fushimi**, "Generalized Cauchy formula for magnetic resonance electrical property tomography," *ACCA-UK/JP Third International Workshop*, London, UK, Mar. 2017. (Invited)

[13] T. Nara, T. Furuichi, **M. Fushimi**, and S. Ando, "A Direct Reconstruction Formula for the Conductivity and Permittivity from the Measurements of the Time-harmonic Magnetic Field," *ICCOPT 2016*, Tokyo, Japan, Aug. 2016. (Invited)

Presentations at Domestic Conferences

[1] N. Eda, **M. Fushimi**, and T. Nara, "An Iterative Reconstruction Method for the Electric Field and Electrical Properties Using MRI Based on the Helmholtz Identity," *Proc. SICE 37th Sensing Forum*, pp. 130–133, Online, Sep. 2020. (In Japanese)

[2] T. Nara, and **M. Fushimi**, "Direct Reconstruction of Electric Properties Using MRI—Zero-point Control of the Electric Field and Estimation Using Only the Phase Image," *Proc. Japan Biomagnetism and Bioelectromagnetics Society 34th Annual Meeting*, vol. 32, no. 1, pp. 184–185, Hokkaido, Japan, Jun. 2019. (In Japanese)

[3] **M. Fushimi**, and T. Nara, "Three-Dimensional Reconstruction of Electrical Properties Using MRI Based on the Integral Formula for Generalized Analytic Functions," *IEICE Technical Report*, vol. 117, no. 518, pp. 135–140, MI2017-103, Okinawa, Japan, Mar. 2018. (In Japanese)

[4] **M. Fushimi**, and T. Nara, "Stabilization of the Direct Reconstruction Method for Magnetic Resonance Electrical Properties Tomography: Regularization and Zero-Point Control of the Electric Field," *Proc. SICE 34th Sensing Forum*, pp. 314–319, Kumamoto, Japan, Sep. 2017. (In Japanese)

[5] **M. Fushimi**, T. Furuichi, and T. Nara, "Boundary Value Estimation and Distribution Reconstruction of Electrical Properties on a Plane Using MRI," *IEICE Technical Report*, vol. 116, no. 224, pp. 9–12, MICT2016-35, Tokyo, Japan, Sep. 2016. (In Japanese)
[6] **M. Fushimi**, T. Furuichi, and T. Nara, "Electrical Properties Tomography from MRI Data Based on the Weighted Integral Method," *Proc. SICE 33rd Sensing Forum*, p. 206, Wakayama, Japan, Sep. 2016. (In Japanese)
[7] T. Furuichi, **M. Fushimi**, and T. Nara, "A D-bar Equation Approach for MRI-based Electric Properties Tomography," *Proc. SICE 33rd Sensing Forum*, pp. 198–202, Wakayama, Japan, Sep. 2016. (In Japanese)

Honors and Awards

[1] ISMRM, 28th Annual Meeting, Magna Cum Laude Merit Award, Aug. 2020.
[2] SICE, Measurement Division, Distinguished Paper Award in 2019, Aug. 2019.
[3] SICE, 34th Sensing Forum, Research Encouragement Award, Sep. 2017.
[4] IEICE, MI Study Group, Research Encouragement Award in 2016, May 2017.
[5] SICE, 33rd Sensing Forum, Distinguished Poster Award, Sep. 2016.

Appendix A

Fundamentals of Mathematical Analysis

This appendix provides fundamental theorems used in this thesis to derive IEs for the impedivity. In section A.1, Helmholtz's decomposition is reviewed in detail and the representation formulae of vector and tensor fields by their divergence and curl are derived. The relation between those representation formulae and Helmholtz's decomposition is also discussed. In, section A.2, some complex differential and integral operators playing fundamental roles in complex analysis are introduced and the integral formulae of a complex function are reviewed.

A.1 Vector and Tensor Analysis

A.1.1 Helmholtz's Decomposition

Helmholtz's theorem gives a decomposition of vector fields and has numerous applications in a wide range of fields [173]. First, we review Helmholtz's theorem in the entire plane.

If a vector field $\boldsymbol{f} \in C^1(\mathbb{R}^3)$ is continuous and rapidly vanishes at infinity, then $\boldsymbol{f}$ can be uniquely decomposed into the sum of an irrotational field $\boldsymbol{f}_{\mathrm{L}}$ and a solenoidal field $\boldsymbol{f}_{\mathrm{T}}$ as

$$\boldsymbol{f} = \boldsymbol{f}_{\mathrm{L}} + \boldsymbol{f}_{\mathrm{T}} = -\nabla\phi + \nabla \times \boldsymbol{A}, \tag{A.1}$$

where ϕ and $\boldsymbol{A}$ are given as

$$\phi(\boldsymbol{r}) = \int_{\mathbb{R}^3} \frac{\nabla \cdot \boldsymbol{f}(\boldsymbol{r}')}{4\pi|\boldsymbol{r}' - \boldsymbol{r}|} \mathrm{d}V', \tag{A.2}$$

$$\boldsymbol{A}(\boldsymbol{r}) = \int_{\mathbb{R}^3} \frac{\nabla \times \boldsymbol{f}(\boldsymbol{r}')}{4\pi|\boldsymbol{r}' - \boldsymbol{r}|} \mathrm{d}V'. \tag{A.3}$$

Helmholtz's theorem for tensor fields is discussed in [174]. If a tensor field $\boldsymbol{f} \in C^1(\mathbb{R}^3)$ is continuous and rapidly vanishes at infinity, then $\boldsymbol{f}$ can be uniquely decomposed into the sum of an irrotational field $\boldsymbol{f}_{\mathrm{L}}$ and a solenoidal field $\boldsymbol{f}_{\mathrm{T}}$ as

$$\boldsymbol{f} = \boldsymbol{f}_{\mathrm{L}} + \boldsymbol{f}_{\mathrm{T}} = -\nabla\boldsymbol{\phi} + \nabla \times \boldsymbol{A}, \tag{A.4}$$

where $\boldsymbol{\phi}$ and $\boldsymbol{A}$ are given as

$$\boldsymbol{\phi}(\boldsymbol{r}) = \int_{\mathbb{R}^3} \frac{\nabla \cdot \boldsymbol{f}(\boldsymbol{r}')}{4\pi|\boldsymbol{r}' - \boldsymbol{r}|} \mathrm{d}V', \tag{A.5}$$

$$\boldsymbol{A}(\boldsymbol{r}) = \int_{\mathbb{R}^3} \frac{\nabla \times \boldsymbol{f}(\boldsymbol{r}')}{4\pi|\boldsymbol{r}' - \boldsymbol{r}|} \mathrm{d}V'. \tag{A.6}$$

The irrotational and solenoidal fields are also respectively known as the longitudinal and transverse components of the original vector field. This is because the frequency spectrum of the longitudinal component is parallel to the wave number vector $\boldsymbol{k}$ and that of the transverse component is perpendicular to it. In fact, it holds that

$$\mathcal{F}[\nabla \times \boldsymbol{f}_{\mathrm{L}}](\boldsymbol{k}) = \mathrm{i}\boldsymbol{k} \times \mathcal{F}[\boldsymbol{f}_{\mathrm{L}}](\boldsymbol{k}) = \boldsymbol{0}, \qquad \mathcal{F}[\nabla \cdot \boldsymbol{f}_{\mathrm{T}}](\boldsymbol{k}) = \mathrm{i}\boldsymbol{k} \cdot \mathcal{F}[\boldsymbol{f}_{\mathrm{T}}](\boldsymbol{k}) = 0, \tag{A.7}$$

$$\mathcal{F}[\nabla \times \boldsymbol{f}_{\mathrm{L}}](\boldsymbol{k}) = \mathrm{i}\boldsymbol{k} \times \mathcal{F}[\boldsymbol{f}_{\mathrm{L}}](\boldsymbol{k}) = \boldsymbol{0}, \qquad \mathcal{F}[\nabla \cdot \boldsymbol{f}_{\mathrm{T}}](\boldsymbol{k}) = \mathrm{i}\boldsymbol{k} \cdot \mathcal{F}[\boldsymbol{f}_{\mathrm{T}}](\boldsymbol{k}) = \boldsymbol{0}. \tag{A.8}$$

This observation leads to the orthogonality and uniqueness of the decomposition. Since $\mathcal{F}[\boldsymbol{f}_{\mathrm{L}}]$ is parallel to $\boldsymbol{k}$ and $\mathcal{F}[\boldsymbol{f}_{\mathrm{T}}]$ is perpendicular to it, they are orthogonal with each other, and thus it holds that

$$\langle \mathcal{F}[\boldsymbol{f}_{\mathrm{L}}](\boldsymbol{k}), \mathcal{F}[\boldsymbol{f}_{\mathrm{T}}](\boldsymbol{k}) \rangle \equiv 0, \tag{A.9}$$

$$\langle \mathcal{F}[\boldsymbol{f}_{\mathrm{L}}](\boldsymbol{k}), \mathcal{F}[\boldsymbol{f}_{\mathrm{T}}](\boldsymbol{k}) \rangle \equiv 0 \tag{A.10}$$

for all $\boldsymbol{k} \in \mathbb{R}^3$. Therefore, it holds in the frequency domain that

$$\langle\!\langle \mathcal{F}[\boldsymbol{f}_{\mathrm{L}}], \mathcal{F}[\boldsymbol{f}_{\mathrm{T}}] \rangle\!\rangle_{\mathbb{R}^3} = \int_{\mathbb{R}^3} \langle \mathcal{F}[\boldsymbol{f}_{\mathrm{L}}](\boldsymbol{k}), \mathcal{F}[\boldsymbol{f}_{\mathrm{T}}](\boldsymbol{k}) \rangle \mathrm{d}^3\boldsymbol{k} = \int_{\mathbb{R}^3} 0 \mathrm{d}^3\boldsymbol{k} = 0, \tag{A.11}$$

$$\langle\!\langle \mathcal{F}[\boldsymbol{f}_{\mathrm{L}}], \mathcal{F}[\boldsymbol{f}_{\mathrm{T}}] \rangle\!\rangle_{\mathbb{R}^3} = \int_{\mathbb{R}^3} \langle \mathcal{F}[\boldsymbol{f}_{\mathrm{L}}](\boldsymbol{k}), \mathcal{F}[\boldsymbol{f}_{\mathrm{T}}](\boldsymbol{k}) \rangle \mathrm{d}^3\boldsymbol{k} = \int_{\mathbb{R}^3} 0 \mathrm{d}^3\boldsymbol{k} = 0. \tag{A.12}$$

Hence, Parseval's theorem leads to the orthogonality in the original spatial domain.

$$\langle\!\langle \boldsymbol{f}_{\mathrm{L}}, \boldsymbol{f}_{\mathrm{T}} \rangle\!\rangle_{\mathbb{R}^3} = \frac{1}{2\pi} \langle\!\langle \mathcal{F}[\boldsymbol{f}_{\mathrm{L}}], \mathcal{F}[\boldsymbol{f}_{\mathrm{T}}] \rangle\!\rangle_{\mathbb{R}^3} = 0, \tag{A.13}$$

$$\langle\!\langle \boldsymbol{f}_{\mathrm{L}}, \boldsymbol{f}_{\mathrm{T}} \rangle\!\rangle_{\mathbb{R}^3} = \frac{1}{2\pi} \langle\!\langle \mathcal{F}[\boldsymbol{f}_{\mathrm{L}}], \mathcal{F}[\boldsymbol{f}_{\mathrm{T}}] \rangle\!\rangle_{\mathbb{R}^3} = 0. \tag{A.14}$$

Helmholtz's theorem can be extended to a bounded domain as extensively discussed in [173, 175].

Theorem A.1 (Helmholtz's theorem for vector fields)**.** Let $\Omega \subseteq \mathbb{R}^3$ be a domain whose boundary $\partial\Omega$ is a piecewise smooth surface. If a vector field $\boldsymbol{f} \in C^1(\Omega)$ is bounded and continuous on $\partial\Omega$, then $\boldsymbol{f}$ can be decomposed into the sum of an irrotational field $\boldsymbol{f}_{\mathrm{L}}$ and a solenoidal field $\boldsymbol{f}_{\mathrm{T}}$ as

$$\boldsymbol{f} = \boldsymbol{f}_{\mathrm{L}} + \boldsymbol{f}_{\mathrm{T}} = -\nabla\phi + \nabla \times \boldsymbol{A}, \tag{A.15}$$

where ϕ and $\boldsymbol{A}$ are expressed as

$$\phi(\boldsymbol{r}) = \int_{\Omega} \frac{\nabla \cdot \boldsymbol{f}(\boldsymbol{r}')}{4\pi|\boldsymbol{r}' - \boldsymbol{r}|} \mathrm{d}V' - \oint_{\partial\Omega} \frac{\boldsymbol{n}(\boldsymbol{r}') \cdot \boldsymbol{f}(\boldsymbol{r}')}{4\pi|\boldsymbol{r}' - \boldsymbol{r}|} \mathrm{d}S', \tag{A.16}$$

$$\boldsymbol{A}(\boldsymbol{r}) = \int_{\Omega} \frac{\nabla \times \boldsymbol{f}(\boldsymbol{r}')}{4\pi|\boldsymbol{r}' - \boldsymbol{r}|} \mathrm{d}V' - \oint_{\partial\Omega} \frac{\boldsymbol{n}(\boldsymbol{r}') \times \boldsymbol{f}(\boldsymbol{r}')}{4\pi|\boldsymbol{r}' - \boldsymbol{r}|} \mathrm{d}S'. \tag{A.17}$$

Similarly, the following can be stated for tensor fields.

Theorem A.2 (Helmholtz's theorem for tensor fields)**.** If a tensor field $\boldsymbol{f} \in C^1(\Omega)$ is bounded and continuous on $\partial\Omega$, then $\boldsymbol{f}$ can be decomposed into the sum of an irrotational

field $\boldsymbol{f}_{\mathrm{L}}$ and a solenoidal field $\boldsymbol{f}_{\mathrm{T}}$ as

$$\boldsymbol{f} = \boldsymbol{f}_{\mathrm{L}} + \boldsymbol{f}_{\mathrm{T}} = -\nabla\boldsymbol{\phi} + \nabla \times \boldsymbol{A}, \tag{A.18}$$

where ϕ and $\boldsymbol{A}$ are expressed as

$$\boldsymbol{\phi}(\boldsymbol{r}) = \int_{\Omega} \frac{\nabla \cdot \boldsymbol{f}(\boldsymbol{r}')}{4\pi|\boldsymbol{r}' - \boldsymbol{r}|}\mathrm{d}V' - \oint_{\partial\Omega} \frac{\boldsymbol{n}(\boldsymbol{r}') \cdot \boldsymbol{f}(\boldsymbol{r}')}{4\pi|\boldsymbol{r}' - \boldsymbol{r}|}\mathrm{d}S', \tag{A.19}$$

$$\boldsymbol{A}(\boldsymbol{r}) = \int_{\Omega} \frac{\nabla \times \boldsymbol{f}(\boldsymbol{r}')}{4\pi|\boldsymbol{r}' - \boldsymbol{r}|}\mathrm{d}V' - \oint_{\partial\Omega} \frac{\boldsymbol{n}(\boldsymbol{r}') \times \boldsymbol{f}(\boldsymbol{r}')}{4\pi|\boldsymbol{r}' - \boldsymbol{r}|}\mathrm{d}S'. \tag{A.20}$$

Note that the orthogonality and uniqueness of the decomposition do not hold in general [173]. To ensure orthogonality and uniqueness, one could impose that $\boldsymbol{f}_{\mathrm{L}}$ is normal to the surface on $\partial\Omega$ and $\boldsymbol{f}_{\mathrm{T}}$ is tangential to the surface on $\partial\Omega$ [175]. Another way is to extend the function defined over a bounded domain $\boldsymbol{f} : \Omega \to \mathbb{C}^3$ to $\tilde{\boldsymbol{f}} : \mathbb{R}^3 \to \mathbb{C}^3$ in the following manner:

$$\tilde{\boldsymbol{f}}(\boldsymbol{r}) = \begin{cases} \boldsymbol{f}(\boldsymbol{r}) & \boldsymbol{r} \in \Omega, \\ \boldsymbol{0} & \boldsymbol{r} \in \mathbb{R}^3 \setminus \Omega, \end{cases} \tag{A.21}$$

$$\tilde{\boldsymbol{f}}(\boldsymbol{r}) = \begin{cases} \boldsymbol{f}(\boldsymbol{r}) & \boldsymbol{r} \in \Omega, \\ \boldsymbol{0} & \boldsymbol{r} \in \mathbb{R}^3 \setminus \Omega. \end{cases} \tag{A.22}$$

Then, for this extended function defined over the entire plane, the original Helmholtz decomposition holds and so the orthogonality of the decomposition. In the following, we derive several representation formulae of vector and tensor fields in terms of their gradient, divergence, and curl as well as the fields themselves.

A.1.2 Green's Identities for Vector and Tensor Fields

Integrating the product rules of differentiation

$$\nabla \cdot (w\nabla\boldsymbol{f}) = w\Delta\boldsymbol{f} + \nabla w \cdot \nabla\boldsymbol{f}, \tag{A.23}$$

$$\nabla \cdot (w\nabla\boldsymbol{f}) = w\Delta\boldsymbol{f} + \nabla w \cdot \nabla\boldsymbol{f}, \tag{A.24}$$

and applying Gauss' theorem yields Green's first identities as presented below.

Let Ω be a domain with a piecewise smooth boundary $\partial\Omega$. If $w \in C^1(\Omega)$ and $\boldsymbol{f}, \boldsymbol{f} \in C^2(\Omega)$, then it holds that

$$\int_{\Omega} w\Delta\boldsymbol{f}\mathrm{d}V = \oint_{\partial\Omega} \boldsymbol{n} \cdot w\nabla\boldsymbol{f}\mathrm{d}S - \int_{\Omega} \nabla w \cdot \nabla\boldsymbol{f}\mathrm{d}V, \tag{A.25}$$

$$\int_{\Omega} w\Delta\boldsymbol{f}\mathrm{d}V = \oint_{\partial\Omega} \boldsymbol{n} \cdot w\nabla\boldsymbol{f}\mathrm{d}S - \int_{\Omega} \nabla w \cdot \nabla\boldsymbol{f}\mathrm{d}V, \tag{A.26}$$

where $\boldsymbol{n}$ is the outward unit normal vector on $\partial\Omega$.

Eqs. (A.25) and (A.26) represent the second-order derivatives of the fields by their first-order derivatives. We refer to Eqs. (A.25) and (A.26) as the grad versions of Green's first identity. Once again integrating both sides of the product rules

$$\nabla \cdot (\nabla w\boldsymbol{f}) = \Delta w\boldsymbol{f} + \nabla w \cdot \nabla\boldsymbol{f}, \tag{A.27}$$

$$\nabla \cdot (\nabla w\boldsymbol{f}) = \Delta w\boldsymbol{f} + \nabla w \cdot \nabla\boldsymbol{f} \tag{A.28}$$

and applying Gauss' theorem yields Green's second identities given below.

Let Ω be a domain with a piecewise smooth boundary $\partial\Omega$. If $w \in C^2(\Omega)$ and $\boldsymbol{f}, \boldsymbol{f} \in C^2(\Omega)$, then it holds that

$$\int_\Omega w\Delta \boldsymbol{f} \mathrm{d}V = \oint_{\partial\Omega} \boldsymbol{n} \cdot (w\nabla \boldsymbol{f} - \nabla w \boldsymbol{f}) \mathrm{d}S + \int_\Omega \Delta w \boldsymbol{f} \mathrm{d}V, \tag{A.29}$$

$$\int_\Omega w\Delta \boldsymbol{f} \mathrm{d}V = \oint_{\partial\Omega} \boldsymbol{n} \cdot (w\nabla \boldsymbol{f} - \nabla w \boldsymbol{f}) \mathrm{d}S + \int_\Omega \Delta w \boldsymbol{f} \mathrm{d}V, \tag{A.30}$$

where $\boldsymbol{n}$ is the outward unit normal vector on $\partial\Omega$.

Eqs. (A.29) and (A.30) represent the second-order derivatives of the fields by themselves. We refer to Eqs. (A.29) and (A.30) as the grad versions of Green's second identity.

The above equations represent vector and tensor fields using their gradient. Although these formulae lead to a simple expression of a field, representing a field by its divergence and curl provides us with geometric and physical insights. By the properties of the Laplacian, it holds that

$$\int_\Omega w\Delta \boldsymbol{f} \mathrm{d}V = \int_\Omega w\nabla(\nabla \cdot \boldsymbol{f}) \mathrm{d}V - \int_\Omega w\nabla \times (\nabla \times \boldsymbol{f}) \mathrm{d}V, \tag{A.31}$$

$$\int_\Omega w\Delta \boldsymbol{f} \mathrm{d}V = \int_\Omega w\nabla(\nabla \cdot \boldsymbol{f}) \mathrm{d}V - \int_\Omega w\nabla \times (\nabla \times \boldsymbol{f}) \mathrm{d}V. \tag{A.32}$$

Using the identities

$$\nabla(w\nabla \cdot \boldsymbol{f}) = w\nabla(\nabla \cdot \boldsymbol{f}) + \nabla w\nabla \cdot \boldsymbol{f}, \tag{A.33}$$

$$\nabla \times (w\nabla \times \boldsymbol{f}) = w\nabla \times (\nabla \times \boldsymbol{f}) + \nabla w \times (\nabla \times \boldsymbol{f}), \tag{A.34}$$

$$\nabla(w\nabla \cdot \boldsymbol{f}) = w\nabla(\nabla \cdot \boldsymbol{f}) + \nabla w\nabla \cdot \boldsymbol{f}, \tag{A.35}$$

$$\nabla \times (w\nabla \times \boldsymbol{f}) = w\nabla \times (\nabla \times \boldsymbol{f}) + \nabla w \times (\nabla \times \boldsymbol{f}), \tag{A.36}$$

and integrating by parts, we obtain Green's first identity for vector and tensor fields.

Theorem A.3 (Green's first identity)**.** Let Ω be a domain with a piecewise smooth boundary $\partial\Omega$. If $w \in C^1(\Omega)$ and $\boldsymbol{f}, \boldsymbol{f} \in C^2(\Omega)$, then it holds that

$$\int_\Omega w\Delta \boldsymbol{f} \mathrm{d}V = \oint_{\partial\Omega} \boldsymbol{n}w(\nabla \cdot \boldsymbol{f}) - \boldsymbol{n} \times w(\nabla \times \boldsymbol{f}) \mathrm{d}S - \int_\Omega \nabla w(\nabla \cdot \boldsymbol{f}) - \nabla w \times (\nabla \times \boldsymbol{f}) \mathrm{d}V, \tag{A.37}$$

$$\int_\Omega w\Delta \boldsymbol{f} \mathrm{d}V = \oint_{\partial\Omega} \boldsymbol{n}w(\nabla \cdot \boldsymbol{f}) - \boldsymbol{n} \times w(\nabla \times \boldsymbol{f}) \mathrm{d}S - \int_\Omega \nabla w(\nabla \cdot \boldsymbol{f}) - \nabla w \times (\nabla \times \boldsymbol{f}) \mathrm{d}V, \tag{A.38}$$

where $\boldsymbol{n}$ is the outward unit normal vector on $\partial\Omega$.

Equations (A.37) and (A.38) relate the Laplacian of the fields with their first-order derivatives like Eqs. (A.25) and (A.26), but they use the divergence and curl of the fields instead of their gradient. We refer to Eqs. (A.37) and (A.38) as the div–curl version of Green's first identity. Once again integrating both sides of the identities

$$\nabla w(\nabla \cdot \boldsymbol{f}) - \nabla w \times (\nabla \times \boldsymbol{f}) = \nabla \cdot (\boldsymbol{f}\nabla w) + \nabla \cdot (\nabla w \boldsymbol{f}) - \nabla(\nabla w \cdot \boldsymbol{f}) - \Delta w \boldsymbol{f}, \tag{A.39}$$

$$\nabla w(\nabla \cdot \boldsymbol{f}) - \nabla w \times (\nabla \times \boldsymbol{f}) = (\nabla \cdot (\boldsymbol{f}\nabla w))^\mathsf{T} + \nabla \cdot (\nabla w \boldsymbol{f}) - \nabla(\nabla w \cdot \boldsymbol{f}) - \Delta w \boldsymbol{f}, \tag{A.40}$$

and integrating by parts, we obtain

$$\int_\Omega w\Delta \boldsymbol{f}\mathrm{d}V = \oint_{\partial\Omega} \boldsymbol{n}w(\nabla\cdot\boldsymbol{f}) - \boldsymbol{n}\times w(\nabla\times\boldsymbol{f})\mathrm{d}S \\ - \oint_{\partial\Omega} \boldsymbol{n}\cdot\boldsymbol{f}\nabla w + \boldsymbol{n}\cdot\nabla w\boldsymbol{f} - \boldsymbol{n}\nabla w\cdot\boldsymbol{f}\mathrm{d}S + \int_\Omega \Delta w\boldsymbol{f}\mathrm{d}V, \quad \text{(A.41)}$$

$$\int_\Omega w\Delta \boldsymbol{f}\mathrm{d}V = \oint_{\partial\Omega} \boldsymbol{n}w(\nabla\cdot\boldsymbol{f}) - \boldsymbol{n}\times w(\nabla\times\boldsymbol{f})\mathrm{d}S \\ - \oint_{\partial\Omega} (\boldsymbol{n}\cdot\boldsymbol{f}\nabla w)^{\mathsf{T}} + \boldsymbol{n}\cdot\nabla w\boldsymbol{f} - \boldsymbol{n}\nabla w\cdot\boldsymbol{f}\mathrm{d}S + \int_\Omega \Delta w\boldsymbol{f}\mathrm{d}V. \quad \text{(A.42)}$$

Substituting the triplet identities

$$\boldsymbol{n}\nabla w\cdot\boldsymbol{f} - \boldsymbol{n}\cdot\nabla w\boldsymbol{f} = \nabla w\times(\boldsymbol{n}\times\boldsymbol{f}), \quad \text{(A.43)}$$

$$\boldsymbol{n}\nabla w\cdot\boldsymbol{f} - \boldsymbol{n}\cdot\nabla w\boldsymbol{f} = \nabla w\times(\boldsymbol{n}\times\boldsymbol{f}) \quad \text{(A.44)}$$

into the above equations yields the following theorem.

Theorem A.4 (Green's second identity)**.** Let Ω be a domain with a piecewise smooth boundary $\partial\Omega$. If $w\in C^2(\Omega)$ and $\boldsymbol{f},\boldsymbol{f}\in C^2(\Omega)$, then it holds that

$$\int_\Omega w\Delta \boldsymbol{f}\mathrm{d}V = \oint_{\partial\Omega} \boldsymbol{n}w(\nabla\cdot\boldsymbol{f}) - \boldsymbol{n}\times w(\nabla\times\boldsymbol{f})\mathrm{d}S \\ - \oint_{\partial\Omega} \nabla w(\boldsymbol{n}\cdot\boldsymbol{f}) - \nabla w\times(\boldsymbol{n}\times\boldsymbol{f})\mathrm{d}S + \int_\Omega \Delta w\boldsymbol{f}\mathrm{d}V, \quad \text{(A.45)}$$

$$\int_\Omega w\Delta \boldsymbol{f}\mathrm{d}V = \oint_{\partial\Omega} \boldsymbol{n}w(\nabla\cdot\boldsymbol{f}) - \boldsymbol{n}\times w(\nabla\times\boldsymbol{f})\mathrm{d}S \\ - \oint_{\partial\Omega} \nabla w(\boldsymbol{n}\cdot\boldsymbol{f}) - \nabla w\times(\boldsymbol{n}\times\boldsymbol{f})\mathrm{d}S + \int_\Omega \Delta w\boldsymbol{f}\mathrm{d}V, \quad \text{(A.46)}$$

where $\boldsymbol{n}$ is the outward unit normal vector on $\partial\Omega$.

Equations (A.45) and (A.46) relate the Laplacian of the fields with themselves like Eqs. (A.29) and (A.30), but they use the divergence and curl of the fields instead of their gradient on the boundary of the domain. We refer to Eqs. (A.45) and (A.46) as the div–curl version of Green's second identities.

A.1.3 Representation Formulae of Vector and Tensor Fields

Using Green's identities described above, several representation formulae of vector and tensor fields can be deduced. First, taking the difference of the grad version of Green's first and second identities yields

$$\int_\Omega \Delta w\boldsymbol{f}\mathrm{d}V = \oint_{\partial\Omega} \boldsymbol{n}\cdot\nabla w\boldsymbol{f}\mathrm{d}S - \int_\Omega \nabla w\cdot\nabla\boldsymbol{f}\mathrm{d}V, \quad \text{(A.47)}$$

$$\int_\Omega \Delta w\boldsymbol{f}\mathrm{d}V = \oint_{\partial\Omega} \boldsymbol{n}\cdot\nabla w\boldsymbol{f}\mathrm{d}S - \int_\Omega \nabla w\cdot\nabla\boldsymbol{f}\mathrm{d}V. \quad \text{(A.48)}$$

If we choose the fundamental solution G of the Laplace operator as a weighting function w, i.e.,

$$w(\boldsymbol{r}') = G(\boldsymbol{r}';\boldsymbol{r}) = \frac{1}{4\pi|\boldsymbol{r}'-\boldsymbol{r}|}, \tag{A.49}$$

then it holds that $\Delta w(\boldsymbol{r}') = -\delta(\boldsymbol{r}'-\boldsymbol{r})$, and thus we have

$$\boldsymbol{f}(\boldsymbol{r}) = -\oint_{\partial\Omega} \boldsymbol{n}(\boldsymbol{r}')\cdot\nabla G(\boldsymbol{r}';\boldsymbol{r})\boldsymbol{f}(\boldsymbol{r}')\mathrm{d}S' + \int_{\Omega} \nabla G(\boldsymbol{r}';\boldsymbol{r})\cdot\nabla\boldsymbol{f}(\boldsymbol{r}')\mathrm{d}V', \tag{A.50}$$

$$\boldsymbol{f}(\boldsymbol{r}) = -\oint_{\partial\Omega} \boldsymbol{n}(\boldsymbol{r}')\cdot\nabla G(\boldsymbol{r}';\boldsymbol{r})\boldsymbol{f}(\boldsymbol{r}')\mathrm{d}S' + \int_{\Omega} \nabla G(\boldsymbol{r}';\boldsymbol{r})\cdot\nabla\boldsymbol{f}(\boldsymbol{r}')\mathrm{d}V'. \tag{A.51}$$

Equations (A.50) and (A.50) represent the fields defined on a bounded domain by their gradient inside the domain and the fields themselves on the boundary.

Similarly, taking the difference of the div–curl version of Green's first and second identities yields

$$\int_{\Omega} \Delta w\boldsymbol{f}\mathrm{d}V = \oint_{\partial\Omega} \nabla w(\boldsymbol{n}\cdot\boldsymbol{f}) - \nabla w\times(\boldsymbol{n}\times\boldsymbol{f})\mathrm{d}S - \int_{\Omega} \nabla w(\nabla\cdot\boldsymbol{f}) - \nabla w\times(\nabla\times\boldsymbol{f})\mathrm{d}V, \tag{A.52}$$

$$\int_{\Omega} \Delta w\boldsymbol{f}\mathrm{d}V = \oint_{\partial\Omega} \nabla w(\boldsymbol{n}\cdot\boldsymbol{f}) - \nabla w\times(\boldsymbol{n}\times\boldsymbol{f})\mathrm{d}S - \int_{\Omega} \nabla w(\nabla\cdot\boldsymbol{f}) - \nabla w\times(\nabla\times\boldsymbol{f})\mathrm{d}V. \tag{A.53}$$

If we again take G as the weighting function w, we have the following theorem.

Theorem A.5 (The Div–Curl form representation formula)**.** Let Ω be a domain with a piecewise smooth boundary $\partial\Omega$. If $\boldsymbol{f},\boldsymbol{f}\in C^1(\Omega)$, then it holds thats

$$\begin{aligned}\boldsymbol{f}(\boldsymbol{r}) = &-\oint_{\partial\Omega} \nabla G(\boldsymbol{r}';\boldsymbol{r})(\boldsymbol{n}(\boldsymbol{r}')\cdot\boldsymbol{f}(\boldsymbol{r}'))\mathrm{d}S' + \int_{\Omega} \nabla G(\boldsymbol{r}';\boldsymbol{r})(\nabla\cdot\boldsymbol{f}(\boldsymbol{r}'))\mathrm{d}V' \\ &+\oint_{\partial\Omega} \nabla G(\boldsymbol{r}';\boldsymbol{r})\times(\boldsymbol{n}(\boldsymbol{r}')\times\boldsymbol{f}(\boldsymbol{r}'))\mathrm{d}S' - \int_{\Omega} \nabla G(\boldsymbol{r}';\boldsymbol{r})\times(\nabla\times\boldsymbol{f}(\boldsymbol{r}'))\mathrm{d}V',\end{aligned} \tag{A.54}$$

$$\begin{aligned}\boldsymbol{f}(\boldsymbol{r}) = &-\oint_{\partial\Omega} \nabla G(\boldsymbol{r}';\boldsymbol{r})(\boldsymbol{n}(\boldsymbol{r}')\cdot\boldsymbol{f}(\boldsymbol{r}'))\mathrm{d}S' + \int_{\Omega} \nabla G(\boldsymbol{r}';\boldsymbol{r})(\nabla\cdot\boldsymbol{f}(\boldsymbol{r}'))\mathrm{d}V' \\ &+\oint_{\partial\Omega} \nabla G(\boldsymbol{r}';\boldsymbol{r})\times(\boldsymbol{n}(\boldsymbol{r}')\times\boldsymbol{f}(\boldsymbol{r}'))\mathrm{d}S' - \int_{\Omega} \nabla G(\boldsymbol{r}';\boldsymbol{r})\times(\nabla\times\boldsymbol{f}(\boldsymbol{r}'))\mathrm{d}V'.\end{aligned} \tag{A.55}$$

where $\boldsymbol{n}$ is the outward unit normal vector on $\partial\Omega$.

Equations (A.54) and (A.55) represent the fields defined on a bounded domain by their divergence and curl inside the domain and the fields themselves on the boundary.

This div–curl version of representation formulae is closely related to Helmholtz's theorem. To see this, let us first define the following operators:

$$\boldsymbol{P}_{\mathrm{L}}[\boldsymbol{f}](\boldsymbol{r}) \coloneqq -\oint_{\partial\Omega} \nabla G(\boldsymbol{r}';\boldsymbol{r})(\boldsymbol{n}(\boldsymbol{r}')\cdot\boldsymbol{f}(\boldsymbol{r}'))\mathrm{d}S' + \int_{\Omega} \nabla G(\boldsymbol{r}';\boldsymbol{r})(\nabla\cdot\boldsymbol{f}(\boldsymbol{r}'))\mathrm{d}V', \tag{A.56}$$

$$\boldsymbol{P}_{\mathrm{T}}[\boldsymbol{f}](\boldsymbol{r}) \coloneqq \oint_{\partial\Omega} \nabla G(\boldsymbol{r}';\boldsymbol{r})\times(\boldsymbol{n}(\boldsymbol{r}')\times\boldsymbol{f}(\boldsymbol{r}'))\mathrm{d}S' - \int_{\Omega} \nabla G(\boldsymbol{r}';\boldsymbol{r})\times(\nabla\times\boldsymbol{f}(\boldsymbol{r}'))\mathrm{d}V'. \tag{A.57}$$

Using the relation $\nabla_{\boldsymbol{r}} G(\boldsymbol{r}';\boldsymbol{r}) = -\nabla_{\boldsymbol{r}'} G(\boldsymbol{r}';\boldsymbol{r})$, $\boldsymbol{P}_{\mathrm{L}}$ and $\boldsymbol{P}_{\mathrm{T}}$ are represented as $\boldsymbol{P}_{\mathrm{L}}[\boldsymbol{f}] = -\nabla\phi$ and $\boldsymbol{P}_{\mathrm{T}}[\boldsymbol{f}] = \nabla \times \boldsymbol{A}$, where

$$\phi(\boldsymbol{r}) = -\oint_{\partial\Omega} G(\boldsymbol{r}';\boldsymbol{r})(\boldsymbol{n}(\boldsymbol{r}') \cdot \boldsymbol{f}(\boldsymbol{r}'))\mathrm{d}S' + \int_{\Omega} G(\boldsymbol{r}';\boldsymbol{r})(\nabla \cdot \boldsymbol{f}(\boldsymbol{r}'))\mathrm{d}V', \tag{A.58}$$

$$\boldsymbol{A}(\boldsymbol{r}) = -\oint_{\partial\Omega} G(\boldsymbol{r}';\boldsymbol{r})(\boldsymbol{n}(\boldsymbol{r}') \times \boldsymbol{f}(\boldsymbol{r}'))\mathrm{d}S' + \int_{\Omega} G(\boldsymbol{r}';\boldsymbol{r})(\nabla \times \boldsymbol{f}(\boldsymbol{r}'))\mathrm{d}V'. \tag{A.59}$$

Hence, for a given vector field $\boldsymbol{f}$, $\boldsymbol{f}_{\mathrm{L}} = \boldsymbol{P}_{\mathrm{L}}[\boldsymbol{f}]$ is the longitudinal component, and $\boldsymbol{f}_{\mathrm{T}} = \boldsymbol{P}_{\mathrm{T}}[\boldsymbol{f}]$ corresponds to the transverse component of the field. Therefore, Eq. (A.54) gives the vector Helmholtz decomposition. For tensor fields, we define the following operators:

$$\boldsymbol{P}_{\mathrm{L}}[\boldsymbol{f}](\boldsymbol{r}) \coloneqq -\oint_{\partial\Omega} \nabla G(\boldsymbol{r}';\boldsymbol{r})(\boldsymbol{n}(\boldsymbol{r}') \cdot \boldsymbol{f}(\boldsymbol{r}'))\mathrm{d}S' + \int_{\Omega} \nabla G(\boldsymbol{r}';\boldsymbol{r})(\nabla \cdot \boldsymbol{f}(\boldsymbol{r}'))\mathrm{d}V', \tag{A.60}$$

$$\boldsymbol{P}_{\mathrm{T}}[\boldsymbol{f}](\boldsymbol{r}) \coloneqq \oint_{\partial\Omega} \nabla G(\boldsymbol{r}';\boldsymbol{r}) \times (\boldsymbol{n}(\boldsymbol{r}') \times \boldsymbol{f}(\boldsymbol{r}'))\mathrm{d}S' - \int_{\Omega} \nabla G(\boldsymbol{r}';\boldsymbol{r}) \times (\nabla \times \boldsymbol{f}(\boldsymbol{r}'))\mathrm{d}V'. \tag{A.61}$$

Using the relation $\nabla_{\boldsymbol{r}} G(\boldsymbol{r}';\boldsymbol{r}) = -\nabla_{\boldsymbol{r}'} G(\boldsymbol{r}';\boldsymbol{r})$, $\boldsymbol{P}_{\mathrm{L}}$ and $\boldsymbol{P}_{\mathrm{T}}$ are represented as $\boldsymbol{P}_{\mathrm{L}}[\boldsymbol{f}] = -\nabla\boldsymbol{\phi}$ and $\boldsymbol{P}_{\mathrm{T}}[\boldsymbol{f}] = \nabla \times \boldsymbol{A}$, where

$$\boldsymbol{\phi}(\boldsymbol{r}) = -\oint_{\partial\Omega} G(\boldsymbol{r}';\boldsymbol{r})(\boldsymbol{n}(\boldsymbol{r}') \cdot \boldsymbol{f}(\boldsymbol{r}'))\mathrm{d}S' + \int_{\Omega} G(\boldsymbol{r}';\boldsymbol{r})(\nabla \cdot \boldsymbol{f}(\boldsymbol{r}'))\mathrm{d}V', \tag{A.62}$$

$$\boldsymbol{A}(\boldsymbol{r}) = -\oint_{\partial\Omega} G(\boldsymbol{r}';\boldsymbol{r})(\boldsymbol{n}(\boldsymbol{r}') \times \boldsymbol{f}(\boldsymbol{r}'))\mathrm{d}S' + \int_{\Omega} G(\boldsymbol{r}';\boldsymbol{r})(\nabla \times \boldsymbol{f}(\boldsymbol{r}'))\mathrm{d}V'. \tag{A.63}$$

Hence, for a given tensor field $\boldsymbol{f}$, $\boldsymbol{f}_{\mathrm{L}} = \boldsymbol{P}_{\mathrm{L}}[\boldsymbol{f}]$ is the longitudinal component, and $\boldsymbol{f}_{\mathrm{T}} = \boldsymbol{P}_{\mathrm{T}}[\boldsymbol{f}]$ corresponds to the transverse component of the field. Therefore, Eq. (A.55) gives the tensor Helmholtz decomposition.

A.2 Complex Analysis

A.2.1 Integral Formulae for Complex Functions

Let $\iota : \mathbb{R}^2 \to \mathbb{C}$ be a mapping given by the relation

$$\iota : (x, y) \mapsto x + \mathrm{i}y. \tag{A.64}$$

The mapping ι is a bijection between $\mathbb{R}^2$ and $\mathbb{C}$. Therefore, under the mapping ι, we regard $\mathbb{C}$ and $\mathbb{R}^2$ as identical to each other. For a complex function $f : \mathbb{C} \to \mathbb{C}$, we introduce a function of two real variables $f' : \mathbb{R}^2 \to \mathbb{C}$ such that $f' = f \circ \iota$. Then, it holds that

$$f'(x, y) = (f \circ \iota)(x, y) = f(\iota(x, y)) = f(\zeta), \tag{A.65}$$

where $\zeta = x + \mathrm{i}y$. We regard f' as identical to f and write $f(\zeta) = f(x, y)$ hereafter. All the continuous and differentiable properties of a complex function f can be defined via the continuity and differentiability of f'.

The following differential operators play a key role in the theory of complex functions that are not necessarily holomorphic.

Definition A.1 (The Wirtinger operator)**.** Let ∂_x and ∂_y be the partial differential opera-

tors with respect to $x, y \in \mathbb{R}^2$. The linear differential operators

$$\bar{\partial} \coloneqq \frac{1}{2}(\partial_x + \mathrm{i}\partial_y), \tag{A.66}$$

$$\partial \coloneqq \frac{1}{2}(\partial_x - \mathrm{i}\partial_y), \tag{A.67}$$

are called the Wirtinger operators.

Because $\bar{\partial}$ and ∂ are defined simply as linear combinations of ∂_x and ∂_y, basic properties such as linearity, the product rule, and the chain rule are all inherited. Using the Wirtinger operators, the Cauchy–Riemann equations can be written in a simple form as $\bar{\partial} f = 0$.

The following Green's theorem is an extension of the fundamental theorem of calculus.

Theorem A.6 (Green's theorem)**.** Let D be a domain whose boundary ∂D is a piecewise smooth Jordan curve. If $f \in C^1(D) \cap C^0(\overline{D})$, then it holds that

$$\int_D \bar{\partial} f(\zeta) \mathrm{d}\zeta \wedge \mathrm{d}\bar{\zeta} = -\oint_{\partial D} f(\zeta) \mathrm{d}\zeta, \tag{A.68}$$

$$\int_D \partial f(\zeta) \mathrm{d}\zeta \wedge \mathrm{d}\bar{\zeta} = \oint_{\partial D} f(\zeta) \mathrm{d}\bar{\zeta}. \tag{A.69}$$

Proof. is found in, e.g., [176]. □

When f is holomorphic in D with respect to ζ and $\bar{\zeta}$, respectively, the L.H.S. of Eqs. (A.68) and (A.69) vanish and Theorem A.6 reduces to Cauchy's theorem.

Using Theorem A.6, we can conduct the integration by parts. For smooth functions w and f, the following product rules hold:

$$\bar{\partial}(wf) = w\bar{\partial} f + f\bar{\partial} w, \tag{A.70}$$

$$\partial(wf) = w\partial f + f\partial w. \tag{A.71}$$

Integrating both sides of Eqs. (A.70) and (A.71) and applying Theorem A.6 leads to

$$\int_D w(\zeta)\bar{\partial} f(\zeta) \mathrm{d}\zeta \wedge \mathrm{d}\bar{\zeta} = -\oint_{\partial D} w(\zeta) f(\zeta) \mathrm{d}\zeta - \int_D f(\zeta)\bar{\partial} w(\zeta) \mathrm{d}\zeta \wedge \mathrm{d}\bar{\zeta}, \tag{A.72}$$

$$\int_D w(\zeta)\partial f(\zeta) \mathrm{d}\zeta \wedge \mathrm{d}\bar{\zeta} = \oint_{\partial D} w(\zeta) f(\zeta) \mathrm{d}\bar{\zeta} - \int_D f(\zeta)\partial w(\zeta) \mathrm{d}\zeta \wedge \mathrm{d}\bar{\zeta}. \tag{A.73}$$

The derivatives of f in the L.H.S. of Eqs. (A.72) and (A.73) are replaced by the derivatives of the weighting function w.

The following Cauchy–Pompeiu formula represents a complex function defined in a domain by its complex derivatives inside the domain.

Theorem A.7 (The Cauchy–Pompeiu formula)**.** Let D be a domain whose boundary ∂D is a piecewise smooth Jordan curve. If $f \in C^1(D) \cap C^0(\overline{D})$, then it holds that

$$f(\zeta) = \frac{1}{2\pi\mathrm{i}} \oint_{\partial D} \frac{f(\zeta')}{\zeta' - \zeta} \mathrm{d}\zeta' + \frac{1}{2\pi\mathrm{i}} \int_D \frac{\bar{\partial} f(\zeta')}{\zeta' - \zeta} \mathrm{d}\zeta' \wedge \mathrm{d}\bar{\zeta}', \tag{A.74}$$

$$f(\zeta) = -\frac{1}{2\pi\mathrm{i}} \oint_{\partial D} \frac{f(\zeta')}{\bar{\zeta}' - \bar{\zeta}} \mathrm{d}\bar{\zeta}' + \frac{1}{2\pi\mathrm{i}} \int_D \frac{\partial f(\zeta')}{\bar{\zeta}' - \bar{\zeta}} \mathrm{d}\zeta' \wedge \mathrm{d}\bar{\zeta}' \tag{A.75}$$

for $\zeta \in D$.

Proof. For $f \in C^1(D) \cap C^0(\overline{D})$, the function $f/(\zeta' - \zeta)$ belongs to the same class in $D \setminus \{\zeta\}$. Hence, applying Theorem A.6 to $f/(\zeta' - \zeta)$ in $D \setminus \overline{U}_\epsilon$, where U_ε is a disk centered at ζ with a radius of ϵ, yields

$$\oint_{\partial D} \frac{f(\zeta')}{\zeta' - \zeta} \mathrm{d}\zeta' - \oint_{\partial U_\varepsilon} \frac{f(\zeta')}{\zeta' - \zeta} \mathrm{d}\zeta' = -\int_{D \setminus \overline{U}_\varepsilon} \frac{\bar{\partial} f(\zeta')}{\zeta' - \zeta} \mathrm{d}\zeta' \wedge \mathrm{d}\bar{\zeta}'.$$

Let us evaluate the limit of each term of the above equation as ϵ approaches 0. By transforming the variable of integration on ∂U_ϵ as $\zeta' = \zeta + \varepsilon \exp(\mathrm{i}\theta)$, the second term of the L.H.S. can be calculated as

$$\lim_{\varepsilon \to 0} \oint_{\partial U_\varepsilon} \frac{f(\zeta')}{\zeta' - \zeta} \mathrm{d}\zeta' = \lim_{\varepsilon \to 0} \int_{-\pi}^{+\pi} \frac{f(\zeta + \varepsilon \exp(\mathrm{i}\theta))}{\varepsilon \exp(\mathrm{i}\theta)} \varepsilon \mathrm{i} \exp(\mathrm{i}\theta) \mathrm{d}\theta = 2\pi \mathrm{i} f(\zeta),$$

where we changed the order of integration and the limit based on the continuity of f. By transforming the variable of integration in U_ϵ as $\zeta' = \zeta + r \exp(\mathrm{i}\theta)$, the R.H.S. can be calculated as

$$\left| \int_{U_\varepsilon} \frac{\bar{\partial} f(\zeta')}{\zeta' - \zeta} \mathrm{d}\zeta' \wedge \mathrm{d}\bar{\zeta}' \right| \leq \int_{U_\epsilon} \frac{|\bar{\partial} f(\zeta')|}{|\zeta' - \zeta|} |\mathrm{d}\zeta' \wedge \mathrm{d}\bar{\zeta}'| = \int_0^\varepsilon \int_{-\pi}^{+\pi} \frac{|\bar{\partial} f(\zeta')|}{r} r \mathrm{d}r \mathrm{d}\theta \leq 2\pi \varepsilon M,$$

where $M = \sup|\bar{\partial} f|$, the existence of which is guaranteed by the boundedness of $\bar{\partial} f$. Hence, the R.H.S. can be evaluated as the principal value integral and thereby Eq. (A.74) holds. By applying Eq. (A.74) to $\bar{f}$ and taking the complex conjugate, we obtain Eq. (A.75). □

When f is holomorphic in D with respect to each of ζ and $\bar{\zeta}$, Theorem A.7 reduces to the Cauchy formula.

The Cauchy–Pompeiu formula gives the explicit representation of the solution of the so-called Dbar equation

$$\bar{\partial} f = g \tag{A.76}$$

with the Dirichlet BC, and is utilized in the 2D EPT and MRE problems [35, 135].

A.2.2 Integral Formulae for Integrable Functions

We extend the theorems discussed above to functions that are not continuous or differentiable in a classical sense. The derivatives of such functions are defined through integration instead of differentiation as described below.

Let D be a domain and $f \in L^1_{\mathrm{loc}}(D)$. If there exists $g \in L^1_{\mathrm{loc}}(D)$ that satisfies the relation

$$\int_D f(\zeta) \partial \phi(\zeta) \mathrm{d}\zeta \wedge \mathrm{d}\bar{\zeta} = -\int_D g(\zeta) \phi(\zeta) \mathrm{d}\zeta \wedge \mathrm{d}\bar{\zeta}, \tag{A.77}$$

$$\int_D f(\zeta) \bar{\partial} \phi(\zeta) \mathrm{d}\zeta \wedge \mathrm{d}\bar{\zeta} = -\int_D g(\zeta) \phi(\zeta) \mathrm{d}\zeta \wedge \mathrm{d}\bar{\zeta} \tag{A.78}$$

for an arbitrary function $\phi \in C^1_0(D)$, then g is called the weak derivative of f with respect to ζ and $\bar{\zeta}$, respectively. Given a piecewise smooth function $f \in C^1(D)$, its ordinary derivatives $g = \partial f$ and $g = \bar{\partial} f$ obviously satisfy Eqs. (A.77) and (A.78), respectively. Therefore, we use the same notation as the ordinary derivatives, i.e., ∂f and $\bar{\partial} f$, respectively. We note that it still holds that f is holomorphic inside D if $\bar{\partial} f = 0$ in D.

We define the domain integral operators in Eqs. (A.74) as the T-operators:

Definition A.2 (T-operator)**.** Let D be a bounded domain and $f \in C^0(D)$. We refer to the integral operators

$$T[f](\zeta) = \frac{1}{2\pi \mathrm{i}} \iint_D \frac{f(\zeta')}{\zeta' - \zeta} \mathrm{d}\zeta' \wedge \mathrm{d}\bar{\zeta}', \tag{A.79}$$

$$\bar{T}[f](\zeta) = \frac{1}{2\pi \mathrm{i}} \iint_D \frac{f(\zeta')}{\bar{\zeta}' - \bar{\zeta}} \mathrm{d}\zeta' \wedge \mathrm{d}\bar{\zeta}', \tag{A.80}$$

where $\zeta \in D$, as the T-operators.

The existence of $T[f]$ and $\bar{T}[f]$ for continuous functions f are proved as follows. Let $g \in L^p(D)$, $p > 2$ and let us consider the function

$$G(\zeta) = \int_D \frac{g(\zeta')}{|\zeta' - \zeta|} \mathrm{d}x'\mathrm{d}y' = \int_{D^*} \frac{g(\zeta'' + \zeta)}{|\zeta''|} \mathrm{d}x''\mathrm{d}y'', \qquad \zeta \in D \tag{A.81}$$

where D is a bounded domain and $\zeta = x + \mathrm{i}y$. The last equation is obtained by transforming the variable of integration as $\zeta'' = \zeta' - \zeta$. The corresponding domain of integration D^* is bounded because $\zeta, \zeta' \in D$. Using the Hölder inequality, the variation of G can be evaluated as follows:

$$\begin{aligned} G(\zeta + \Delta\zeta) - G(\zeta) &= \int_{D^*} \frac{g(\zeta'' + \zeta + \Delta\zeta) - g(\zeta'' + \zeta)}{|\zeta''|} \mathrm{d}x''\mathrm{d}y'' \\ &\leq \left(\int_{D^*} |g(\zeta'' + \zeta + \Delta\zeta) - g(\zeta'' + \zeta)|^p \mathrm{d}x''\mathrm{d}y'' \right)^{1/p} \left(\int_{D^*} \frac{1}{|\zeta''|^q} \mathrm{d}x''\mathrm{d}y'' \right)^{1/q}, \end{aligned}$$

where $q = p/(p-1)$ is the conjugate index of p. The second factor of the last equation is the Calderón–Zygmund integral and known to be finite [177], and the first factor vanishes as $\Delta\zeta$ approaches to 0 due to the mean-continuous property of L^p functions. As a result, the variation $G(\zeta + \Delta\zeta) - G(\zeta)$ goes to 0 as $\Delta\zeta$ approaches to 0 and thereby G is continuous. Hence, given an integrable function f, the function $|f|G$ is also integrable, and thus it holds that

$$\int_D |f(\zeta)| G(\zeta) \mathrm{d}x\mathrm{d}y = \int_D |f(\zeta)| \left(\int_D \frac{g(\zeta')}{|\zeta' - \zeta|} \mathrm{d}x'\mathrm{d}y' \right) \mathrm{d}x\mathrm{d}y = \int_D g(\zeta') \left(\int_D \frac{|f(\zeta)|}{|\zeta - \zeta'|} \mathrm{d}x\mathrm{d}y \right) \mathrm{d}x'\mathrm{d}y',$$

from which the existence of

$$F(\zeta) = \int_D \frac{|f(\zeta')|}{|\zeta' - \zeta|} \mathrm{d}x'\mathrm{d}y', \qquad \zeta \in D \tag{A.82}$$

and $|T[f](\zeta)| \leq F(\zeta)$ is concluded.

By theorem 1.13 in [178], $T[f], \bar{T}[f] \in L^p(D)$ where p is an arbitrary number satisfying $1 \leq p < 2$. By theorem 1.19 in [178], if $f \in L^p(D), p > 2$, then $T[f]$ belongs to the class $C^{0,\alpha}(\overline{D}), \alpha = (p-2)/p$. Note that $T[f]$ and $\bar{T}[f]$ could have discontinuities when $1 \leq p \leq 2$.

Now we consider the derivatives of $T[f]$. Let $\phi \in C_0^1(D)$. Then ϕ vanishes on the boundary ∂D, and thus it follows from Theorem A.7 that $\phi = T[\bar{\partial}\phi]$. Hence, it follows that

$$\begin{aligned} \int_D T[f](\zeta) \bar{\partial}\phi(\zeta) \mathrm{d}\zeta \wedge \mathrm{d}\bar{\zeta} &= \int_D \left(\frac{1}{2\pi \mathrm{i}} \iint_D \frac{f(\zeta')}{\zeta' - \zeta} \mathrm{d}\zeta' \wedge \mathrm{d}\bar{\zeta}' \right) \bar{\partial}\phi(\zeta) \mathrm{d}\zeta \wedge \mathrm{d}\bar{\zeta} \\ &= -\int_D f(\zeta') \left(\frac{1}{2\pi \mathrm{i}} \iint_D \frac{\bar{\partial}\phi(\zeta)}{\zeta - \zeta'} \mathrm{d}\zeta \wedge \mathrm{d}\bar{\zeta} \right) \mathrm{d}\zeta' \wedge \mathrm{d}\bar{\zeta}' = -\int_D f(\zeta') \phi(\zeta') \mathrm{d}\zeta' \wedge \mathrm{d}\bar{\zeta}', \end{aligned}$$

implying that the weak derivatives of $T[f]$ and $\bar{T}[f]$ with respect to $\bar{\zeta}$ and ζ, respectively, exist and are given as

$$\bar{\partial} T[f] = f, \tag{A.83}$$

$$\partial \bar{T}[f] = f. \tag{A.84}$$

Next, we extend the Cauchy–Pompeiu formula to continuous but not differentiable functions. Let us first introduce the following lemma.

Lemma A.1 (Cauchy integral of the T-operators)**.** Let D be a domain whose boundary ∂D is a piecewise smooth Jordan curve. If $f \in L^p(D)$, $p > 2$, then it holds that

$$\frac{1}{2\pi \mathrm{i}} \oint_{\partial D} \frac{T[f](\zeta')}{\zeta' - \zeta} \mathrm{d}\zeta' \equiv 0 \tag{A.85}$$

for $\zeta \in D$.

Proof. Since $T[f]$ is Hölder continuous in $\overline{D}$ for $f \in L^p(D)$, $p > 2$, the function is well-defined on ∂D. The L.H.S. of Eq. (A.85) can be expressed as

$$\begin{aligned}\frac{1}{2\pi \mathrm{i}} \oint_{\partial D} \frac{T[f](\zeta')}{\zeta' - \zeta} \mathrm{d}\zeta' &= \frac{1}{2\pi \mathrm{i}} \oint_{\partial D} \left(\frac{1}{2\pi \mathrm{i}} \iint_D \frac{f(\zeta'')}{\zeta'' - \zeta'} \mathrm{d}\zeta'' \wedge \mathrm{d}\bar{\zeta}'' \right) \frac{1}{\zeta' - \zeta} \mathrm{d}\zeta' \\ &= \frac{1}{2\pi \mathrm{i}} \iint_D \left(\frac{1}{2\pi \mathrm{i}} \oint_{\partial D} \frac{1}{(\zeta' - \zeta)(\zeta'' - \zeta')} \mathrm{d}\zeta' \right) f(\zeta'') \mathrm{d}\zeta'' \wedge \mathrm{d}\bar{\zeta}''.\end{aligned}$$

The factor inside the parentheses of the last equation can be calculated as

$$\frac{1}{2\pi \mathrm{i}} \oint_{\partial D} \frac{1}{(\zeta' - \zeta)(\zeta'' - \zeta')} \mathrm{d}\zeta' = \begin{cases} \dfrac{1}{2\pi \mathrm{i}} \dfrac{1}{\zeta'' - \zeta} \displaystyle\oint_{\partial D} \left(\frac{1}{\zeta' - \zeta} - \frac{1}{\zeta' - \zeta''} \right) \mathrm{d}\zeta' & (\zeta \neq \zeta''), \\ \dfrac{1}{2\pi \mathrm{i}} \displaystyle\oint_{\partial D} \frac{1}{(\zeta' - \zeta)^2} \mathrm{d}\zeta' & (\zeta = \zeta''), \end{cases}$$

which vanishes in both cases according to the residue theorem. □

Using Lemma A.1, we can prove the Cauchy–Pompeiu formula.

Theorem A.8 (The Cauchy–Pompeiu formula)**.** Let D be a domain whose boundary ∂D is a piecewise smooth Jordan curve. If $f \in C^0(\overline{D})$ and $\bar{\partial} f \in L^p(D)$, $p > 2$, then it holds that

$$f(\zeta) = \frac{1}{2\pi \mathrm{i}} \oint_{\partial D} \frac{f(\zeta')}{\zeta' - \zeta} \mathrm{d}\zeta' + T[\bar{\partial} f](\zeta), \tag{A.86}$$

$$f(\zeta) = -\frac{1}{2\pi \mathrm{i}} \oint_{\partial D} \frac{f(\zeta')}{\zeta' - \zeta} \mathrm{d}\bar{\zeta}' + \bar{T}[\partial f](\zeta) \tag{A.87}$$

for $\zeta \in D$.

Proof. Let us consider a function $\phi \coloneqq f - T[\bar{\partial} f]$. Since $\bar{\partial}\phi = \bar{\partial} f - \bar{\partial} f = 0$, the function ϕ is holomorphic in D. In addition, $T[\bar{\partial} f]$ is (Hölder) continuous in D since $\bar{\partial} f \in L^p(D)$, $p > 2$. Hence, ϕ is also continuous on ∂D. Therefore, we can apply Cauchy's formula to yield

$$\phi(\zeta) = \frac{1}{2\pi \mathrm{i}} \oint_{\partial D} \frac{f(\zeta') - T[\bar{\partial} f](\zeta')}{\zeta' - \zeta} \mathrm{d}\zeta' = \frac{1}{2\pi \mathrm{i}} \oint_{\partial D} \frac{f(\zeta')}{\zeta' - \zeta} \mathrm{d}\zeta' - \frac{1}{2\pi \mathrm{i}} \oint_{\partial D} \frac{T[\bar{\partial} f](\zeta')}{\zeta' - \zeta} \mathrm{d}\zeta'.$$

The second term of the R.H.S. vanishes according to Lemma A.1, from which Eq. (A.86) follows. □

Next, we extend Green's theorem to continuous but not differentiable functions. Let us first introduce the following lemma.

Lemma A.2 (Green's theorem for the T-operators)**.** Let D be a domain whose boundary ∂D is a piecewise smooth Jordan curve. If $f \in C^0(D)$ and $f \in L^p(D)$, $p > 2$, then it holds that

$$\oint_{\partial D} T[f](\zeta)\mathrm{d}\zeta = -\int_D f(\zeta)\mathrm{d}\zeta \wedge \mathrm{d}\bar{\zeta} \tag{A.88}$$

$$\oint_{\partial D} \bar{T}[f](\zeta)\mathrm{d}\bar{\zeta} = \int_D f(\zeta)\mathrm{d}\zeta \wedge \mathrm{d}\bar{\zeta} \tag{A.89}$$

Proof. The functions $T[f]$ and $\bar{T}[f]$ are (Hölder) continuous in $\overline{D}$ for $f \in L^p(D)$, $p > 2$. In addition, $\bar{\partial} T[f] = \partial \bar{T}[f] = f$ are continuous in D. Therefore, we can apply Theorem. A.6 to $T[f]$ and $\bar{T}[f]$, yielding

$$\oint_{\partial D} T[f](\zeta)\mathrm{d}\zeta = -\int_D \bar{\partial} T[f](\zeta)\mathrm{d}\zeta \wedge \mathrm{d}\bar{\zeta} = -\int_D f(\zeta)\mathrm{d}\zeta \wedge \mathrm{d}\bar{\zeta},$$

$$\oint_{\partial D} \bar{T}[f](\zeta)\mathrm{d}\bar{\zeta} = \int_D \partial \bar{T}[f](\zeta)\mathrm{d}\zeta \wedge \mathrm{d}\bar{\zeta} = \int_D f(\zeta)\mathrm{d}\zeta \wedge \mathrm{d}\bar{\zeta},$$

which was to be proved. □

Using Lemma A.2, we can prove Green's theorem.

Theorem A.9 (Green's theorem)**.** Let D be a domain whose boundary ∂D is a piecewise smooth Jordan curve. If $f \in C^0(\overline{D})$ and $\bar{\partial} f \in L^p(D)$, $p > 2$, then it holds that

$$\int_D \bar{\partial} f(\zeta)\mathrm{d}\zeta \wedge \mathrm{d}\bar{\zeta} = -\oint_{\partial D} f(\zeta)\mathrm{d}\zeta, \tag{A.90}$$

$$\int_D \partial f(\zeta)\mathrm{d}\zeta \wedge \mathrm{d}\bar{\zeta} = \oint_{\partial D} f(\zeta)\mathrm{d}\bar{\zeta}. \tag{A.91}$$

Proof. Let us consider a function $\phi \coloneqq f - T[\bar{\partial} f]$. By integrating both sides, we obtain

$$\oint_{\partial D} f(\zeta)\mathrm{d}\zeta = \oint_{\partial D} \phi(\zeta)\mathrm{d}\zeta + \oint_{\partial D} T[\bar{\partial} f](\zeta)\mathrm{d}\zeta.$$

Since $\bar{\partial}\phi = \bar{\partial} f - \bar{\partial} f = 0$, the function ϕ is holomorphic in D. Besides, $T[\bar{\partial} f]$ is (Hölder) continuous in D since $\bar{\partial} f \in L^p(D)$, $p > 2$. Hence, ϕ is also continuous on ∂D. Therefore, the first term of the R.H.S. vanishes according to Cauchy's theorem. In addition, since $f \in C^0(\overline{D})$ and $\partial f \in L^p(D)$, $p > 2$, it holds by Lemma A.2 that

$$\oint_{\partial D} T[\bar{\partial} f](\zeta)\mathrm{d}\zeta = -\int_D \bar{\partial} f(\zeta)\mathrm{d}\zeta \wedge \mathrm{d}\bar{\zeta},$$

from which Eq. (A.90) follows. Applying Eq. (A.90) to $\bar{f}$ and taking the complex conjugate yields Eq. (A.91). □

A.2.3 Differential Properties of the T-Operator

In the following, we review the derivative of the T-operator, which will be used in Chapter 4 to construct integral formulae for the boundary value problems of the Dbar equation.

Definition A.3 (Π-operator)**.** Let D be a domain whose boundary ∂D belongs to the class $C^{1,\alpha}(\overline{D}), 0 < \alpha < 1$. If $f \in C^{0,\alpha}(\overline{D})$, then the Cauchy principal value integral

$$\Pi[f](\zeta) \coloneqq \frac{1}{2\pi \mathrm{i}} \iint_D \frac{f(\zeta')}{(\zeta' - \zeta)^2} \mathrm{d}\zeta' \wedge \mathrm{d}\bar{\zeta}', \quad \zeta \in D, \tag{A.92}$$

$$\bar{\Pi}[f](\zeta) \coloneqq \frac{1}{2\pi \mathrm{i}} \iint_D \frac{f(\zeta')}{(\bar{\zeta}' - \bar{\zeta})^2} \mathrm{d}\zeta' \wedge \mathrm{d}\bar{\zeta}', \quad \zeta \in D \tag{A.93}$$

exists for all points in D.

The existence of the Π-operator can be proved by considering the following integral over $D \setminus \overline{U}_\epsilon$, where U_ϵ is a disk centered at ζ with radius ϵ:

$$\int_{D\setminus\overline{U}_\epsilon} \frac{f(\zeta')}{(\zeta' - \zeta)^2} \mathrm{d}\zeta' \wedge \mathrm{d}\bar{\zeta}' = \int_{D\setminus\overline{U}_\epsilon} \frac{f(\zeta') - f(\zeta)}{(\zeta' - \zeta)^2} \mathrm{d}\zeta' \wedge \mathrm{d}\bar{\zeta}' + f(\zeta) \int_{D\setminus\overline{U}_\epsilon} \frac{1}{(\zeta' - \zeta)^2} \mathrm{d}\zeta' \wedge \mathrm{d}\bar{\zeta}' \tag{A.94}$$

Let us evaluate the limit of each term of the above equation as ϵ approaches 0. By transforming the variable of integration in U_ϵ as $\zeta' = \zeta + r\exp(\mathrm{i}\theta)$, the Taylor series expansion of $f(\zeta')$ around ζ is given as

$$f(\zeta') = f(\zeta) + \partial f(\zeta) r \exp(\mathrm{i}\theta) + \bar{\partial} f(\zeta) r \exp(-\mathrm{i}\theta) + o(r^2). \tag{A.95}$$

Then, the first term of the R.H.S. can be evaluated as

$$\begin{aligned}\left| \int_{U_\epsilon} \frac{f(\zeta') - f(\zeta)}{(\zeta' - \zeta)^2} \mathrm{d}\zeta' \wedge \mathrm{d}\bar{\zeta}' \right| &\leq \int_{U_\epsilon} \frac{|f(\zeta') - f(\zeta)|}{|\zeta' - \zeta|^2} |\mathrm{d}\zeta' \wedge \mathrm{d}\bar{\zeta}'| \\ &= \int_0^\epsilon \int_{-\pi}^{+\pi} (|\partial f(\zeta)| + |\bar{\partial} f(\zeta)| + o(r)) \mathrm{d}r\mathrm{d}\theta \leq 2\pi\epsilon M,\end{aligned}$$

where $M = \sup(|\partial f| + |\bar{\partial} f|)$, the existence of which is guaranteed because of the boundedness of ∂f and $\bar{\partial} f$. Hence, it vanishes as ϵ approaches 0. The second term of the R.H.S. can be calculated as

$$\int_{U_\epsilon} \frac{1}{(\zeta' - \zeta)^2} \mathrm{d}\zeta' \wedge \mathrm{d}\bar{\zeta}' = -\int_D \partial\left(\frac{1}{\zeta' - \zeta}\right) \mathrm{d}\zeta' \wedge \mathrm{d}\bar{\zeta}'. \tag{A.96}$$

Applying Theorem A.6 to the R.H.S. of the above equation yields

$$\int_{U_\epsilon} \frac{1}{(\zeta' - \zeta)^2} \mathrm{d}\zeta' \wedge \mathrm{d}\bar{\zeta}' = \oint_{\partial U_\epsilon} \frac{1}{\zeta' - \zeta} \mathrm{d}\bar{\zeta}' = \int_{-\pi}^{+\pi} \frac{1}{\epsilon \exp(\mathrm{i}\theta)} (-\mathrm{i}\epsilon \exp(-\mathrm{i}\theta)) \mathrm{d}\theta = 0.$$

Hence, Eq. (A.94) can be evaluated as the principal value integral as follows:

$$\frac{1}{2\pi \mathrm{i}} \iint_D \frac{f(\zeta')}{(\zeta' - \zeta)^2} \mathrm{d}\zeta' \wedge \mathrm{d}\bar{\zeta}' = \frac{1}{2\pi \mathrm{i}} \iint_D \frac{f(\zeta') - f(\zeta)}{(\zeta' - \zeta)^2} \mathrm{d}\zeta' \wedge \mathrm{d}\bar{\zeta}' + \frac{f(\zeta)}{2\pi \mathrm{i}} \iint_D \frac{1}{(\zeta' - \zeta)^2} \mathrm{d}\zeta' \wedge \mathrm{d}\bar{\zeta}' \tag{A.97}$$

Applying Eq. (A.94) to $\bar{f}$ and taking the complex conjugate yields the other equation.

By theorem 1.32 in [178], $\Pi[f]$ and $\bar{\Pi}[f]$ belong to the class $C^{0,\alpha}(\overline{D})$ if f belongs to this class. Further, also by theorem 1.32 in [178], if $f \in C^{0,\alpha}(\overline{D})$, then $T[f] \in C^{1,\alpha}(\overline{D})$ and it holds that

$$\partial T[f] = \Pi[f], \quad \zeta \in D, \tag{A.98}$$

$$\bar{\partial}\bar{T}[f] = \bar{\Pi}[f], \quad \zeta \in D. \tag{A.99}$$

This property is utilized in Chapter 4 to deduce the proposed integral formulae of the solution of the Dbar equation.

Appendix B

Principles of Magnetic Resonance Imaging

This appendix reviews fundamental principles of MR imaging. This is a polished version of previously published review article [179] by the author. In section B.1, we first describe the fundamental physics on which MRI lies. Section B.2 explains how to generate and detect the MRI signal using transmit and receive coils. The Fourier imaging in which the MR signal is spatially resolved to create an image is explained in section B.3. Section B.4 describes the sources of image contrast and the mechanism for encoding these information into the MRI signal. Finally, section B.5 explains the usual imaging sequences by considering the principles of echo formation.

For more detailed and comprehensive description of MRI including advanced imaging techniques, hardware and software, and clinical applications, see, e.g., [180–182].

B.1 Nuclear Magnetic Resonance

B.1.1 Proton as a Spin

According to quantum physics, unpaired electrons and nucleons have their intrinsic properties of spic angular momentum $\boldsymbol{s}$ and corresponding magnetic moment $\boldsymbol{\mu}$. This fact can be acknowledged to some extent by classical physics; if we consider electrons and nucleons as spinning charged particles, they can be seen as magnetic dipoles. Indeed, a particle with mass m, electric charge $q = ge_0$, and angular momentum $\boldsymbol{s}$ has magnetic moment

$$\boldsymbol{\mu} = g\frac{e_0}{2m}\boldsymbol{s}, \tag{B.1}$$

where e_0 is the elementary charge. Note that the experimental values of g for the electron, neutron, and proton are $g_\mathrm{e} = -2.002$, $g_\mathrm{n} = -3.826$, and $g_\mathrm{p} = 5.585$, respectively, which are significantly different from theoretically expected values of $g_\mathrm{e} = -1$, $g_\mathrm{n} = 0$, and $g_\mathrm{p} = 1$. To accurately predict the value of g for each particle, quantum physics is required.

In most MRI studies, we focus on hydrogen nuclei, or protons, due to their abundance in the human body as water molecules. The coefficient $\gamma_0 \coloneqq g_\mathrm{p}e_0/2m_\mathrm{p} \simeq 2\pi \times 42.58$ MHz/T, where m_p is the mass of protons, is called the gyromagnetic ratio of protons.

What we can detect using an MR scanner is not magnetic moments of individual protons but the net magnetic moment of their microscopic ensemble, which is called spin in MRI literature. In the absence of an external magnetic field, the individual protons are oriented in random directions and therefore no net magnetic moment is generated. However, once they are exposed to an external magnetic field, the angle between the magnetic field and the

protons are constrained, resulting in the macroscopic net magnetization given as

$$\boldsymbol{M} = \sum_{i \in V} \boldsymbol{\mu}_i = \gamma_0 \sum_{i \in V} \boldsymbol{s}_i = \gamma_0 \boldsymbol{J}, \tag{B.2}$$

where i is the index of protons inside the microscopic volume and $\boldsymbol{J}$ is angular momentum of the spin. We will study the time evolution of $\boldsymbol{M}$ in the preceding sections.

B.1.2 Precession of a Spin

A spin with magnetization $\boldsymbol{M}$ in a magnetic field $\boldsymbol{B}$ experiences a torque $\boldsymbol{M} \times \boldsymbol{B}$ to change the angular momentum $\boldsymbol{J}$ as follows:

$$\frac{\mathrm{d}\boldsymbol{J}}{\mathrm{d}t} = \boldsymbol{M} \times \boldsymbol{B}. \tag{B.3}$$

By substituting Eq. (B.2), the time evolution of $\boldsymbol{M}$ is described as

$$\frac{\mathrm{d}\boldsymbol{M}}{\mathrm{d}t} = -\gamma_0 \boldsymbol{B} \times \boldsymbol{M}. \tag{B.4}$$

Hence, the magnetization moves towards the direction perpendicular to both $\boldsymbol{B}$ and $\boldsymbol{M}$, causing it rotating around the magnetic field at the velocity $\boldsymbol{\omega} = -\gamma_0 \boldsymbol{B}$. The magnitude of $\boldsymbol{\omega}$ is referred to as the Larmor frequency $\omega = |\gamma_0 \boldsymbol{B}|$.

Let us examine Eq. (B.4) in the Cartesian coordinate system, or the laboratory frame, whose bases are denoted as $(\boldsymbol{e}_x, \boldsymbol{e}_y, \boldsymbol{e}_z)$. The following relations hold:

$$\left[\frac{\mathrm{d}\boldsymbol{f}}{\mathrm{d}t}\right]_{\mathrm{lab}} \coloneqq \frac{\mathrm{d}f_i}{\mathrm{d}t}\boldsymbol{e}_i = \frac{\mathrm{d}(f_i \boldsymbol{e}_i)}{\mathrm{d}t} = \frac{\mathrm{d}\boldsymbol{f}}{\mathrm{d}t}, \tag{B.5}$$

$$\left[\boldsymbol{g} \times \boldsymbol{f}\right]_{\mathrm{lab}} \coloneqq \epsilon_{ijk} g_i f_j \boldsymbol{e}_k = g_i \boldsymbol{e}_i \times f_j \boldsymbol{e}_j = \boldsymbol{g} \times \boldsymbol{f}, \tag{B.6}$$

where $\boldsymbol{f} = f_i \boldsymbol{e}_i$ and $\boldsymbol{g} = g_i \boldsymbol{e}_i$. By using them, Eq. (B.4) can be rewritten as

$$\left[\frac{\mathrm{d}\boldsymbol{M}}{\mathrm{d}t}\right]_{\mathrm{lab}} = \left[-\gamma_0 \boldsymbol{B} \times \boldsymbol{M}\right]_{\mathrm{lab}}. \tag{B.7}$$

Hence, it holds for $\mathbf{M} \coloneqq (M_x, M_y, M_z), \mathbf{B} = (B_x, B_y, B_z)$ that

$$\frac{\mathrm{d}\mathbf{M}}{\mathrm{d}t} = -\gamma_0 \mathbf{B} \times \mathbf{M}. \tag{B.8}$$

In MRI, a static and homogeneous magnetic field is applied to the human body, which is called the B0 field. Following convention, we assume the B0 field to be oriented to the positive z-axis with the magnitude of B_0. Then, the governing equation is decoupled and written as

$$\frac{\mathrm{d}M_\perp}{\mathrm{d}t} = -\mathrm{i}\gamma_0 B_0 M_\perp, \tag{B.9}$$

$$\frac{\mathrm{d}M_z}{\mathrm{d}t} = 0, \tag{B.10}$$

where we defined $M_\perp$ as $M_x + \mathrm{i}M_y$. The solutions are given as follows:

$$M_\perp(t) = M_\perp^0 \exp(-\mathrm{i}\omega_0 t), \tag{B.11}$$

$$M_z(t) \equiv M_z^0. \tag{B.12}$$

In other words, once the magnetization is tilted to the xy-plane, it rotates in the azimuth direction at $-\omega_0$ while maintaining its zenith angle.

B.2 Signal Transmission and Reception

To tip the magnetization toward the xy-plane, we apply an RF magnetic field rotating in the xy-plane, which is called the B1 field. To clarify the effect of the B1 field while the B0 field is also present, we introduce the so-called rotating frame. The bases in the rotating frame are denoted as $(\tilde{\boldsymbol{e}}_x, \tilde{\boldsymbol{e}}_y, \tilde{\boldsymbol{e}}_z)$. While $\boldsymbol{e}_i$ are static, $\tilde{\boldsymbol{e}}_i$ change with time as follows:

$$\frac{\mathrm{d}\tilde{\boldsymbol{e}}_i}{\mathrm{d}t} = \boldsymbol{\omega}' \times \tilde{\boldsymbol{e}}_i, \tag{B.13}$$

where $\boldsymbol{\omega}'$ is the angular velocity of the rotation. Then, the following relations hold:

$$\left[\frac{\mathrm{d}\boldsymbol{f}}{\mathrm{d}t}\right]_{\mathrm{rot}} \coloneqq \frac{\mathrm{d}\tilde{f}_i}{\mathrm{d}t}\tilde{\boldsymbol{e}}_i = \frac{\mathrm{d}(\tilde{f}_i\tilde{\boldsymbol{e}}_i)}{\mathrm{d}t} - \tilde{f}_i\frac{\mathrm{d}\tilde{\boldsymbol{e}}_i}{\mathrm{d}t} = \frac{\mathrm{d}\boldsymbol{f}}{\mathrm{d}t} - \boldsymbol{\omega}' \times \boldsymbol{f}, \tag{B.14}$$

$$\left[\boldsymbol{g} \times \boldsymbol{f}\right]_{\mathrm{rot}} \coloneqq \epsilon_{ijk}\tilde{g}_i\tilde{f}_j\tilde{\boldsymbol{e}}_k = \tilde{g}_i\tilde{\boldsymbol{e}}_i \times \tilde{f}_j\tilde{\boldsymbol{e}}_j = \boldsymbol{g} \times \boldsymbol{f}, \tag{B.15}$$

where $\boldsymbol{f} = \tilde{f}_i\tilde{\boldsymbol{e}}_i, \boldsymbol{g} = \tilde{g}_i\tilde{\boldsymbol{e}}_i$. By using them, Eq. (B.4) can be rewritten as

$$\left[\frac{\mathrm{d}\boldsymbol{M}}{\mathrm{d}t}\right]_{\mathrm{rot}} = \left[-\gamma_0\left(\boldsymbol{B} + \frac{\boldsymbol{\omega}'}{\gamma_0}\right) \times \boldsymbol{M}\right]_{\mathrm{rot}} = \left[-\gamma_0\boldsymbol{B}^{\mathrm{eff}} \times \boldsymbol{M}\right]_{\mathrm{rot}}. \tag{B.16}$$

The effective field $\boldsymbol{B}^{\mathrm{eff}} \coloneqq \boldsymbol{B} + \boldsymbol{\omega}'/\gamma_0$ represents the magnetic field experienced by a spin on the rotating frame. Hence, it holds for $\tilde{\mathbf{M}} \coloneqq (\tilde{M}_x, \tilde{M}_y, \tilde{M}_z), \tilde{\mathbf{B}} = (\tilde{B}_x, \tilde{B}_y, \tilde{B}_z)$ that

$$\frac{\mathrm{d}\tilde{\mathbf{M}}}{\mathrm{d}t} = -\gamma_0\tilde{\mathbf{B}}^{\mathrm{eff}} \times \tilde{\mathbf{M}}. \tag{B.17}$$

B.2.1 Signal Transmission

From the above discussion, a stationary magnetic field oriented horizontally in a rotating frame needs to be applied to tip down the magnetization. We generate a magnetic field at the target position by applying a current oscillating at ω_1 to the transmit coil perpendicular to the xy-plane. When a current oscillating at ω_1 with the complex amplitude $I(t)$ is applied to the transmit coil with the area A_{T}, we can assume that there is an equivalent magnetic dipole perpendicular to the cross section of the coil with intensity

$$m(t) = \mathrm{Re}[A_{\mathrm{T}}I(t)\exp(-\mathrm{i}\omega_1 t)]. \tag{B.18}$$

The magnetic field created by this magnetic dipole also oscillates with frequency ω_1, and its amplitude and phase depend on the configuration of the coil and its relative position to the target location. Let the magnetic field generated at the target position be

$$\boldsymbol{B}_{1\mathrm{T}} = \mathrm{Re}[B_{1\mathrm{T},x}\exp(-\mathrm{i}\omega_1 t)]\boldsymbol{e}_x + \mathrm{Re}[B_{1\mathrm{T},y}\exp(-\mathrm{i}\omega_1 t)]\boldsymbol{e}_y. \tag{B.19}$$

If the complex magnetic field $B_\perp \coloneqq B_x + \mathrm{i}B_y$ is divided into positively and negatively rotating components with respect to $-\omega_1$, it can be expressed as follows:

$$\begin{aligned} B_{1\mathrm{T},\perp} &= \mathrm{Re}[B_{1\mathrm{T},x}\exp(-\mathrm{i}\omega_1 t)] + \mathrm{i}\,\mathrm{Re}[B_{1\mathrm{T},y}\exp(-\mathrm{i}\omega_1 t)] \\ &= \frac{B_{1\mathrm{T},x} + \mathrm{i}B_{1\mathrm{T},y}}{2}\exp(-\mathrm{i}\omega_1 t) + \frac{\bar{B}_{1\mathrm{T},x} + \mathrm{i}\bar{B}_{1\mathrm{T},y}}{2}\exp(\mathrm{i}\omega_1 t) \\ &= B_{1\mathrm{T}}^{+}\exp(-\mathrm{i}\omega_1 t) + \bar{B}_{1\mathrm{T}}^{-}\exp(\mathrm{i}\omega_1 t), \end{aligned} \tag{B.20}$$

where $B^{\pm} \coloneqq (B_x \pm \mathrm{i}B_y)/2$. We assume $\omega_1 \simeq \omega_0$, hereafter. Only the positively rotating component of the magnetic field can continuously act on the magnetization flipping onto the xy-plane. The counter-rotating component does not contribute to the MR signal; it only causes tissue heating. Quadrature excitation from two channels (I and Q channels) is often used to suppress this unwanted tissue heating. Let the transfer functions from the equivalent magnetization at the I-channel coil to each component of the magnetic field be $c_{\mathrm{T},x}$ and $c_{\mathrm{T},y}$. Then it holds that $B_{1\mathrm{T},x} = A_{\mathrm{T}} I(t) c_{\mathrm{T},x}$ and $B_{1\mathrm{T},y} = A_{\mathrm{T}} I(t) c_{\mathrm{T},y}$. From geometric considerations, the transfer functions from the equivalent magnetization at the Q-channel coil to each component of the magnetic field are given as $-c_{\mathrm{T},y}$ and $c_{\mathrm{T},x}$. If the phase of the current flowing in the Q-channel coil is set to be delayed by 90° (advanced by 90° degrees in the direction of rotation), the magnetic field is expressed as $B'_{1\mathrm{T},x} = -\mathrm{i}AI(t)c_{\mathrm{T},y} = -\mathrm{i}B_{1\mathrm{T},y}$ and $B'_{1\mathrm{T},y} = \mathrm{i}AI(t)c_{\mathrm{T},x} = \mathrm{i}B_{1\mathrm{T},x}$ and the complex magnetic field is written as

$$\begin{aligned} B'_{1\mathrm{T},\perp} &= \mathrm{Re}[-\mathrm{i}B_{1\mathrm{T},y}\exp(-\mathrm{i}\omega_1 t)] + \mathrm{i}\,\mathrm{Re}[\mathrm{i}B_{1\mathrm{T},x}\exp(-\mathrm{i}\omega_1 t)] \\ &= \frac{-\mathrm{i}B_{1\mathrm{T},y} + \mathrm{i}(\mathrm{i}B_{1\mathrm{T},x})}{2}\exp(-\mathrm{i}\omega_1 t) + \frac{\mathrm{i}\bar{B}_{1\mathrm{T},y} + \mathrm{i}(-\mathrm{i}\bar{B}_{1\mathrm{T},x})}{2}\exp(\mathrm{i}\omega_1 t) \\ &= B^{+}_{1\mathrm{T}}\exp(-\mathrm{i}\omega_1 t) - \bar{B}^{-}_{1\mathrm{T}}\exp(\mathrm{i}\omega_1 t). \end{aligned} \tag{B.21}$$

Summing them up leads to $B_{1\mathrm{T},\perp} = 2B^{+}_{1\mathrm{T}}\exp(-\mathrm{i}\omega_1 t)$, which means that the transmission efficiency is doubled and the SAR is reduced by half. In the following, we will denote this doubled value as $B^{+}_{1\mathrm{T}}$.

Let us investigate the time evolution of magnetization due to RF excitation. The governing equations of the magnetization in the rotating frame are expressed as follows:

$$\frac{\mathrm{d}\tilde{M}_\perp}{\mathrm{d}t} = \mathrm{i}\gamma_0\tilde{B}_{\mathrm{T},\perp}\tilde{M}_z = \mathrm{i}\gamma_0\tilde{B}^{+}_{1\mathrm{T}}\tilde{M}_z, \tag{B.22}$$

$$\frac{\mathrm{d}\tilde{M}_z}{\mathrm{d}t} = -\,\mathrm{Im}[\gamma_0\bar{B}_{\mathrm{T},\perp}M_\perp] = -\,\mathrm{Im}[\gamma_0\bar{B}^{+}_{1\mathrm{T}}\tilde{M}_\perp], \tag{B.23}$$

where we used the identity $f_x g_y - f_y g_x = \mathrm{i}(f_\perp \bar{g}_\perp - \bar{f}_\perp g_\perp)/2 = \mathrm{Im}[\bar{f}_\perp g_\perp]$. Note that the amplitude of the $B^{\pm}_1$ is a function of time but its phase is independent of time. The solution is given as

$$M_\perp(t) = \mathrm{i}M_0 \sin\!\left(\int_0^t \gamma_0 |B^{+}_{1\mathrm{T}}(t')|\mathrm{d}t'\right)\exp(\mathrm{i}\angle B^{+}_{1\mathrm{T}})\exp(-\mathrm{i}\omega_0 t), \tag{B.24}$$

$$M_z(t) = M_0 \cos\!\left(\int_0^t \gamma_0 |B^{+}_{1\mathrm{T}}(t')|\mathrm{d}t'\right), \tag{B.25}$$

which can be confirmed by substituting it into the original governing equations. In the azimuth direction, the magnetization rotates at the Larmor frequency 90° behind the phase of the B1 field (multiplying i means 90° delay since the rotation is negative), and in the zenith direction, it flips at the angular velocity of $\omega_{\mathrm{B1}} = \gamma_0 |B^{+}_{1\mathrm{T}}|$. The angle of tilt

$$\alpha_\tau \coloneqq \int_0^\tau \omega_{\mathrm{B1}}(t)\mathrm{d}t \coloneqq \int_0^\tau \gamma_0 |B^{+}_{1\mathrm{T}}(t)|\mathrm{d}t \tag{B.26}$$

when an RF pulse of duration τ is applied is called the flip angle.

B.2.2 Signal Reception

When the B1 field is turned off after τ, the magnetization rotates in the xy-plane at an angular velocity ω_0 while maintaining the flip angle α_τ. The transverse component of the magnetization $M_\perp$ follows the solution of the governing equation of the static field, where the initial

condition is the solution of the equation at τ. We will denote this as

$$M_\perp^\tau \coloneqq M_\perp(\tau) = \mathrm{i}M_0 \sin\left(\int_0^\tau \gamma_0 |B_{1\mathrm{T}}^+(t)|\mathrm{d}t\right) \exp(\mathrm{i}\angle B_{1\mathrm{T}}^+) \exp(-\mathrm{i}\omega_0\tau). \tag{B.27}$$

The receive coil detects the magnetic field generated by this rotating magnetization as induced electromotive force.

From the principle of reciprocity, the magnetic field generated at the receive coil by the magnetization at the target location is equal to the magnetic field generated at the target location by the transmit coil. Suppose that a current with complex amplitude I and carrier frequency $-\omega_0$ is applied to the receive coil with area A_R to generate a magnetic dipole of magnitude $m'(t) = \mathrm{Re}[A_\mathrm{R} I \exp(-\mathrm{i}\omega_0 t)]$ and direction perpendicular to the receive coil, creating a magnetic field $\mathrm{Re}[B_{1\mathrm{R},x} \exp(-\mathrm{i}\omega_0 t)]\boldsymbol{e}_x, \mathrm{Re}[B_{1\mathrm{R},y} \exp(-\mathrm{i}\omega_0 t)]\boldsymbol{e}_y$ at the target location. This means that the transfer functions can be expressed as

$$c_{\mathrm{R},x} = A_\mathrm{R} I B_{1\mathrm{R},x}, \tag{B.28}$$

$$c_{\mathrm{R},y} = A_\mathrm{R} I B_{1\mathrm{R},y}. \tag{B.29}$$

The reciprocity principle means that the transfer functions remain the same when the positions of the source and target are switched. Therefore, the magnetic fields at the receive coil perpendicular to it created by the magnetic dipoles at the target position orienting x- and y-directions with magnitudes of $M_x^\tau = \mathrm{Re}[M_\perp^\tau \exp(-\mathrm{i}\omega_0 t)], M_y^\tau = \mathrm{Im}[M_\perp^\tau \exp(-\mathrm{i}\omega_0 t)] = \mathrm{Re}[-\mathrm{i}M_\perp^\tau \exp(-\mathrm{i}\omega_0 t)]$ are given as

$$B_\mathrm{R}^x = \mathrm{Re}[M_\perp^\tau c_{\mathrm{R},x} \exp(-\mathrm{i}\omega_0 t)] = \mathrm{Re}\left[\frac{M_\perp^\tau}{A_\mathrm{R} I} B_{1\mathrm{R},x} \exp(-\mathrm{i}\omega_0 t)\right], \tag{B.30}$$

$$B_\mathrm{R}^y = \mathrm{Re}[-\mathrm{i}M_\perp^\tau c_{\mathrm{R},y} \exp(-\mathrm{i}\omega_0 t)] = \mathrm{Re}\left[-\mathrm{i}\frac{M_\perp^\tau}{A_\mathrm{R} I} B_{1\mathrm{R},y} \exp(-\mathrm{i}\omega_0 t)\right]. \tag{B.31}$$

Therefore, the induced electromotive force detected by the receive coil is given as

$$V(t) = -A_\mathrm{R} \frac{\mathrm{d}(B_\mathrm{R}^x + B_\mathrm{R}^y)}{\mathrm{d}t} = \mathrm{Re}\left[\frac{2\omega_0}{I} \mathrm{i}M_\perp^\tau B_{1\mathrm{R}}^- \exp(-\mathrm{i}\omega_0 t)\right]. \tag{B.32}$$

Now we consider the case of using the quadrature birdcage coil for signal reception. From geometric considerations, it holds that $c'_{x,\mathrm{R}} = -c_{\mathrm{R},y}$ and $c'_{y,\mathrm{R}} = c_{\mathrm{R},x}$. This time, we add the signals detected by the Q-channel coil with the phase advanced by 90° (delayed 90° with respect to the direction of rotation). In Practical situations, the phase of the Q-channel signal after detection is shifted and added, but here we consider that the phase of the magnetic field is shifted hypothetically and added to the I-channel signal as follows:

$$B_\mathrm{R}^{x'} = \mathrm{Re}\left[-\mathrm{i}\frac{M_\perp^\tau}{A_\mathrm{R} I} B_{1\mathrm{R},y} \exp(-\mathrm{i}\omega_0 t)\right], \tag{B.33}$$

$$B_\mathrm{R}^{y'} = \mathrm{Re}\left[\frac{M_\perp^\tau}{A_\mathrm{R} I} B_{1\mathrm{R},x} \exp(-\mathrm{i}\omega_0 t)\right]. \tag{B.34}$$

In this case, the induced electromotive force detected by the Q-channel coil is given as

$$V_\mathrm{Q}(t) = -A_\mathrm{R} \frac{\mathrm{d}(B_\mathrm{R}^{x'} + B_\mathrm{R}^{y'})}{\mathrm{d}t} = \mathrm{Re}\left[\frac{2\omega_0}{I} \mathrm{i}M_\perp^\tau B_{1\mathrm{R}}^- \exp(-\mathrm{i}\omega_0 t)\right]. \tag{B.35}$$

Therefore, the combined signal of both channels is doubled, and the SNR is improved by a factor of $\sqrt{2}$. In the following, the combined signal will be denoted as V.

By substituting the transmission equation, V is expressed as

$$V(t) = \mathrm{Re}\left[\frac{2\omega_0}{I}\mathrm{i}M_0 \sin\left(\int_0^\tau \gamma_0 |B_{1\mathrm{T}}^+(t')|\mathrm{d}t'\right)|B_{1\mathrm{R}}^-| \exp(\mathrm{i}(\angle B_{1\mathrm{T}}^+ + \angle B_{1\mathrm{R}}^-)) \exp(-\mathrm{i}\omega_0\tau) \exp(-\mathrm{i}\omega_0 t)\right]. \tag{B.36}$$

Then, this signal is demodulated by the quadrature detection during which the phase factor $-\omega_0\tau$ is also compensated. The final detected signal is written as

$$S = \frac{2\omega_0}{I}\mathrm{i}M_0 \sin\left(\int_0^\tau \gamma_0 |B_{1\mathrm{T}}^+(t')|\mathrm{d}t'\right)|B_{1\mathrm{R}}^-| \exp(\mathrm{i}(\angle B_{1\mathrm{T}}^+ + \angle B_{1\mathrm{R}}^-)). \tag{B.37}$$

The contribution of the B1 magnetic fields and other constants are combined together and written as $S = cM_0$, hereafter.

B.3 Image Formation

In the previous section, we considered the signal generated by a single proton. However, the purpose of MRI is to measure the spatial pattern of magnetization $M_0(\boldsymbol{r})$ generated by an ensemble of spins inside the human body. The essence of the nuclear magnetic resonance is that a magnetization is excited with a frequency proportional to the intensity of the external magnetic field. Therefore, changing the field strength spatially by creating a gradient in the B0 field, or rotational frequency allows to encode spatial information into the phase of the MR signal.

B.3.1 Spatially Selective Excitation

It is necessary to limit the magnetization to be excited to a certain range to prevent signals outside the FOV from being mixed in unless the FOV completely encloses the object. Io achieve this, the magnitude of the B1 field $|B_{1\mathrm{T}}^+|$ in the rotating frame needs to change in time. To see the time evolution of the RF excitation, we generally divide the RF pulse into small time segments Δt and approximate each segment as a hard pulse with constant value and consider the limit of Δt to be 0. However, the solution cannot be obtained analytically, and numerical calculation is required. A special case where the analytical solution can be obtained is called the small tip-angle approximation (STA). In STA, we consider the case where the flip angle is sufficiently small. In this case, if we consider a coordinate system rotating clockwise at $\omega_0 + \gamma_0 \boldsymbol{G}\cdot\boldsymbol{r}$, the magnetic field produced by a hard pulse with a small time width Δt starting at time t is written as $B_{1\mathrm{T}}^+ \exp(\mathrm{i}\gamma_0 \boldsymbol{G}\cdot\boldsymbol{r}t)$ and the magnetization excited by this field is given as

$$\Delta\tilde{M}_\perp = \mathrm{i}M_0 \exp(\mathrm{i}\angle B_{1\mathrm{T}}^+) \exp(\mathrm{i}\gamma_0 \boldsymbol{G}\cdot\boldsymbol{r}t) \sin(\gamma_0 |B_{1\mathrm{T}}^+|\Delta t) \tag{B.38}$$

$$\simeq \mathrm{i}\gamma_0 M_0 \exp(\mathrm{i}\angle B_{1\mathrm{T}}^+) \exp(\mathrm{i}\gamma_0 \boldsymbol{G}\cdot\boldsymbol{r}t)|B_{1\mathrm{T}}^+|\Delta t. \tag{B.39}$$

Each hard pulse is considered to excite the spins independently by a small angle. The sum of all the effects is given as

$$\tilde{M}_\perp = \mathrm{i}\gamma_0 M_0 \exp(\mathrm{i}\angle B_{1\mathrm{T}}^+) \int_0^\tau |B_{1\mathrm{T}}^+| \exp(\mathrm{i}\gamma_0 \boldsymbol{G}\cdot\boldsymbol{r}t)\mathrm{d}t. \tag{B.40}$$

Returning to the rotating frame at ω_0 yields

$$\tilde{M}_\perp(\boldsymbol{r}) = \mathrm{i}\gamma_0 M_0 \exp(\mathrm{i}\angle B_{1\mathrm{T}}^+) \exp(-\mathrm{i}\gamma_0 \boldsymbol{G}\cdot\boldsymbol{r}\tau) \int_0^\tau |B_{1\mathrm{T}}^+(t)| \exp(\mathrm{i}\gamma_0 \boldsymbol{G}\cdot\boldsymbol{r}t)\mathrm{d}t. \tag{B.41}$$

If the support of $B_{1\mathrm{T}}^{+}$ is restricted between 0 and t, then the interval of integration can be extended to infinity as

$$\tilde{M}_{\perp}(\boldsymbol{r}) = \mathrm{i}\gamma_0 M_0 \exp(\mathrm{i}\angle B_{1\mathrm{T}}^{+}) \exp\left(-\mathrm{i}\frac{\gamma_0 \boldsymbol{G}\cdot\boldsymbol{r}\tau}{2}\right) \int_{-\tau/2}^{+\tau/2} |B_{1\mathrm{T}}^{+}(t+\tau/2)| \exp(\mathrm{i}\gamma_0 \boldsymbol{G}\cdot\boldsymbol{r}t)\mathrm{d}t \tag{B.42}$$

$$= \mathrm{i}\gamma_0 M_0 \exp(\mathrm{i}\angle B_{1\mathrm{T}}^{+}) \exp\left(-\mathrm{i}\frac{\gamma_0 \boldsymbol{G}\cdot\boldsymbol{r}\tau}{2}\right) \int_{-\infty}^{+\infty} |B_{1\mathrm{T}}^{+}| \exp(\mathrm{i}\gamma_0 \boldsymbol{G}\cdot\boldsymbol{r}t)\mathrm{d}t \tag{B.43}$$

$$= \mathrm{i}\gamma_0 M_0 \exp(\mathrm{i}\angle B_{1\mathrm{T}}^{+}) \exp\left(-\mathrm{i}\frac{\gamma_0 \boldsymbol{G}\cdot\boldsymbol{r}\tau}{2}\right) \mathcal{F}[|B_{1\mathrm{T}}^{+}|](-\Delta\omega(\boldsymbol{r})). \tag{B.44}$$

The magnetization is determined by the temporal frequency spectrum of the B1 field.

After the RF pulse is applied, a negative gradient field must be applied to re-phase the spin. This is because the gradient field causes the frequency to change linearly within the FOV, and thus the phase at each point in the region is dispersed after the RF pulse is applied. Therefore, the phase difference between each point in the region is compensated for by applying a gradient field of opposite polarity as follows:

$$\tilde{M}_{\perp}(\boldsymbol{r}) = \mathrm{i}\gamma_0 M_0 \exp(\mathrm{i}\angle B_{1\mathrm{T}}^{+}) \mathcal{F}[|B_{1\mathrm{T}}^{+}|](-\Delta\omega(\boldsymbol{r})). \tag{B.45}$$

Since the Fourier transform of a real symmetric function (even function) is a real function, the magnitude and phase of the magnetization become $\gamma_0 M_0 \mathcal{F}[|B_{1\mathrm{T}}^{+}|](-\Delta\omega(\boldsymbol{r}))$ and $\angle B_{1\mathrm{T}}^{+} + \pi/2$.

In practice, a gradient field $G_z z$ is applied simultaneously with the RF pulse to change the resonance frequency along the z-axis as follows:

$$\omega(z) = \gamma_0(B_0 + G_z z) = \omega_0 + \gamma_0 G_z z. \tag{B.46}$$

Consider that this excites only a specific slice or slab $[z_{\mathrm{c}} - \Delta z/2, z_{\mathrm{c}} + \Delta z/2]$ with a uniform intensity and does not excite outside the section. We should apply a waveform that has finite values only in the corresponding band $[\omega_0 + \gamma_0 G_z(z_{\mathrm{c}} - \Delta z/2), \omega_0 + \gamma_0 G_z(z_{\mathrm{c}} + \Delta z/2)]$ and not in the outer band. Such a frequency spectrum can be realized by the sinc function.

Since the sinc function has an infinite support, it must be truncated at a certain time width, causing the Gibbs ringing in the excitation profile. A windows function such as the Hann window is used to suppress the Gibbs ringing.

B.3.2 Spatial Information Encoding

We consider the situation where only the magnetization in a particular slice or slab is excited by slice-selective excitation explained above. After the excitation by an RF pulse, a magnetic field $\boldsymbol{G}_{\mathrm{PE}}\cdot\boldsymbol{r}$ linearly varying with position is applied in the axial direction for a time period T, and the phase is offset to

$$\phi_{\mathrm{PE}}(\boldsymbol{r}) = \gamma_0 \int_0^T \boldsymbol{G}_{\mathrm{PE}}(t)\cdot\boldsymbol{r}\mathrm{d}t. \tag{B.47}$$

The above method is called phase encoding because spatial information is encoded into the phase offset.

Next, let us consider the situation where only the magnetization in a specific slice is excited by slice-selective excitation, and the initial phase is offset by applying a phase-encoding gradient field. By applying a constant gradient field $\boldsymbol{G}_{\mathrm{FE}}\cdot\boldsymbol{r}$ during the signal readout, the precession frequency is shifted from ω_0 to

$$\omega_{\mathrm{FE}}(\boldsymbol{r}, t) = \gamma_0 \boldsymbol{G}_{\mathrm{FE}}(t)\cdot\boldsymbol{r} \tag{B.48}$$

so that the phase at the time $0 < t < T_{\mathrm{acq}}$ after the application of the gradient field is given in the rotating frame as follows:

$$\phi(\boldsymbol{r}, t) = \phi_{\mathrm{PE}}(\boldsymbol{r}) + \int_0^t \omega_{\mathrm{FE}}(\boldsymbol{r}, t')\mathrm{d}t', \qquad 0 \le t \le T_{\mathrm{acq}}. \tag{B.49}$$

In order to make the temporal profile of the signal symmetrical, a gradient field of opposite polarity is applied beforehand, and the correct method is as follows:

$$\phi(\boldsymbol{r}, t) = \phi_{\mathrm{PE}}(\boldsymbol{r}) + \int_0^t \omega_{\mathrm{FE}}(\boldsymbol{r}, t')\left(t' - \frac{T_{\mathrm{acq}}}{2}\right)\mathrm{d}t', \qquad 0 \le t \le T_{\mathrm{acq}}. \tag{B.50}$$

The above method is called frequency encoding because spatial information is encoded into the frequency change.

Finally, the signal is read out as a time-series signal:

$$s(t) = \int_V c(\boldsymbol{r}) M_0(\boldsymbol{r}) \exp(-\mathrm{i}\boldsymbol{k}(t) \cdot \boldsymbol{r}) \exp(-\mathrm{i}\omega_0 t)\mathrm{d}^3\boldsymbol{r}, \tag{B.51}$$

where

$$\boldsymbol{k}(t) = \gamma_0 \int_0^T \boldsymbol{G}_{\mathrm{PE}}(t') \cdot \boldsymbol{r}\mathrm{d}t' + \gamma_0 \int_0^t \boldsymbol{G}_{\mathrm{FE}}(t') \cdot \boldsymbol{r}\left(t' - \frac{T_{\mathrm{acq}}}{2}\right)\mathrm{d}t'. \tag{B.52}$$

Since it holds that $\gamma_0 \boldsymbol{G} \cdot \boldsymbol{r} \ll \omega_0$, the signal $s(t)$ is narrow-band with its central frequency being ω_0. Therefore, we can filter out the career frequency by the quadrature detection to obtain

$$S(\boldsymbol{k}(t)) = \int_V c(\boldsymbol{r}) M_0(\boldsymbol{r}) \exp(-\mathrm{i}\boldsymbol{k} \cdot \boldsymbol{r})\mathrm{d}^3\boldsymbol{r}. \tag{B.53}$$

Since the magnetization outside the FOV is not excited, the integration range can be considered as an infinite domain, and the inverse Fourier transform gives

$$c(\boldsymbol{r}) M_0(\boldsymbol{r}) = \mathcal{F}^{-1}[S(\boldsymbol{k})](\boldsymbol{r}). \tag{B.54}$$

When the B1 field is sufficiently uniform and c can be regarded as a constant, it directly represents the distribution of magnetization M_0.

From the above equation, $\boldsymbol{k}$ represents the spatial frequency and S can be regarded as the spatial frequency spectrum of cM_0. The trajectory of $\boldsymbol{k}$ depends on the profile of $\boldsymbol{G}$. The region of spatial frequency is called the k-space, and Fourier imaging is the technique to fill the k-space by repeatedly measuring signals while changing $\boldsymbol{G}$.

There are two major methods for filling k-space: the spin warp method, which is based on Cartesian coordinates, and the radial method, which is based on the polar coordinates. In the spin warp method, phase encoding is performed in the y-direction in 2D imaging, and in the y- and z-directions in 3D imaging, and frequency encoding is performed in the x-direction. In the case of the y-direction, the phase is changed by applying a gradient magnetic field $G_y y$ for a fixed time T_{p} as follows:

$$\phi(x, y) = \gamma_0 G_y y T_{\mathrm{p}}. \tag{B.55}$$

For each fixed value of G_y, a point $k_y = \gamma_0 G_y y T_{\mathrm{p}}$ in the k-space is filled. Therefore, by repeating this phase encoding while varying the magnitude of G_y, a line of the k-space along with the y-axis is filled.

B.4 Image Contrast

So far, we have considered a population of isolated spins with no interaction. As a result, magnetization (proton density) is a sole factor of image contrast. There are actually electrons and lattices in addition to protons. The interactions between these protons as well as electrons and lattices beget the image contrast reflecting the cellularity, molecularity, and vascularity of the living organism and provides superb rich contrast.

B.4.1 Longitudinal and Transverse Relaxation

Molecules inside tissue experience tumbling: intramolecular rotation and intermolecular collision, but proton–proton interaction affecting relaxation can be considered to act only intramolecularly. There are two types of proton–proton interaction: spin–lattice relaxation (longitudinal relaxation) and spin–spin relaxation (transverse relaxation). The equation of precession is modified to incorporate the effect of relaxation as follows:

$$\frac{\partial \boldsymbol{M}}{\partial t} = -\gamma_0 \boldsymbol{B} \times \boldsymbol{M} - \frac{M_x \boldsymbol{e}_x + M_y \boldsymbol{e}_y}{T_2} - \frac{(M_0 - M_z)\boldsymbol{e}_z}{T_1}, \tag{B.56}$$

where T_1 and T_2 is the time constants of the longitudinal and transverse relaxation. This phenomenological equation is called the Bloch equation and is extensively discussed in e.g., [183]. The solution of Eq. (B.56) is given as

$$M_\perp(t) = M_\perp^0 \exp\left(-\frac{t}{T_2}\right), \tag{B.57}$$

$$M_z(t) = M_z^0 \exp\left(-\frac{t}{T_1}\right) + M_0\left(1 - \exp\left(-\frac{t}{T_1}\right)\right). \tag{B.58}$$

The above equations provide fundamentals of MR echo formation.

The Bloch equation has been extended to incorporate other proton interactions such as chemical exchange and magnetization saturation transfer [183].

B.4.2 Coherent and Incoherent Motion

Diffusion and blood flow can be analyzed using gradient encoding. Diffusion is caused by an incoherent microscopic motion, whereas macroscopic flow is caused by a coherent motion.

The Torrey equation describes the time evolution of the magnetization under diffusion:

$$\frac{\partial \boldsymbol{M}}{\partial t} = -\gamma_0 \boldsymbol{B} \times \boldsymbol{M} + \nabla \cdot (\boldsymbol{D} \cdot \nabla \boldsymbol{M}), \tag{B.59}$$

where $\boldsymbol{D}$ is the diffusion tensor. By ignoring the spatial variation of $\boldsymbol{D}$, the governing equation for $\tilde{M}_\perp$ is written as

$$\frac{\partial \tilde{M}_\perp}{\partial t} = -\mathrm{i}\gamma_0 \boldsymbol{G} \cdot \boldsymbol{r} \tilde{M}_\perp + \boldsymbol{D} : \nabla\nabla \tilde{M}_\perp, \tag{B.60}$$

the solution of which is given as

$$\tilde{M}_\perp(\boldsymbol{r}, t) = \tilde{M}_\perp^0 \exp\left(-\int_0^t \boldsymbol{q}(t') \cdot \boldsymbol{D} \cdot \boldsymbol{q}(t') \mathrm{d}t'\right) \exp(-\mathrm{i}\boldsymbol{q}(t) \cdot \boldsymbol{r}), \tag{B.61}$$

where

$$\boldsymbol{q}(t) \coloneqq \int_0^t \gamma_0 \boldsymbol{G}(t') \mathrm{d}t'. \tag{B.62}$$

A bipolar gradient with duration δ and gap $\Delta - \delta$ is used to encode the diffusion tensor into the MRI signal. Let be the additional gradient field $\boldsymbol{G}$ expressed as

$$\boldsymbol{G}(t) = \begin{cases} \boldsymbol{G}_0 & 0 \le t \le \delta \\ \boldsymbol{0} & \delta < t < \Delta \\ -\boldsymbol{G}_0 & \Delta \le t \le \Delta + \delta \end{cases} \tag{B.63}$$

is applied after RF excitation. Then it follows that

$$\boldsymbol{q}(t) = \begin{cases} \gamma_0 \boldsymbol{G}_0 t & 0 \le t \le \delta \\ \gamma_0 \boldsymbol{G}_0 \delta & \delta < t < \Delta \\ \gamma_0 \boldsymbol{G}_0 (\Delta + \delta - t) & \Delta \le t \le \Delta + \delta \end{cases}, \tag{B.64}$$

and thus we obtain

$$\tilde{M}_\perp(\boldsymbol{r}, \Delta + \delta) = \tilde{M}_\perp^0 \exp(-\gamma_0^2 b \boldsymbol{G}_0 \cdot \boldsymbol{D} \cdot \boldsymbol{G}_0), \qquad b \coloneqq \delta^2 \left(\Delta - \frac{\delta}{3} \right). \tag{B.65}$$

The other factors contributing to magnitude decay are cancelled by considering the ratio of the measurement without bipolar gradient. The symmetric tensor $\boldsymbol{D}$ can be determined by changing the direction of the gradient field in six or more directions and repeating the measurement.

The effect of any incoherent movement on the voxel scale such as the flow through the complex capillary is included in the above relation. Therefore, the estimated $\boldsymbol{D}$ using the above method is called the apparent diffusion coefficient (ADC).

The time evolution of the magnetization under the velocity $\boldsymbol{v}$ is governed by the following equation:

$$\frac{\partial \boldsymbol{M}}{\partial t} = -\gamma_0 \boldsymbol{B} \times \boldsymbol{M} - \nabla \cdot (\boldsymbol{v} \boldsymbol{M}), \tag{B.66}$$

which can be solved analytically by neglecting the spatial variation of $\boldsymbol{v}$ and assuming that the spatial variation of the initial magnetization is sufficiently small. In this case, the governing equation is written as

$$\frac{\partial \tilde{M}_\perp}{\partial t} = -\mathrm{i} \gamma_0 \boldsymbol{G} \cdot \boldsymbol{r} \tilde{M}_\perp + \boldsymbol{v} \cdot \nabla \tilde{M}_\perp, \tag{B.67}$$

and the solution is given as

$$\tilde{M}_\perp(\boldsymbol{r}, t) = \tilde{M}_\perp^0 \exp\left(-\mathrm{i} \left(\boldsymbol{q}(t) \cdot \boldsymbol{r} + \int_0^t \boldsymbol{q}(t') \cdot \boldsymbol{v}(t') \mathrm{d}t' \right) \right). \tag{B.68}$$

A bipolar gradient with no gap is used to encode the velocity into the MRI signal. Let be the additional gradient field $\boldsymbol{G}$ expressed as

$$\boldsymbol{G}(t) = \begin{cases} \boldsymbol{G}_0 & 0 \le t \le \delta \\ -\boldsymbol{G}_0 & \delta \le t \le 2\delta \end{cases} \tag{B.69}$$

is applied after RF excitation. Then it follows that

$$\boldsymbol{q}(t) = \begin{cases} \gamma_0 \boldsymbol{G}_0 t & 0 \le t \le \delta \\ \gamma_0 \boldsymbol{G}_0 (2\delta - t) & \delta \le t \le 2\delta, \end{cases} \tag{B.70}$$

and thus we obtain

$$\tilde{M}_\perp(\boldsymbol{r}, 2\delta) = \tilde{M}_\perp^0 \exp(-\mathrm{i} \gamma_0 \delta^2 \boldsymbol{G}_0 \cdot \boldsymbol{v}). \tag{B.71}$$

Other phase contributions are canceled by taking the difference between two measurements with the reversed bipolar gradient.

We note that the blood flow and perfusion can be analyzed by some other techniques such as spin labeling and contrast enhanced imaging.

B.4.3 Other Contrast Sources Treated in This Thesis

The relaxation effect considered in the former section arises from short-range intramolecular interactions. There are also long-range intermolecular interactions in which spins at a macroscopically distant location can alter the MRI signal.

Magnetic properties of tissues caused by proton–electron interaction modulate the B0 field, resulting in precession frequency shift, while electric properties of tissues modulate initial phase and magnitude of the B1 field. Therefore, these electromagnetic tissue properties can be investigated by measuring the B0 and B1 fields, giving the fundamental concepts of EPT and QSM explored in Chapters 2, 4, and 5. Mechanical properties of tissues affect how viscoelastic waves propagate when externally oscillated. This long-range effect can be studied by MRE as described in Chapter 3.

B.5 Echo Formation

This section explains how to form MR echo signals. We first refer to the notion of T_2^*-relaxation. Depending on the magnetic field distribution in a voxel, phase dispersion occurs in the voxel and transverse relaxation is further enhanced. If we assume that the magnetic field distribution in the voxel follows the Lorentz distribution (also known as the Cauchy distribution), then the frequency spectrum of the magnetization in a voxel is expressed as

$$\mathcal{F}[M](\omega) = M_0 \frac{(\gamma_0 B_{\mathrm{FWHM}}/2)^2}{(\gamma_0 B_{\mathrm{FWHM}}/2)^2 + (\omega - \omega_0)^2}. \tag{B.72}$$

Note that the Lorentz distribution does not have moments such as expectation and variance and the full width at half maximum (FWHM) is usually taken as the parameter characterizing the distribution. Then, the time constant T_2^* is given as

$$\frac{1}{T_2^*} = \frac{1}{T_2} + \frac{1}{2}\gamma_0 B_{\mathrm{FWHM}}. \tag{B.73}$$

Note that T_2^* does not purely reflect the property of the object but depends on the imaging parameters such as the size of the voxels.

B.5.1 Spin Echo (SE)

SE imaging reverses the T_2^*-relaxation effect to produce a strong echo. The longitudinal magnetization $T_{\mathrm{E}}/2$ after the 90°-pulse is given as

$$M_{z,-}(T_{\mathrm{E}}/2) = M_0\left(1 - \exp\left(-\frac{T_{\mathrm{E}}/2}{T_1}\right)\right). \tag{B.74}$$

After that, the longitudinal magnetization is negated by the reversal pulse, and then recovered by longitudinal relaxation for $T_R - T_E/2$.

$$\begin{aligned} M_{z,-}^{ss} &= -M_0\left(1 - \exp\left(-\frac{T_E/2}{T_1}\right)\right)\exp\left(-\frac{T_R - T_E/2}{T_1}\right) + M_0\left(1 - \exp\left(-\frac{T_R - T_E/2}{T_1}\right)\right) \\ &= M_0\left(1 - 2\exp\left(-\frac{T_R - T_E/2}{T_1}\right) + \exp\left(-\frac{T_R}{T_1}\right)\right) \\ &\simeq M_0\left(1 - \exp\left(-\frac{T_R}{T_1}\right)\right), \end{aligned} \tag{B.75}$$

where we assumed that $T_R \gg T_E$. In this situation, the horizontal magnetization disappears. The initial value of the transverse magnetization is the one that tips to the horizontal plane with a 90°-pulse, and the transverse magnetization relaxes horizontally

$$M_\perp(T_E) = M_0\left(1 - \exp\left(-\frac{T_R}{T_1}\right)\right)\exp\left(-\frac{T_E}{T_2}\right). \tag{B.76}$$

This is the peak value of the envelope of the MR signal.

The SE signal shows different contrast depending on T_E and T_R. When $T_E \ll T_2$, we can assume that $T_R \sim T_1$, yielding

$$M_\perp(T_E) \simeq M_0\left(1 - \exp\left(-\frac{T_R}{T_1}\right)\right), \tag{B.77}$$

which reflects T_1 distribution and is called the T1 weighted (T1w) image. On the other hand, when $T_R \gg T_1$, we can assume that $T_E \sim T_2$, yielding

$$M_\perp(T_E) \simeq M_0 \exp\left(-\frac{T_E}{T_2}\right), \tag{B.78}$$

which reflects T_2 distribution and is called the T2 weighted (T2w) image.

B.5.2 Gradient Echo (GRE)

Since no inversion pulse is applied in GRE, the transverse relaxation proceeds with the time constant T_2^*. Instead, T_R can be shortened, which makes GRE sequence suitable for high-speed imaging. In this case, a spoiler gradient is applied to eliminate the residual transverse magnetization due to the short repetition interval. The echo signal at the steady state is given as

$$M_{z,-}^{ss} = M_{z,+}^{ss}\exp\left(-\frac{T_R}{T_1}\right) + M_0\left(1 - \exp\left(-\frac{T_R}{T_1}\right)\right). \tag{B.79}$$

Substituting

$$M_{z,+}^{ss} = M_{z,-}^{ss}\cos\alpha \tag{B.80}$$

into the above equation yields

$$M_{z,-}^{ss} = \frac{M_0(1 - \exp(-T_R/T_1))}{1 - \cos\alpha\exp(-T_R/T_1)}. \tag{B.81}$$

Since the transverse magnetization relaxes with T_1 with the initial value being the flipped magnetization by the α-pulse, it holds that

$$M_\perp(T_E) = \frac{M_0(1 - \exp(-T_R/T_1))}{1 - \cos\alpha\exp(-T_R/T_1)}\sin\alpha\exp\left(-\frac{T_E}{T_2^*}\right). \tag{B.82}$$

If we set α as a large value and make T_E short, the image becomes a T1w image; if we make T_R relatively long, the image becomes a T2w image.